Mechanics and Mechanisms of Ultrasonic Metal Welding

Dissertation

Presented in Partial Fulfillment of the Requirements for the Degree

Doctor of Philosophy

In the Graduate School of The Ohio State University

By

Dipl. Ing. Edgar de Vries (FH)

****

The Ohio State University
2004

Dissertation Committee:

Professor Karl Graff, Adviser

Professor Charles Albright

Professor Avraham Benatar

Professor Stanislav Rokhlin

Approved by

_____

Adviser

Welding Engineering Graduate Program

Abstract

During ultrasonic welding of sheet metal, normal and shear forces act on the parts to be welded and the weld interface. These forces are a result of the ultrasonic vibrations of the tool, pressed onto the parts to be welded. Furthermore they determine the weld quality and the power that is needed to produce the weld. The main goal in this study is to measure and calculate the tangential forces during ultrasonic metal welding that act on the parts and the weld interface and correlate them to weld quality. In this study a mechanics based model was developed which included a model for the temperature generation during welding and its effect on the mechanical material properties. This model was then used to calculate the interface forces during welding. The model results were in good agreement with the experimental results, which included the measured shear force during welding.

With the knowledge of the forces that act at the interface it might be possible to control weld quality (strength) and avoid sonotrode welding (sticking of the sonotrode to the parts). Without a solution to these two problems USMW will never be applicable to large scale automated production use, despite its advantages.
In the experiments the influence of part dimensions, friction coefficient, normal force and vibration amplitude on weld quality and sonotrode adhesion were examined.

The presented model is capable of predicting and explaining unfavorable welding conditions, therefore making it possible to predetermine weld locations on larger parts or

what surface preparation of the parts to be welded would lead to an improved welding result. Furthermore shear force at the anvil measured during welding could be correlated to changing welding conditions.

This is a new approach of explaining the process of USMW, because it is based on mechanical considerations. The use of a shear force measuring anvil has the potential to be implemented into welding systems and the shear force would provide an additional means of process control.

ACKNOWLEDGMENTS

VITA

May 19, 1975…………………   Born – Leer, Germany

2000……………………..……...   ME (Diplom Ingenieur FH) University of

Applied Science

Oldenbung/Ostfriesland/Wilhelmshaven

Engineering Physiks

April 2001-present…………….   Graduate Research Associate

The Ohio State University, Columbus Ohio

PUBLICATIONS

1. de Vries, E., Graff, K., "The Mechanics of Ultrasonic Metal Welding, Part 2", Ultrasonic Industry Association Symposium, Indianapolis IN, Sep. 2003

2. de Vries, E., Graff, K., "The Mechanism of Ultrasonic Metal Welding" Ultrasonic Industry Association Symposium, New York NY, Sep. 2002

3. de Vries, E., "Twin-Spot laser welding with CO_2 high-power Laser", Laser Opto, Dec. 1999

FIELDS OF STUDY

Applied Physics:

- Material Science

- Laser Technology

Welding Engineering:

- Welding Processes

- Non Destructive Evaluation

- Vibrations

TABLE OF CONTENTS

THE TWO DIMENSIONAL STRESS STATE AND THE CORRESPONDING SHEAR
YIELD CONDITION

DRIVING POINT IMPEDANCE ANALYSIS FOR FORCED LONGITUDINAL ROD
VIBRATIONS

OPTICAL 'FOTONIC' SENSOR

DATA ACQUISITION SYSTEM AND ULTRASONIC WELD MONITOR
SOFTWARE

ULTRASONIC PROJECTION WELDING

LIST OF TABLES

LIST OF FIGURES

xvii

ABBREVIATIONS

A: Cross section area

A_{DZ}:   Deformation zone area

A_{FR}:   Friction area

A_{NC}:   No contact area

A_S: Sonotrode area

A_W: Weld area

β: Included knurl angle

c: Longitudinal thin rod wave velocity

C_d: Centerline distance

d: Part thickness

dy: Deformation zone thickness

D_k: Knurl width

ΔX: Elastic shear strain

E: Young's modulus

F_A: Tangential anvil force

F_{AM}:   Excitation force

F_I: Tangential interface force

F_N: Normal force

F_S: Maximum tangential sonotrode force

F_W: Tangential welding force

f_W: Welding frequency (Hz)

G: Shear modulus

γ: Deformation angle

h: Knurl depth

I_{RMS}:   RMS-Current

j:	Velocity build up constant
k:	Weld area growth constant
L:	Evaluation length
l:	Extension length
m:	Mass of the reduced top part
μ_S:	Static friction coefficient
P:	Power
$\dot{q}_{FR}$:	Friction heat flux
$\dot{q}_W$:	Welding heat flux
R_a:	Roughness average
ρ:	Density
σ_N:	Normal stress
t:	Time
T:	Temperature
τ_Y:	Shear yield stress
V_{DZ}:	Deformation zone volume
V_{RMS}:	RMS-Voltage
v_S:	Sonotrode velocity
W:	Work
ω_E:	Anvil excitation frequency (Radians/time)
ξ_0:	Sonotrode amplitude
ξ_{avg}:	Equivalent rigid body amplitude
ξ_{int}:	Interface amplitude
Y(T):	Temperature dependent yield strength
υ:	Poisons ratio
Ω:	Sonotrode excitation frequency (Radians/time)

CHAPTER 1

INTRODUCTION AND PROBLEM STATEMENT

Ultrasonic metal welding (USMW) was invented over 50 years ago and has now been in use in industry for many years. USMW is a process in which two metals are joined by the application of ultrasonic vibrations, under moderate pressure, in which the vibrations are applied parallel to the interface between the parts. The high frequency relative motion between the parts forms a solid-state weld through progressive shearing and plastic deformation between surface asperities that disperses oxides and contaminants and brings an increasing area of pure metal contact between, and bonding of, the adjacent surfaces.

The principle set up for ultrasonic spot welding is illustrated in figure 1.1. In this particular illustration what is known as a "wedge reed" welding system is shown. In a typical weld the joining of the overlapping sheets will occur in the deformation zone at the part interface directly beneath the sonotrode.
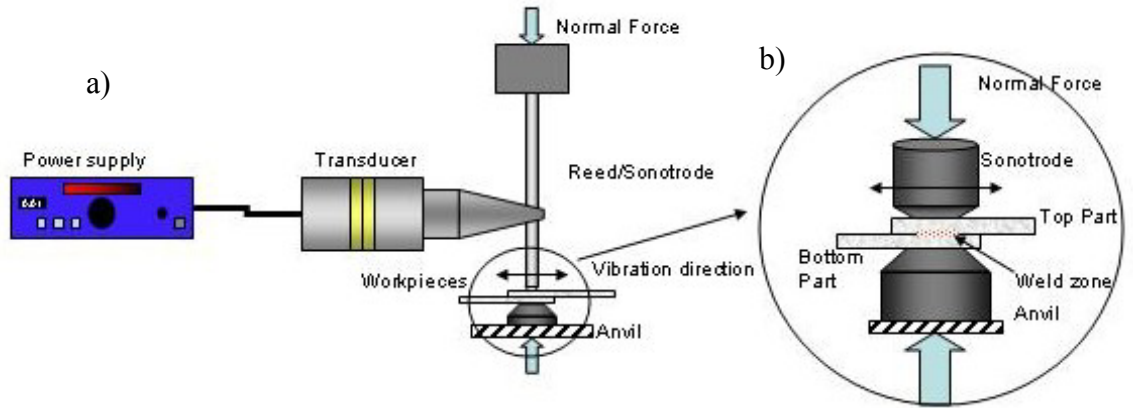
Figure 1.1: Principle USMW set up for spot welding.

It is to be noted that ultrasonic metal welding is quite distinct from an allied ultrasonic joining process, that of plastic welding. Whereas the ultrasonic vibrations in metal welding are parallel to the part surfaces, they are at perpendicular to the surfaces in plastic welding. And, whereas the nature of the bond in metal welding is solid state – that is, without melting and fusion of the adjacent metals, the plastic welding process depends on melting and coalescence of adjacent plastic material. Nevertheless, it frequently occurs that many components of the ultrasonic equipment, such as transducers, power supplies and horns, may be similar, if not identical, between the two processes. Even though USMW has been known for a number of years, a complete understanding of the fundamental mechanism of the process is far from complete. This lack of full understanding is particularly pronounced as it relates to the basic mechanics of the weld, and the relation of the weld mechanics to the overall dynamics of the ultrasonic welding system. In the case of weld mechanics, the lack of knowledge of the shear and normal forces, and plastic deformation in the weld zone are to be especially noted. While

extensive studies of USMW have been made, most have been focused on the resulting weld metallurgy, or on the weldability of various metal combinations. Efforts have also gone into the problem of finding the equivalent electrical circuit representation for the ultrasonic welding system. Substantial efforts have also gone into the ultrasonic microjoining process, widely used in microelectronics for linking microchips to circuits.

Despite an extensive body of prior work, users of USMW face significant challenges in extending the process to heavy duty welding of structural components that can find use in automotive and aerospace structures. Specifically, this relates to joining of 5XXX and 6XXX series aluminums, widely used in the automobile industry, and to 2XXX, 6XXX and 7XXX aluminums used in the aerospace industries. These challenges arise in part because of the thickness and in part because of elastic vibrations of the parts. These problems do not emerge while welding metal wires and foils.

From a practical applications standpoint, two key areas have emerged that impede progress [1-4]. The first problem is that of varying weld quality when successive welds are made with what appear to be identical system welding parameters. The second problem is that of "sticking" between the parts being welded and the weld tooling. This sticking which is, in fact, a welding of the parts to the tooling (with this welding being in addition to the welding between the parts, or sometimes being instead of welding between the parts), usually is found to occur, when it does occur, between the top part and the vibrating tool on the welding sonotrode. Without a solution to these problems it will be difficult to extend USMW to high production, larger scale welding of structures, despite other potential advantages of the process.

3

It is the purpose of this dissertation to address these two key issues of USMW. The basis of the approach will be to understand the underlying mechanics, involving the welding forces occurring at the part interfaces (i.e. at the part-part and part-tool interfaces), and within the parts, during welding, and from this understanding, to better explain the root causes of "sticking" and weld variability.

USMW systems employ means of controlling input process parameters, and the in-process weld cycle that are intended to reduce weld variability. Thus, the most common practice to control the process is by measuring and controlling the electrical input to the transducer. In certain systems, this is sufficient to control the velocity of the sonotrode, but does not provide information on the forces at the weld interface and their effect on weld quality. Overall systems representations have been developed, representing the ultrasonic welding system as an equivalent electrical network. While these can give an electrical input impedance of the transducer, their relationship to the mechanical impedance at the weld is separated by several "transfer functions" involving the transducer, acoustic transmission components and weld tooling, from the weld itself. Thus, it has been found that knowledge purely of electrical input parameters to a welding system do not provide the ability to eliminate the key issues of variability and tool sticking.

In examining interface forces, it is found that the influence of the top part dimensions can profoundly influence the interface forces. While USMW is considered a solid-state bonding process, that is it occurs without melting and fusion of the parts, it will nevertheless be found that heat generation and temperature rises play a very important role in the process. From knowledge of the interface forces and their

4

dependence on dimensions and surface condition, it will be found possible to better predict the performance of the welding process, thus reducing issues of variability and "sticking." A further benefit of the work will be that some of the sensors and measuring techniques developed to provide insight into the process may, in fact, have potential for use as weld quality control tools.

In this work a model will be developed based on mechanical considerations and will also include the results of a wide variety of experiments and numerical simulations that support the model. The model is based on two assessments for USMW. The first one is that the welding and joint formation occurs due to plastic deformation at the weld interface and that this allows for metallic adhesion to occur. Every subsequent steps in the process, such as diffusion and re-crystallization are consequences of the heating that occurs during plastic deformation and friction between the parts. The second assessment is that the stresses that occur during welding can be calculated using a two-dimensional stress state, which limits the scope of this work to welding situations were a flat face sonotrode is used.

The material used was chosen because the required material property data was readily available; otherwise the choice of material was arbitrary. Choosing to base the model on mechanical principles only makes the model readily adaptable for other material selections, and the same predictions and calculations can be made for different materials in addition to the AA6061-T6 alloy used here.

In Chapter 4 the model for the weld is developed. The shear and normal forces operating on the parts during welding are identified. These forces are superimposed and the forces necessary for plastic deformation within the deformation zone are calculated,

taking into account the temperature dependent material properties of the part materials. It will be found possible to calculate the temperatures that occur during welding through determining the amount of work done during the weld, and converting this to a heat flux from the deformation zone into the parts, sonotrode and anvil. The work expended at the weld interface will itself be temperature dependent, because the amount of work necessary to plastically deform the metal depends on its temperature and properties at this temperature. This interconnection of heat generation and temperature is a nonlinear problem, unsuitable for an analytical solution when the time depending weld area growth and vibration amplitude are considered as well. Therefore a nonlinear boundary condition is developed that can be used in numerical simulations.

In Chapter 5 the measurement equipment will be briefly described and material properties listed. The measurement equipment such as the infrared camera, the high speed camera and the optical sensor are complex experimental tools and an exhaustive description of all their features would exceed the scope of this work. Therefore only the features used are noted. The implementation of a shear force sensor in an existing welding system has not been done before; therefore its features and impact on the overall welding system design will be described in more detail. The material composition, the temperature dependent yield strength, Young's modulus, shear modulus, the surface roughness and the static friction coefficient for different surface conditions are all provided or determined.

In Chapter 6 the experimental and numerical simulation results are presented. Since it was important to measure the inputs into the weld interface, every effort was made to measure forces and motions as close as possible to the actual weld. Thus, the

amplitude of vibration of the sonotrode was measured and a high speed camera was used to observe the interaction of the sonotrode and the top part surface during welding. A unique feature of this research was the measurement of shear forces during welding. Through use of a shear force sensor located in the weld anvil, it was found possible to determine shear forces very close to the actual weld zone. In fact, analysis of the dynamics of the sensor system suggests the forces measured are in fact those at the weld interface itself. The influence of the top part dimensions on the weld strength was also studied for the special case of longitudinal excitation of the top part.

Using an infrared camera, the temperatures developed at the weld interface and at the top part surface at the sonotrode edge were measured. The temperatures were then correlated to extrusion and weld strength. The influence of the friction coefficient on the weld strength and shear forces was also studied. Finally numerical analysis of temperature fields was done and the theoretical shear forces calculated and compared to the measured shear forces during welding. The numerical analysis of the temperatures that occur during welding and the subsequent calculation of the shear forces acting on the parts provides insight into the interpretation of the shape and features of the measured shear force curves during welding as well as the weld quality that can be expected from a certain weld set up.

The insight gained by the contact stress analysis and the influence of friction during welding is used to introduce a new welding concept, that of "ultrasonic projection welding". It is found possible by welding onto projections (indentations) made on the top part to increase weld strength for thicker sheet materials and reduce sonotrode extrusion and sticking. Ultrasonic projection welding has the advantage that it concentrates the

7

compressive stresses at the welding location and eliminates energy-absorbing frictional stresses between the weld surfaces. The potential benefits of ultrasonic projection welding are explained by the model developed in this dissertation. Ultrasonic projection welding is a byproduct of this work and is briefly described in appendix E. Nevertheless, the potential benefits would make an extensive study on this variation in the USMW process worthwhile.

The underlying hypothesis of this dissertation is that when the forces that act during welding are understood, the problems of weld quality variation and tip sticking can be controlled much better. Thus, the mechanics of the welding process, involving shear and normal forces, plastic deformation and heat transfer, dictate the ultimate conditions whereby a metallurgical bond is established. Further, the welding mechanics, and hence weld quality, occurring at the tool, material weld zone are of a complex nature, and not easily controlled remotely at the input electrical terminals of the welding transducer through settings of electrical power or energy, weld time, impedance parameters or other such indirect measures. Instead, improved means of control will require sensing techniques that make direct measurements closer to the actual weld. The shear force sensor is hopefully but one of several new methods that might emerge.

CHAPTER 2

PRINCIPLES OF ULTRASONIC METAL WELDING

It will be useful to set forth the principles of the USMW process, including

variations from the most commonly used welding systems, prior to considering the body

of work that will be discussed in the literature review. This will provide a common

framework for discussion of these works.

The application of ultrasound to metal joining, for improving grain refinement of

fusion welds, and for brazing and soldering, dates back over 60 years. The first steps to

the discovery of ultrasonic metal welding (USMW) "as we now know it" occurred in the

late 1940's when, in research at the Aeroprojects Company of West Chester,

Pennsylavania (the forerunner of the current Sonobond Corporation), ultrasonic

vibrations were applied to conventional resistance welding equipment, with the objective

of decreasing surface resistance in spot welding of aluminums [5]. In the course of this

work, it was discovered that ultrasound alone was capable of producing a bonding of the

metals. Initial equipment used a longitudinal mode of vibration to the workpieces,

similar to that used today for ultrasonic plastic welding. Further study showed that lateral

vibration components of the sonotrode were in fact responsible for the traces of bonding

observed in the parts. Added development was aimed at enhancing this transverse

vibration, and led, by the mid-1950's, to both the wedge-reed and lateral drive

configurations now in use. Extensive research efforts spread to other laboratories in the

United States by the late 1950's, and soon after that, research groups throughout the

world, but especially in the (former) Soviet Union, initiated efforts.
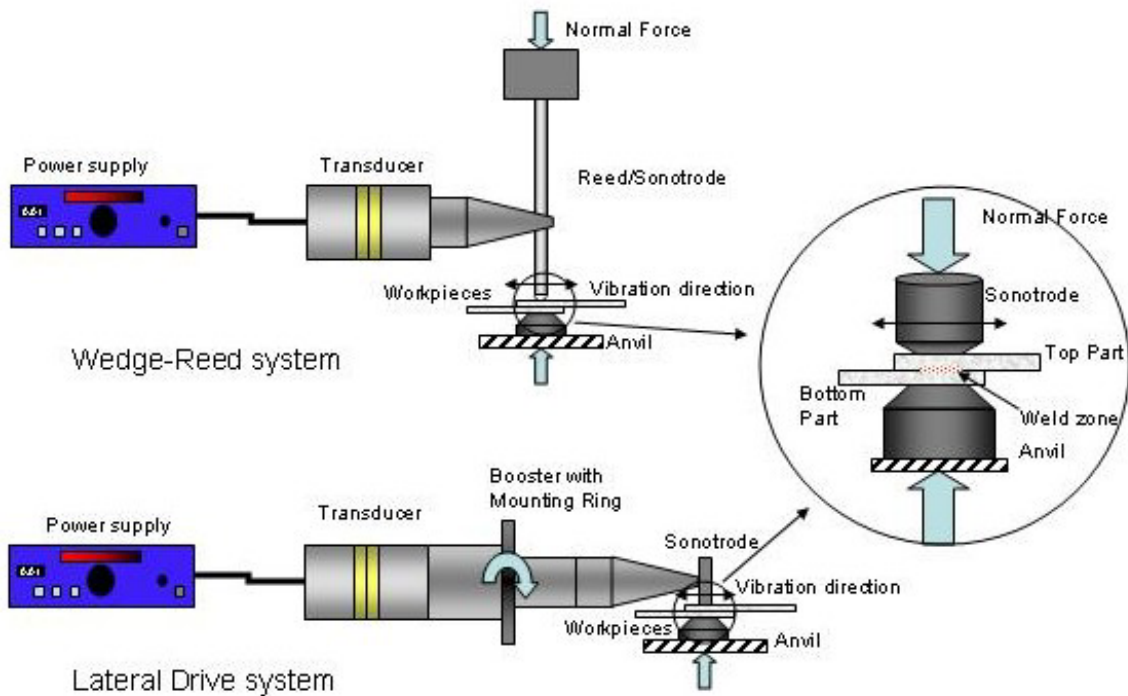
Figure 2.1: Wedge-Reed and Lateral Drive ultrasonic welding systems.

In Figure 2.1 the two most widely used systems for ultrasonic spot welding, the

wedge-reed and the lateral-drive system are shown. Thus for the wedge-reed system

electrical power is converted into mechanical longitudinal vibrations by the transducer.

This longitudinal vibration is amplified and transmitted into the reed by a metal wedge,

brazed to the reed forcing it into transverse vibrations. The normal force is applied by a

pneumatic cylinder onto the mass at the top of the reed. It is seen that the ultrasonic

vibration is transmitted into the parts being welded via the transverse vibration occurring

at the end of the reed. For the lateral-drive welder, the system components are the

transducer, a booster with mounting ring and a horn with sonotrode (sometimes known as

the 'stack'). Booster and horn amplify the longitudinal vibrations generated by the

transducer. The booster also serves as mount for the entire stack, at which either a torque

or a linear downward force is applied, so that the sonotrode is pressed onto the parts. The

sonotrode is mounted perpendicular to the vibration direction of the horn and therefore

vibrating transversely. The ultrasonic energy is transmitted into the workpieces via the

transverse vibration occurring at the tip of the welding horn. In both systems, the

vibrations at the sonotrode are transverse, and occur in a linear, cyclic manner. Both

systems are designed to be in resonance at their specific operating frequency - deviation

from this frequency by a few hundred Hertz will eliminate the vibration amplification

thereby reduce the amplitude at the sonotrode significantly. The amplitude of vibration at

the workpieces varies by system, by tool design and by power settings for a given

application. Nevertheless, they typically will fall into the range of 10 – 100 microns,

peak-to-peak. Likewise, the static forces applied to the weld will also vary by system and

application, but will typically fall in the range of a few hundred Newton to several kilo

Newtons. These static forces alone are well below those necessary to impart any

noticeable plastic deformation to the workpieces.

The details of the welding action at the workpieces are shown in the encircled

area of figure 2.1. Thus, in the wedge-reed and lateral-drive systems shown, there is little

difference of the welding action at the workpieces. However, what has been shown are

the cases of rigid anvils, for both the wedge-reed and lateral-drive systems. In the most widely used versions of the wedge-reed system, the anvil itself is also a vibrating element, flexing in a similar manner to the reed. In particular, the anvil is designed to be "contra-resonant" [6], vibrating in a manner to achieve an increased relative motion at the workpieces.

There are other types of USMW systems that find uses for special welding applications. Thus, an ultrasonic seam welder utilizes a rotating disc as the sonotrode. With this method the vibrations can be transmitted continuously to the work as it rolls through the sonotrode-anvil jaw. Welders of that type are capable of producing seam welds in metals of foil thickness. Ultrasonic torsion welders introduce the vibrations not in a linear but a circular mode, making them suitable to weld rotational symmetric welds. The main current application of this type of welder is to seal metal packages. While it is believed that the principles of ultrasonic metal spot welding that are developed in this dissertation will find application to enhancing these related processes, these modes of ultrasonic metal welding will not be examined here.

In addition, experimental welders have been developed that operate in other vibration modes and/or apply ultrasonic vibrations of very high power levels to the process. Among the welding systems that are or have been studied are welders that operate in a complex vibrating mode, apply the vibrations from the top and the bottom and welders that are capable of butt welding. Welders using complex vibration modes are in principle wedge reed welders, where the wedges and transducers are attached perpendicular to each other on the same reed. These two wedges then have different operating frequencies so that a complex vibration pattern (Lissajous pattern) is generated

12

at the sonotrode parallel to the weld interface. A second scheme for generating a complex vibration pattern is to utilize a slotted booster and horn in a lateral-drive system. The slotted booster vibrates in a combined longitudinal and torsional mode, causing a complex welding pattern. To apply the vibration from both sides, a second welding system is taken as an anvil, so that top and bottom part are excited simultaneously to opposing vibrations. Butt welding is performed with a high power system using an array of multiple transducers that drive a horn with a clamp at the end. The part to be welded is then clamped to the horn and vibrating transversely. Simplified this system is lateral drive system, welding the sonotrode to the workpieces, and then detaching the sonotrode from the horn. Commercially these types of welders are of low relevance. Welders with a very high power output can spot weld sheet metal up to 3mm thickness, when the vibrations are applied only from one side. With the ultrasonic butt welding system up to 10mm thick Aluminum can be successfully welded.

In a similar vein, it has been noted that ultrasonic microbonding, used in making bonds in microcircuits, and typically involving wire sizes on the order of 0.025mm (0.001") or less, in soft gold, aluminum or copper wires, is extensively used in the electronics industry. The typical microbonding apparatus uses a variant of the wedge-reed system, operating at 60 kHz or higher frequency, and involves power levels of a few watts. While a number of significant contributions to the literature of this field were also reviewed, it is not clear that there is a direct connection between the bonding mechanisms involving these very soft metals and substrates, and hard, thick aluminum alloys of the current study. While not necessarily suggesting that there is a completely different bonding mechanism between microbonding and high power USMW of the present work,

the 'scale' differences in power, frequency, material hardness's and dimensions are so significant as to raise question as to direct applicability of results from one field to the other. For this reason, while the microbonding literature was consulted (and will be noted in selected references that follow), it was viewed as having limited application to resolving issues of welding automotive/aerospace grades and thicknesses of aluminum.

The most important parameters that have to be considered in USMW can be separated into system and materials parameters. The main system parameters are:

- Welding time

- Amplitude of vibration

- Static pressure on the parts (Clamping Force)

- Electrical Power

- Frequency

The material parameters, including workpiece features, include:

- Sample cleanliness (Oxides or Contaminants)

- Crystal structure

- Hardness

- Dimensions

As mentioned it can be assumed that the formation of the bond can have different causes, depending on the scale of the application and the properties of the material. The joining process should be clearly separated into small and large scale applications. The separation is of course not that clear and simple, but in an application in which an amplitude in excess of 10 μm and a power level exceeding a few hundred watts it is safe

14

to talk of a large scale application. For these power levels and amplitudes only welding

systems that operate at 20kHz or lower can be used. In large-scale applications typically

sheet metal is welded where the bending stiffness of the sheets to be welded reaches

noticeable levels. Small-scale applications use higher frequencies (>20kHz up to several

hundred kHz) and smaller amplitude (<10µm). Small-scale applications are commonly

wire bonding and foil welding.

A key attractive feature of USMW is that it is a solid-state bonding process, so

that issues involving melting, resolidification of the base metals, with resulting impact on

material properties, are not present. This becomes clear when the ultrasonic process is

compared to resistance spot welding (RSW) of aluminum [7]. The mechanical and

chemical properties are generally not changed by the USMW process. In resistance

welding the weld spot melts and re-solidifies and the adjacent areas to the weld are

strongly influenced by the high temperatures during welding. This means if a heat

treated aluminum alloy is resistance spot welded it loses its properties gained by heat

treating. The resulting resistance spot weld is therefore weaker then a comparable US

spot weld. In addition, the energy consumption during USMW is considerably less then

in RSW. This eliminates the need for water cooling and heavy transformers. Other

significant advantages of USMW are that welding of two different materials and

thickness is possible and that the external deformation of the parts can be as low as 5%

[8].

CHAPTER 3

LITERATURE REVIEW

It will be the purpose of this chapter to review the current knowledge base in specific areas of USMW research. It must be noted here that, as mentioned, the main emphasis of this review is the body of work done on ultrasonic sheet metal welding, since ultrasonic wire bonding is viewed as a significantly different process and that the achieved contributions are only of limited value for this work.

3.1 Prior work on the mechanism of USMW

While USMW is widely used in applications ranging from welding microscopic connections on microchips to tube sealing, including extensively for electrical interconnections, the focus of this work will be on sheet metal welding, where the weld mechanism is believed to be different than for fine wires and thin foils. In the following USMW will be used as term for sheet metal welding or high power welding, involving hundreds to thousand of watts power. More specifically, the spot welding (versus seam or torsion welding) of two overlapping sheets of metal will be considered.
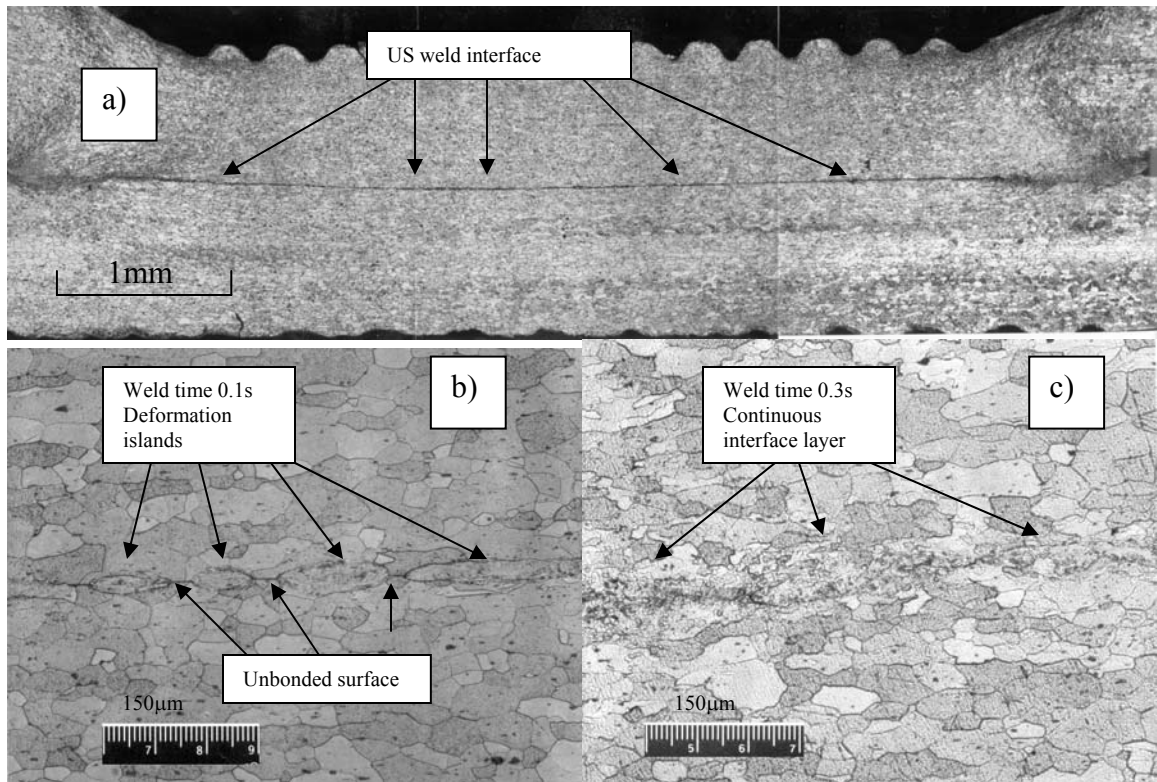
Figure 3.1: US weld cross section, entire interface after 0.3s (a), deformation islands after 0.1s (b), and high magnification picture of the continuous weld layer (c)[7].

The mechanism of USMW is a solid-state metallic adhesion or bonding at a thin interface layer [9] [10], independent of the material thickness [8]. The bonding is possible due to intense plastic deformation at the interface. In Figure 3.1 a typical microstructure of an ultrasonic aluminum weld [7] is shown. One can see the typical overview of the entire cross section for a competed weld. It can be seen that the interface is a very thin layer (approximately 50μm) of deformed material. This layer consists of very fine grain structure resulting from heavy plastic deformation. After 0.1s (i.e. approximately 1/3 of a 0.3s weld cycle, figure 3.1(b)) one can see discrete deformation

islands or microwelds separated by unbonded surface. The external deformation of the parts is generally insignificant. Figure 3.1(a) shows external deformation in the magnitude of 10-15% of the material thickness. It was found though that strong welds can be achieved with minimal/no external deformation (thickness reduction of the weld nugget) at all [7]. The plastic deformation also generates heat, very localized at the interface, which can itself cause re-crystallization, diffusion and even melting [11]. Melting can only occur in the case when a soft material with low melting temperature is welded to a hard material with a high melting temperature. In this special case and only for long weld times can it occur that the heat generated by the plastic deformation of the hard material is enough to melt the soft material in small regions at the interface. The heat generated at the interface is also dependent on the welding parameters such as the normal force, vibration amplitude and the weld time. The welding mechanism has also been compared to fretting caused by friction and wear [12]. This conclusion was reached because when no fretting was observed between the parts, then no weld was formed.

During a typical ultrasonic spot welding cycle, the sonotrode is pressed on the parts to be welded, and then the ultrasonic power is applied. The top part (part facing the sonotrode) starts to vibrate in the direction of sonotrode motion, resulting in a relative motion between the surfaces at the interface [12]. This relative motion at the beginning of the welding cycle cleans the surfaces in contact to each other and plastically deforms asperities [13] [14]. Almost immediately microwelds occur between points of contact of the adjacent surfaces, where bare metals are in contact with each other [15]. These micowelds spread out until a sufficient weld area is build up so there is insufficient power to cause further internal plastic deformation [16]. Other authors consider the sliding

18

during the welding cycle as fretting action between the two surfaces [12] [17], which persists over the entire welding cycle. The microwelds are areas in which the friction exceeds the flow stress level of the material and plastic material flow has started [18]. It is important to notice that the parts to be welded are displaced in opposition to each other over the entire welding cycle if the power is sufficiently large and if a minimum threshold value for the vibration amplitude is reached. If this condition is not met, no weld will be formed. In Rozenberg's literature review [19] it is noted that polishing was observed prior to microweld formation. It was also mentioned that the gripping (deformation) zones are oriented parallel to the vibration direction.

If the friction between the two parts becomes larger than the friction between sonotrode and top part or between anvil and lower part, the motion at the interface stops and the work pieces will either slide over the anvil, or the sonotrode will loose traction on the top part. In this event the parts can become welded to the sonotrode or the anvil [7], this being the "tool sticking" issue previously noted. For that reason it is desirable to design sonotrode and anvil in a way that no sliding occurs between sonotrode and top part and anvil and bottom part. Such design would also minimize frictional losses at those interfaces. A zone of heavily deformed metal mainly characterizes the resulting microstructure at the interface. The original microstructure of the parent material will be completely transformed into a microstructure with much smaller grain size. Dependent on the temperature, other processes such as re-crystallization, diffusion [15] or even fusion can take place.

Harthoorn [20] [21] compared low frequency vibration welding with ultrasonic welding of aluminum. He found that after the same number of cycles the joints formed

were of equal nature. From this he concluded that neither diffusion nor re-crystallization could play a role in USMW, because the temperature for the low frequency welds stayed at room temperature. He also found that the weld itself is an approximately 30μm thick layer of deformed material, very similar to that observed by de Vries [7]. In contradiction to Joshi [22] Harthoorn clearly states that the sheets move relative to each other.

Heymann et al. [23] studied the effect of surface preparation of the weld samples prior to welding. It was found that degreased samples developed the strongest welds, very closely followed by unprepared samples and etched samples. Electrolytically polished and artificially oxidized samples developed the weakest joints. The welds were made with the same weld power and weld time. A spherical sonotrode was used in these experiments. During this investigation it was also found that sonotrode adhesion increased with sample cleanliness. It was also noted that prior investigators did not measure a significant change in weld strength depending on the surface preparation, when the welding parameters were adjusted appropriately.

Chang and Frisch [18] studied the weld mechanism of a sphere being welded to a plate considering the theories developed by Mindlin [24]. It was found that the experimental results were in good agreement with the theory of elastic spheres under normal load with superposition of oscillating tangential forces. The theory predicts for small tangential forces that sliding of the sphere occurs at an annulus of the contact surface. When the tangential force is increased the sliding area would increase toward the center of the contact surface until eventually the entire sphere slides over the opposing elastic body. It was found that "Ultrasonic welding of metals consist of

20

interrelated, complex processes such as plastic deformation, work hardening, breaking of contaminant films, fatigue crack formation and propagation, fracture, generation of heat by friction and plastic deformation, re-crystallization, and interdiffusion." Further, that "The dominating mechanism for ultrasonic welding is solid state bonding, and it is accomplished by two different processes: Slip and plastic deformation."

Examination of the microstructure at an ultrasonic weld interface with transmission electron microscopy showed that the grain size in a very thin layer is very small [25] [26]. It was concluded that this could only be explained, if the layer melted and re-solidified. However, temperature measurements could not support these findings.

Copper and soft iron has been welded to examine re-crystallization in ultrasonic welds metallurgical and using x-ray diffraction methods [27]. No evidence of re-crystallization could be found; instead it was found that at the interface the orientation of the diffraction planes of was random. The lack of clear crystal orientation was contributed to the intense plastic deformation at the interface, which destroyed the original crystal structure. This then led to the conclusion that re-crystallization could not be responsible for the joint formation in USMW.

Beyer [28] observed diffusion for extended periods of welding time in copper and aluminum welds. Because of the presence of diffusion it was concluded that the temperatures reached during welding can locally reach melting temperatures and can even exceed it. But from metallurgical examination no clear evidence for melting was found. During this study it was also noted that almost immediately after the ultrasound was applied micro-joints could be observed at the weld interface. Hazlett et al [29] found that diffusion occurred along grain boundaries rather then in the bulk of the material. It

21

was concluded that main mechanism of bond formation in USMW is metallic adhesion due to intense mixing at the interface. It was also found that in some strong welds there was only little evidence of mechanical intermixing.

As stated above there is a significant difference in welding metals of sheet thickness and wire and foil welding. In the following, the main differences of welding metal wires will be discussed briefly. Thus, Pflueger et al. [30] share the opinion of Hazelett [29] that in wire bonding there is no gross interface sliding but a great deal of external plastic deformation. They acknowledge that the mechanism in sheet metal welding is different and that there must be more internal or sublayer deformation due to interface sliding. In wire bonding the wire welded to a substrate does not move relative to it. This causes less internal deformation and therefore less heat generation at the interface. Instead the wire is squeezed onto the substrate with a great deal of external deformation. Wire bonding was discussed in detail by Joshi [22]. The results were quite different than from the majority of the results found for sheet metal welding (i.e. no sliding, no heating).

Ultrasonic bonding of metals to ceramics and glasses has also been carried out. The mechanism of bonding metal to ceramics or glass is different from the mechanism of joint formation in metal welds. Since glass or ceramics deform very little the joint formation relies on the formation of an interface layer by diffusion to which both materials can adhere [31] [32]. In the case of welding aluminum to glass this interface layer was the aluminum oxide.

3.2 Theory of the microscopic bonding mechanism without fusion

Ultrasonic welding is a special form of welding in the solid state. As with other forms of solid state welding, joint formation takes place in three stages. Wodara [33] has summarized this theory [9] [34-42], and will be reviewed in the following.

In the first stage, the surfaces that will be welded are drawn together. This will cause the surfaces to align themselves, due to the normal stress acting on the surfaces. In the second stage, the atoms of the joining surfaces are activated (i.e. dislocations are generated) and, at close approach, chemical (electron) exchange effects take place (namely a metallic bond is formed). In the third stage, which leads to the formation of a strong joint, exchange effects occur between the metallic substances, both in the weld and the neighboring areas. The exchange effects are diffusion of atoms on a microscopic scale, due to the deformation of the unit cells and the very high dislocation density. This theory is a general approach to explain joint formation in the solid state not limited to USMW. The three stages during the bond formation take place within very short time intervals and are therefore hard to separate. The three stages of bond formation are described in more detail in the following.

In the first stage, as soon as the static pressure and the tangential force of the sonotrode are applied, asperities wear down and bring the surfaces into close contact. At some places in the interface, metallic contact occurs but most parts of the surfaces are still covered by oxide and contaminants, which need to be dispersed by the ongoing plastic deformation of the surfaces. The close contact of the surfaces allows van der Waals forces to take effect. This is valid when identical or similar metals are being

welded. If the metals are very different in hardness, the softer material deforms more than the harder metal. In that case there are more dislocations generated at the surface of the softer material. Therefore metallic bonding can take place by electron exchange between both surfaces.

In the second stage, metallic bonds are formed because of the increasing amount of atoms coming in contact at the surfaces. At a distance of 4 to 5 Å between the metal atoms, chemical bonds form between them and an exchange of electrons takes place between the surfaces. On the other hand, dislocation centers form because of the plastic deformation, which are the origin of the processes in the third stage. The metal combinations being welded mostly influence the duration of the second stage. When similar metals are welded the first stage proceeds directly to the third stage, because both surfaces deform simultaneously and active (dislocation) centers are formed immediately. If the metals are extremely different in hardness it takes longer to form active centers on the surface of the harder material. For this to happen, the heat from internal and external friction is necessary to increase the ductility and allow eventually a phase change that will increase the deformability of the harder metal.

In the third stage that follows immediately after metallic bonding takes place in the weld region, interactions between the joint metals start in the weld region and in adjacent areas (sublayer). Plastic deformation has destroyed crystals and grains in the interface. Next to those plastically deformed regions, elastic deformed regions exist, causing residual stresses and areas with elevated energy. After a certain time, the residual stresses will relax, favored by the elevated temperatures and the altering superimposed stresses caused by the ultrasonic vibrations. The reasons for this relaxation

process are atoms that change their functional locations in the crystal lattice structure. All the above takes place simultaneously; therefore, not only is relaxation taking place but also re-crystallization and diffusion. Diffusion processes have little effect on the formation of the joint, yet always result in strengthening the joint. Unfortunately there was no reason or explanation given for this phenomenon by Wodara. In metals, which have no solubility in each other in the solid state, the joint strength relies only on inter atomic interaction and is according to this not very strong.

Since USMW is a solid state bonding process it is imperative to have some degree of understanding of the processes that take place on a microscopic scale within the bonding area of an ultrasonic metal weld. Therefore this theory was introduced here briefly with no claim of completeness. It is also necessary to understand the source of residual stresses and their potential impact on weld strength after long periods of time.

3.3 The temperature within the weld zone

During USMW, plastic deformation, elastic hysteresis and friction generate heat at the weld interface. In the following some results are presented from researchers that have tried to measure and explain the temperatures at the interface during welding.

At the initial state of welding the temperature rises significantly due to the friction and plastic deformation of the asperities between the two parts. In the later stages of welding the temperature can rise, stay the same or even drop, depending on the welding parameters and the material properties. Theoretical analysis, based on assumed energy,

25

dissipated in the weld zone, a planar heat sink and the thermal properties of aluminum, have indicated a possible temperature of about 600^0C [16]. With an infrared measuring method the temperatures have been measured for several metals. The measured temperatures were in the range of 60-80% of the melting temperature of the material [43] [44]. These high temperatures led to the conclusion that the temperature has a significant role in the bond formation. Richter [45] comes to the conclusion that USMW is more related to friction welding then to cold welding, which implies the temperature must play a significant role.

The energy loss of two solids in contact under normal and alternating shear forces has been considered by Neppiras [46]. It was found when the tangential force exceeds a critical value, macroscopic sliding of the solids occurs and the dissipated energy increases significantly. This condition is usually achieved in ultrasonic sheet metal welding, but not necessarily in wire bonding.

The temperature in the weld area is of course dependent on the energy delivered to it by the ultrasonic vibrations. Several techniques have been used to determine this energy. These techniques are [47] [48]:

- Measurement of the electrical power delivered to the transducer with consideration of the losses of the system.

- Determination of the standing wave ratio at some element of the coupler system with strain gauges.

- Measuring the acoustical power at the weld itself.

- Calorimetric methods.

The first two techniques have been successfully used to determine the power delivered to the sonotrode.

Temperatures have been measured with thermocouples and IR techniques. Thus, thermocouples have been used to measure the temperature at the weld interface [47] [49] [50]. It was found that the temperatures rises very quickly in the initial stage of welding and then remains stable for the remaining weld time. The temperature in the latter stages of the weld increased with decreasing normal pressure and increased electrical power, as summarized in Table 1 for ultrasonic welds of aluminum. Wagner et al. [51] used an aluminum interlayer between two relatively brittle materials during welding. This means that the plastic deformation occurred in the aluminum alone, therefore permitting the temperature to be compared to aluminum-to-aluminum welds. Table 1 summarizes the temperatures that were measured during aluminum welding using different techniques. The measured temperatures during USMW vary considerably dependent on the materials being welded and the welding parameters. Melting is generally considered as not possible in mono metal welds.

Reference	48	46	44	52
Temperatures	150-320^{0}C	390^{0}C	400^{0}C	412^{0}C

Table 1: Temperatures measured during welding of aluminum.

Richter [45] calculated the temperature at the weld interface with a simple heat balance equation, for a one-dimensional model of the weld zone and adjoining sonotrode and anvil. He calculated the heat flux into the parts to be equal to the temperature

dependant shear strength times the average velocity at the interface. The heat flux out of

the parts is then given by a simple heat transfer equation dependent on the materials used

and the geometries of anvil/sonotrode. The calculations are based purely on mechanical

considerations. The temperatures calculated in this way were too high, which was

attributed to an insufficient knowledge of the temperature dependent yield strength.

Hazlett [29] concluded that the weld temperature is a very important factor for strong

weld formation. This was found when dissimilar metals were welded.

3.4 Systems model

The ultrasonic welder, parts to be welded and the weld interface can be viewed as

an overall system. The inputs for this system are the current and voltage, while the

output is the shear force and the tangential velocity at the weld interface. There are

several ways of analyzing the system and representing it. The goal of every systems

analysis has been to find the relationship of input and output and the effect of the output

on weld quality. In figure 3.2 alternate systems representations of an USMW are shown.
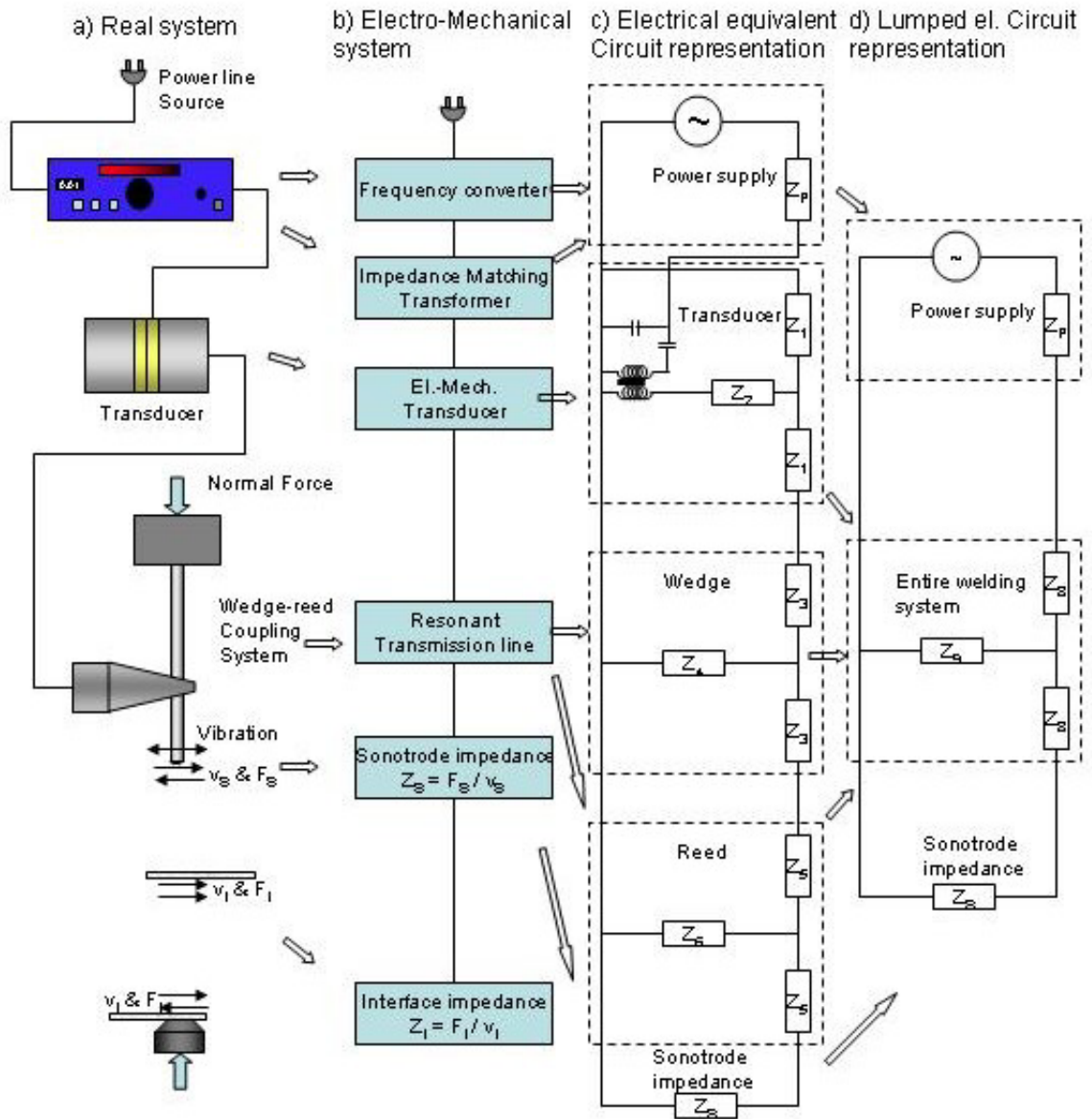
Figure 3.2: USMW systems representations, a)real system, b)electromechanical system, c)electrical equivalent representation and d) lumped el. circuit representation.

In figure 3.2(a) the actual USMW system, in this case a wedge reed type welder is shown. In figure 3.2(b) the equivalent electro-mechanical block diagram representation

is shown. A similar systems representation was used by Jones at al. [48] [49]. In both reports the energy delivered to the weld has been measured from the standing wave ratio at the transmission line. In figure 3.2(c) an electric equivalent circuit representation is shown that can be calculated by finding the electrical equivalent for each system component. Figure 3.2(c) can then be reduced to a lumped systems representation with the theory for electrical transmission lines, this is shown in figure 3.2(d).

For an USMW system, which is an electromechanical system, a purely electrical representation can be found, using the concepts of equivalent circuits. This electrical representation then expresses the mechanical impedance at the sonotrode dependent on the electrical input at the transducer. The mathematical foundation is given by Mason [52] to transform the electromechanical system to an electrical equivalent circuit. This was done by Harthoorn [21] for a lateral drive welding system. As a result it was possible to calculate the tangential force at the sonotrode as a function of the current to the transducer. Such current measurements found that the force would increase very rapidly and stay constant throughout the weld cycle. It was also found that there was little correlation between tangential force and weld strength.

An attempt at calculating the mechanical power, based on mechanical considerations, and comparing it to the electrical power was made by Povstyan [53]. It assumed that the mechanical power is dependent on the weld area, shear modulus, frequency, ultimate tensile strength and sheet thickness.

Niebuhr et al. [10] realized explicitly that the top part, bottom part and anvil are part of the welding system. This is of importance because most researchers assumed that all the energy being transmitted to the sonotrode is also being transmitted to the weld.

The most recent equivalent circuit representation of the USMW system was developed by Bilgutay [54]. The basis for the model was a lateral drive system driven by a phase-locked loop power supply. The main goal of this study was to find a way of controlling weld quality by controlling current, voltage and frequency. Expressions were found linking the load velocity and the load force to the voltage and frequency, if the current was held constant. The approach in this study was similar to that of Harthoorn [21], but Bilgutay considered the effect of loading and its effect on the input impedance of the welder. Due to the advances in calculating the equivalent circuit the hope was expressed that knowing the relationship of shear force and velocity dependence at the load to voltage, current and impedance at the input, could lead to a nondestructive, in-process testing method for ultrasonic joints [54].

During the welding cycle the amplitude of vibration usually decreases because of the changing acoustical properties of the parts and the welder as the weld develops. The vibrations are coupled increasingly into the bottom part and the anvil. For the welding system this is equal to a higher load on the sonotrode. The amplitude changes are dependent on the welding equipment, with some ultrasonic welders having the capability to compensate for changing load conditions and maintaining a certain vibration amplitude.

3.5 Controlling USMW

A method of weld quality control was developed which did involve careful sample preparation and measurement of the vibrations transmitted to the anvil [55]. It

was found that with carefully prepared samples the reproducibility of weld quality was very consistent. It was also found that the vibration amplitude of the anvil was dependent on the temperature of the weld itself. The vibration amplitude decreased when the specimen was quenched during welding, which was attributed to a higher shear force at the interface during quenching. The electrical resistance across an ultrasonic weld was used successfully to determine weld quality during welding of aluminum wires to a silver substrate [56]. This method has not yet been applied to ultrasonic sheet metal welding.

If the surface of the metals to be welded is contaminated, the weld time has to be adjusted accordingly [57]. It was found that the change in anvil vibrations and electrical power could give an indication of the weld condition and weld strength. In experiments a welding system was used that maintained certain vibration amplitude during welding, so that only the electrical power and the anvil vibrations could be used as control parameters. The vibration amplitude had to be predetermined. Unfortunately the dependence of the measured parameters on the weld strength is very complex and no control algorithm was suggested.

It was also attempted to control the weld quality by measuring the anvil vibrations [58]. This attempt had only limited success. Efforts were made to find a dependence of the weld quality on anvil vibrations and the other measured process parameters. It was found that even when great care was taken in sample preparation and controlling all other input parameters, that quality control was not possible. Nevertheless a correlation was found between the fast Fourier transformation of the anvil vibration signal and the weld quality, but if welding conditions changed, this correlation disappeared.

3.6 The influence of Sheet Dimensions on the USMW process

For USMW the dimensions of the top part are of greatest importance. The bottom part has usually very little effect on the welding result. In the following the influence of the dimensions of the top part will be reviewed. So far this area of research has received little attention, with work in this area having been done by Wodara et al [59] and Vitec et al. [60], and briefly noted by Rozenberg [19].

3.6.1 Thickness

It has been noted that in ultrasonic welding, the joint forms due to the relative motion of the parts at the interface. The ultrasound is coupled into the top part and has to propagate through it to the weld, with losses occurring due to internal friction and the resulting heat generation. For the amplitude of displacement at the weld interface to be optimal, the vibration amplitude of the sonotrode has to be adjusted with respect to the thickness of the top part. The losses can be described in an exponential expression [59].

$$p_x = p_0 \cdot e^{-\frac{k}{20} \cdot x} \qquad\qquad\qquad \text{(Eq. 3-1)}$$

where: p_x, p_0: alternating acoustic pressure

k: absorption coefficient

x: thickness

The acoustic pressure in equation 3-1 is the superimposed normal and shear stress, caused by the sonotrode on the top part surface (p_0) and its decay trough the

33

thickness of the parts. The exponential behavior of the weld strength vs. the top part thickness can be seen in figure 3.3.
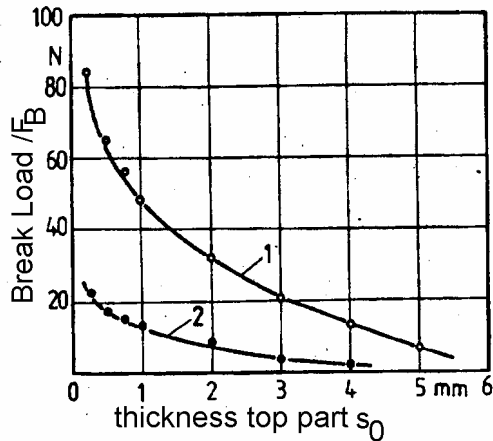
Figure 3.3: Dependence of failure load on top part thickness, material Al 99.5, 1-bottom part thickness 80μm, 2- 20μm [59].

Based on this, the thickness of the top part is mainly limited by the electrical power delivered to the transducer. In addition the absorption coefficient was found to be approximately proportional to frequency, so that for thicker sheets high frequencies are not desirable.

Another effect of the top part thickness on the USMW process is the effect on contact stresses at the interface [19]. The difference in stress distribution at the interface was pointed out for spherical and flat sonotrodes, and for varying sheet thicknesses. For thicker sheets the compressive stress at the interface will spread out and decrease the reduction of amplitude at the interface will also become significant.

34

3.6.2 Width of the top part

The width of the top part refers to the dimension parallel to the vibration direction. When the weld is made in the middle of the part, a significant decrease in weld strength can be observed, if the width is half of the longitudinal wavelength. The wavelength of a material can be calculated with following equation:

$$\lambda = \frac{c}{f} = \frac{\sqrt{\frac{E}{\rho}}}{f}$$
(Eq. 3-2)

where: c: Speed of sound in a thin rod

E: Young's modulus

ρ: Density

f: Frequency

If the width of the part is $\lambda/2$, the vibration is excited in a node position of the vibrating part (i.e. a node position for free longitudinal vibrations in the plane parallel to the weld interface and in the vibration direction). Experiments have been done with 0.5 mm thick copper sheets, to verify the unfavorable effect. The results are shown in figure 3.4.
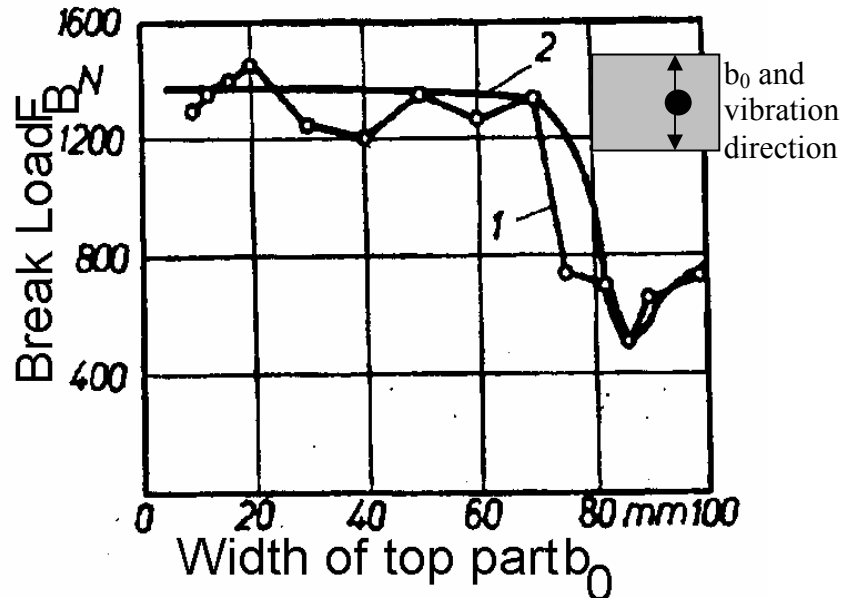
Figure 3.4: Influence of the width of the top part on the break load of the joint P_S=1800W; t_S=0.8s; F_S=1100N; f=21.5kHz; plane sonotrode $\varnothing$=5mm 1-measured break loads, 2-theoretical curve [59].

The wavelength is dependent on the material and the frequency. The half wavelength decreases with an increase in frequency. This also changes the critical part dimensions. Critical in this case means the dimensions at which the weld strength decreases significantly. In the case of Copper the wavelength is 172mm at 21.5kHz, and figure 3.4 clearly shows a decrease in weld strength for a part with of $\lambda/2$.

3.6.3 Length of the top part

If the lengthwise dimension of the part is parallel to the vibration direction, the length has an influence on the weld strength too, but when the part is rotated by 90^0, the

36

influence of the length can no longer be detected. The length has for the same reason as the width a strong influence on the weld strength. In these experiments the part was welded at the edge and not in the middle, so that the critical length was $(2n+1)\lambda/4$, where $n=1,2,\ldots$. In figure 3.5 the failure load of the weld as a function of the length of the sample is shown. The samples have been welded lengthwise and perpendicular to the vibration direction.
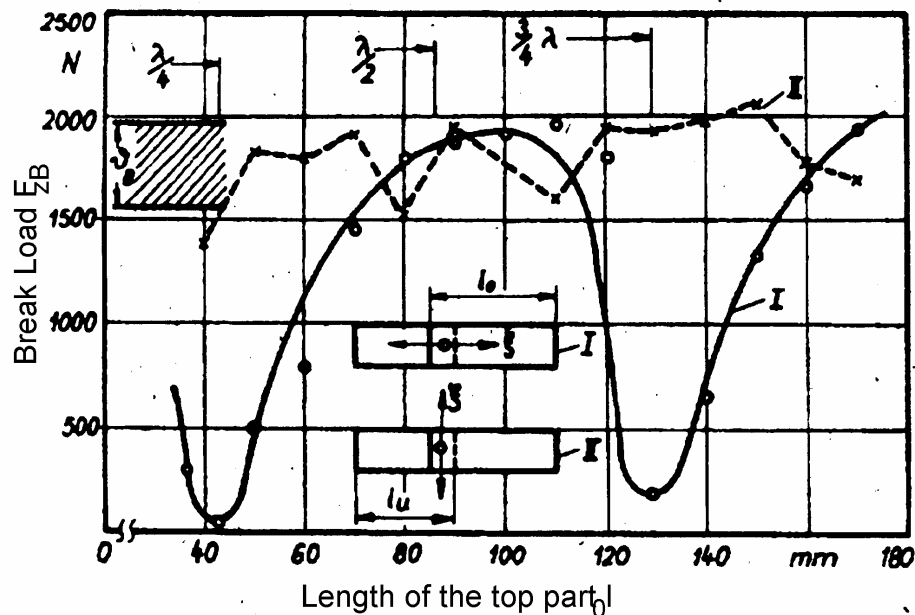
Figure 3.5: Influence of the length of the top part on the failure load; P_S=1700W; s=0.8mm t_S=2.5s; F_S=1550N; f=21.5kHz; plane sonotrode $\varnothing$=5mm [49].

At the critical length the failure load of the welds clearly decreases. At this length the sonotrode deforms the top part heavily, but little or no welding occurs. If the vibration direction is perpendicular to the lengthwise direction of the top part, the length

does not influence the failure load. If the length is nλ/2 the part is vibrating in resonance with the exciting vibration. In this case a very good weld with very little deformation of the top part can be achieved. It must be said that these effects only occur with certain part dimensions and certain weld positions. In practical use, critical dimensions could be easily avoided.

In the Rozenberg review [19] note was taken of experiments examining the effects of longitudinal and flexural vibrations on strips that were of multiple wavelengths. The strips were excited at an anti-node position and clamped at other node and anti-node positions. The resulting vibrations were measured by a microscope and with a thin layer of lead foil. It was found that at clamps positioned at node points no vibrations could be observed while at anti-node positions strong vibrations occurred, even some distance away from the point of excitation. It was also mentioned that flexural waves were harmful for other weld spots on the same sheet while longitudinal vibrations were not.

3.7 Summary of the literature review

The mechanism of ultrasonic welding that emerges from this extensive body of prior work is that of a solid-state bond, caused by the relative motion-induced plastic deformation and fracture, dispersal of oxides and contaminants, thus allowing interatomic attraction to take effect. Even though there is some controversy about re-crystallization and diffusion in the weld zone, these events, if present, are the consequence of the heat generated at the weld interface by plastic deformation. It must be mentioned that experiments conducted to find the weld mechanism were done with a wide variety of

materials, equipment and weld parameters. Different methods of examination have also been used, which then lead eventually to different conclusions. When bonding wires, the metallic bond is made possible by external deformation rather then internal deformation. The temperatures generated in microbonding are considerably less than those in sheet metal welding. Metal to glass and ceramic welds rely on diffusion to create an interface layer to which both material can adhere. In many cases of metal to glass/ceramic welds the glass is coated with a thin layer of metal prior to welding by conventional techniques.

Numerous researchers have measured the temperatures arising at the weld interface during USMW. The temperatures are dependent on the material used, as well as the welding parameters. In most cases the measured temperatures were 60 to 80 percent of the melting temperature of the metals. Theoretical approaches to temperature prediction are difficult because of insufficient knowledge of the material properties at elevated temperatures and the rather complex geometries of the parts and the adjoining sonotrode and anvil. These factors have made an analytical approach to the problem difficult, with no evidence of advanced simulation capabilities being applied to this area.

Over the years some advances have taken place in understanding the relationship between the input electrical impedance of the welder and the resulting forces and amplitudes at the tool tip in contact with the surface of the top part. Nevertheless, while helpful, these studies did not provide information on the critical interface forces. Manufactures of ultrasonic welding systems have developed sophisticated power supplies with a great variety of control features. The electrical and acoustical power delivered to the sonotrode can be calculated and measured in different ways. But so far attempts to control the weld quality by these means have been not very successful.

In part, this difficulty arises because the effect of part dimensions and surface condition have not been included into the systems representation. All the researches, even though claiming to calculate or measure the power input into the weld, basically calculated or measured the power at the sonotrode, not at the weld interface.

Some understanding of the influence of part dimensions on the weld quality has emerged in terms of general phenomenological explanations, but in general this important area has received little attention in the ultrasonic welding community. So far only dimensions for which resonance could occur at the welding frequency have been considered. The influence of top part thickness has been found to be two fold, that of the decrease in vibration amplitude due to the elastic shear deformation across the thickness and the change of contact stress at the weld interface.

The above briefly describes only a few aspects important for this work about USMW. For a more comprehensive overview over all aspects of USMW the reader is referred to Rozenberg [19] and the Welding Handbook [61]. Rozenberg's book, even though from 1970, gives a very comprehensive review of the available literature up to that time. For a basic introduction to USMW, The American Welding Society handbook is most helpful.

CHAPTER 4

THE MECHANICS OF USMW

In this chapter a mechanics-based model for the ultrasonic welding process will be developed. The situation under consideration, first shown as figure 1.1, is represented in more detail in figure 4.1. Thus, the basic USMW process is shown in figure 4.1 (a), with an enlarged view of the weld zone shown in figure 4.1 (b). The static clamping force is the net external force on the weld. In figure 4.1 (c) a separation of the parts through the weld zone has been made, showing not only the net static force F_N, but the net shear force, F_I that acts at the interface as a result of the transverse vibration of the sonotrode.

It must be pointed out here that the model developed here simplifies the compressive stress under the sonotrode so that it is uniform and time independent. If a spherical sonotrode is used, the compressive stress is not uniform and it will also be time dependent. But the same development that is shown here could also be done if a spherical or otherwise shaped sonotrode is used.
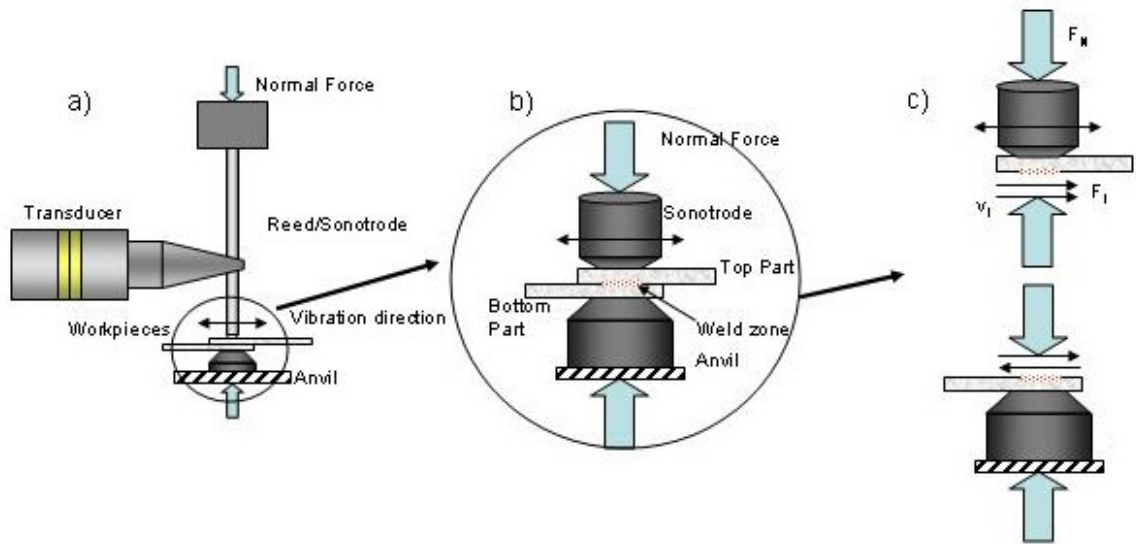
Figure 4.1: Overview of the net forces acting at the weld interface.

It is the primary objective of this work, in investigating the "Mechanics of USMW" to arrive at a process model that permits prediction of the weld-producing shear force F_I. Encompassed in the model will be factors such as the effect of the distribution of the static force F_N at the interface, the critical issue of heating caused by the welding action, both at the weld interface and at the sonotrode-top part interface, and the influence of the part mass and geometry on the welding process.

The stresses occurring during welding at the weld interface and the sonotrode top part interface will be reduced to a two dimensional state and the heating occurring during welding will be reduced to a heat flux from the deforming material at the interface and the friction between the parts into the parts/tooling. The resulting model will predict the forces that occur during USMW and from that predict unstable welding conditions.

Throughout the development reference will be made to different areas within the weld zone as follows:

- A_S: The sonotrode area, this is the area of the contact between the sonotrode and the top part top surface. In the case considered here the sonotrode tip is flat, therefore the sonotrode area is equal to the sonotrode tip area.

- A_{DZ}: The deformation zone area, this is the area in which the weld can form, i.e. plastic deformation and welding can occur. This area is for thin sheets and a flat sonotrode tip equal to the sonotrode area A_S.

- A_W: The weld area, this is the area of the actual weld, i.e. plastic deformation took place and material joining will occur. A_W is dependent on time, starting at 0 at the beginning of the weld and ultimately becoming equal to A_{DZ} and A_S.

- A_{FR}: The friction area, this is the area were the surfaces of the sheets are in contact, but no welding occurs due to contaminants and oxides.

- A_{NC}: The area of no contact, this is the area across the interface of the sheets were the sheet surfaces are not in contact.

4.1 Shear forces at the sonotrode tip

The general components of an ultrasonic welding system have been shown above. In order to examine the stresses and plastic deformation occurring throughout the weld cycle one has to take a yet closer look at the sonotrode, top and bottom part and anvil, shown in figure 4.2. This detail shows the toolhead "knurl" pattern that is present in nearly all USMW tooling. The purpose of the pattern is to engage into the parts surface and thus prevent slipping between the parts and the tooling. While the details of the knurl pattern may vary, a simple pyramid pattern is shown here.
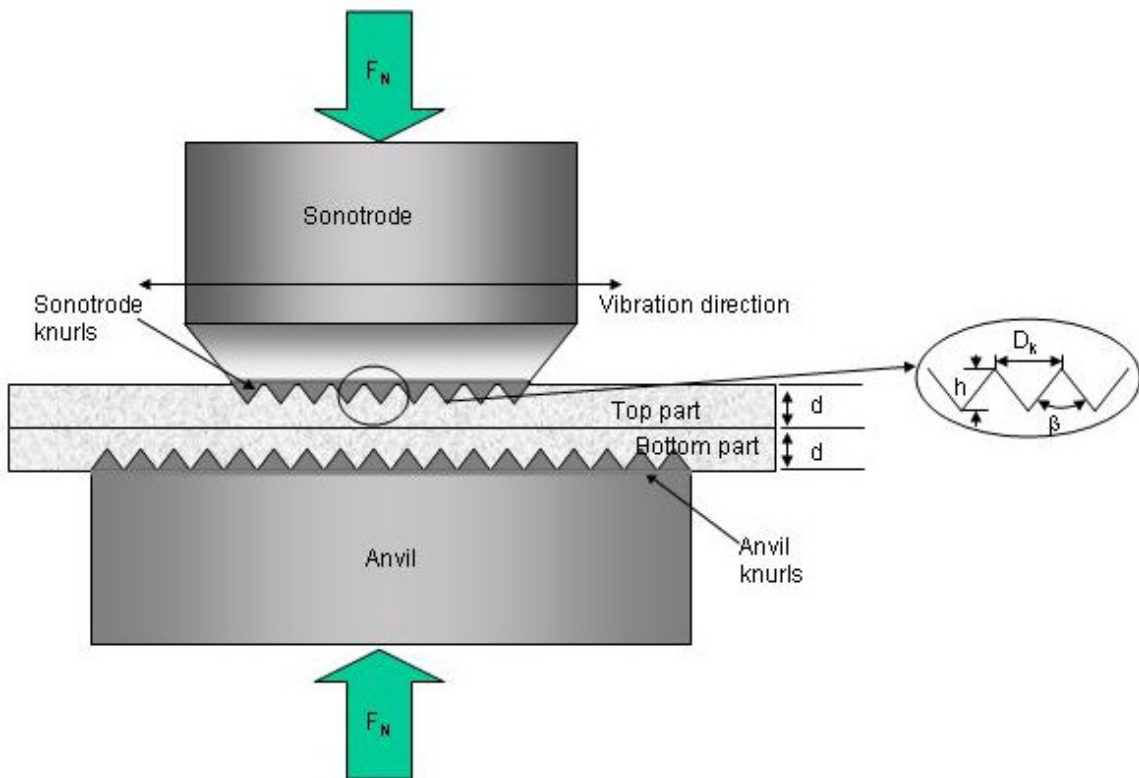
Figure 4.2: Detailed schematic representation of the USMW weld zone.

The knurls dimensions are usually small compared to the area dimensions of the sonotrode/anvil faces and the part thicknesses. Thus, typically the knurl width, D_k (see figure 4.2) is much less that the width/depth dimensions of the sonotrode, and the knurl depth h is much less than the part thicknesses (e.g. a typical value of D_k is 0.2mm, compared to 5mm for a diameter of a sonotrode face, while a typical h value is 0.15mm, compared to 1mm for a typical part thickness). If the static force is applied alone, the penetration of the knurls into the top and bottom parts is found to be negligible; only the tangentially applied force during welding causes the knurl pattern to sink into the top and bottom parts. The anvil may be either stationary or be itself in vibration, depending on the design of the welding system. In some systems it is designed to undergo bending vibrations, and thereby increasing the relative motion between the two parts. In other systems the anvil is designed to be very stiff, thus undergoing no/very little displacement. The latter case will be considered in this model.

The indentation of the knurling pattern of sonotrode/anvil results in a complex local stress pattern due to the sharp peaks of the knurls, and the elastic-plastic nature of the deformation at the peaks and in the valleys of the knurls. This effect is shown in figure 4.3(a). Nevertheless, this complex stress pattern will die out a very short distance away from the surface, leading to a nearly uniform stress distribution under the greater part of the sonotrode area, as shown in figure 4.3 b), c), d) and e). Thus, some distance from the knurl pattern, the details of the knurl effect are no longer evident in the stress field (This is somewhat analogous to "St. Venant's Principle" from elasticity, which says

45

roughly, that far from the point of application of forces, the details of the applied force cannot be established).
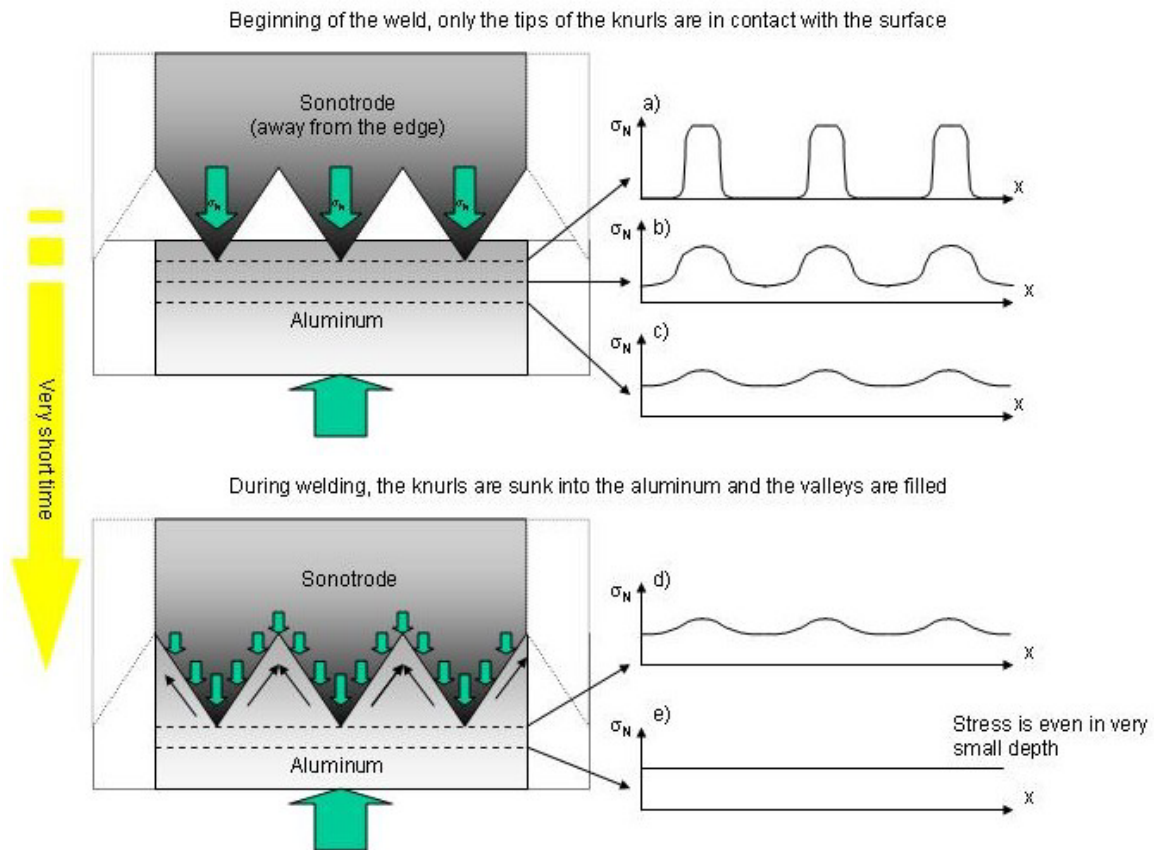
Figure 4.3: Compressive stress distribution at the knurls pattern at the beginning of the weld and during welding.

An elastic-plastic stress analysis was conducted for this 'indenter' problem, to obtain an estimate as to exactly how rapidly the complex stress field decayed to its near uniform condition [62]. The results show that for an indenter with the dimensions

D_k=0.215mm and h=0.152mm the compressive stress is uniform at 0.05mm beneath the tip of the indenter (see section 6.2 for details).

Considering these conditions of stress uniformity a short distance from the knurl indentations, the stress state a short distance from the sonotrode can be examined in greater detail. An element of the top part in the region of uniform compressive stress is shown in figure 4.4.
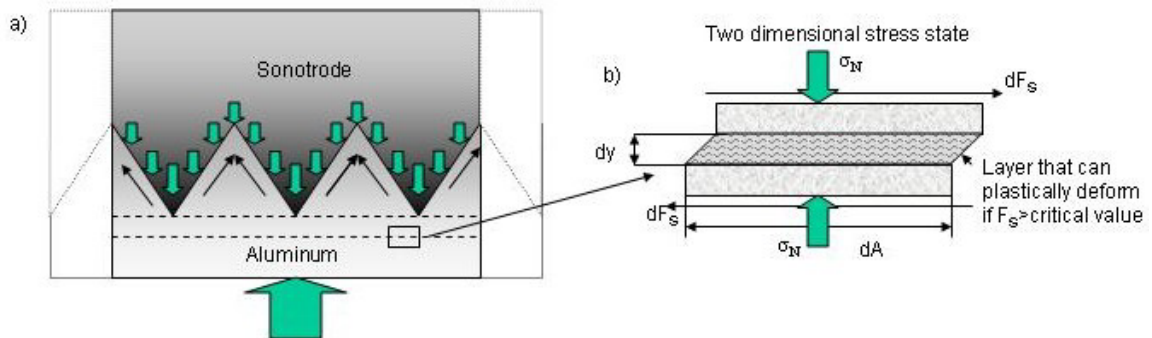
Figure 4.4: Element in the area of uniform compressive stress under the sonotrode.

Being outside the region of elastic-plastic deformation due to the knurl indentation, the stresses in this region may be considered to be governed by simple elastic conditions. However, during welding this element is subject to significant shear stresses. At some point, the combined compressive-shearing stresses may be sufficient to cause plastic deformation in the material that was once elastic (in the following only a rigid perfectly plastic material will be considered). This shearing of the sublayer is shown in figure 4.4 (b). The stress limits at which this occurs can be found by applying a yield

condition. Using Tresca's yield condition and a two dimensional stress state (see

appendix A) it can be shown that the limiting shear force is given by:

$$F_S \leq \sqrt{\left(\frac{Y(T)}{2}\right)^2 - \left(\frac{F_N/A_S}{2}\right)^2} * A_S = \tau_Y * A_S \qquad\qquad \text{(Eq. 4-1)}$$

Where: F_S: Sonotrode shear force
                                                   $Y(T)$: Temperature dependent yield strength
                                                   F_N: Normal force
                                                   A_S: Sonotrode area
                                                   τ_Y: Shear yield stress

If the l.h.s. of condition of 4-1 is smaller then the r.h.s. the top part will vibrate

simultaneously with the sonotrode with no relative motion between sonotrode and top

part. If this l.h.s. is equal to the r.h.s. yielding of the top part surface will occur, causing

relative motion between sonotrode and top part and therefore extrusion and bonding of

the sonotrode to the part – i.e. "tip sticking".

Extrusion will occur at the sonotrode tip top part top surface interface, because the

stresses will be the highest there. The mechanism of extrusion can be shown, by

reducing the sonotrode to a flat surface sonotrode and then considering the extrusion

process during one vibration cycle. Reducing the knurl pattern to a flat surface is in this

case a valid simplification, because it is already known that the stress is with good

approximation uniform beneath the sonotrode, when it is engaged into the material. In

figure 4.5 a flat surface sonotrode engaged into the surface of the top part is depicted.

The figure captures the point in time were l.h.s. and r.h.s. of condition 4-1 are equal for

the first time. This means in the next welding cycle there will be relative motion between

the top part and sonotrode and yielding occurs under the entire sonotrode area (i.e. the material beneath the sonotrode is in a plastic state).
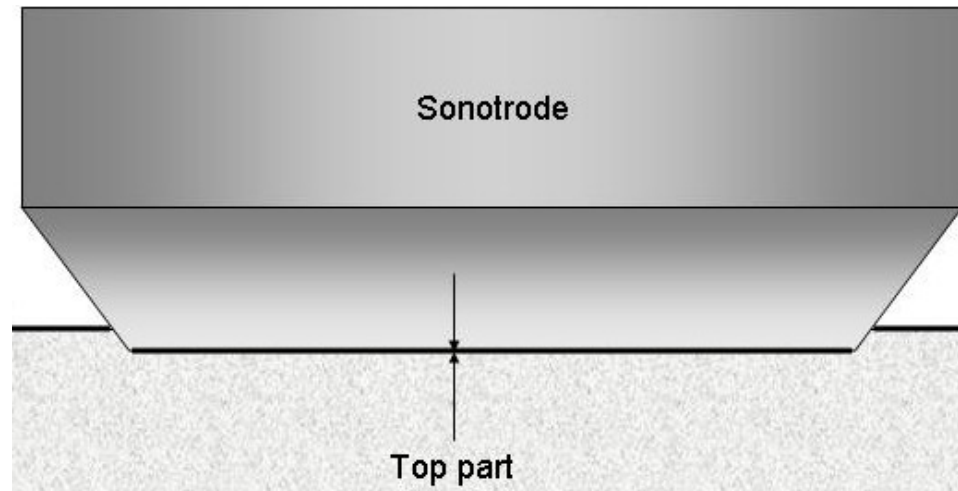
Figure 4.5: Flat surface sonotrode engaged into the top part and the yielding condition is met.

The sequence in figure 4.6 shows the events that take place when the sonotrode moves relative to the top part and the material beneath the sonotrode is in a plastic state. The arrows in the middle of the figures indicate the amount of relative motion. In the first ¼ cycle material that was once adjacent to the right of the sonotrode is pushed away onto the original part surface. Simultaneously material from beneath the sonotrode will be squeezed into the opening gab on the left side of the sonotrode. This only happens, because the material under the sonotrode is in a plastic flow state. The material from beneath the sonotrode will then remain in that gap since here the yield condition is not met (normal stress is removed). Since material has been removed from beneath the sonotrode, it will engage a little deeper into the part to compensate for the lost volume.

After ½ cycle the process is reversed. Material on the left side of the sonotrode will be pushed onto the original surface, the opening gab on the right side will be filled and the sonotrode sinks in a little further.
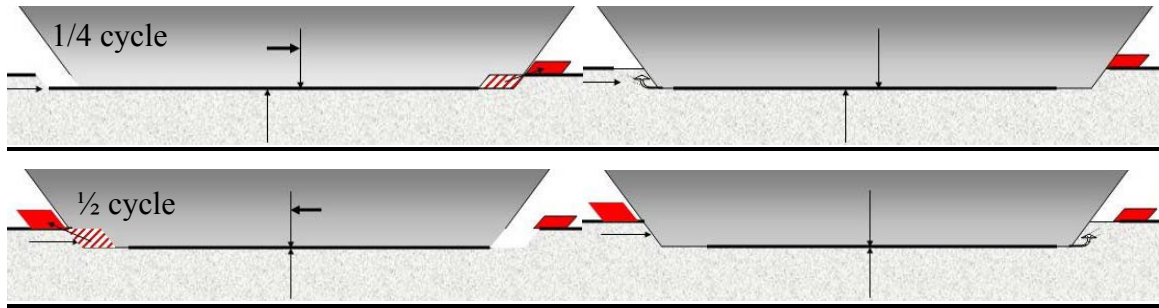
Figure 4.6: The extrusion process during 1/2 welding cycle.

The process described above will then repeat itself every vibration cycle, and thereby in some cases consume the entire thickness of the top part. Since during this process of extrusion sublayer deformation occurs beneath the sonotrode, it will be welded to the parts, because sublayer plastic deformation and the subsequent atomic adhesion are the main joining mechanisms during USMW.

4.2 Contact stresses

As one moves away from the sonotrode, the compressive stress field "spreads out" beyond the area of the sonotrode, effectively distributing the compressive stresses over larger areas, further from the sonotrode. This is important to realize since the

welding interface is some distance away from the sonotrode, depending on the top part

thickness. These compressive stresses are simply the contact stresses between the parts at

the interface, as shown in figure 4.7.
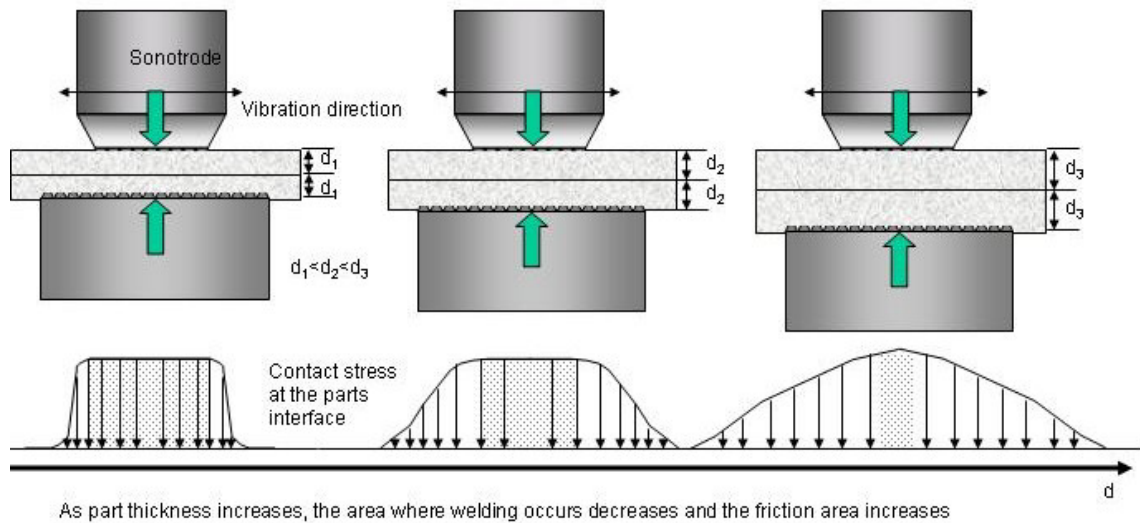
**Figure 4.7: The effect of contact stresses at the parts interface depending on
thickness.**

The contact stress distribution is also dependent on the sonotrode shape. In the

case for a spherical sonotrode for example, the contact stress will be very high in the

middle and drop of very rapidly toward the edges off the sonotrode. This thickness effect

and the effect of different sonotrode shapes on the contact stresses always have to be kept

in mind when using the model representation and equations developed here. The case

considered here is that the thickness of the sheet is thin enough so that a uniform stress

distribution, shown on the left of figure 4.7 can be considered.

4.3 The shear forces in the weld zone

In order to calculate the shear forces in the weld zone one has to separate the problem into two parts. The first deals with the dynamics of the top part, the other deals with the forces acting at the interface between the parts. Both these problems will be addressed in the following.

4.3.1 The dynamics of the top part

First one needs to take a look at the forces acting on the parts as one unit, as shown in figure 4.8. It shows the parts isolated from the sonotrode and anvil with the shear and normal force components acting on the parts. Both parts are considered rigid and reduced in size, so that they have the same area as the sonotrode. While the parts are assumed to be rigid, it will need to be determined if, in fact, the elastic shear deformation is negligible. This will be revisited in section 4.5. The bottom part is fixed to the anvil and the top part is fixed to, and moves with the sonotrode.
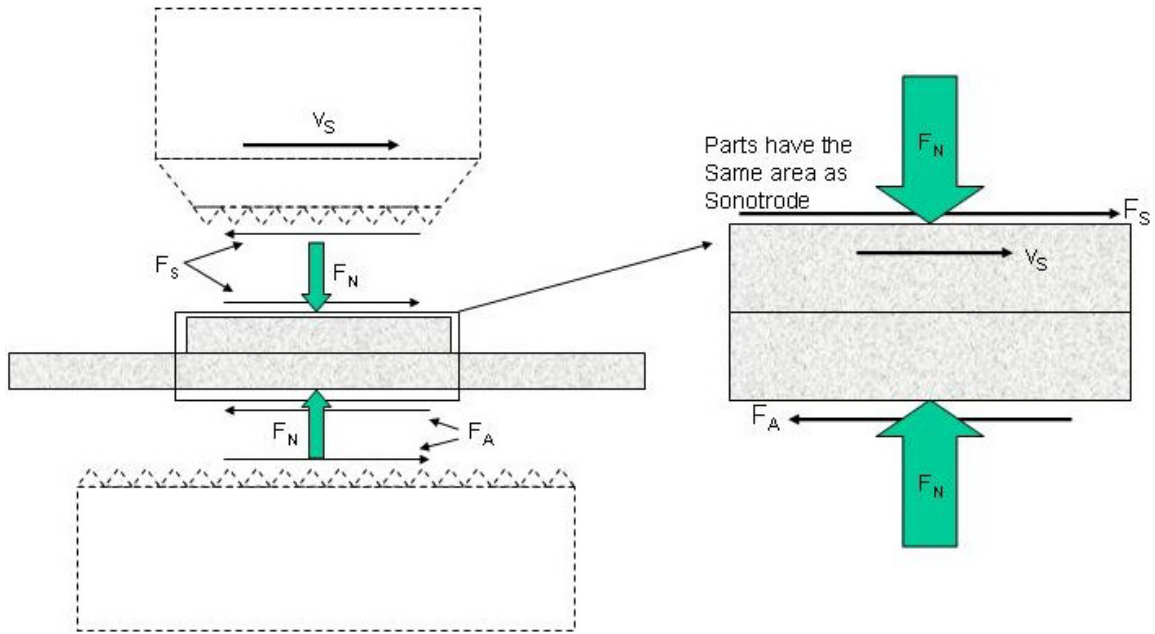
Figure 4.8: Free body diagram of the reduced parts.

It is realized that the oscillations of the sonotrode will result in an oscillating force on the parts. The convention of a rightward velocity as positive is adopted, and shown in figure 4.8. For the rightward moving sonotrode there will be resulting shear forces set up as on the top and bottom part.

As noted, initially the parts will be assumed to be the same size as the sonotrode itself, as shown in figure 4.8. This will permit the dynamics of the part to be treated as rigid body motion, without being concerned with resonance effects that can occur for larger parts. The case of larger parts will be considered later in this section. The parts are separated in figure 4.9, exposing the interface force F_I. It is a key objective of this work to determine this force during welding.
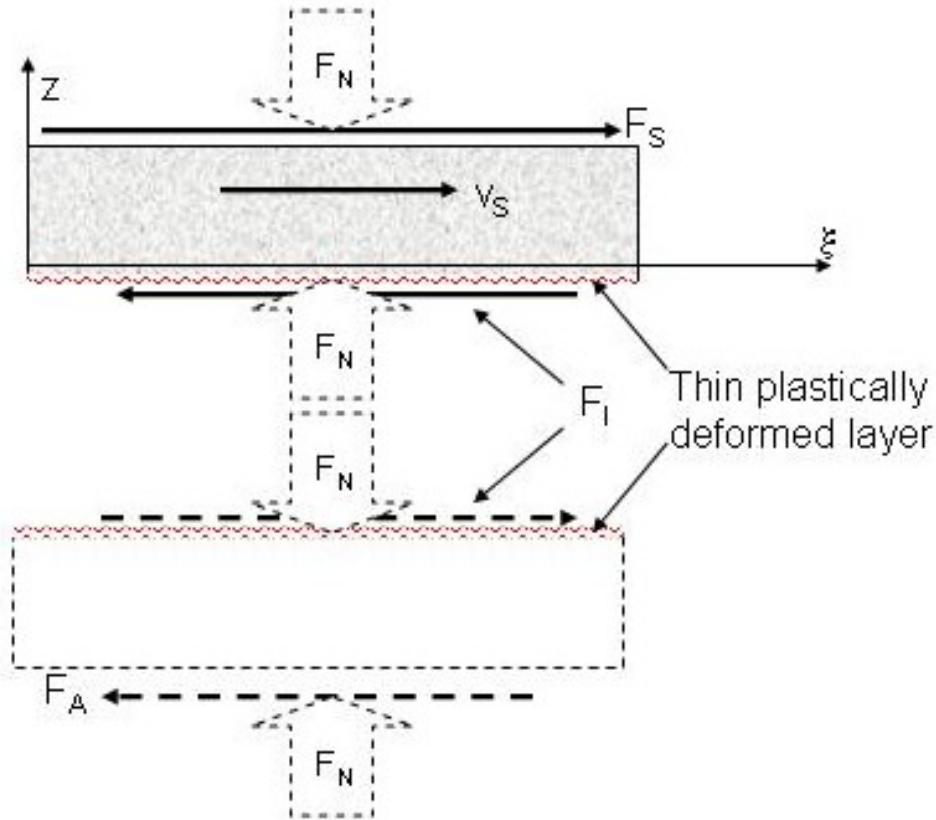
Figure 4.9: Free body diagram of the parts alone.

During welding, it has been noted that a thin zone of intense plastic deformation, shearing and bonding develops between the parts. This is, of course, the location of the ultrasonic weld. In separating the top and bottom parts as shown in figure 4.9, we have in effect cut through the middle of weld zone, so that there is a thin plastically deformed layer on both surfaces. Except for this layer, the bulk of the remaining material is considered rigid. The top part undergoes rigid body motion together with the sonotrode vibrations and with the same amplitude. The sonotrode vibration can be simply written down as:

$$\xi(t) = \xi_0 \sin(\Omega t) \tag{Eq. 4-2}$$

Where:
Ω: Vibration frequency (Radiants/time)
ξ_0: Sonotrode amplitude

The acceleration of the top part is, because of the previous statement that top part and sonotrode move simultaneously and with equal amplitude, equal to the acceleration of the sonotrode and can be written down as:

$$\frac{d^2\xi}{dt^2} = -\Omega^2 \xi_0 \sin(\Omega t) \tag{Eq. 4-3}$$

The interface and the sonotrode forces have a maximum, when the deflection of the top part is the largest; therefore the maximum acceleration has to be considered in the equation of motion. The moments resulting from the difference of interface and sonotrode force will be neglected.

With the above the equation of motion for the top part is:

$$m * \ddot{\xi}_{max} = F_S - F_I$$
$$A_S * d * \rho * \Omega^2 * \xi_0 = F_S - F_I \tag{Eq. 4-4}$$

Where:
m: Mass of the top part
A_S: Area of the part (= sonotrode area)
ρ: Density of the material

For the bottom part the same arguments for neglecting shear strains through the parts apply, with thin plastic zones present at the interface and the knurl pattern. Since

55

the bottom part is assumed be rigid and fixed to the anvil, and the anvil is assumed to be fixed, there is no motion of the bottom part, and the interface force F_I is equal to the anvil force, that is,

$$F_A = F_I \qquad \text{(Eq. 4-5)}$$

Equation 4-5 will be very important when the data gathered with the shear force sensor at the is be discussed. It seldom occurs that part sizes are the same as the sonotrode size, as in this special situation (although this does occur in welding electrical contact pads). Let us now consider what occurs when the parts extend well beyond the weld area, such as the top part extending parallel, perpendicular or in both directions from the excitation direction. In other words, let the part take the form of an extended rod, beam or plate. At some point, considering the top part as a rigid mass will no longer apply, and one must consider the elastic vibrations of the part. This limit would be expected to occur when part dimensions begin approaching vibrational wavelengths for longitudinal and bending vibrations of the part. The first case considered will be for the part extending in the direction parallel to the excitation direction. Similar considerations can be made for dimension changes in other directions as well.

When the part is extended parallel to the vibration and only in one direction, the extension can be treated as rod forced to vibrate in a longitudinal fashion. This is schematically illustrated in figure 4.10. The part with its extension of the length (l) (figure 4.10 (a)) can be broken down into two separate parts (figure 4.10 (b)). The parts are the rigid mass beneath the sonotrode and the elastic extension that is capable of

longitudinal vibrations. The extension can then be treated as a rod excited with a certain

velocity (figure 4.10 (c)).
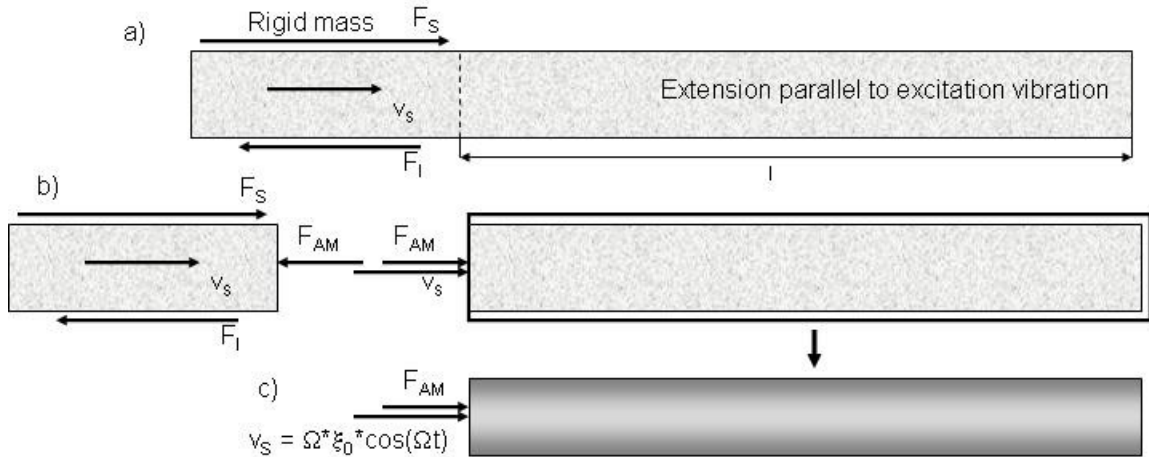
Figure 4.10: Forced vibration problem for extended top part.

Using figure 4.10 one can now write down the equation of motion for the top part,

again, considering that the force F_{AM} that is needed to excite the extension has its

maximum, when the excitation point (i.e. the face of the extension) is at its maximum

deflection.

$$m * \ddot{\xi}_{max} = F_S - F_I - F_{AM} \qquad \text{(Eq. 4-6)}$$

The sonotrode will vibrate with a certain velocity in a typical welding scenario

once the ultrasonics are enabled. The welder that was used in this study experiences

changes in the vibration amplitude during one weld cycle, especially if it is used in its

original set up with a contra-resonant anvil. Nevertheless, when the original anvil was replaced with the rigid anvil and shear force sensor, the amplitude of vibration was to a good approximation constant during a weld cycle. Using either anvil the experimental results did not show any difference. For the subsequent calculation a constant vibration amplitude was assumed.

The section of the top part under the sonotrode is rigid and moving with the sonotrode; so therefore is the extension of the top part excited with the sonotrode velocity and the sonotrode frequency. The force at the excitation point, as a function of part length, necessary to excite the extension of the top part can be calculated from (see appendix B):

$$F_{AM} = E * A * \frac{\Omega}{c} * \xi_0 * \tan\left(\frac{\Omega}{c} * l\right)$$
(Eq. 4-7)

Where: E: Young's modulus
                                                          A: Area of the cross section
                                                          perpendicular to the vibration
                                                          c: Longitudinal wave velocity
                                                          l: Length of the extension

if the right end of the rod is free, and with

$$F_{AM} = E * A * \frac{\Omega}{c} * \xi_0 * \cot\left(\frac{\Omega}{c} * l\right)$$
(Eq. 4-8)

if the end is fixed.

From these equations it is clear that if $\Omega*l/c=(2n+1)\pi/2$ in the first case and $\Omega*l/c=n\pi$ (with n=0,1,…) in the second case that the excitation force becomes infinite. Using for $E=68*10^9$Pa, A=12.7mm^2, $\xi_0=10\mu$m, c=5018m/s and $\Omega=2*\pi*20000$Hz (values

58

typical for the USMW of AA6061) one can calculate F_{AM}, for both cases given by 4-7 and 4-8. The results are shown in figure 4.11.
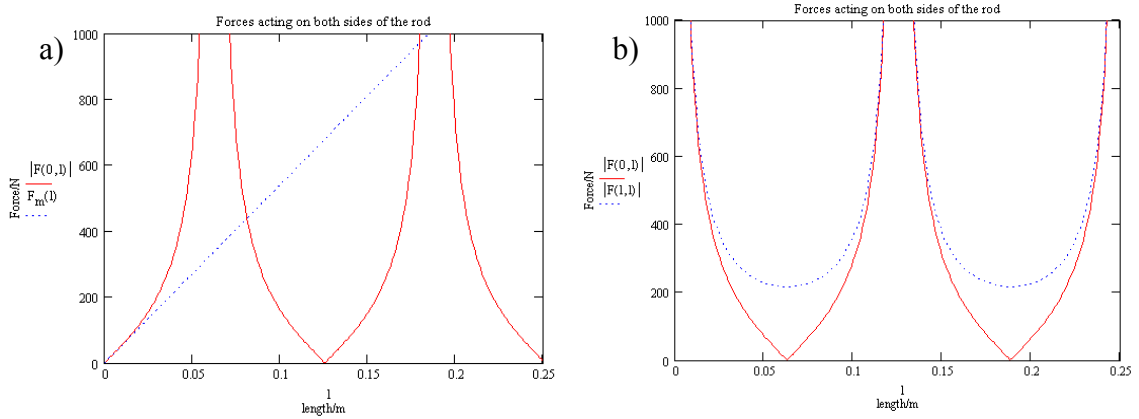
Figure 4.11: Excitation forces in the case of an excited-free (a) and excited-clamped (b) extension.

In figure 4.11 the solid lines represent the force F_{AM} that is needed to excite the extension dependent on length (figure 4.11 (a): excited-free, figure 4.11 (b): excited clamped). In figure 4.11(a) the dashed line shows the excitation forces, if the extension would be treated as a rigid body as well. It is clear from this analysis that for a very short extension length the forced vibration problem has to be considered. In figure 4.11 (b) the dashed line represents the forces that act at the clamp at the other end of the rod. Instances, in which F_{AM} becomes large will be called anti-resonance cases in the following.

Even though the part beneath the sonotrode has been treated as a rigid part, it is known from 4-1 that it has its plastic limits. Solving 4-6 for F_S and substituting it into 4-1 one gets:

$$m\ddot{\xi}_{max} + F_I + F_{AM} \leq \sqrt{\left(\frac{Y(T)}{2}\right)^2 - \left(\frac{F_N/A_S}{2}\right)^2} * A_S \qquad \text{(Eq.4-9)}$$

Clearly, the sum on the l.h.s. of 4-9 must not become equal to the r.h.s. if yielding and extrusion must not occur, but now the term F_{AM} which is dependent on the extension length is included in the l.h.s.. This means, if F_{AM} becomes large, both sides of condition 4-9 become equal and extrusion and tip sticking will occur. Furthermore it can be said that the r.h.s. of 4-9 represents the maximum force with which the part can be excited. (This can be done because the material is considered rigid and perfectly plastic with no work hardening). If yielding occurs at the sonotrode due to anti-resonance of the top part extension (F_{AM}=large) it is valid:

$$m\ddot{\xi}_{max} + F_I + F_{AM} = \sqrt{\left(\frac{Y(T)}{2}\right)^2 - \left(\frac{F_N/A_S}{2}\right)^2} * A_S \qquad \text{(Eq. 4-10)}$$

Solving 4-10 for F_I

$$F_I = \sqrt{\left(\frac{Y(T)}{2}\right)^2 - \left(\frac{F_N/A_S}{2}\right)^2} * A_S - m\ddot{\xi}_{max} - F_{AM} \qquad \text{(Eq. 4-11)}$$

Now one can discuss the terms in the r.h.s. of 4-11 separately. The first term is of limited value, dependent on the temperature and the normal force. The second term is in

60

all instances constant for a given material and given geometry. F_{AM} will become very large in the case of longitudinal anti-resonance in the top part extension. This means, that F_I must become very small for the case of extension anti-resonance. And this in return means that welding is not possible. It will be seen later that some amount of interface force is necessary in order to accomplish welding.

4.3.2 Interface forces

We now will review the proposed development of an ultrasonic weld from initiation to completion of the ultrasonic vibration cycle, including development of the interface forces. The sequence of events is as follows:

- Initial condition. Initially the surfaces of the parts are covered with oxides, lubricants and absorbed moisture. These contaminants prevent bonding of the parts when they are simply pressed together. Thus, when the static force (F_N) is applied asperities of the two surfaces come in contact, but contamination still prevents the parts from bonding, because the normal force is not sufficient to cause gross plastic deformation and local cleaning of the surfaces (figure 4.12 (a)).

- When the ultrasonic vibration starts, the asperities in contact will undergo shearing deformation. First very localized to a few asperities, under continued vibration these contact areas will grow in number and size (figure 4.12 (b) and (c)). During this process the contaminants are disrupted so that a metal-to-metal contact and adhesion can occur. During

61

this process of continued shear deformation a substantial amount of heat is generated, lowering continuously the yield strength of the material, as the weld area grows.

- At the end of the weld cycle the area is (ideally) covered entirely with deformed material, allowing metal to metal contact to occur everywhere in the weld zone (figure 4.12 (d)).
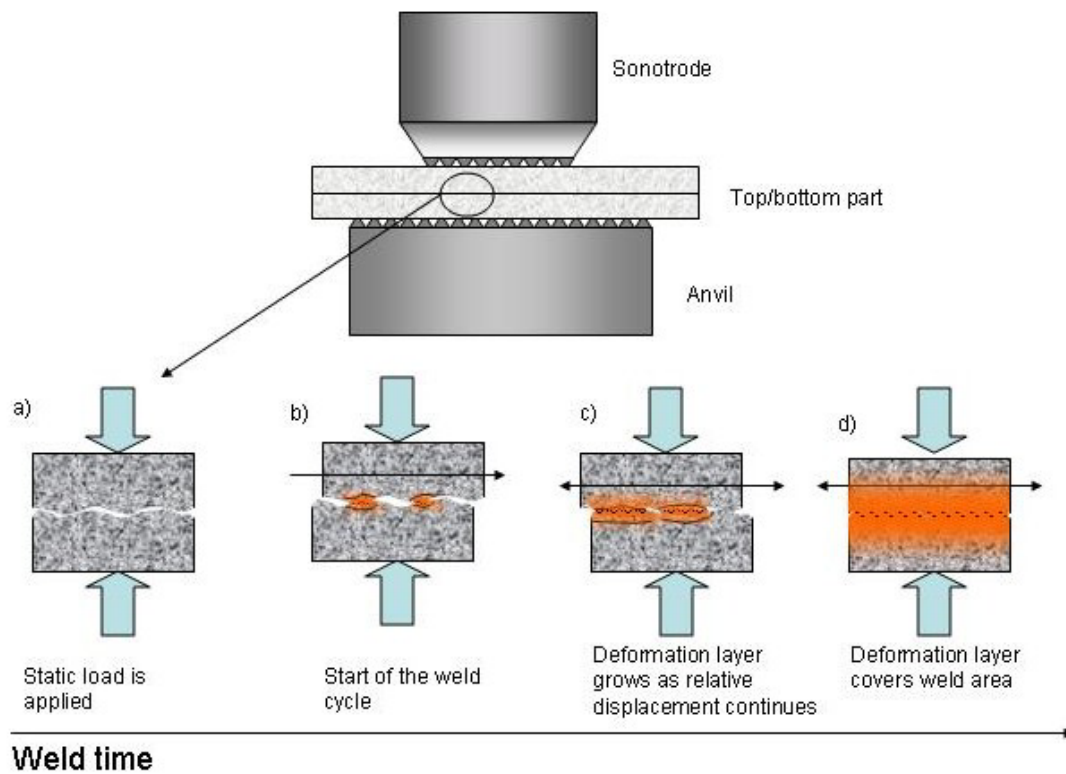
Figure 4.12: Weld development at the interface.

It is shown in figure 4.12 that all the asperities undergo plastic deformation, but this does not mean that welding occurs at all asperities in contact. There is evidence

within the weld zone that the surfaces have been in contact, but were not welded. In figure 4.13 four different contact scenarios are illustrated. These are possible during welding within the deformation zone. In this figure the parts have been reduced again to the size of the sonotrode.
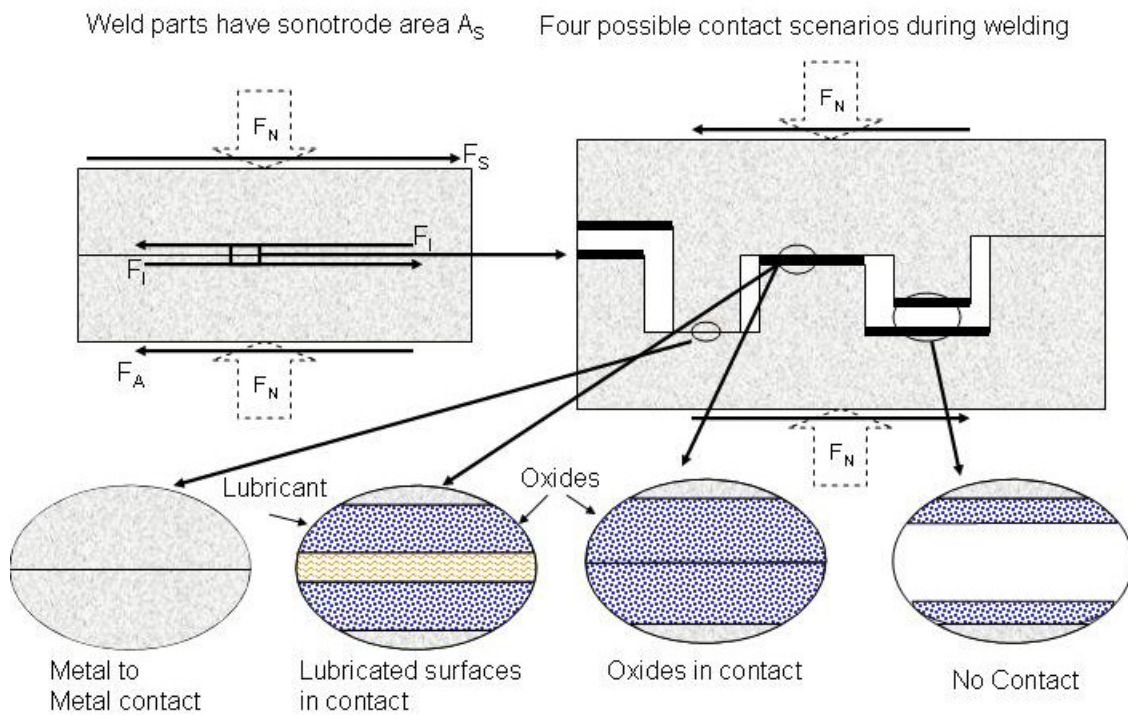
Figure 4.13: Plastic shear deformation at the interface.

The deformation zone area (equal to the sonotrode area A_S) is comprised of three different area types, which are separated by the nature of the contact between the surfaces.

1. The weld area A_W, where plastic deformation at the metal to metal contact forms the joint.

2. The friction area A_{FR}, where friction like plastic deformation occurs but no welding takes place (the friction force that arises will be discussed later in this section).

3. The area of no contact A_{NC}, where the surfaces are not in contact.

During welding the weld areas will develop differently. The weld area will start at $A_W(0)=0$, grow in size until it eventually covers the entire deformation zone area. The friction and no contact area will start at some unknown value between $0 \leq A_{FR} \leq A_{DZ}$ and $A_{DZ} \leq A_{NC} \leq 0$ and then decrease in size during welding, until they eventually disappear. The limits of the contact stress at the deformation zone area are therefore:

$$\frac{F_N}{A_{DZ}} \leq \frac{F_N}{A_W + A_{FR}} << \frac{F_N}{\lim\xrightarrow{A_{NC}} A_{DZ}} \qquad \text{(Eq. 4-12)}$$

The left limit is known in 4-12, therefore $F_N/A_{DZ}=\sigma_N$ is chosen as contact stress within the weld zone for further calculations. After calculating the welding forces, the error that will be made by this simplification will be estimated. In light of the latter numerical simulation it is even necessary to make this simplification, because of the potential danger of generating a singularity in the heat flux equation.

In figure 4.14 an differential element from the area in which metals are in contact and welding occurs is shown, using F_N/A_{DZ} as the normal stress as described above.
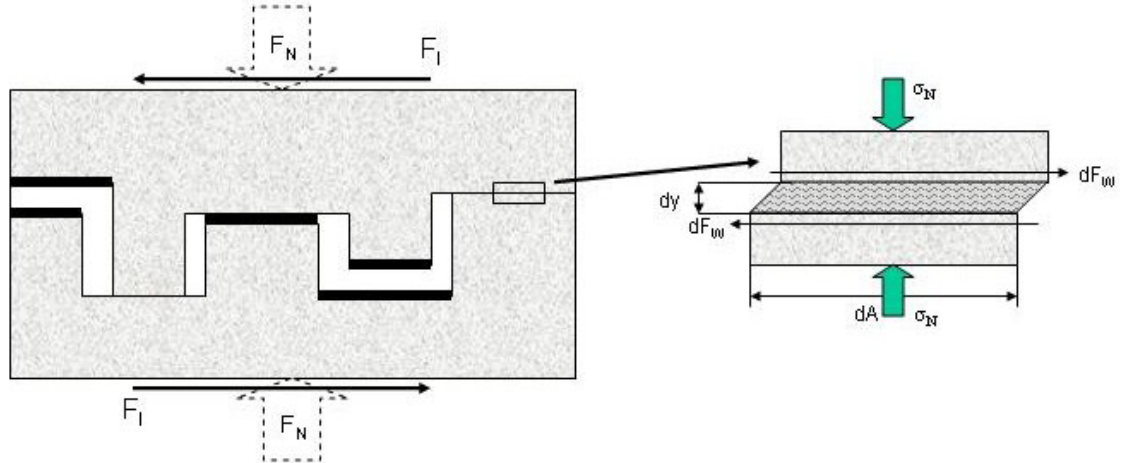
Figure 4.14: Plastic shear deformation at a metal to metal contact at the interface.

For the differential element in figure 4.14 the critical shear yield stress can be calculated form (see appendix A for details):

$$\frac{dF_W}{dA} = \sqrt{\left(\frac{Y(T)}{2}\right)^2 - \left(\frac{F_N/A_{DZ}}{2}\right)^2} = \tau_Y(T) \qquad \text{(Eq. 4-13)}$$

In equation 4-13 the shear yield stress is shown as dependent on the temperature, through $Y(T)$ and the normal force F_N. This relationship shows the way to determine the welding force F_W, as:

$$F_W = \int_{A_W(t)} \sqrt{\left(\frac{Y(T)}{2}\right)^2 - \left(\frac{F_N/A_{DZ}}{2}\right)^2} \, dA \qquad \text{(Eq. 4-14)}$$

However in order to evaluate this integral one clearly needs the weld area and further, how this weld area develops with time over the weld cycle, i.e. the time dependent weld area $A_W(t)$ must be determined. The approach that will be taken here will be to make use of experimental data which indicated how the weld area grows under typical welding conditions.

Because a constant normal stress is used in the square root function, it is not dependent on time. It is only dependent on the temperature and the normal forces. Even though the temperature will change with time, it is by itself an independent variable that will be later determined by numerical simulation. After integration over the time dependent weld area one can then calculate the welding force depending on temperature, normal force and time with:

$$F_W(T, F_N, t) = \sqrt{\left(\frac{Y(T)}{2}\right)^2 - \left(\frac{F_N/A_{DZ}}{2}\right)^2} * A_W(t) \qquad \text{(Eq.4-15)}$$

At this point, one can address the magnitude of error that will occur in the calculation, if the normal stress is assumed to be constant and equal F_N/A_{DZ}. The welder used in this study is capable of applying up to 2000N of normal force (in this case the error is the greatest), the maximum weld area is 20mm^2 and the room temperature yield strength of AA6061-T6 is 275MPa. Substituting these values into 4-15 and using the weld area as independent variable, one can then simply plot the difference in weld force for the two cases in which the normal stress is F_N/A_{DZ} (i.e. constant) or F_N/A_W (i.e. depending on the weld area).

66
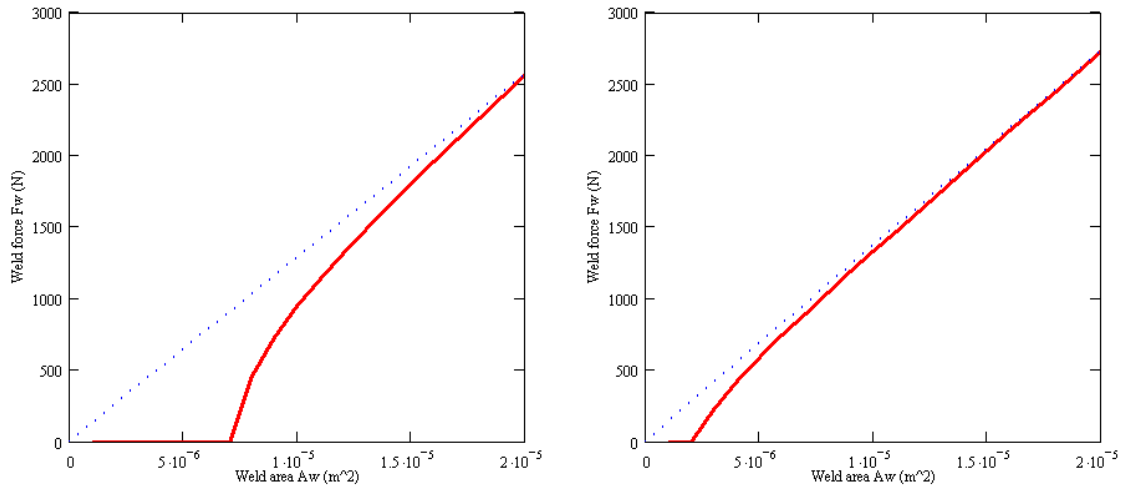
Figure 4.15: Determination of the calculation error when constant normal stress is used.

In figure 4.15 the difference in weld force for constant normal stress (dashed line 2000N/A_{DZ} left, 700N/A_{DZ} right) and normal stress dependent on the weld area (solid line 2000N/A_S left, 700N/A_S right) is shown. The two lines in each plot show the two most extreme possible welding forces, dependent on the weld area. In the left graph the normal force is high, and the maximum error is up to $A_W=A_S/2$ significant, but if a high normal force is used, the weld area growth is very rapid (see results in Section 6.8). Furthermore photographs of the peeled weld interface indicate that the area of non contact will disappear after a very short weld time so that the normal stress will be constant for the main part of the weld cycle. For lower normal forces the error is less, even if the weld area growth is slower then with high normal forces.

Recall this was developed for the special case of the welded parts being exactly the dimensions of the sonotrode (see figure 4.13). Now we look at the effects on stresses that result when part dimensions are increased.

As previously illustrated (see for example figure 4.7), the contact stresses between the parts will "spread out" depending on part thicknesses and anvil area. The stress distributions on the top and interface surfaces for a thin sheet are shown in figure 4.16 at the end of a weld cycle, when the weld area A_W covers the entire deformation zone area A_{DZ}. The photograph in the top left of figure 4.16 shows the nature of an actual ultrasonic weld interface. The deformation zone area is outlined by the white circle. However, it is clearly seen that unwelded, but abraded areas are formed outside the weld, as well as inside the deformation zone area (in this case the weld was not completed in order to be able to peel the weld). This is a strong indication of an abrasive, friction-like process that is itself capable of contributing to the total interface force during the welding process. This lead to the conclusion that the total interface force is comprised of two force components, the shear force arising from equation 4-15 that is responsible for the welding process and a net friction force that does not contribute to the actual bonding of the material, i.e. the friction force present inside the deformation zone during welding and the friction force that arises from the surface contact outside the deformation zone.
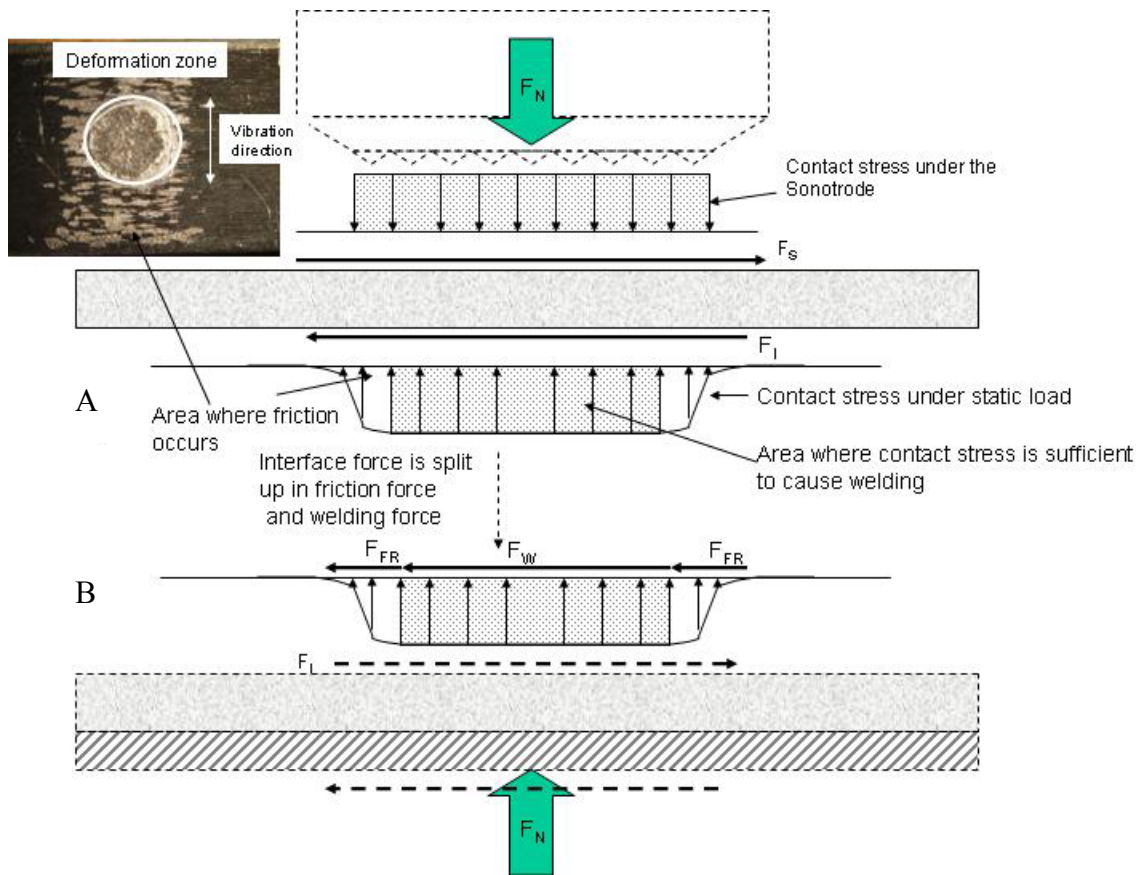
Figure 4.16: Separation of interface forces into two components.

The issue now becomes one of separating these two forces that act at different areas of the interface. In figure 4.16 the separation is done by going from A to B. It has to be kept in mind that the separation is done at the end of a weld cycle; during welding there is also a frictional force within the deformation zone as discussed earlier. In the following the friction force from inside the deformation zone and outside the deformation zone will be summarized as F_{FR}. The interface force is therefore $F_I=F_{FR}+F_W$. The welding force has already been explained earlier. The frictional force component is more difficult to determine because the ultrasonic vibration might influence the friction coefficient of the parts and the force will also change with increasing weld area (the

friction force within the deformation zone will disappear). The frictional force

component can be described with:

$$F_{FR} = \mu_s * \sigma_N * A_{Fr}$$
(Eq.4-16)

Where: μ_S: Static friction coefficient

To evaluate equation 4-16 would be very complicated, because neither the normal

stress outside the deformation zone is known exactly, or the development of A_{FR} during

the weld cycle. Nevertheless, in section 6.5 it is shown that calculating the friction with

the friction law is a sufficient approximation.

$$F_{FR} = \mu_S * F_N$$
(Eq. 4-17)

Equation 4-17 will also be used to approximate the heat generation by friction during

welding and then in section 6.8.3 to calculate the total interface force.

One has to keep in mind, that as the parts become thicker, the area over which the

frictional force is operating spreads out, together with the contact stress (figure 4.7). This

effect and the effect of a different sonotrode shape on the contact stresses always have to

be kept in mind when using the model representation and equations developed here.

In figure 4.17 the weld zone and all the shear and normal stresses acting on the

individual components are summarized, as they have been developed in the preceding

discussion. It shows the top part has been reduced to a small section of the original part.

This small section is considered rigid and only the top and bottom surface can undergo

plastic deformation when the yield condition is met. The compressive stress on this part

is constant and uniform and given by the normal force (F_N) divided by the sonotrode area

($A_S = A_{DZ}$). Furthermore it has been assessed that the area in which welding occurs (e.g.

deformation zone) does not exceed the sonotrode area. This means for the weld area

$A_W \leq A_S$ at all times. The extensions of the top part have been treated as elastic rods,

excited at the face in contact with the rigid top part. The bottom part is rigid and fixed as

well as the anvil, therefore the forces that act on the surfaces are of equal amount and in

opposite direction. The force acting on the sonotrode area is limited by the earlier

discussed material limits.
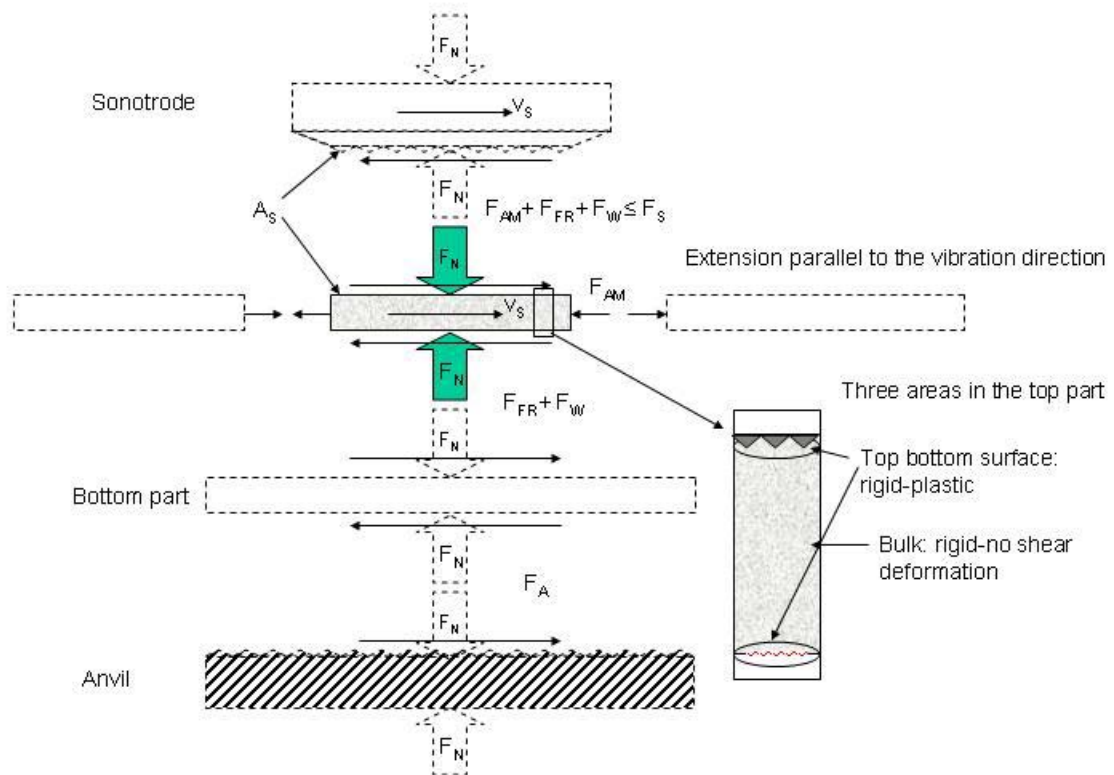
Figure 4.17: Summary of all forces acting on the individual components in the weld zone.

The equation of motion for the top part can be written down as:

$$m * \ddot{\xi}_{max} = F_S - F_W - F_{FR} - F_{AM}$$ (Eq. 4-18)

The single components in equation 4-18 are then given by:

- $m\ddot{\xi}_{max}$ is given by the dimensions, density and excitation amplitude of the reduced top part.

- The limit of the sonotrode force (F_S) is given by equation 4-1.

- The welding force (F_W) is given by equation 4-15.

- The friction force (F_{FR}) is given by equation 4-17.

- The force to excite the extension (F_{AM}) is given by equations 4-7 and 4-8.

By solving equation 4-18 for F_S and substitution into 4-1 one arrives at following condition:

$$m * \ddot{\xi}_{max} + F_W + F_{FR} + F_{AM} \leq \sqrt{\left(\frac{Y(T)}{2}\right)^2 - \left(\frac{F_N/A_S}{2}\right)^2} * A_S$$ (Eq. 4-19)

If the l.h.s of condition 4-19 is not smaller then the r.h.s. throughout the welding cycle, yielding will occur beneath the sonotrode and consequently sonotrode sticking and extrusion. In addition to that an unstable weld condition will arise at which one can not be certain about the weld quality (i.e. condition 4-19 is not met prior to weld completion).

4.4 The heat generation and conduction at the weld

During USMW a substantial amount of heat is generated at the weld interface and the surrounding area, due to plastic deformation and friction as well as at the sonotrode-top surface interface. This generation of heat and the subsequent change of temperature have a significant impact on the material properties. The ulterior motive during this development is to generate equations, that would give a good approximation of the acoustical power (force times velocity; developed theoretically in the previous section) dissipated at the weld interface.

It is realized that in the initial phase of welding plastic deformation occurs at the sonotrode top part interface while the sonotrode knurls engage into the top part surface. By this, heat is generated as well, but it was found (see section 6.1) that a welding cycle is of the order 20 to 25 times longer then this initial phase. Therefore this initial heating phase at the sonotrode has been neglected. For practical purposes the heat inputs due to plastic deformation and due to friction have been separated. The heat input due to plastic deformation has been confined to the deformation zone area (i.e. the sonotrode area A_S in this model) and the heat input due to friction to the friction area surrounding the weld area. The friction area was experimentally determined in section 6.3.2.

4.4.1 Heat generation due to deformation

To model the heat input into the parts and temperatures that occur during welding one has to take a closer look at the distribution of the heat sources, which are the deformation islands or microbonds, across the deformation zone and their development during the weld cycle. This is shown schematically in figure 4.18.

At the beginning of the weld cycle the deformation islands occur randomly across the deformation zone. Because of the high thermal conductivity of aluminum the temperature will even out very rapidly across the deformation zone. By this one can argue that the total power developed in all deformation islands is distributed evenly over the entire volume of the deformation zone. If one considers each deformation island to be equal in size and by that delivering an equal amount of power (P_i) the preceding is given by:

$$\frac{P\_total}{V\_deformation\_zone} = \frac{\sum P_i}{V\_deformation\_zone} \qquad \text{(Eq. 4-20)}$$

or in integral form (using V_{DZ} as deformation zone volume)

$$\frac{P_{total}}{V_{DZ}} = \frac{\int dP}{V_{DZ}} \qquad \text{(Eq. 4-21)}$$

This uniform distribution of power will then result in an average temperature that can be measured. As the weld develops from figure 4.18 A to 4.18 C the number of deformation islands (and consequently heat sources) will increase as well as the size of individual deformation islands, until eventually the entire deformation zone is covered with plastically deforming material, or sonotrode extrusion occurs. The picture in figure 4.18 shows an actual weld interface in which the distribution of microbonds can be seen [21].
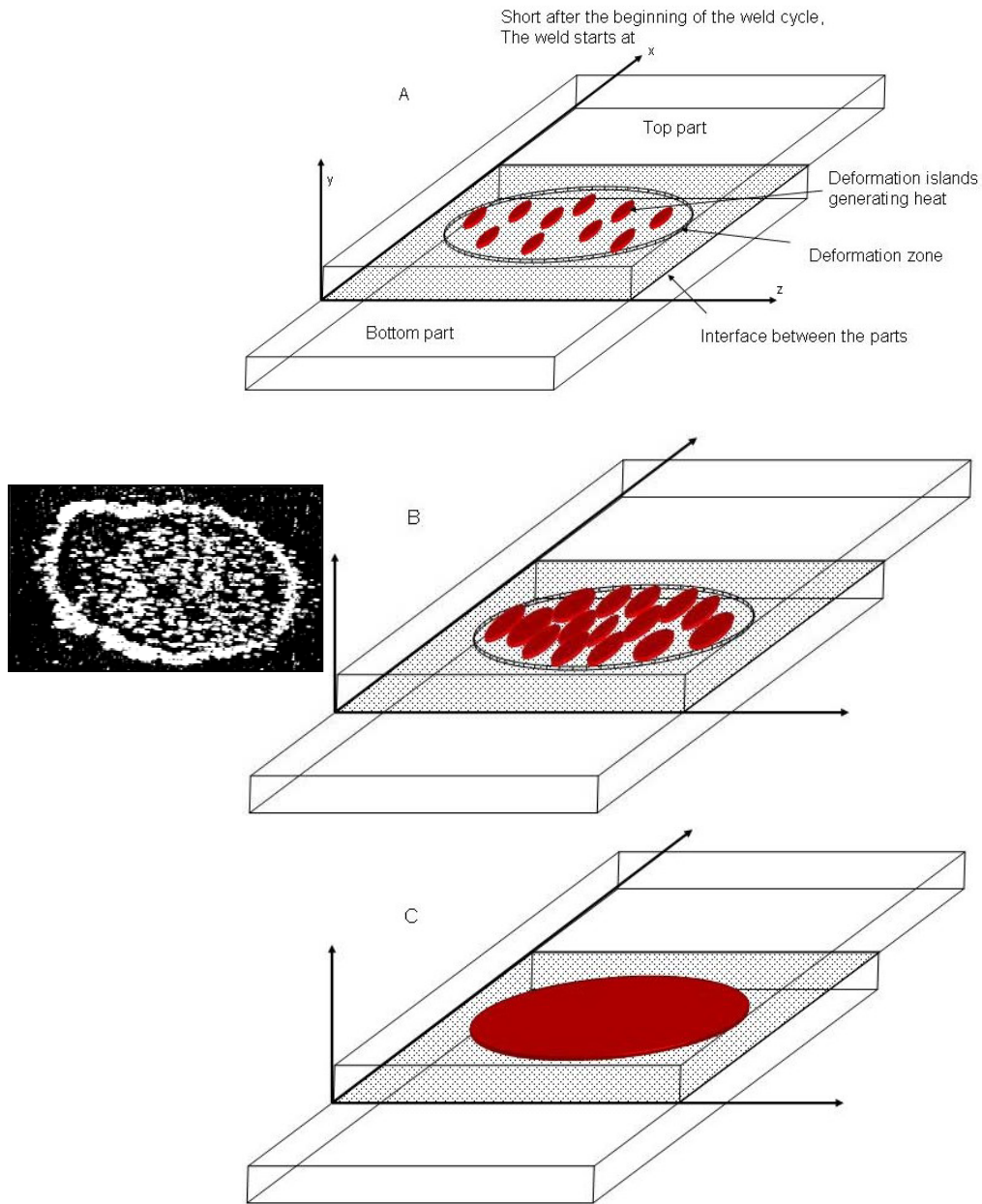
Figure 4.18: The growth of heat sources within the deformation zone during welding.

To calculate the heat generated by the deformation islands one has to look at a differential shear element that undergoes plastic shear deformation across a thin layer. In

figure 4.19 a schematic of such an element is shown, where the volume dy*dA is plastically deformed.
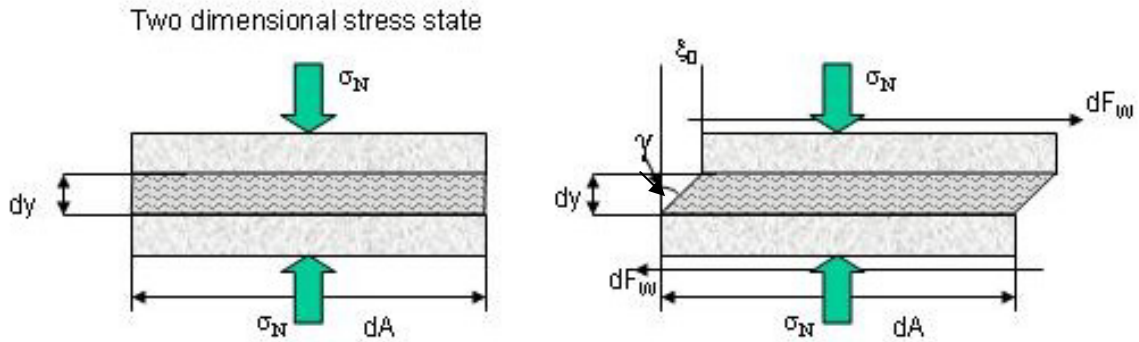
Figure 4.19: Shear element undergoing shear strain.

For an elastic shear element the work done on the strained volume is the shear stress (τ) multiplied by the shear angle (γ). In this special case the shear stress is equal the shear yield stress of that volume. This will also be the maximum stress that can occur if one assumes a perfectly plastic material that undergoes no work hardening, regardless of the amount of shear strain. Thus, for shear deformation following equation is valid for the work done across the deformed volume.

$$\frac{dW}{dV} = \tau_y * \gamma \qquad \text{(Eq. 4-22)}$$

Where: W: Work
                                                         V: Deformed volume
                                                         γ: deformation angle

77

The work done on the volume in a certain period of time, is equal to the angle change during the same amount of time. The angle is to a good approximation the deflection of the top part divided by the thickness of the deformed layer, giving:

$$\frac{\Delta dW}{\Delta t} * \frac{1}{dV} = \tau_Y * \frac{\Delta \xi}{\Delta t * dy} \qquad \text{(Eq. 4-23)}$$

The change of work (or energy) over time is of course equal to the power (P) and the change of amplitude with time is simply the average vibration speed (in contrast to the average velocity which is zero), which for a frequency f_w and amplitude ξ_0 is given by:

$$\frac{\Delta W}{\Delta t} = P \qquad \text{(Eq. 4-24)}$$

$$\frac{\Delta \xi}{\Delta t} = v_{avg} = \frac{1}{T} \int_0^T |\Omega * \xi_0 \cos(\Omega t)| = 4 * \xi_0 * f_W \qquad \text{(Eq. 4-25)}$$

Where: f: Vibration frequency
                                                                                            T: Vibration period

Equation 4-24 and 4-25 can be substituted into 2-23. This gives then an expression for the average power, dissipated at any point in time:

$$\frac{dP}{dV} = \tau_y * \frac{v_{avg}}{dy} \qquad \text{(Eq. 4-26)}$$

78

The thickness of the deformed element is constant therefore the differential volume dV can be rewritten as dA*dy. By doing so and multiplying both sides with dy one arrives at:

$$\frac{dP}{dA} = \tau_y * v_{avg} \text{ or } dP = \tau_y * v_{avg} * dA$$

(Eq. 4-27)

Equation 4-27 now gives an expression for the average differential power as it is needed in equation 4-21. The equation shows also that the average differential power is only dependent on the differential area element. Substituting 4-27 into 4-21 one gets:

$$\frac{P_{totol}}{V_{DZ}} = \frac{\int dA * \tau_y * v_{avg}}{V_{DZ}}$$

(Eq.4-28)

Similarly then in equation 4-13 the integration needs to be done over the weld area $A_W(t)$ doing so and replacing V_{DZ} by $A_{DZ}*dy$ and multiplying both sides of the equation by dy one gets:

$$\frac{P_{total}}{A_{DZ}} = \frac{\tau_y * A_W(t) * v_{avg}}{A_{DZ}} = \frac{F_W(t) * v_{avg}}{A_{DZ}}$$

(Eq. 4-29)

We have now arrived at an expression that gives us the amount of acoustic power that is generated by plastic deformation or welding over the deformation zone area. A

heat flux is a power dissipated over an area, therefore one can rewrite 4-29 substituting 4-15 as the weld force and 4-25 as the average speed to be the temperature and time dependent heat flux for the deformation area that was sought.

$$\dot{q}_W = \frac{\sqrt{\left(\frac{Y(T)}{2}\right)^2 - \left(\frac{F_N/A_{DZ}}{2}\right)^2} * A_W(t)}{A_{DZ}} * 4 * \xi_0(t) * f_W \qquad \text{(Eq. 4-30)}$$

The time dependence of the amplitude in 4-30 is caused by the initial period of in the weld cycle, in which the sonotrode engages into the top part. During this period the amplitude at the interface will not be equal to the amplitude of the sonotrode.

4.4.2 Heat generation due to friction

The power dissipated due to friction at the interface can be calculated in a very similar fashion. The power can simply be calculated with the product of friction force (F_{FR}) and the average speed. Essentially the same development for the heat input due to friction was put forward for plastic welding by Stokes [71]. This power is dissipated over the friction area (A_{FR}), which is the area over which the friction occurs. This area has to be determined by experiment for individual sheet thicknesses (which will be described in section 6.3.2). The above considerations then lead to the following equation.

$$\frac{P_{FR}}{A_{FR}} = F_{FR} * v_{Avg} \qquad \text{(Eq.4-31)}$$

Now one can write down the heat flux boundary condition for the friction area, using equation 4-17, 4-25 and 4-31 remembering of course that the amplitude changes with time.

$$\dot{q}_{FR} = \frac{\mu_S * F_N * 4 * \xi_0(t) * f_W}{A_{FR}} \qquad \text{(Eq.4-32)}$$

4.4.3 Heat conduction from the weld interface

These boundary conditions even though developed through simple equations and with simplifications due to certain assumptions, are fairly complicated, and would lead to a nonlinear, non-homogeneous heat conduction equation. The equations would be very hard to solve analytically (if there is even a closed form solution). It was therefore chosen to solve the heat conduction problem by finite element analysis (FEA), using the program ANSYS.

The geometry of the model is shown in figure 4.20. The model is axi-symmetric around the axis of the circular weld sonotrode, which leads to a significant reduction of computation time. In the model the heat generated during the beginning phase of the weld cycle at the sonotrode top part interface has been neglected, as mentioned before, this was done because of the short duration of the initial time period.

81

Symmetry axis

Sonotrode (Steel)

Axi-symmetric model for FEA

Welding area

Friction area

Top part (AL)

$\frac{1}{2}\dot{q}_w$

1mm $1/2\dot{q}_{s}$

1mm $1/2\dot{q}_{s}$

Bottom part (AL)

$\frac{1}{2}\dot{q}_w$

2.5mm

5mm

Anvil (Steel)

Material properties:
Steel $c_{St} = 460\ J/(kg^*K)$
         $k_{St} = 24.3\ W/(m^*K)$
         $\rho_{St} = 7800\ kg/m^3$
Aluminum $c_{Al} = 896\ J/(kg^*K)$
         $k_{Al} = 180\ W/(m^*K)$
         $\rho_{Al} = 2700\ kg/m^3$
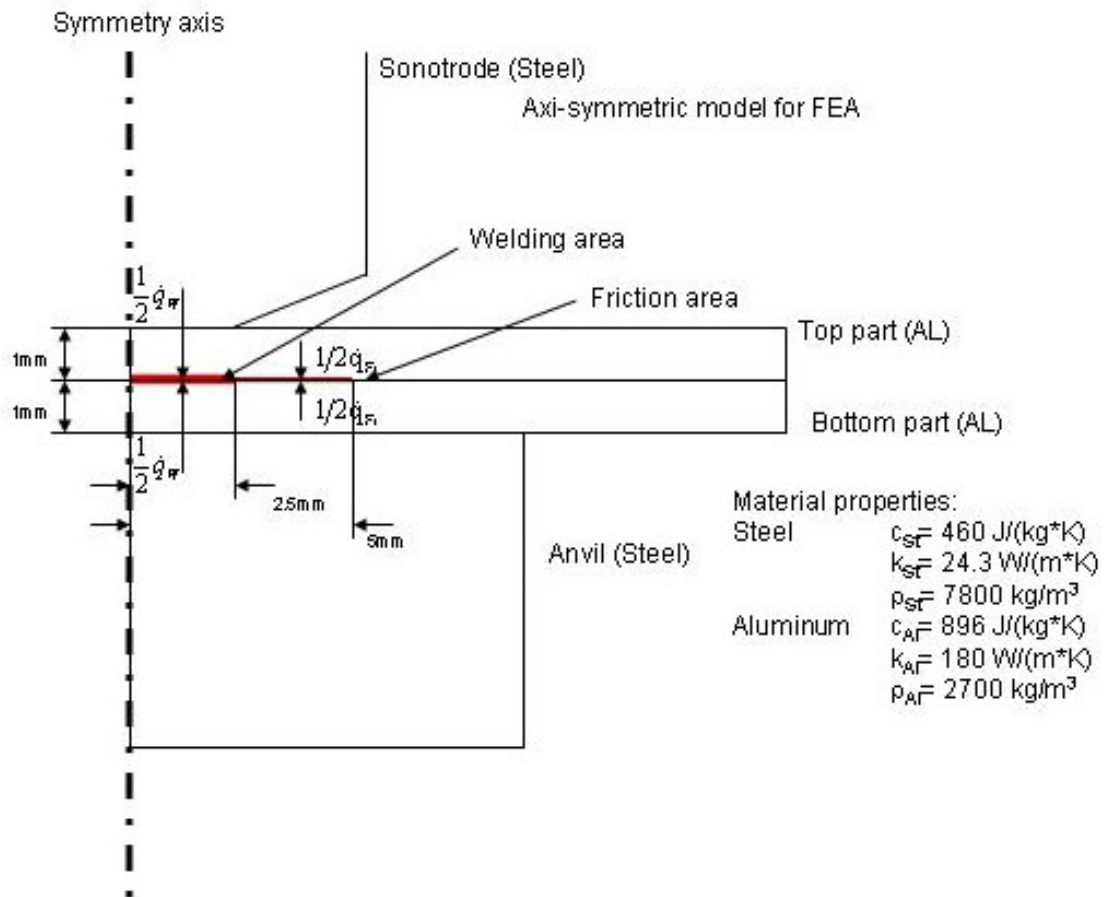
Figure 4.20: FEA heat conduction model.

The heat fluxes are applied at the weld area and the surrounding friction area. From experiments (see section 6.3.2) it is known that the friction area has approximately twice the radius then the weld area. It needs to be assured for the heat flux at the weld area that the heat flux is dependent on the temperature of that area on which it is applied.

4.5 Elastic shear strain of the parts

Up to now the elastic shear strain of the parts has been neglected. In this section
the error, introduced to the model developed in the preceding sections by the neglect of
elastic shear strain, is estimated. This unfortunately can not be done in general terms but
by anticipating some of the experimental results. The reduced top part at rest and at
maximum deflection is schematically shown in figure 4.21. The deflection in this case is
the sonotrode amplitude ξ_0. Ignoring the material surrounding the reduced top part will
result in shear strain values that are higher then in a "real" part. In a "real" part stiffness
is added by the surrounding material, therefore lowering the elastic shear strain. The
shear forces will cause plastic deformation of the part, therefore reducing the deflection at
the interface by ΔX.
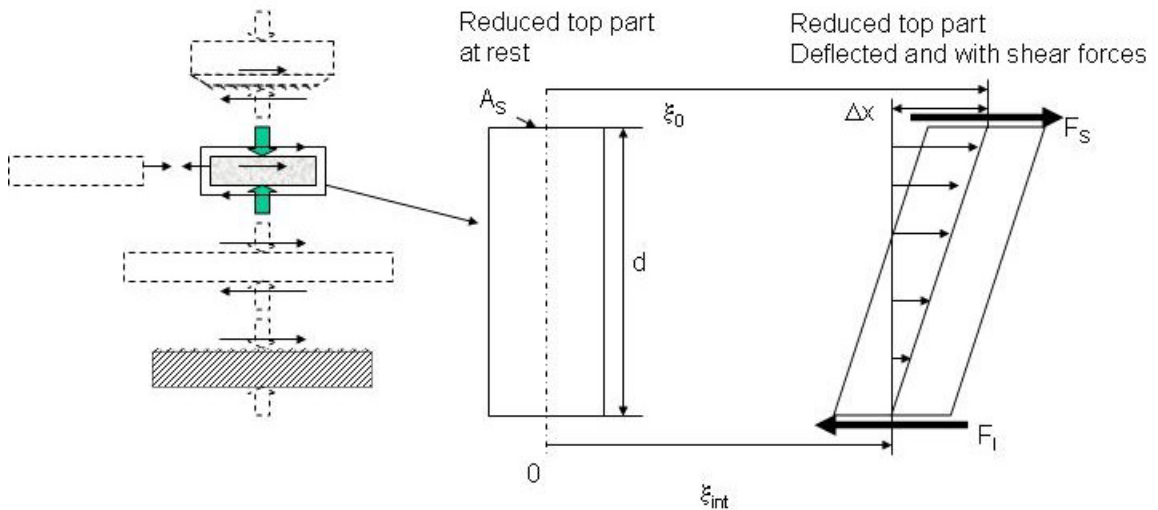
Figure 4.21: Elastic shear strain of the reduced top part.

First one has to calculate the magnitude of ∆X that can be expected for the forces acting during USMW and for the given material (AA6061-T6). The area of the reduced element is equal to the sonotrode area, and the thickness d=1mm for the most experiments. Since the material heats up during welding, the temperature dependent shear modulus needs to be used (see figure 5.8). The elastic shear strain is given by:

$$\Delta X(F,T) = \frac{F * d}{A_S * G(T)} \qquad \text{(Eq. 4-33)}$$

Where: G(T): Temperature dependent shear modulus
                                           F: General shear force

The maximum force that can occur during welding is given by equation 4-1. Substituting equation 4-1 into 4-33, one can calculate the maximum elastic shear strain that could theoretically occur during welding, before yielding occurs. The elastic shear strain (∆X) dependent on different shear forces is shown in figure 4.22. The maximum shear strain that can occur before the yielding condition is met (it is shown for 2000N normal force) is shown as well. The maximum anticipated shear force is 2000N (see section 6.8.4). This means the elastic shear strain can be as high as 4μm for the reduced top part. This seems rather large, because typical vibration amplitudes are in the order of 10μm.

$$\Delta X_{max} = \frac{\sqrt{\left(\frac{Y(T)}{2}\right)^2 - \left(\frac{F_N/A_S}{2}\right)^2} * d}{G(T)} \qquad \text{(Eq. 4-34)}$$
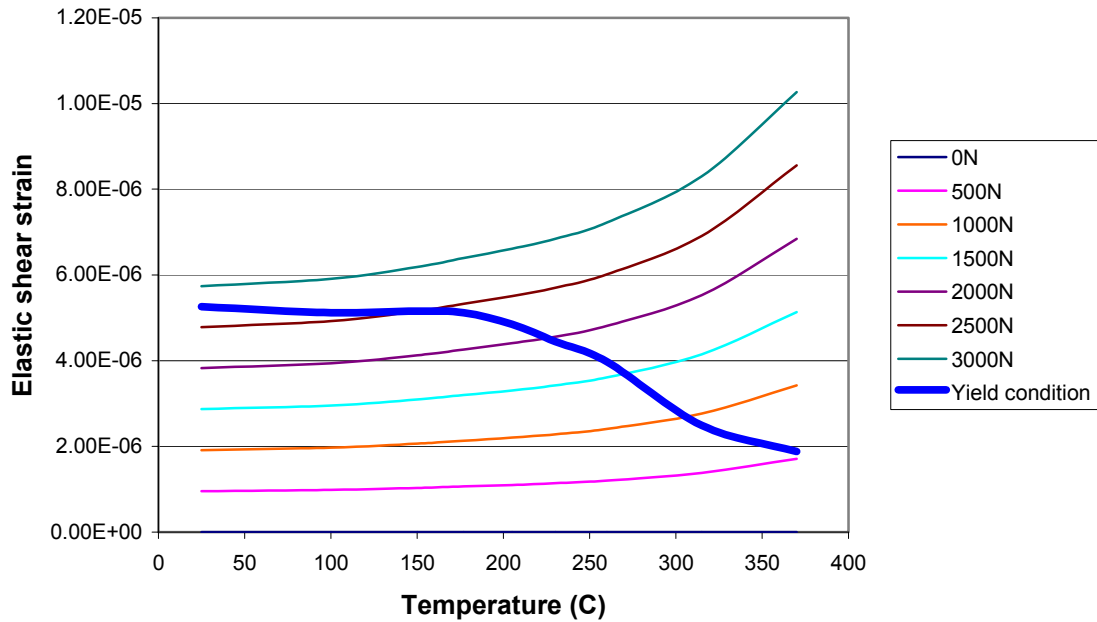
Figure 4.22: Elastic shear strain versus temperature for different shear forces.

At this point one can calculate the influence of the elastic shear strain on the equation of motion of the reduced part (equation 4-4 in this case). The elastic shear strain can be regarded as linear across the cross section of the part. Therefore an average amplitude for the equivalent rigid body motion can be calculated with:

$$\frac{\xi_0 + \xi_0 - \Delta X}{2} = \frac{10\mu m + 6\mu m}{2} = 8\mu m = \xi_{avg} \qquad \text{(Eq. 4-35)}$$

The l.h.s. of equation 4-4 can now be calculated by using ξ_0 and ξ_{avg} and $\Omega=2\pi*20kHz$, d=1mm, A_S=20mm^2 and ρ_{Al}=2700kg/m^3.

$$A_S * d * \rho_{Al} * \Omega^2 * \xi_0 = 8.5N$$

$$A_S * d * \rho_{Al} * \Omega^2 * \xi_{avg} = 6.8N$$

Comparing the two results and then recalling the value for the forces expected (2000N) one can say that the error made in the dynamic model by neglecting the elastic shear strain is very small. In fact the absolute value of this term is so little that it can be neglected all together.

The shear deformation also changes the average interface speed that is used in equations 4-30 and 4-31 to calculate the heat flux during welding. The average speed in both equations is considered constant for the most part of the welding cycle (with a very quick rise time). The heat flux from friction is modeled so that it is applied outside the weld area at the friction area. The friction area is (by measurement, section 6.3.2) four times larger then the weld area. This means the shear force acts on a four times larger area and is therefore four times smaller then the shear strain calculated for the reduced part. This reduces the maximum shear strain to only 1μm and can be neglected (see figure 4.22 and equation 4-33). The same is true for the bottom part.

In the case of heat being generated by plastic deformation, equation 4-30 has two very dominant terms. At the beginning of the weld time the area growth term is dominating and in the latter stages the square root term will dominate. One can put forward two example calculations where at the beginning of the weld the heat input can

be calculated for room temperature and for the latter stages the heat input for elevated temperatures. Interface velocities are then a constant factors, one time neglecting shear strain ($\xi_{int}= \xi_0$) and the other time with shear stain ($\xi_{int}= \xi_0-\Delta X$). It will be shown (section 6.8.1) that the weld area growth function can be approximated by:

$$A_W(t) = 20mm^2 * \left(1 - e^{\frac{k*t}{\sec}}\right)$$ (Eq. 4-36)

Where: k in the order of -20 for typical weld.

The heat flux can be calculated with equations 4-37 (room temperature yield strength) and 4-38 (constant area). The results are shown in figure 4.23. The left graph shows the heat flux at the very beginning of the weld cycle (room temperature yield strength) and the graph on the right shows the heat flux in the latter stages of welding at elevated temperatures. One can see that heat flux at the beginning is dominated by the weld area growth function, so that the difference between the two cases is not very large (circle in the left graph). In the latter stages the heat flux is dominated by the temperature within the weld zone, and for that reason the heat flux difference is not very large (circle in the right graph). Considering the very rapid temperature increase the transition from the left to the right is very quick. This means that the heat input due to plastic deformation is generally small (at the beginning of the weld or at elevated temperatures) in either case (taking elastic shear strain into consideration or not). A slight temperature change at the weld interface would compensate for the difference in heat flux.

$$\dot{q}_W = \frac{\sqrt{\left(\dfrac{Y(room\_temperature)}{2}\right)^2 - \left(\dfrac{F_N/A_{DZ}}{2}\right)^2} * A_W(t)}{A_{DZ}} * 4 * \xi * f_W \qquad \text{(Eq. 4-37)}$$

$$\dot{q}_W = \frac{\sqrt{\left(\dfrac{Y(T)}{2}\right)^2 - \left(\dfrac{F_N/A_{DZ}}{2}\right)^2} * A_{DZ}}{A_{DZ}} * 4 * \xi * f_W \qquad \text{(Eq. 4-38)}$$
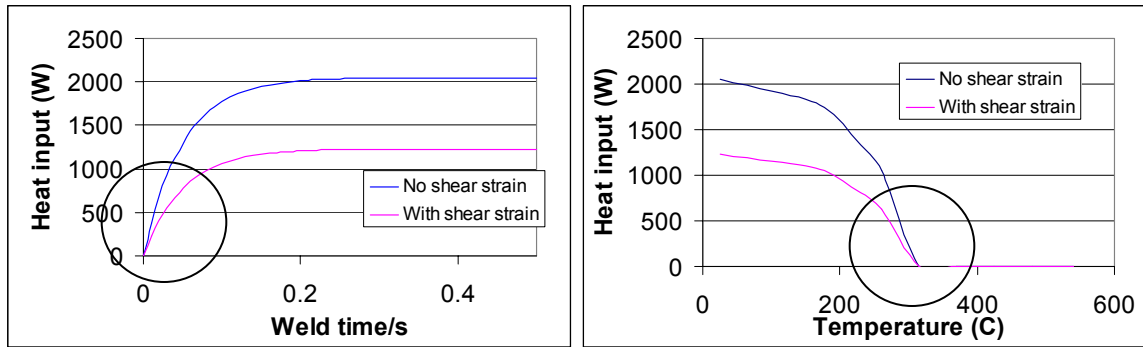
Figure 4.23: Heat fluxes at the beginning of a weld cycle at constant temperature and in the latter stages at elevated temperature.

In summary, one can say that neglecting elastic shear strain results only in a small error, for both the dynamic model and the thermal heat conduction model. The resulting heat will only be slightly elevated during welding. One has to recall that the figure 4.23 is calculated for the absolutely worst cases possible. The shear forces were the highest, that might occur under special welding conditions (the shear forces in an average weld should be in the order of 1000N) and furthermore only the reduced top part are was considered for the shear strain calculation. In real welds the expected shear strain should be much lower. For thicker sheets one has to be cautious, though, because the effects

considered here will be proportional to the thickness. Using the above discussion, then the elastic shear strain for a 3mm thick part would exceed the actual vibration amplitude, and no welding at all would take place.

Another very strong indication for small elastic shear strain is that the phase angle between the voltage and current to the transducer never exceeded 20 degrees, limiting the apparent power to approximately 5% of the total power. The apparent power is a measure of the elastic energy stored in the system during welding. And since the apparent power is very little, this must mean that there is very little elastic strain energy stored in the welding system (parts) during welding.

4.6 Summary of the developed model

In summary here are the essential features of the model. The most important feature of the model is that the temperature dependent material properties were considered and it was realized that the material properties change drastically at elevated temperatures.

The forces that are acting on the mass element beneath the sonotrode were identified. By doing so, welding conditions dependent on the part dimension could be identified under which welding will not be possible. Furthermore it was recognized that the friction coefficient of the parts is more important then it has yet been conceived.

Equations were developed, using full advantage of modern days computation capabilities not being confined to an analytical or approximate solution. By doing so it is

possible to numerically calculate the temperatures that will occur at the weld interface

and the sonotrode part interface.

The temperatures calculated from the FEA can then be used to predict weld and

interface forces, because if the temperatures are known, then the exact material properties

are known.

CHAPTER 5

EQUIPMENT AND MATERIALS

In the following the equipment and materials been used for this work will be described. Since there was a great variety of equipment used the descriptions will be brief, and the description will be limited to the most important equipment properties and features. The principal functionality of standard equipment is assumed (i.e. high speed camera, infrared camera, optical sensor and the tensile test machine). The mechanical, thermal and surface properties of the Al 6061-T6 material will be reviewed.

5.1 Ultrasonic welding system

The welder is a Sonobond FC2025 ultrasonic metal welder. It is a wedge reed system operating at 20kHz. The frequency converter is capable of delivering up to 2500W of power. The principal set up of the welder is shown in figure 1.1. The normal force (F_N) is applied with a pneumatic cylinder, capable of applying up to 450 lbf (2000 N). The welding sonotrode and anvil are made of M2 heat treated tool steel and have a surface knurl geometry shown in figure 5.1. The system in its original set up has a "counter resonant anvil" [6] which is designed to be 130^0 out of phase with the sonotrode

vibrations, thus increasing the relative displacement between the weld pieces [7]. For

force measurements the anvil was replaced by a rigid anvil with a shear force sensor

incorporated (this set up will be explained in more detail later).
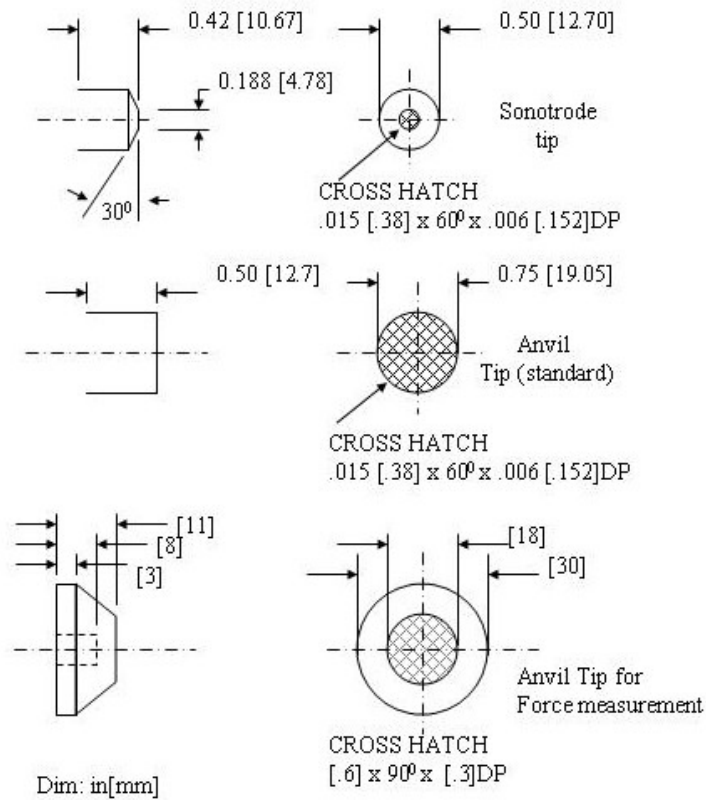
Figure 5.1: Sonotrode and anvil knurl geometries.

The power supply (Sonobond model FC2025) has the following adjustable parameters:

- **Power Level**: 1 to 10 (The AC voltage delivered to the transducer), with the
  calibration between powerlevel and rms-voltage as noted in figure 5.2.

- **Matching**: Setting of A to P: Represents the impedance matching between power
  supply and the acoustic system. The letter selected should match the internal 50

Ohms resistance of the power supply to the more complex impedance of the welding system. Usually the right matching has to be found using an oscilloscope.

- **Squeeze time**: Setting range of 0.1s to 0.9s. The time during which the parts are clamped together before ultrasonic energy is applied.

- **Welding time**: Setting range of 0.1 to 3.0s. This is the duration of the ultrasonic pulse to the transducer.

- **Air Pressure**: Setting range up to 100 psi. This applies the static or normal force to the vertical reed of the system (see figure 1.1 for details), with the calibration between pressure and force as noted in figure 5.2.
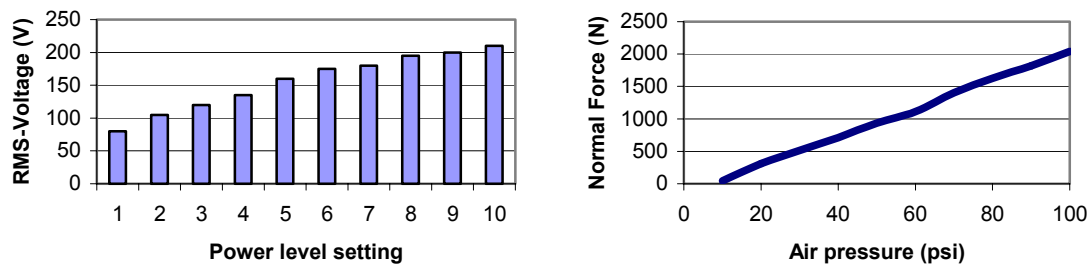
Figure 5.2: Power level vs. RMS-Voltage and Air pressure vs. Normal Force for Sonobond ultrasonic welder.

In some experiments the matching setting was changed from its optimum setting. This resulted in reduced power delivered to the transducer and thus less amplitude or shear force. In the majority of the experiments the matching stetting was adjusted as close to its optimum value as possible.

93

5.2 Shear force sensor

The shear force sensor is a Kistler 'Slim Line' 9146B in combination with a Kistler 5010B Dual mode charge amplifier, as shown in the system schematic of figure 5.3.
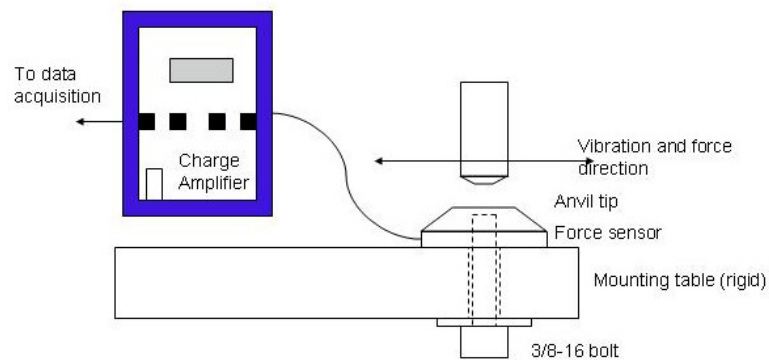
Figure 5.3: Set up for shear force measurement.

For shear force measurements the original contra-resonant anvil assembly was replaced by a 24mm thick steel plate, mounted directly to the frame of the welder, thus providing a rigid foundation, with the sensor then bolted to the plate. The sensor uses two piezoelectric 'shear mode' disks (i.e. polarized to be sensitive to a shearing action). The sensor is insensitive to normal loads because the two disks are mounted to cancel out any polarization in the normal direction. The stress applied by the bolt needs to be great

enough so that no sliding can occur at the anvil, sensor, plate interfaces. This set up is now fairly rigid, but one has to check the frequency response of the anvil tip to make sure its primary resonance is well away from the 20 kHz excitation frequency. For this purpose, the system can be treated as a mass-spring system as shown in figure 5.4.
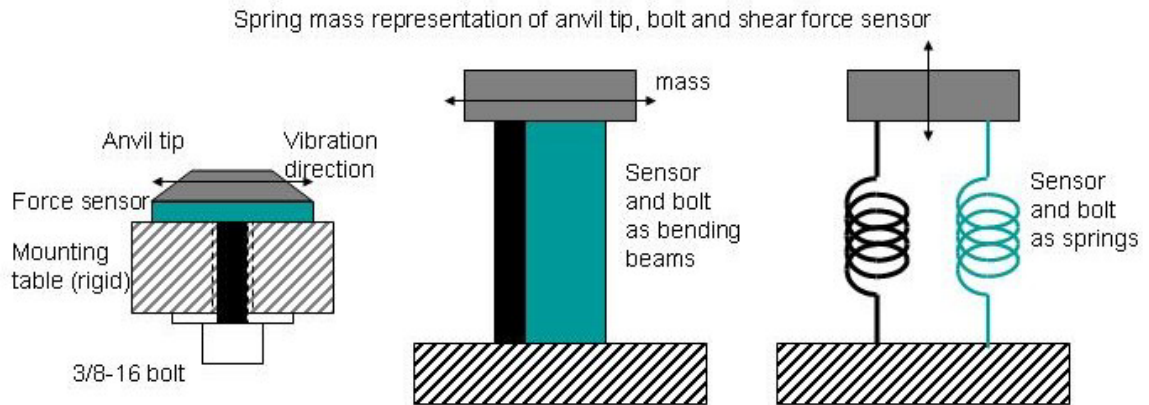
Figure 5.4: Mass-Spring representation of the anvil set up.

The spring constant (i.e. rigidity) of the bolt is approx. $4*10^6$ N/m and the spring constant of the load washer in shear is $2*10^9$N/m. The mass of the anvil tip together with the bolt inside is approximately 50g. With these values the resonance frequency of the system is approximately 31kHz. The frequency response for this system to a 1000N excitation is shown in figure 5.5.
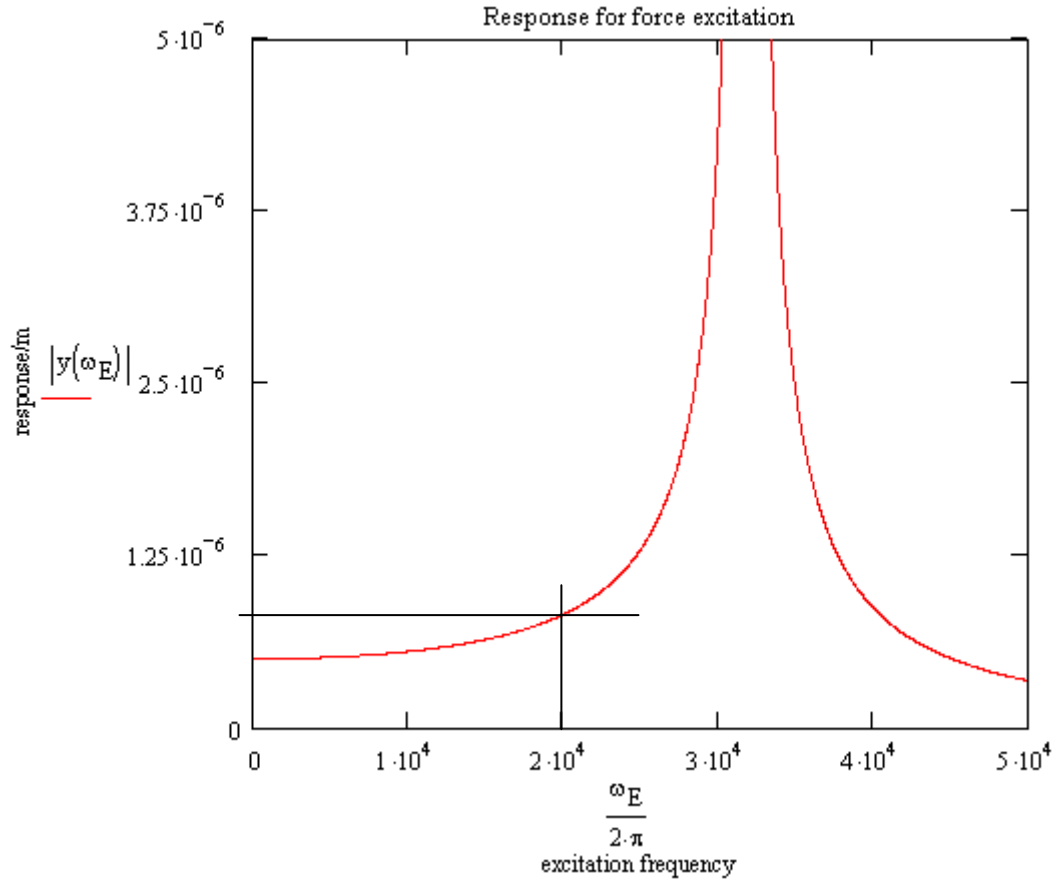
Figure 5.5: Frequency response of the anvil tip.

One can see from figure 5.5 that the response is 1.65 times larger at 20kHz then at low frequencies and therefore assuming a linear dependence of the charge and the displacement it can be said that the real force is only 0.61 times the measured force. This value is unfortunately only a good guess. Since the dependence of charge and displacement is unknown, one needs to be cautious with the absolute measured values. During experimentation it was found that even with the correction factor the measured

forces were still too large, but this deviation from the "real" force was quite consistent and repeatable.

5.3 Optical 'Fotonic' Sensor

The vibration amplitude of sonotrode and anvil has been measured with an MTI 2000 Fotonic Sensor in combination with two sensor modules model 2062R. This sensor was used because it uses fiber optic level displacement sensors, which permits noncontact measurement of surface displacements. Fiber optic level displacement sensors utilize adjacent pairs of light transmitting and light receiving fibers. The operating basis is the interaction between the field of illumination of the transmitting, or source fibers and the field of view of the receiving, or detector fibers. A brief description of the sensor can be found in Appendix C for more detailed information it is referred to the operation manual [63].

5.4 Data acquisition system

An ultrasonic welding data acquisition system (DAQ) was designed to meet the needs to monitor, record and analyze the USMW process [64]. The DAQ consists of hardware components to acquire the data into a PC and software that does the consequent data analysis. The outputs from the DAQ are:

97

- RMS-Voltage

- RMS-Current

- RMS-Power

- RMS-Resistance

- Maximum vibration amplitude in 1ms intervals

- Maximum force in 1ms intervals

Furthermore the DAQ can serve as a digital oscilloscope, recording and viewing the originally recorded voltage, current, vibration and force curves. An overview of the hard-and software components is given in Appendix D. For more detailed information it is referred to the user manual [65]. A photograph of the Ultrasonic welding system and the DAQ is shown in figure 5.6.

Figure 5.6: Ultrasonic welding system and DAQ.

5.5 Tensile machine

An Instron universal testing instrument was used to test welded parts. This
machine consists of a load frame with a moving crosshead, computer controlled driven by
two vertical drive screws, and a PC for the data acquisition and calculations. The
specimen to be tested is physically attached to the load cell by grips for tension testing
and to the crosshead. Tensile forces are then applied by the moving crosshead

(speed:2mm/min). The load cell measures the load, which is then recorded by a PC. The geometry of the specimen is shown in figure 5.7. The joint fracture strength was measured as the indicator of the weld strength. The specimens were 1/2x2 in (12.7x51.4 mm) aluminum coupons, if not stated differently, and they were all welded with a 0.50 in. (12.7 mm) overlap.
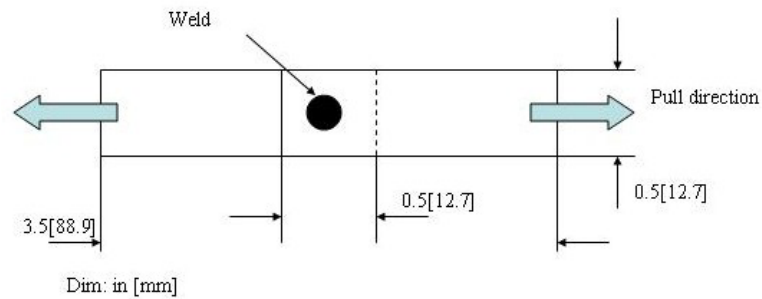
Figure 5.7: Tensile test specimen dimensions

5.6 Infrared and high speed cameras

The Agema Thermovision 550 camera was used for the infrared measurements of this study. The frame rate is 60Hz and the temperature measurement range is from -20^0C up to 1500^0C with standard filter. The detector has a resolution of 320x240 pixels. For more information see [66]. The IR movies were analyzed with Agema's IRwin Research 2.01 software. For more information see [67].

The high speed videos were made with a Phantom v5.0 by Vision Research, Inc. in this study. This camera is capable of 1000Hz frame rate at a resolution of 1024x1024 pixels. The movies were recorded with a PC and then analyzed with Phantom 5.0.545 software. For more information see [68].

5.7 Material

The material used in this program was AA6061-T6 aluminum alloy having the composition given in Table 2. Material properties, such as temperature dependent Young's modulus and shear strength, surface roughness and friction coefficients, were known from standard reference sources or were measured on representative samples. Thus, the temperature dependent properties yield strength and modulus are summarized in Table 3 and in graphical form by figure 5.8 and 5.9. When the influence of certain parameters was studied the experiments were usually interrupted when extrusion and excessive sticking occurred.

Al	Cr	Cu	Fe	Mg	Mn	Si	Ti	Zn
98%	0.04%-0.35%	0.14%-0.4%	Max 0.7%	0.8%-1.2%	Max 0.15%	0.4%-0.8%	Max 0.15%	Max 0.25%

Table 2: AA6061 material composition.

Temperature/K	Yield strength/MPa	Youngs modulus/GPa	Shear modulus*/GPa
298	275	68	26
373	260	66	25
423	250	63	24
450	240	61	23
478	220	59	22
503	195	57	21
533	165	54	20
588	90	47	18
643	55	38	14
698	22		
753	11		
813	8		

Table 3: AA6061 temperature dependent material properties.

$$* G = \frac{E}{2(1+\upsilon)} \quad \upsilon=0.33$$
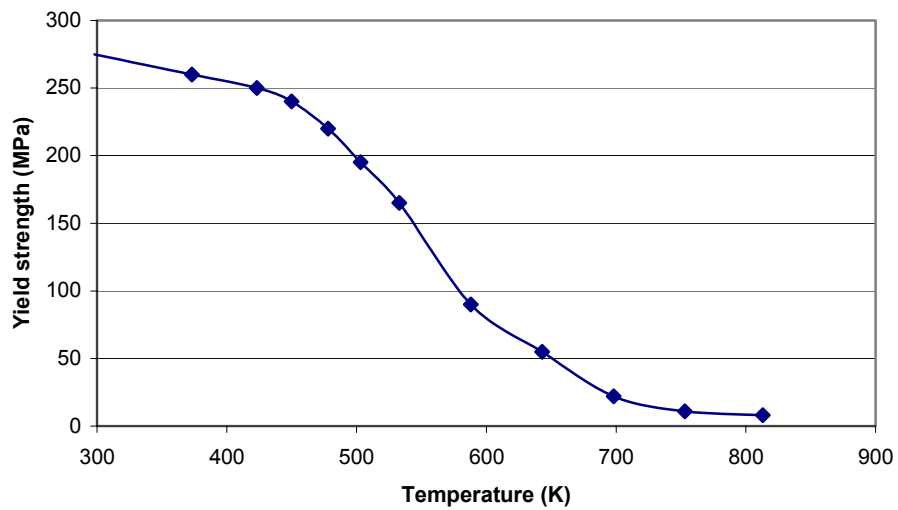
Figure 5.8: AA6061-T6 Temperature dependent yield strength.
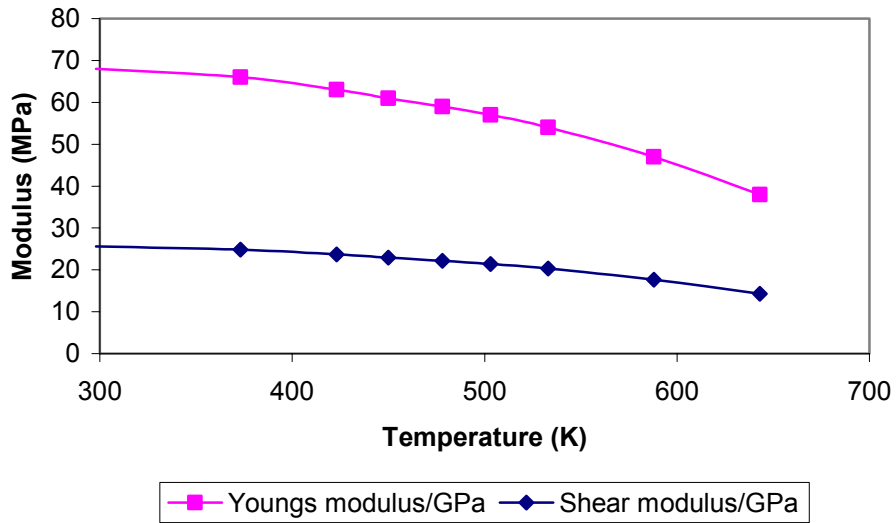
Figure 5.9: AA6061-T6 Temperature dependent Young's and shear modulus.

5.7.1 Sheet roughness

The surface roughness of the aluminum parts was measured with a 'Pocket Surf' Model 1500-311. With this instrument the roughness average (R_a) over a certain distance parallel and perpendicular to the rolling direction has been measured. How the roughness average is determined is shown in figure 5.10.
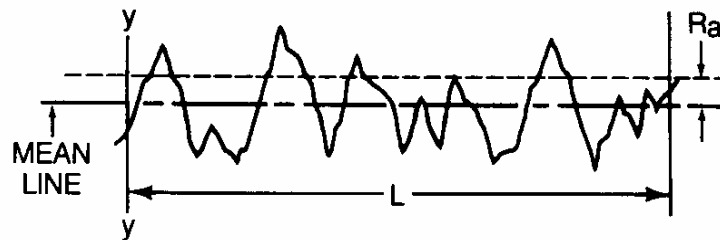
Figure 5.10: Roughness average [70].

The roughness average is the arithmetic average height of roughness irregularities measured from a mean line within the evaluation length (L=5mm) [70]. It is calculated with following equation:

$$R_a = \frac{1}{L}\int_0^L |y|\,dx \qquad\qquad\qquad\qquad \text{(Eq. 5-1)}$$

On a sheet of aluminum the roughness was been measured a total of five times both parallel and perpendicular to the rolling direction on both sides. The results are summarized in table 4.

Measurement		1	2	3	4	5	average
Parallel	$R_a/\mu m$	0.10	0.18	0.20	0.11	0.13	0.14
Perpendicular	$R_a/\mu m$	0.45	0.45	0.41	0.40	0.43	0.43

Table 4: Roughness average measurement results.

It can clearly be seen that the roughness perpendicular to the rolling direction is three times larger then parallel to the rolling direction. The maximum roughness depth, the largest of five maximum peak to valley roughness depths in five successive sampling lengths, was approximately 2.5μm.

5.7.2 Static friction coefficient

The material was used with four different surface conditions. The surface conditions were:

- As received

- Cleaned with acetone

- Lubricated with industrial lubricant 3-36

- Sandblasted

In the first three cases the surface roughness was not altered (i.e. only the amount of contamination was changed), but the static friction coefficient. The set up for the measurements was very simple. Four pairs of $25x10mm^2$ aluminum sheets were prepared as described above. One of the sheets was then mounted onto a table; the other sheet was attached to a scale. The parts were placed on top of each other and then the top part was loaded in 50 gram increments with weights. This set up is schematically shown in figure 5.11. Then a displacement D was carefully applied to the scale in a plane parallel to the plane of the sheets interface. The displacement was applied until the top sheet moved. The maximum weight that occurred during the application of the displacement was automatically stored by a second hand of the scale. In figure 5.12 the slope of the linear approximations is the static friction coefficient.
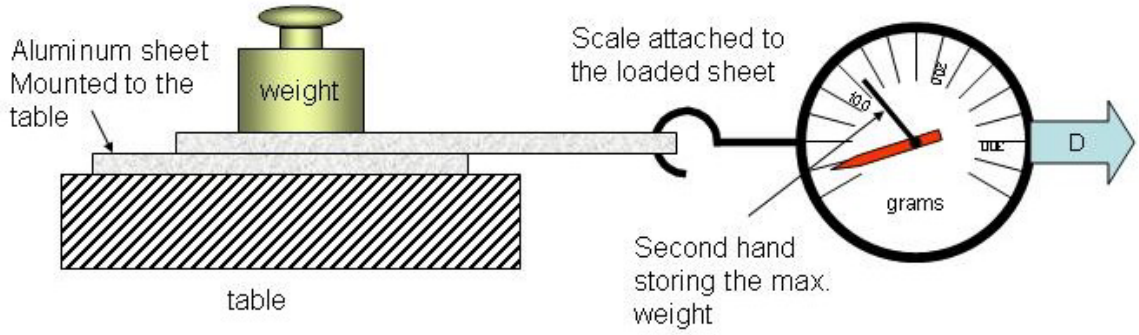
Figure 5.11: Experimental set up to determine the static friction coefficient.
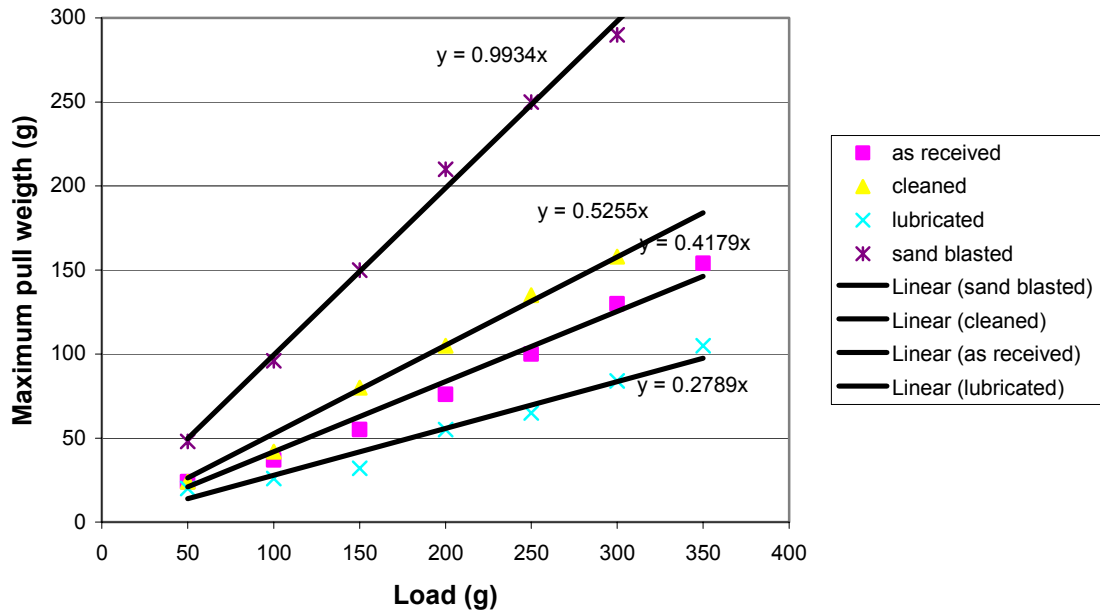
Figure 5.12: Static friction coefficients for different surface conditions.

CHAPTER 6

ULTRASONIC WELDING EXPERIMENTS AND NUMERICAL
SIMULATION RESULTS

In this section the results of the ultrasonic welding experiments and the numerical
simulations will be presented. The results of each experiment will then be discussed
briefly in light of the presented mechanism of USMW. Because of the measured
dependence of roughness on the rolling direction, all welding experiments were
performed by welding perpendicular to the rolling direction.

6.1 The start of a weld cycle

In making an USMW there is a transient start up period. The system is initially at
rest and with weld initiation several processes take place. Since the ultrasonic welder is a
vibrating system with some associated damping, a certain period of time will be needed
to reach its full amplitude of vibration.

At the beginning of the weld the sonotrode is pressed against the surface of the top
part, so that when the ultrasound is activated the sonotrode knurl pattern is driven into the
top part. Sonotrode and top part will then vibrate with the same amplitude and phase

after the knurl pattern has penetrated the surface. Should the sonotrode and top part not vibrate with the same amplitude and phase, then extrusion and sonotrode adhesion occurs (It should be noted that if the weld cycle is long enough extrusion will occur in all welds eventually). These events are schematically illustrated in figure 6.1.
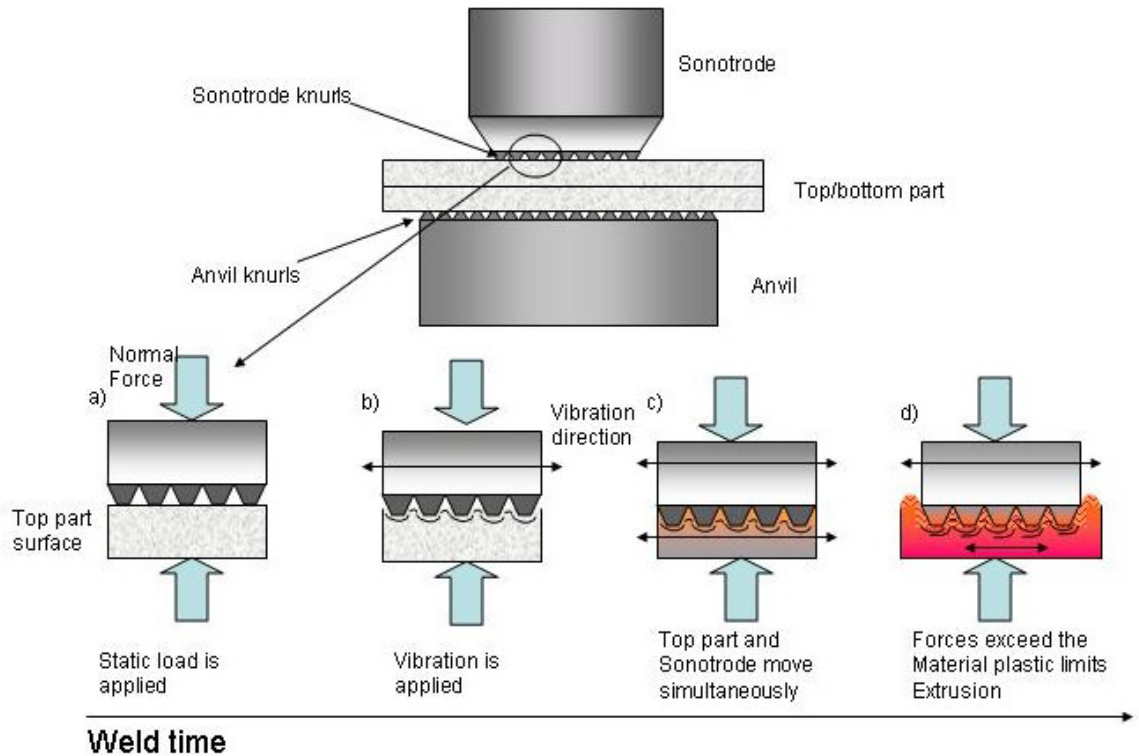
Figure 6.1: Sonotrode interaction with the surface of the top part.

Of particular interest here is the period of time in which the sonotrode knurl pattern penetrates the surface to the top part (b) to c)), because during this period there will be heat generation at the sonotrode top part interface and there will be reduced relative motion at the weld interface (if there is no relative motion between top part and

sonotrode, no heat will be generated at the top part surface, because no plastic

deformation takes place). Two scenarios are possible.

- First (the desired case), the sonotrode and top part quickly vibrate with the

  same amplitude and all of the relative motion takes place at the weld

  interface.

- Second, the shear forces to vibrate the part with the same amplitude as the

  sonotrode are too high so that the sonotrode and top part never reach the

  same amplitude. In this case extrusion and sonotrode welding occur

  immediately.

The advent of extrusion and tip sticking given the first scenario will be examined more

closely later in section 6.8 and is given by condition 4-19, when the temperatures are

simulated and more about the interface and maximum sonotrode force is known.

6.1.1 Experiment to determine the start up period

The Sonotrode surface interaction was observed with a high speed camera, and

the sonotrode vibration was measured with the MTI fiber optic sensor. The set up for the

high-speed movies and the vibration measurements is shown in figure 6.2..
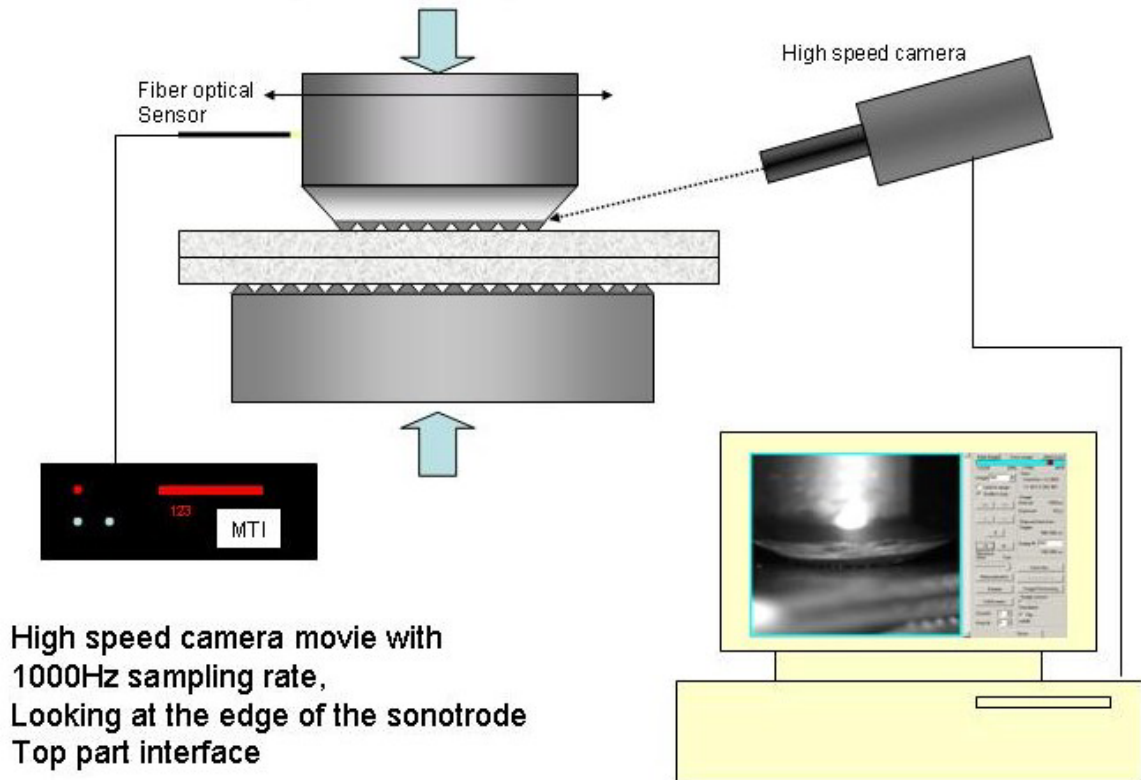
Figure 6.2: Experimental setup for high speed movies and vibration measurement.

The high-speed movies were made with a sampling rate of 1000Hz. The MTI sensor measured the displacement of the sonotrode parallel to its vibration direction. Simultaneously the shear force was also measured with the shear force sensor in the anvil.

110

6.1.2 Results from high speed movies

From the movies it was seen that the weld initiation takes only a few milliseconds, and the vibration amplitude increases to its maximum value in just a few cycles. Pictures of the sonotrode/surface interaction at various stages of the 0.5s total weld cycle time are shown in figures 6.3 to 6.9. Thus, in figure 6.3 one can see the sonotrode pressed against the top part under the static force, before the vibrations are applied (see figure 6.1 (a)).
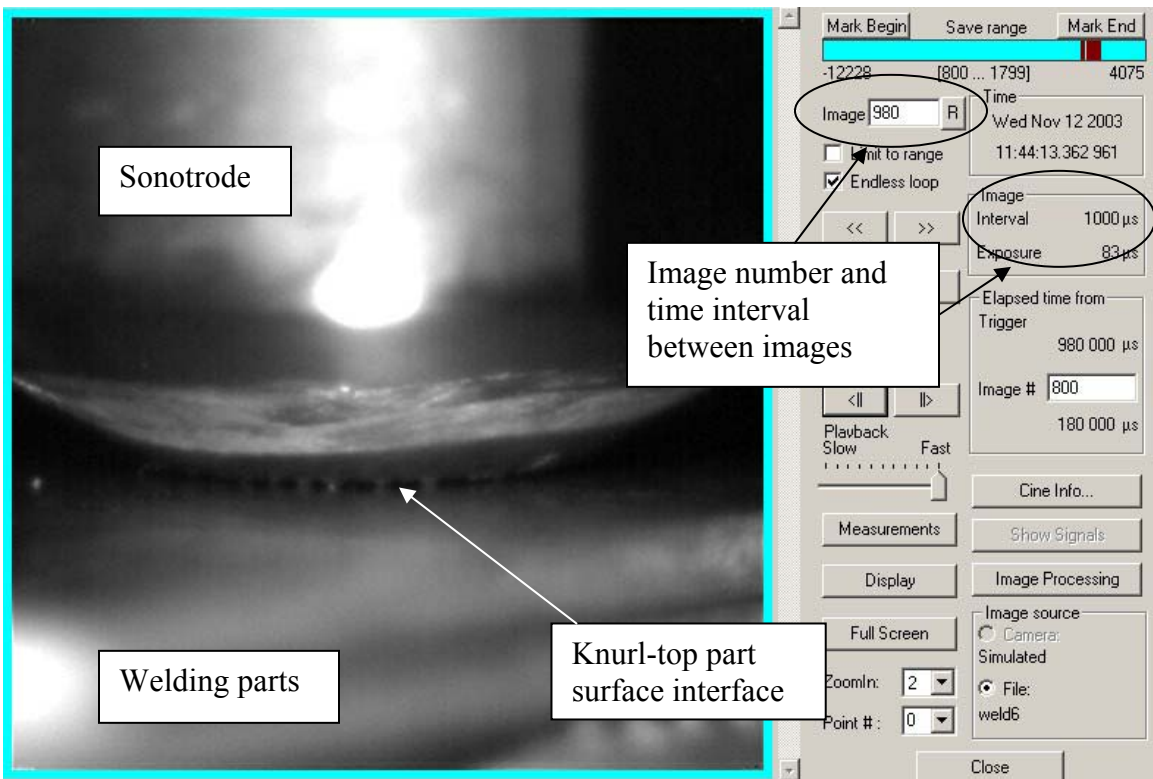
Figure 6.3: Weld time 0s- knurls are pressed onto the top part surface.
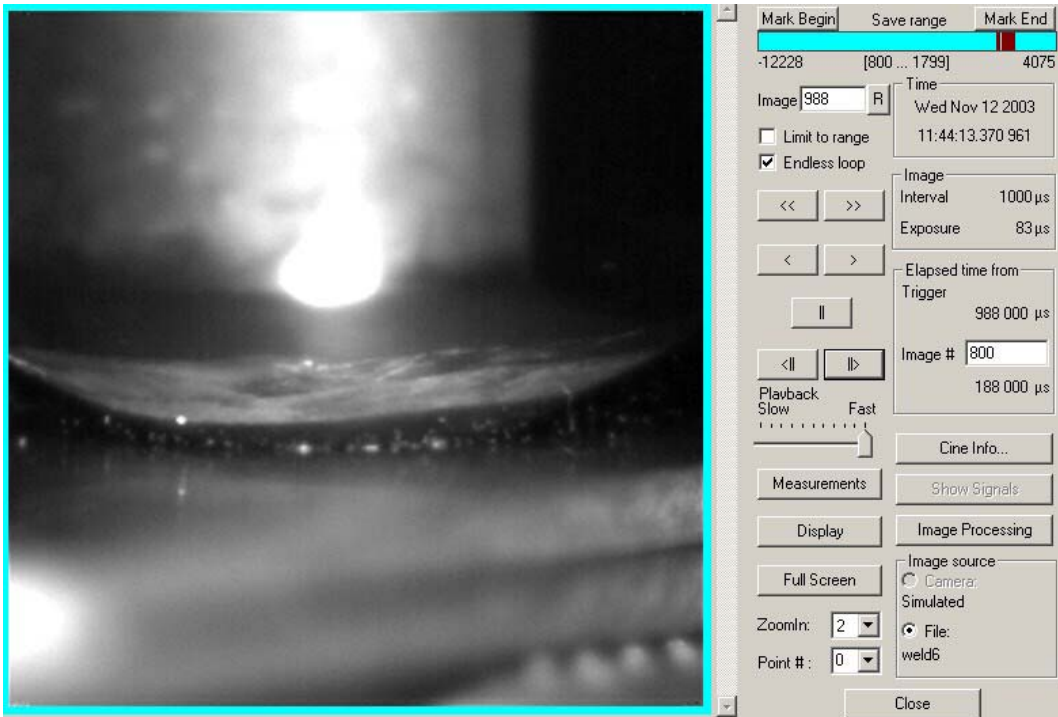
Figure 6.4: Weld time 8ms- knurl penetrated into the top part.
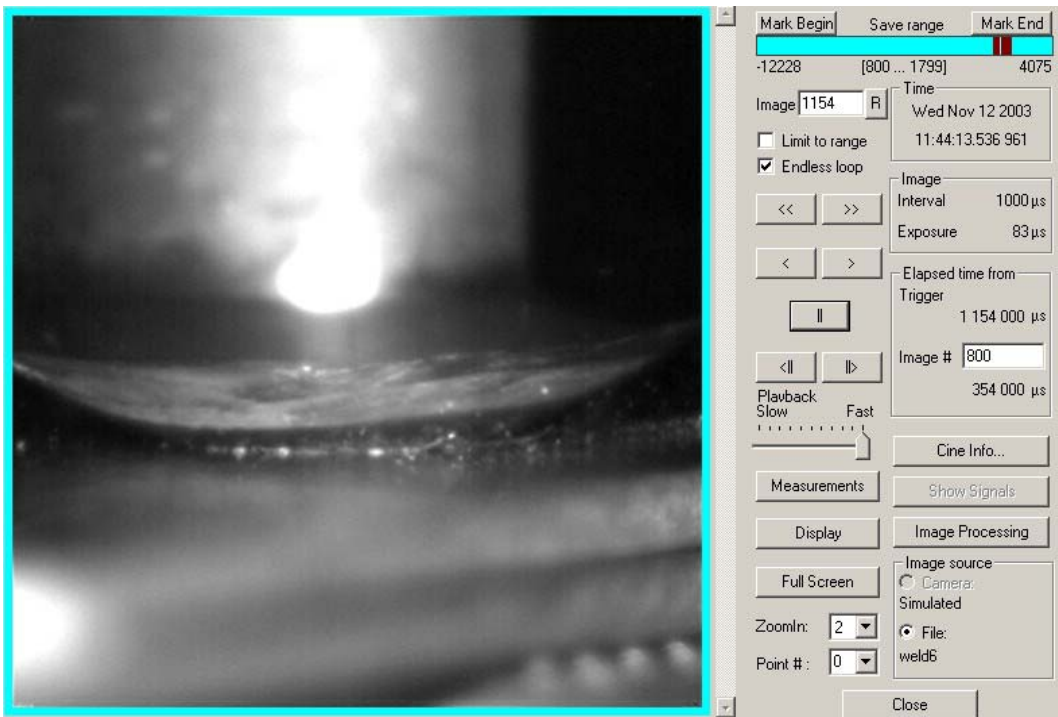
Figure 6.5: Weld time 174ms-up to now no extrusion.
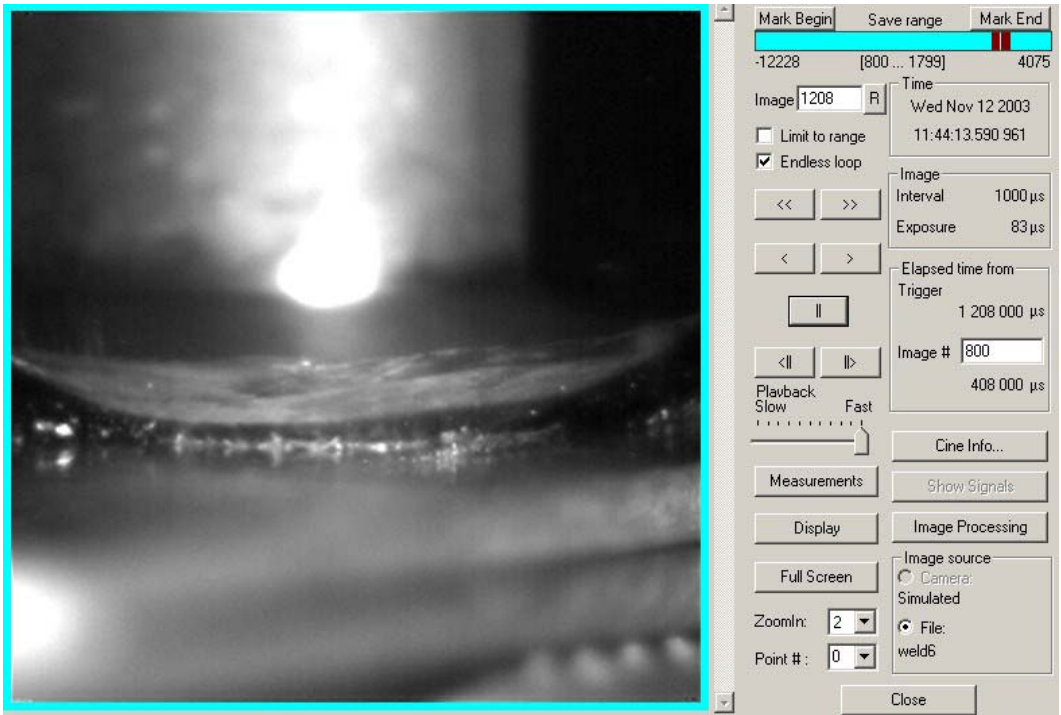
Figure 6.6: Weld time 228ms-extrusion of material has started.
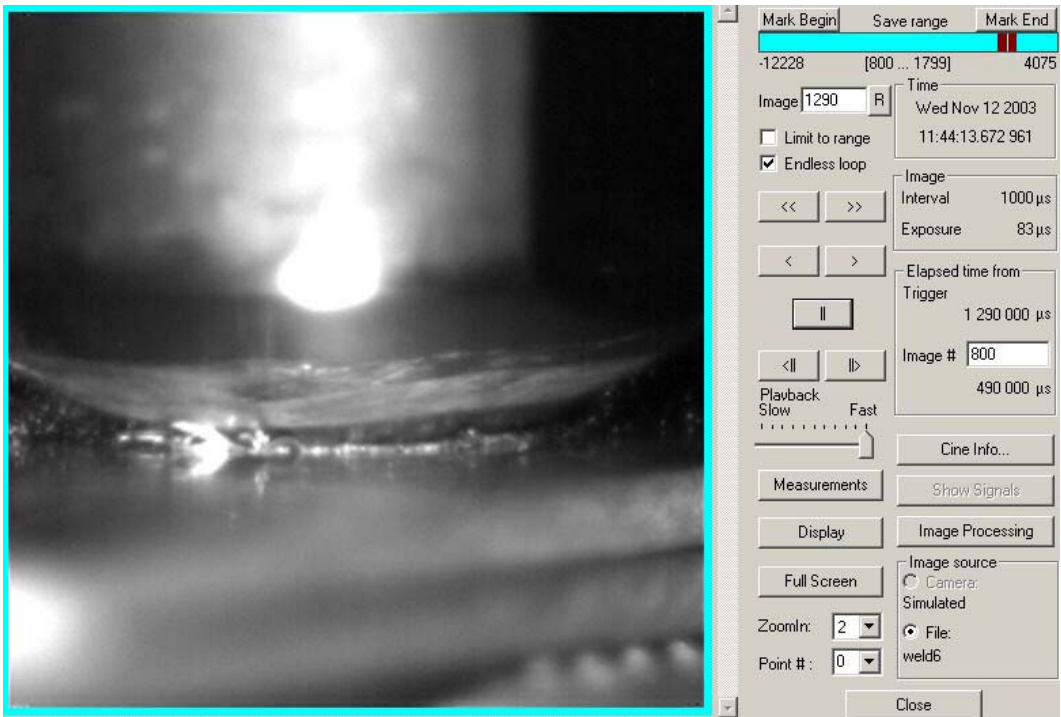
Figure 6.7: Weld time 310 ms- once extrusion has started, it continues.
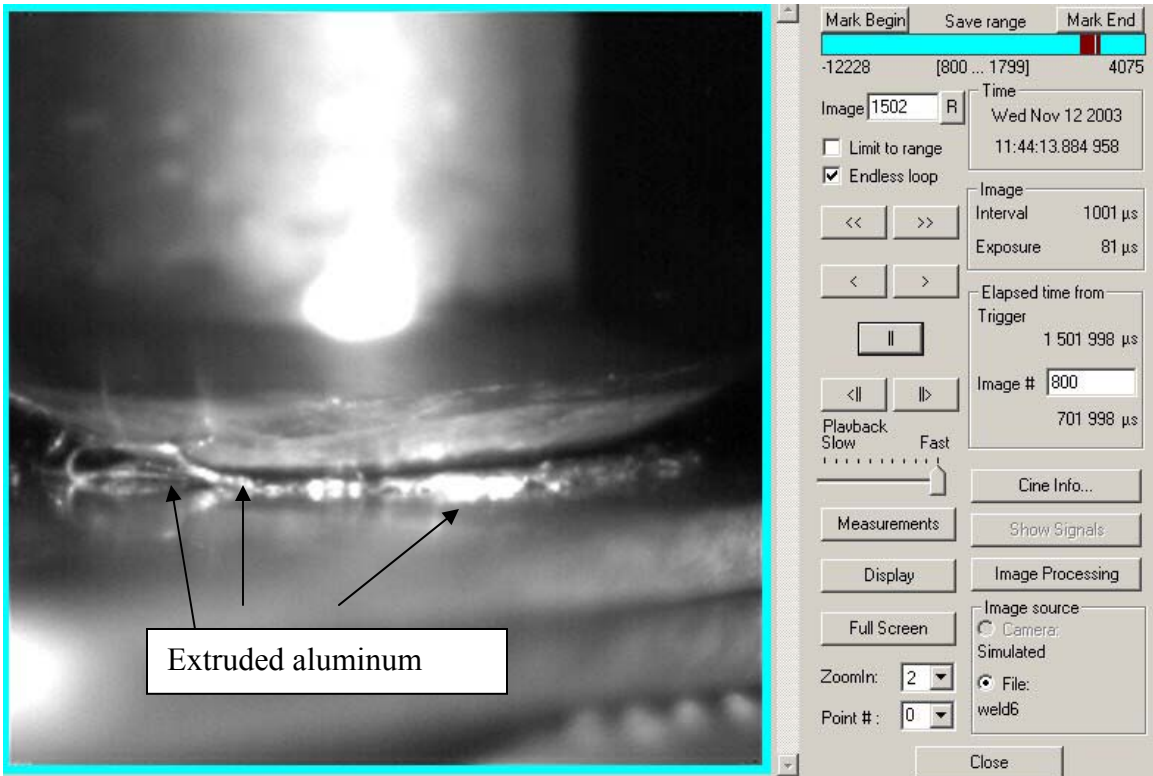
Figure 6.8: Weld time 522ms-at the end of the weld cycle; severe extrusion and tip welding.

The initial stage takes place between figures 6.3 and 6.4 (corresponding to figure 6.1 (b) and (c)). Thus, the penetration of the knurl into the top part occurs in 8ms, which is very fast considering a typical weld cycle is about 200ms. From figure 6.4 to 6.5 166 ms passes with no relative motion between part and sonotrode. From figures 6.5 to 6.6 one can clearly identify the advent of extrusion, which continues on through figures 6.7 and 6.8. The sonotrode and top part at the end of the weld cycle is shown in figure 6.8. The material extruded by the sonotrode is identifiable as the shiny ring around the sonotrode.

Evaluation of several high speed videos showed the maximum time period for the sonotrode to penetrate the top part, and to bring the part into vibration with the sonotrode amplitude is approximately 20ms. This longer time was for lubricated parts under weld conditions unsuitable to produce a strong weld. For a regular weld cycle with typical welding parameters this initial period did not exceed 10ms.

6.1.3 Results from vibration and shear force measurements

The vibration amplitude (in μm) of the sonotrode during the first few vibration cycles is shown in figure 6.9. The amplitude was measured with the MTI sensor, as noted in figure 6.2. One can see that after only 3 vibration cycles the amplitude reaches approximately 13μm (during the entire weld cycle the amplitude does not exceed 14μm). This rapid buildup indicates significant damping (i.e. a low system quality factor, Q) in the total vibratory system.
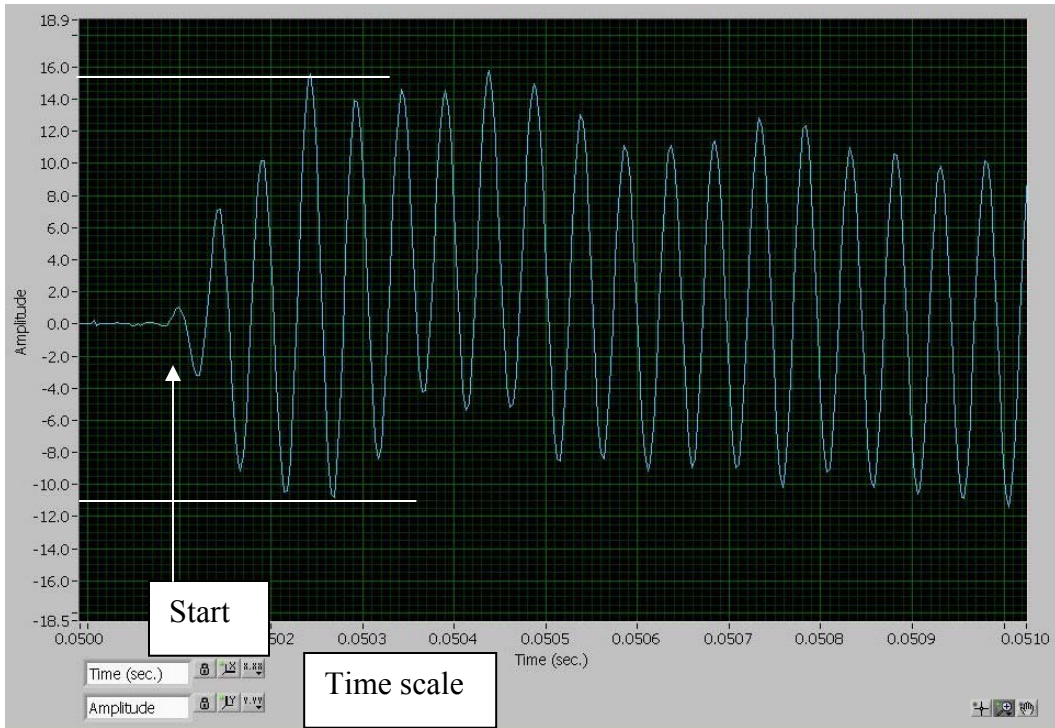
Figure 6.9: Sonotrode vibration-Weld time 0 to 1ms.
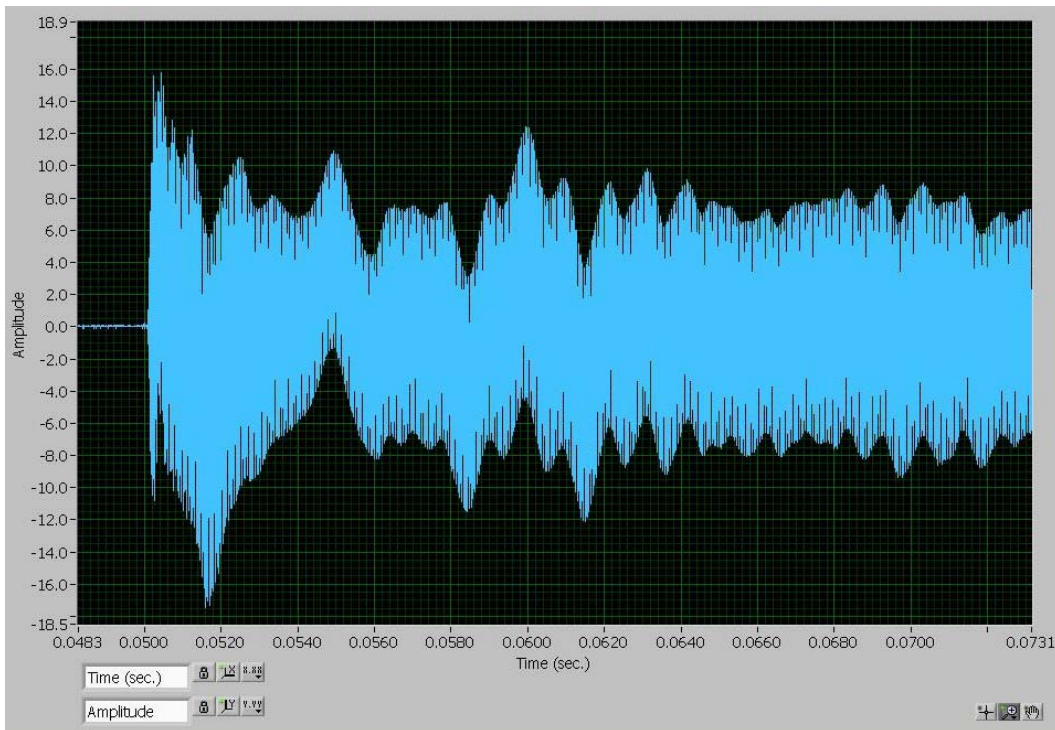
Figure 6.10: Sonotrode vibration-Weld time 0 to 20ms.

116
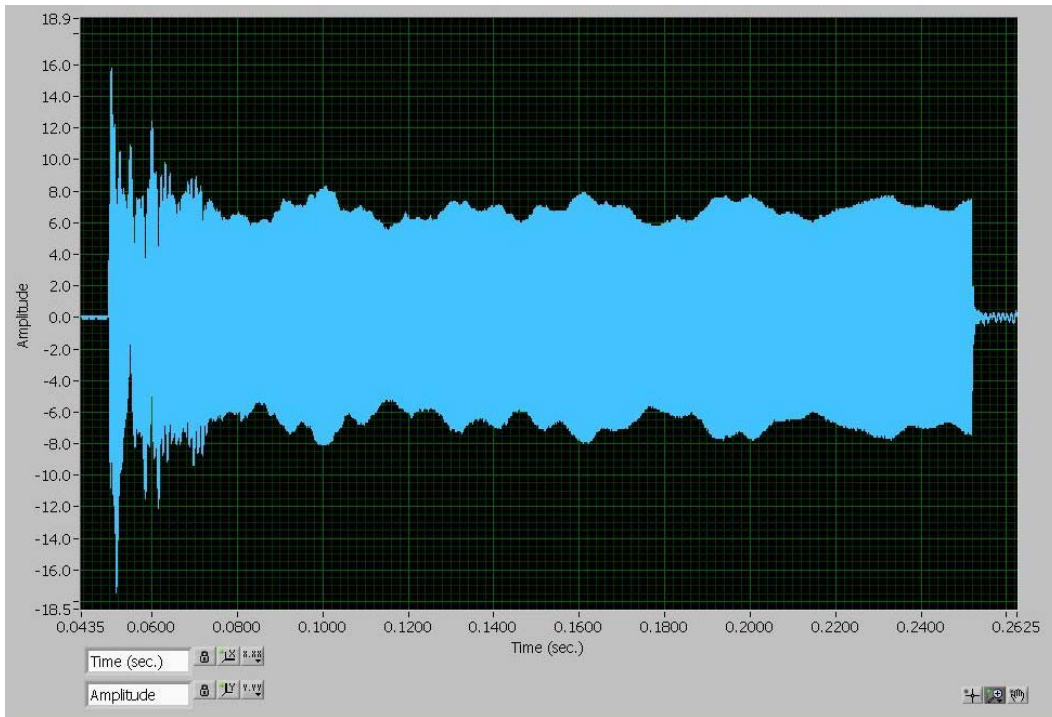
Figure 6.11: Sonotrode vibration-Weld time 0-200ms.

The first 20 ms of the weld cycles are shown in figure 6.10. It is seen that the

20kHz vibrations are superimposed by some lower frequency at the beginning of the

weld. This strong low frequency disturbance disappears after approximately 16ms. The

reason for this initial disturbance can only be speculated. It is possible that it is caused by

the initial shock when the static load is applied or that the sonotrode rocks in its taper

fitting or it may occur because the sonotrode does not vibrate with the same amplitude as

the top part. Another source of this disturbance could be that this low frequency

disturbance is an artifact caused by the low pass filter of the MTI sensor. Fast Fourier

Transform (FFT) analysis of the signal showed that the low frequency disturbance was

not a single frequency; in fact it was not possible to determine via FFT the value of this

low frequency oscillation.

117

The vibration amplitude for the entire weld cycle is shown in figure 6.11. At this point it is not known what causes the low frequency disturbance, but it was observed in all welds where the vibrations were recorded.

One can also look at the shear forces measured at the anvil. The resulting curves are shown in figures 6.12 and 6.13. The measured shear forces are according to equation 4-5 the forces at the weld interface, i.e. the weld and friction forces. An immediate rise in shear force within two vibration cycles is shown in figure 6.12. This is a strong indication of friction at the weld interface, since friction would occur independent from vibration amplitude at the interface and immediately when the vibrations are applied (it is hard to imagine that welding would occur in the first two welding cycles).
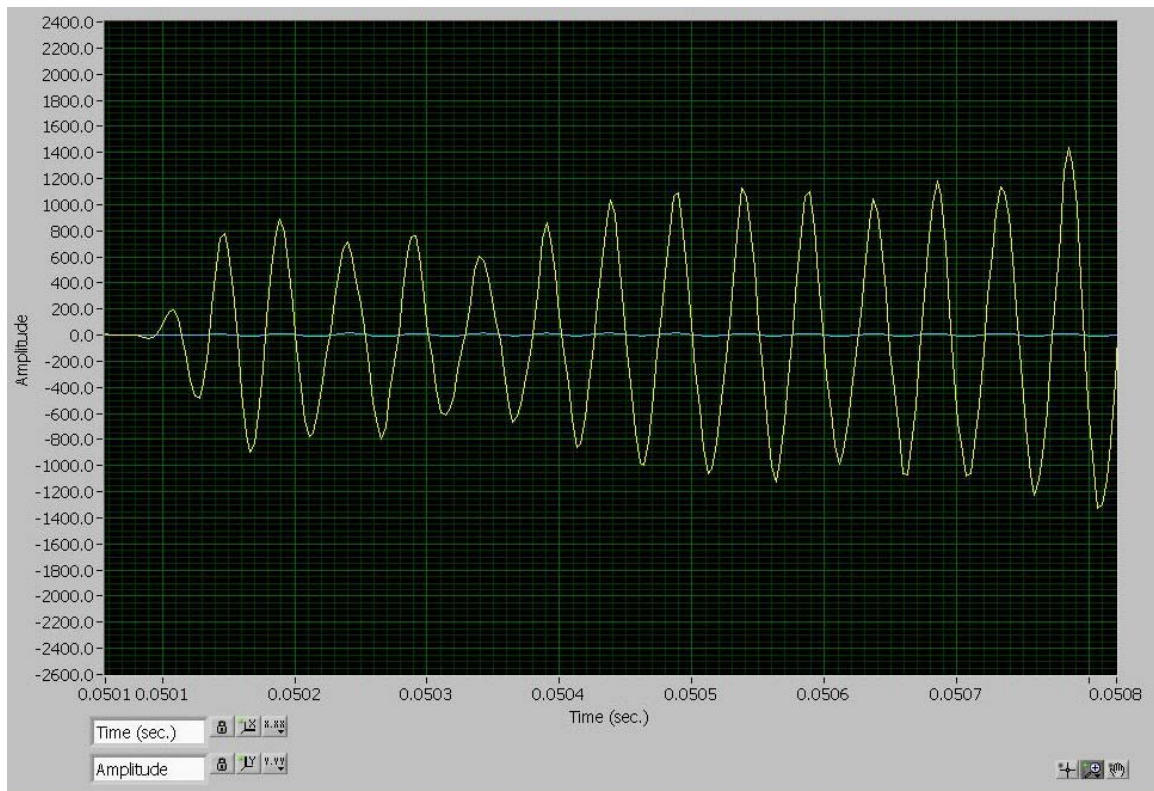
Figure 6.12: Welding shear force for the first 8ms of the weld cycle.

118

From figure 6.12 and 6.13 one can see that the shear force at the anvil builds up with some delay compared to the vibration amplitude. However this can be expected because there is reduced relative motion at the interface during this early stage of the welding cycle and as mentioned earlier, it is hard to imagine that welding occurs within the first few welding cycles.
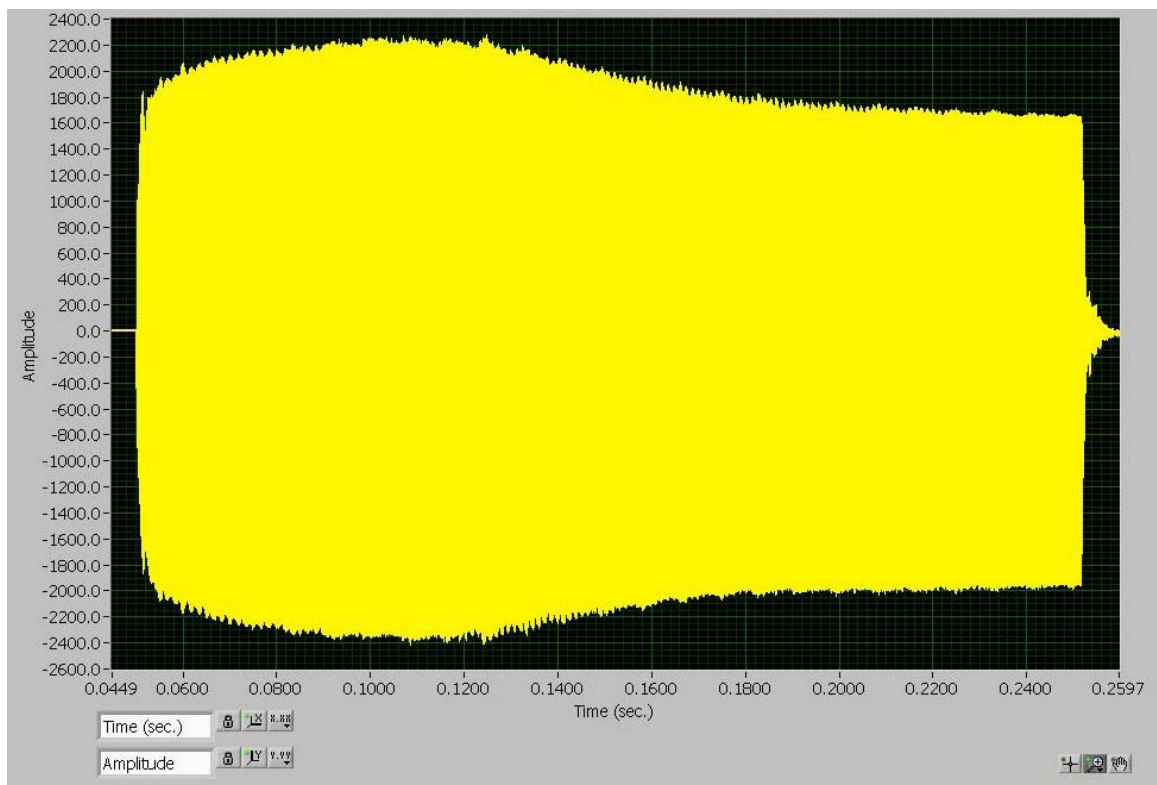
Figure 6.13: Welding shear force for the entire weld cycle.

Figure 6.13 illustrates furthermore how the shear force develops during welding. It is seen that the force builds up rapidly reaches a maximum after approximately 70ms and then reduces in magnitude. At this point exact interpretation of the general behavior

119

of the shear force is not possible. However, from results in section 6.8 it can be seen that, the shape of the shear force curve is a result of the temperatures that develop during welding and the effect of these temperatures on the material properties.

From high speed measurements it can be concluded that for proper welding conditions the top part and the sonotrode are rigidly connected and vibrate with the same amplitude after an initial time period of approximately 10ms, until the critical condition for extrusion is met (equation 4-19).

6.2 Stress analysis under the knurl pattern

The effect of the knurl penetration on the compressive stress distribution beneath the sonotrode will now be examined for the situation of the pattern penetrated into the top part surface. The FEA program ABAQUS has been used [62]. The dimensions of the indenter have been chosen to represent the geometry of the edge of one knurl of the sonotrode.

A small region of the knurl pattern under the sonotrode is schematically illustrated in figure 6.14. The FEA results give the general contour plot of the stress distribution of the part. The boundaries of the model were considered as frictionless rigid walls, so that the contour plot represents the stress distribution beneath a knurl away from the sonotrode edge.
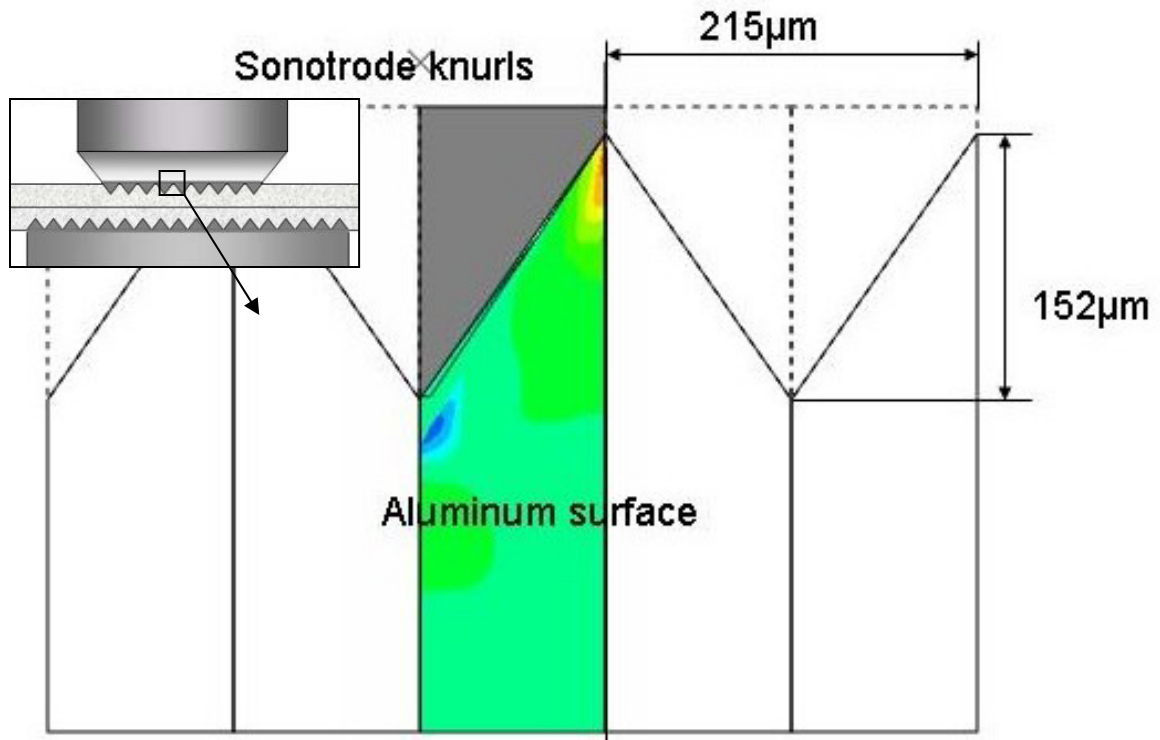
Figure 6.14: Contour plot of the compressive stress distribution below the sonotrode knurl pattern.

The compressive stresses along lines parallel to the force direction is plotted in figure 6.14. It shows that in a depth of 50µm the compressive stresses are equal along the lines. This means, the compressive stress is uniform as described in figure 4.3 e) for a depth of 50µm beneath the tips of the sonotrode knurl pattern.
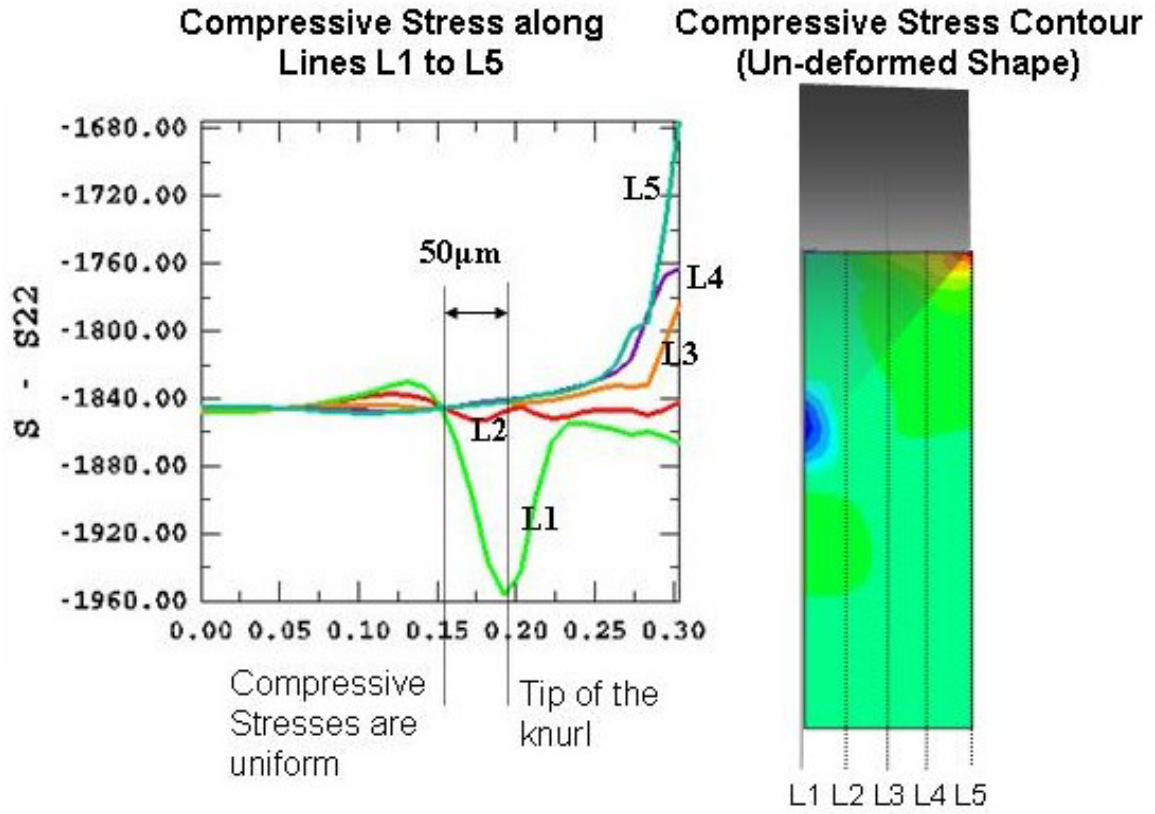
Figure 6.15: Compressive stresses parallel to the force direction.

6.3 Influence of part thickness on contact stresses at the weld interface

In this section the influence of the part thickness on contact stresses at the weld interface will be examined by finite element analysis using the program ABAQUS [62] and the area over which friction occurs outside the deformation zone will be determined experimentally.

6.3.1 Finite element Contact stress analysis

The problem analyzed was that of a circular, flat sonotrode pressed in static contact with two plates, which in turn rested on a flat anvil having a greater area than that of the sonotrode face, as illustrated in figure 6.16 for two different plate thicknesses, 0.6mm and 3.0mm. This figure also shows the stress contour plots the two cases of thickness. The compressive stress distributions for all the sheet thicknesses used in the experiments of this study are graphed in figure 6.17. It is clearly to see that the peak contact stress is significantly reduced for increased sheet thickness. This result was expected and reconfirms the results given in [19].

FEA of interface contact stress
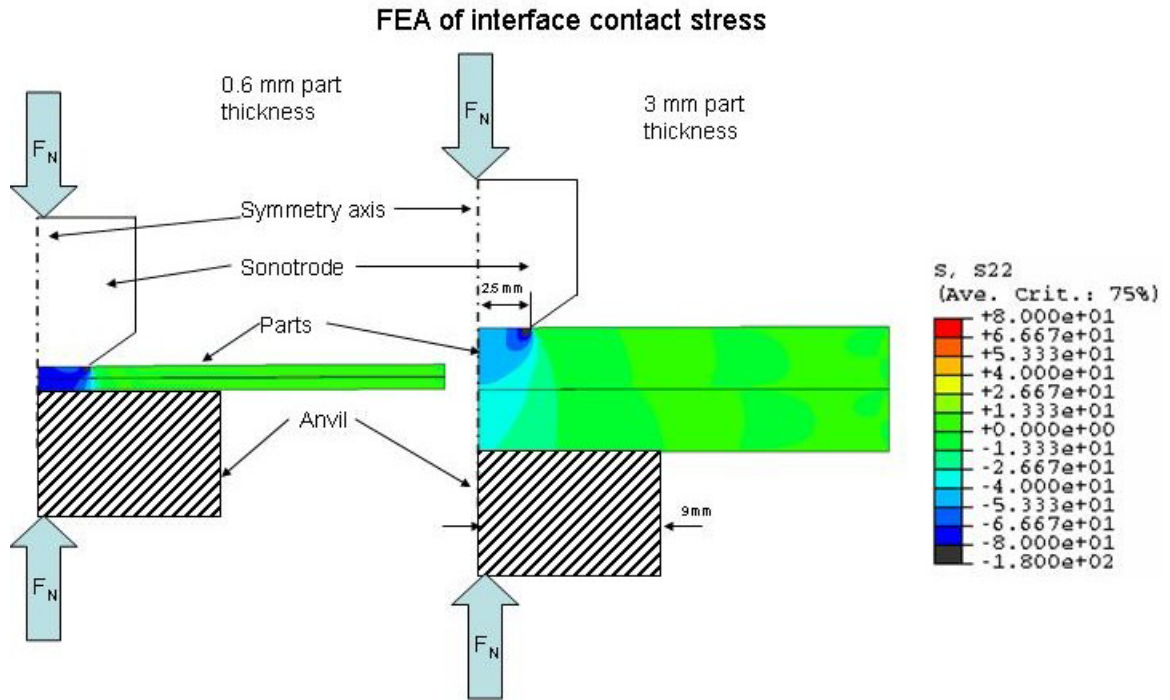
Figure 6.16: Contour plot of the stress distribution through the cross section of the parts.

Compressive stress distribution on the surface of the bottom part
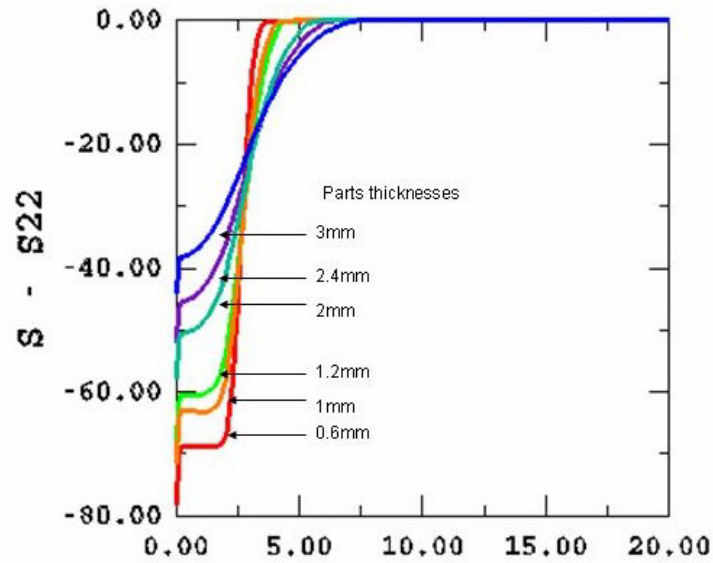
Figure 6.17: Compressive stress distribution on the surface of the bottom part at the interface as function of the distance from the center of the weld, for a 5mm diameter sonotrode.

It is interesting to see is that for sheet thickness of up to 1.2 mm the compressive

stress distribution is almost uniform over the deformation zone area. Then for

thicknesses 2mm and above the peak stress is significantly reduced. It was not possible

to achieve welds for these thicknesses in actual weld tests.

6.3.2 Contact area measurements

To investigate the dependence of the area over which friction is acting, samples

were prepared with various thicknesses. Small $40x40mm^2$ plates were cut and cleaned

with acetone. The welding parameters were: Clamping force setting, 100psi; Power

setting, 10; Match setting, E; Weld time, 0.02s to 1s. The weld time had to be increased

for thicker samples in order to see the abrasion marks resulting from the contact stress

decrease. After welding, the parts were carefully peeled apart to show the contact

surfaces, seen in figure 6.18. The black surface in the pictures is the original part surface,

the white scratch marks show the areas in which the parts were in contact, and the

original surface has been damaged. The black circles indicate the deformation zone area

(i.e. the area where the weld would grow). The white circles indicate the friction area,

were no welding would occur.
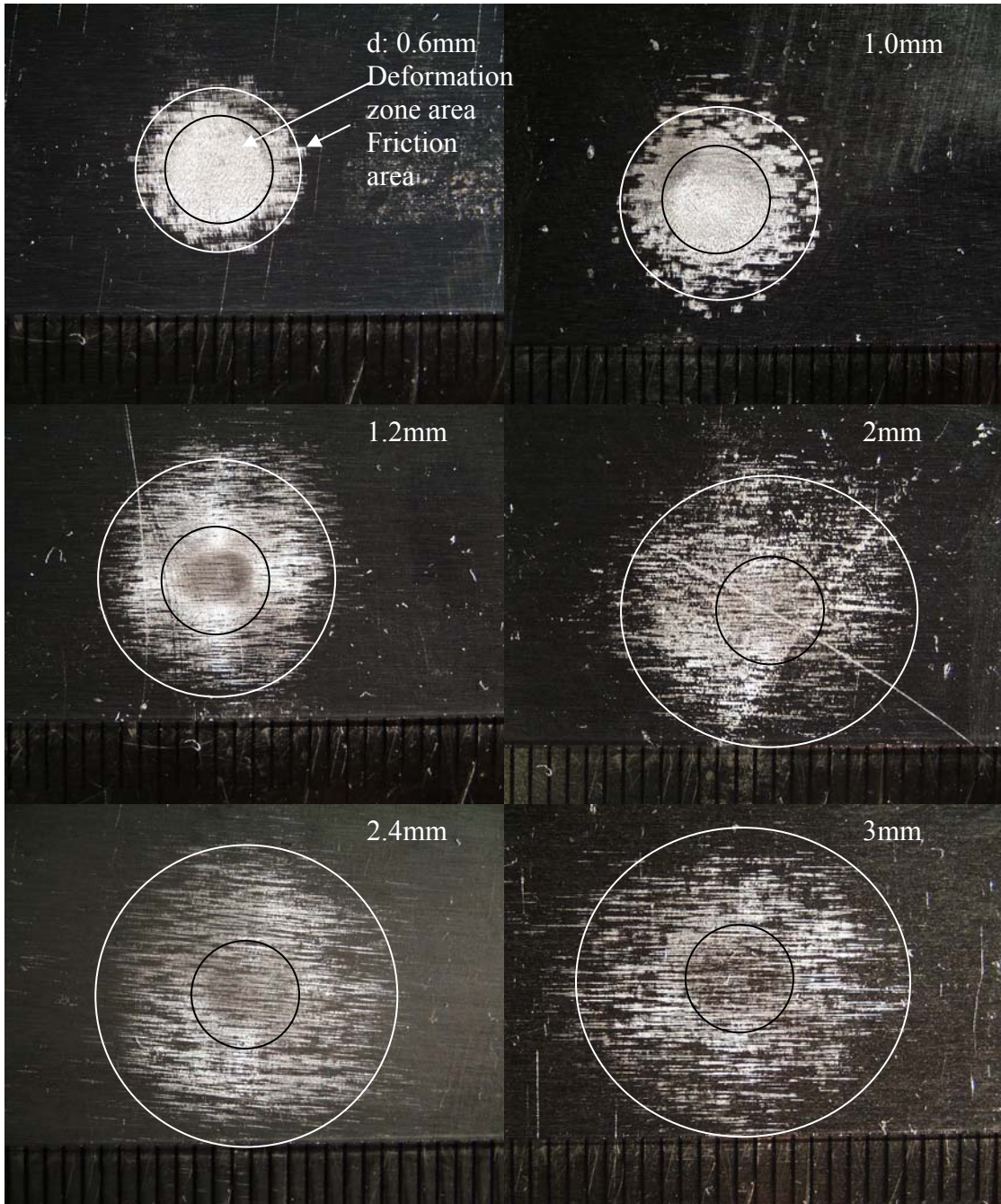
Figure 6.18: Parts interface after peeling apart.

One can clearly see that the area over which friction occurs increases with increasing part thickness. The contact area (i.e. the total area within the 'friction' circle)

127

vs. part thickness is shown in figure 6.19. Not only do the contact stresses spread out,

therefore causing greater friction forces, for the thicker samples, the indication of a clear

deformation zone disappears entirely. Even with weld times up to 1 second there was no

sign of welding. Furthermore the interface for the thin sheets shows that the parts were in

contact over the entire deformation zone (as compared to be only in contact at the weld

area), after a very short period of weld time.
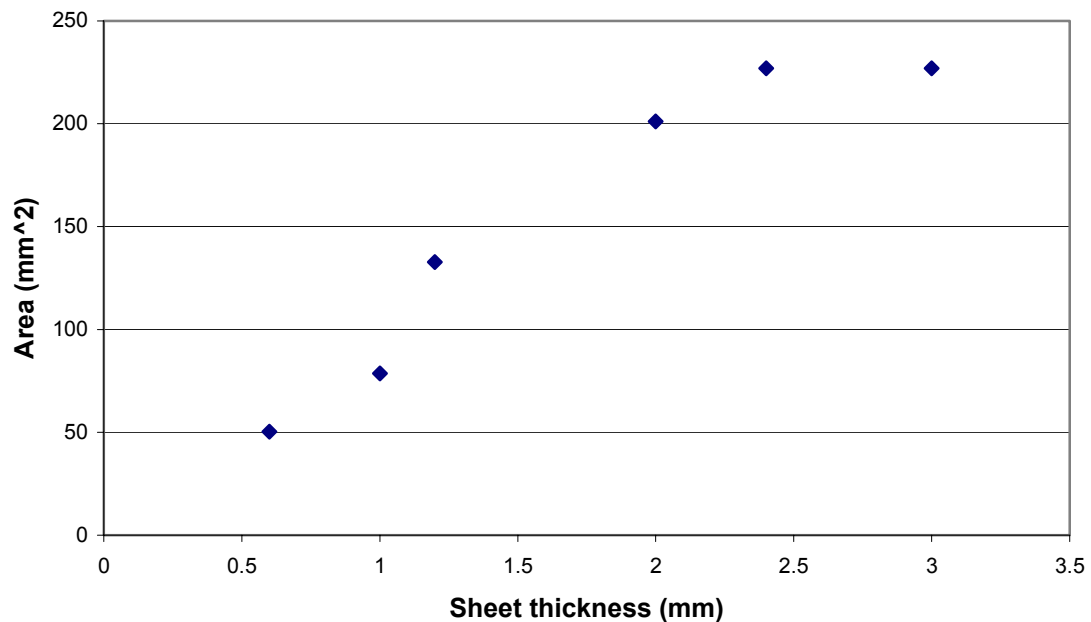
Figure 6.19: Contact area increase vs. part thickness.

To summarize, when the thickness of the samples is increased one can observe

how the contact area increases at the interface. It was not possible to generate any kind

of welding for thicker sheets (2mm to 3mm) for the sonotrode tip diameters and weld

powers available for this work. It even took some time to see the abrasion marks at the

interface. In section 4.5 it was calculated that for thicker sheets the elastic shear strain

can exceed the vibration amplitude of the sonotrode. This might be the reason why it was

a problem to generate abrasion marks for thicker sheets. Even for very thin sheets it can

be observed that the contact area is larger then the actual deformation zone, where

welding occurs. This leads to the conclusion that friction forces outside the weld area

will play an important role during USMW.

In the numerical simulation the compressive stress between the parts is equal to

zero at a distance of 7.5mm from the centerline of the sonotrode (i.e. friction area radius

7.5mm). From the experimental results one can see that the friction area extends much

further then the FEA predicts (9mm vs. 7.5mm radius). This is indicative of the collapse

of asperities within the deformation zone, thereby decreasing the distance between the

centerlines of the parts in the area. This effect is schematically illustrated in figure 6.20.
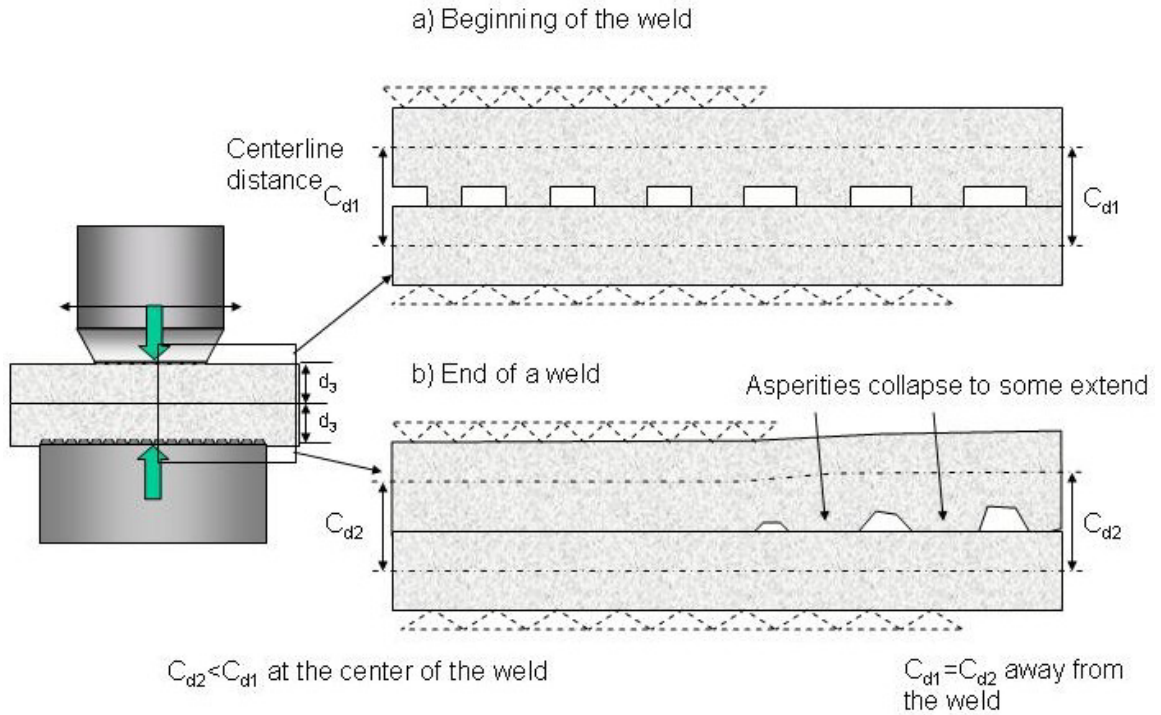
Figure 6.20: The collapse of asperities outside the weld area.

It can bee seen from figure 6.20 that during welding the centerline distance between the sheets is decreasing from its original value. This is due to the collapse of asperities inside the deformation zone. Simultaneously the asperities outside the weld area will also collapse to some extent (but welding does not take place). This will then cause a domino effect, so that more and more asperities will be in contact farther and farther away from the actual deformation zone. This case was not considered in the FEA.

6.4 The influence of the top part dimensions on weld strength

In this set of experiments the influence of the top part dimensions and its boundary conditions on the weld strength of ultrasonically welded AA6061-T6 was measured. Here only longitudinal vibrations in the top part extension, shown below in figure 6.21, are considered (see Section 4.3.1 and Appendix A for the analysis of this problem). The same phenomena that occur here would be expected to occur for transverse and plate vibrations, except that differing beam and plate vibration modes would enter. Longitudinal vibrations of the parts have been chosen in these experiments because they are the most easily understood and mathematically expressed.

6.4.1 Experimental approach

For the experiments the Sonobond welder has been used with the following welding parameters of table 5.
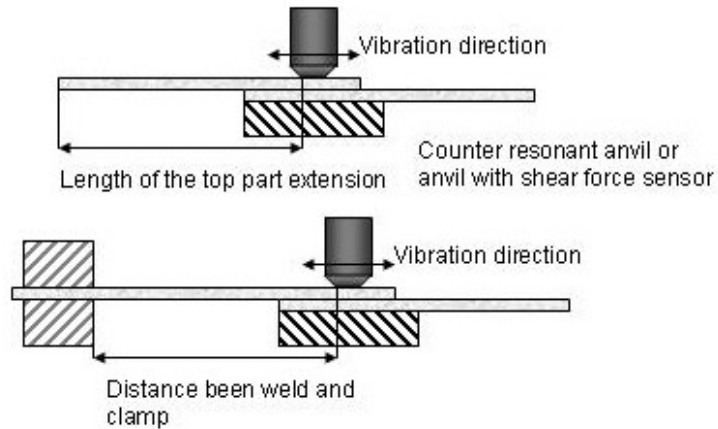
Figure 6.21: Experimental set up to test the influence of part dimensions on weld strength.

Powerlevel	10
Matching	C
Weld time	0.2s
Squeeze time	0.5s
Normal force	1600N (≡80psi)

Table 5: Welding parameters.

The experimental set up is shown in figure 6.21. The length of the extension of the top part was varied, but keeping the projection to the right of the weld constant (20mm). The bottom part length was 5cm in all cases. The length of the extension or the distance of the clamp respectively, was measured from the leading edge of the sonotrode. The parts were cleaned with acetone prior to welding. The length was changed in 10mm steps in all cases. Three welds were done for each length. Additional tests were run on several free end samples using the shear force and displacement sensors.

132

6.4.2 Results

The results for the samples welded with a free end are shown in figure 6.22 through 6.25 and those for the clamped end are shown in figure 6.28 and 6.29. Thus, the strength data versus free end part length is shown in figure 6.22. The circles mark the length values at which no weld strength was achieved; instead the extrusion and sonotrode adhesion were very severe. In some cases the top part was welded to the sonotrode and peeled a nugget, yet left the bottom part unwelded. In figure 6.23 the average weld strength and the standard deviation for the data of figure 6.22 is shown. Important to note here is that for the sample length's 60mm and 190mm no weld was achieved in any of the samples.
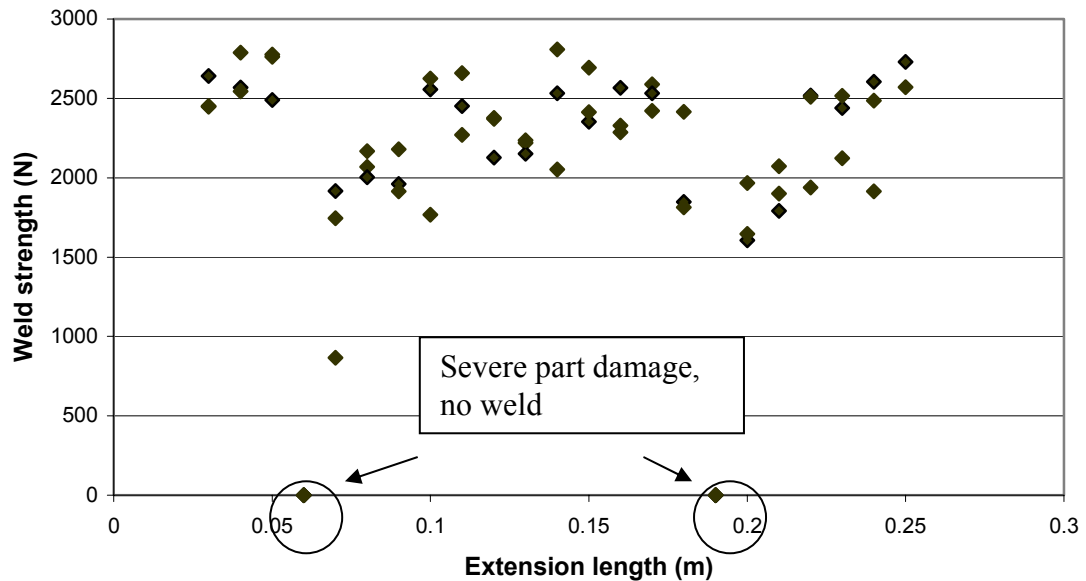
Figure 6.22: Weld strength for free end top part.

133
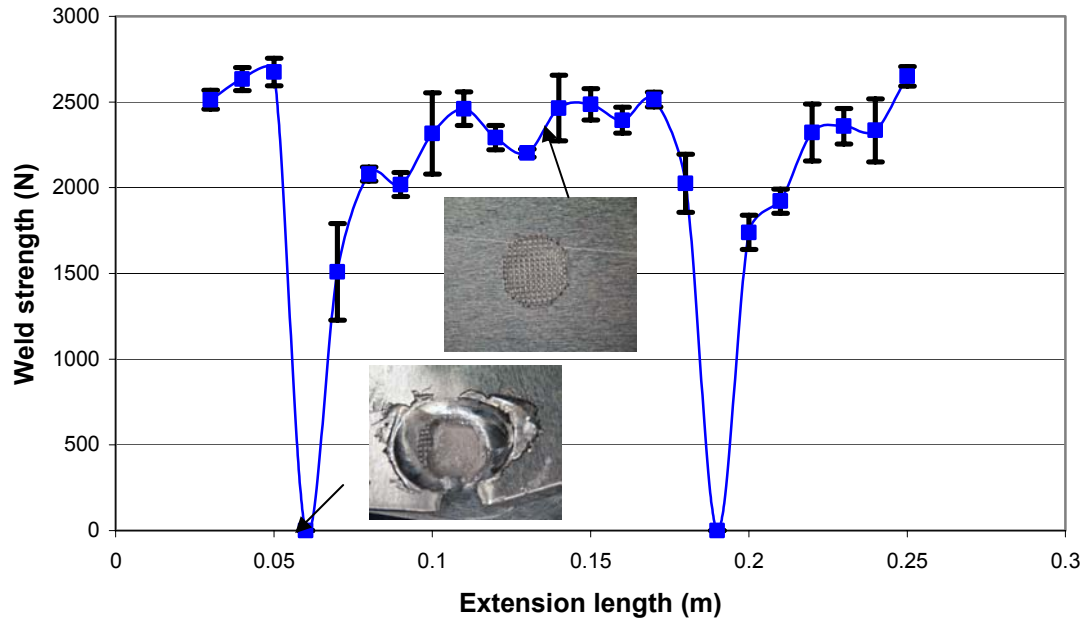
Figure 6.23: Average weld strength and standard deviation (free end).

As previously discussed, the 'no weld' location corresponds to the anti-resonance position of the weld, while the weld location at approximately 125mm corresponds to the resonant location. The photo insets in figure 6.23 show the samples after welding in the anti-resonance and resonance locations. As one can see the sample welded in anti-resonance is severely damaged while the sample at resonance has an even impression of the sonotrode knurl pattern without any sign of extrusion.

The shear forces measured during the weld cycles for the corresponding extension length are shown in figures 6.24 and 6.25. The force in both figures is computed from

134

the voltage output of the amplifier with the correction factor determined in section 5.2 for the frequency response of the anvil set up.

The shear force that was measured during the weld cycles for extension lengths of 40mm to 72mm is shown in figure 6.24. This part length range covers the first anti-resonant range of figure 6.23. The shear force measured is according to equation 4-5 equal to the interface force. It is clearly to see that the shear force rapidly falls of at an extension length of 50mm and slowly comes up at 66mm. Interesting to note is that the shear forces are equal for approximately 10ms at the beginning of the weld cycle (i.e. the initial time when the sonotrode engages into the top part) in all cases and that the forces up to 50mm length are constantly stronger then beyond 66mm. The drop in interface force at the anti-resonance condition was predicted and explained in section 4.3.1, with equation 4-11. According to the discussion in that section the sum of all shear forces that occur during welding is limited by the maximum sonotroded shear force, and in case of one force component becoming very large (i.e. F_{AM}) the others have to decrease accordingly. This very significant drop of in shear force around the anti-resonance condition is a clear indication for the validity of equation 4-11. To clarify the color code plot for the shear forces figure 6.14 also includes cross sections through the 3-d plot. On the left the force vs. weld time for the extension length 56mm is shown and on the right the force vs. extension length at weld time 0.1sec is shown.

Shear Force Color Code
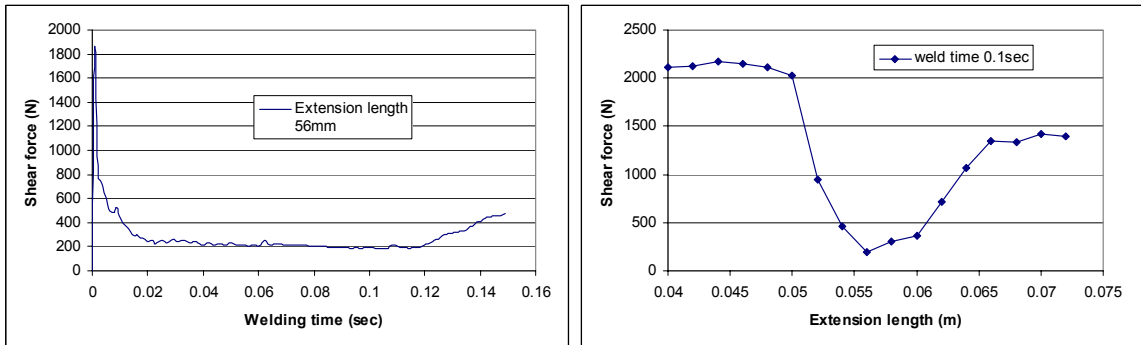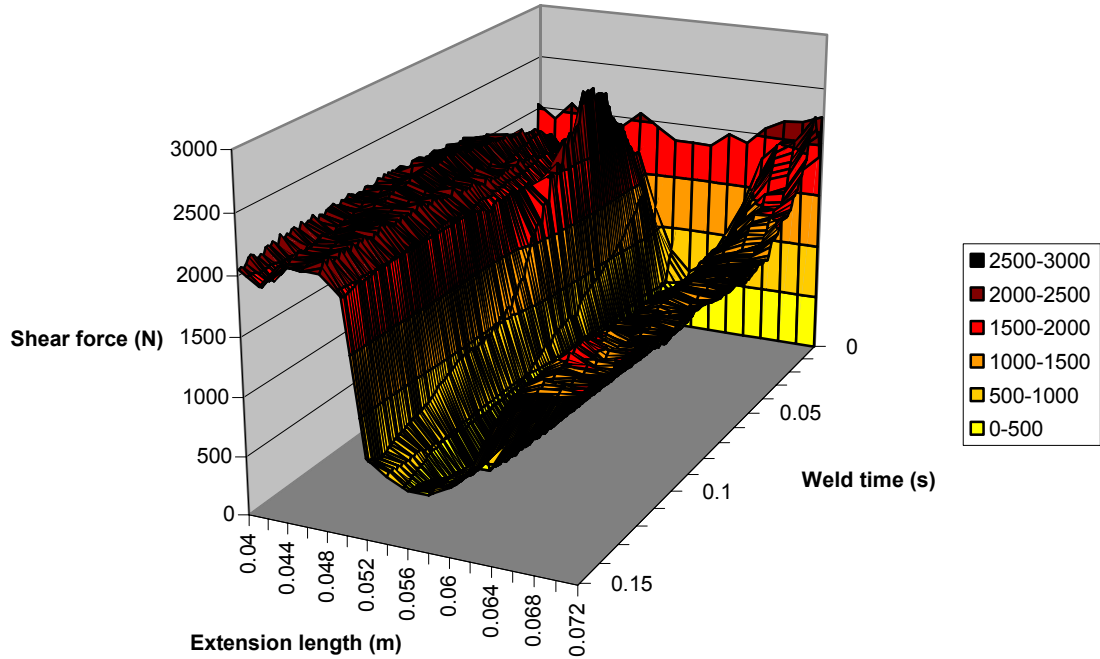
Figure 6.24: Anvil forces at anti-resonance for extension length's 40mm to 72mm.

Figure 6.15 displays the measured forces at a resonant extension length of 110mm

to 130mm as well as cross sections at extension length 120mm and weld time 0.1sec.

The forces in this length range have all the same general shape. They start at approx

2300N and drop off to approximately 1700N at 60ms weld time. It will be shown in section 6.8. that a sudden drop in anvil forces for these particular welding conditions (i.e. clean parts) can be associated with the advent of extrusion at the sonotrode.

Shear force at resononance length
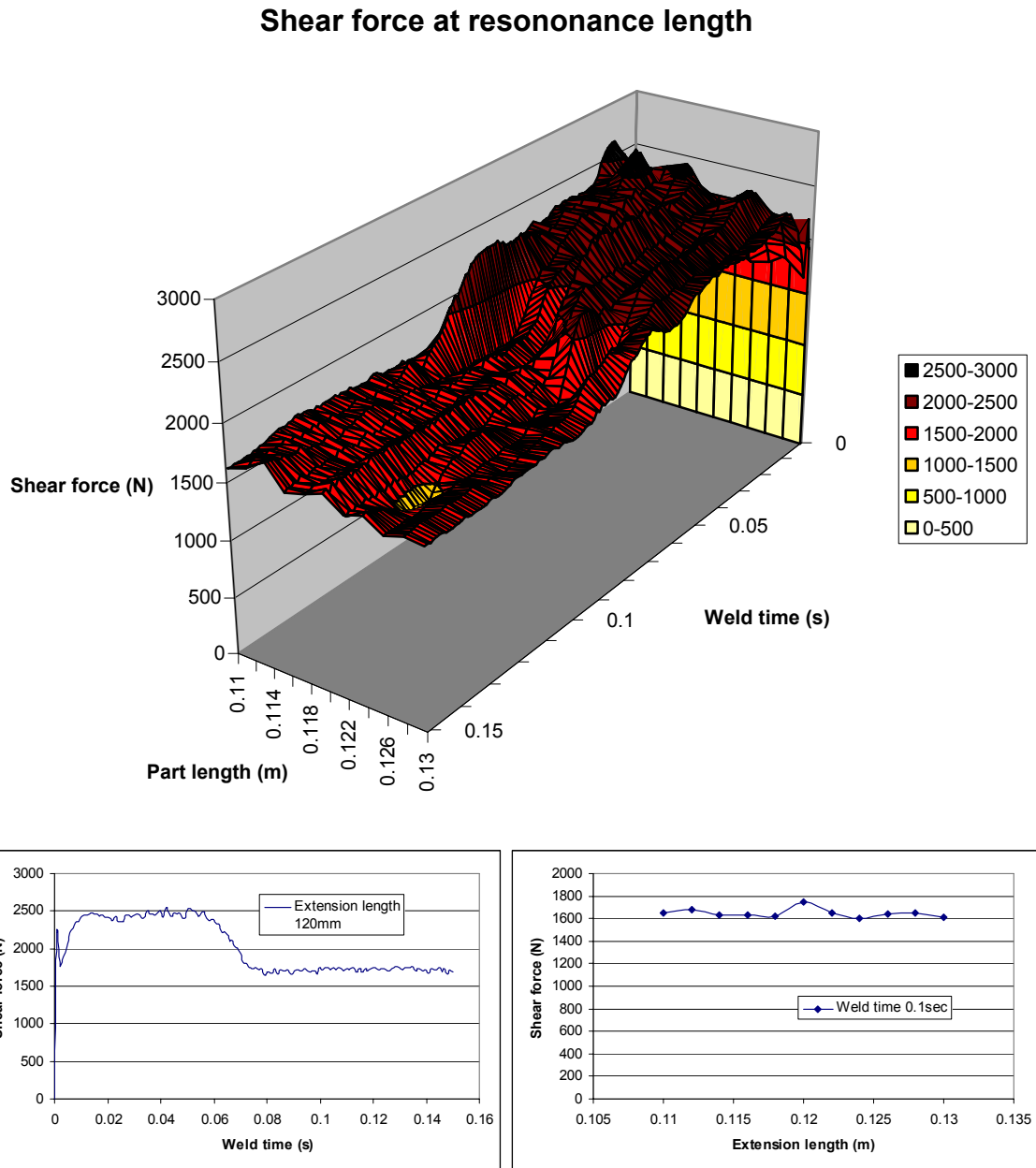
Figure 6.25: Anvil forces for extension length's 110mm to 130mm.

In figure 6.26 and 6.27 the electrical power and sonotrode vibration amplitude for both cases are shown. In the case of power (figure 6.16) it is seen that after approximately 0.06 sec that the power levels for the two lengths are approximately the same. The energy consumed for the anti-resonant part was approximately 120 Joules and the energy used on the resonant was 100 Joules. Each exhibits a high starting transient of about the same amplitude, with differing decay behavior for the two cases. The sharp power peak for the 120mm extension length is an artifact from the data compression algorithm of the data acquisition system (i.e. one spike in the compressed time span will be read out for that time span, these spikes in either voltage or current are clearly identifiable as miss readings in the oscilloscope mode of the DAQ). The high starting transient with its slow decay for the 56mm extension length is believed to be completely different in nature. According to the discussion in section 4, condition 4-19 is met immediately at the beginning of the weld cycle. Since in that case yielding has to occur over the entire sonotrode area (at low temperatures) instead of the time dependent weld area (with increasing temperature over time), higher forces are necessary to vibrate the sonotrode with a certain velocity (figure 6.27), as in the case of resonant condition of the top part. The electrical power is, as a first approximation, equal the average sonotrode speed (given by equation 4-25) times the force at the sonotrode (neglecting the loss in the welder). This approximation can be written as:

$$P_{el} = I_{RMS} * V_{RMS} \approx P_{acoustic} = F_S * v_{avg} \qquad\qquad \text{(Eq. 6-1)}$$

The start up transient for the sonotrode vibrations has been shown to be very short. So it should be clear that power requirement for the sonotrode vibration is increased at the beginning of a weld cycle when the top part has an anti-resonant extension. In other words, in the case of anti-resonance yielding has to occur over the entire sonotrode area at low temperatures, demanding higher power levels. As the temperatures in the weld zone reach similar levels as in the case of welding in resonance, the power requirement will be very similar (as seen in figure 6.26).

The different shapes and magnitudes of the amplitude curves in figure 6.27 can not be explained at this point, since the welder parameters were exactly the same. Nevertheless, it seems that there is no distinctive feature that identifies one weld as 'good', and the other one as 'bad'.
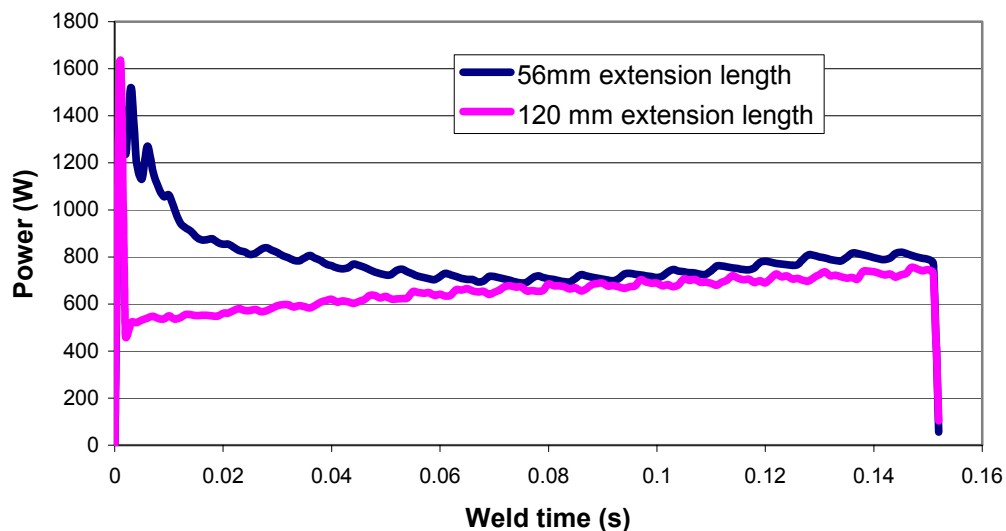
Figure 6.26: Electrical power for 56 and 150mm extension length.

139
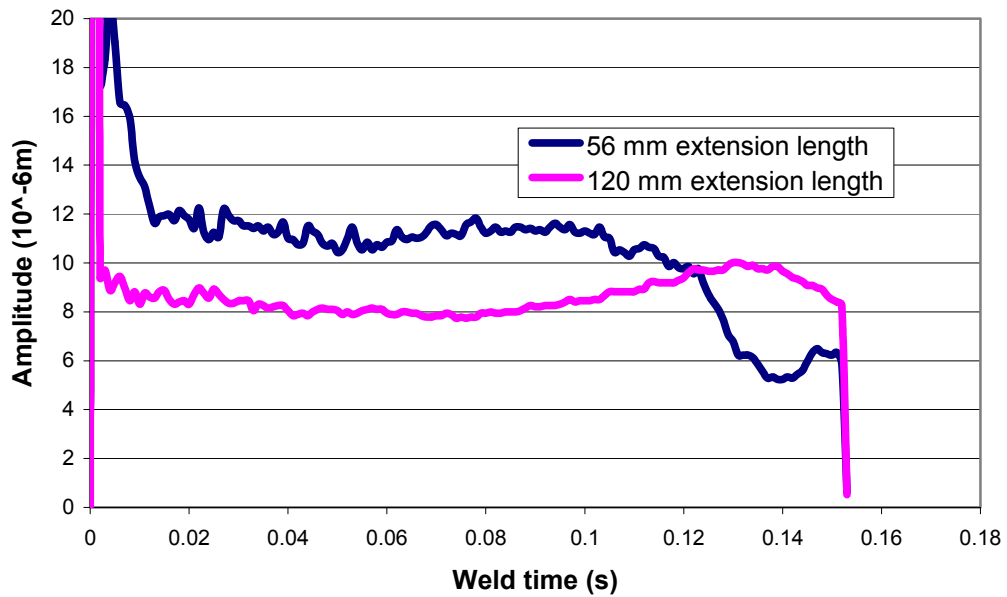
Figure 6.27: Vibration amplitude for 56 and 120mm extension length.

The results for the fixed end tests of the top part (see previous figure 6.21) are shown in figures 6.28 and 6.29. These results are in agreement with the predictions of equation 4-11. In this case of a fixed end top part it was not possible to measure the interface forces, due to the necessary clamping attachment to the welding system.
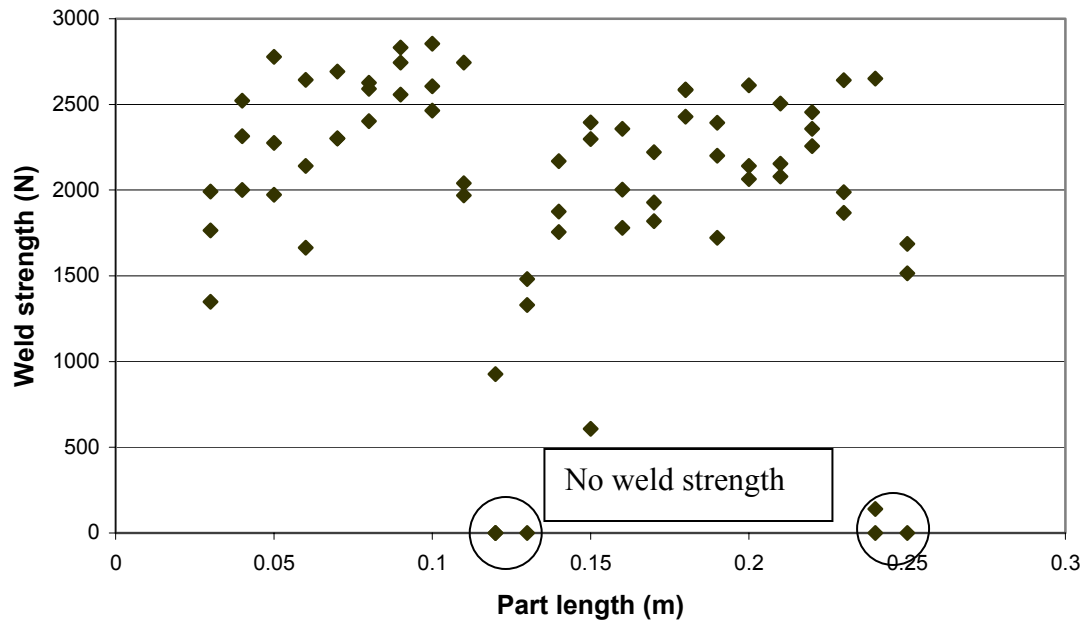
Figure 6.28: Weld strength vs. fixed end extension length.
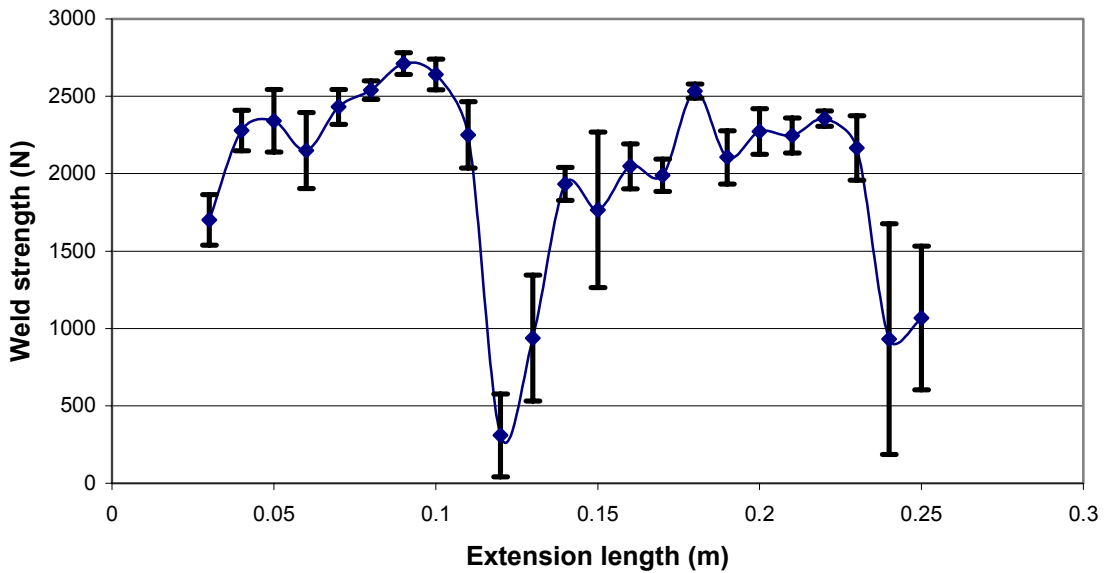
Figure 6.29: Average weld strength and standard deviation for fixed end.

6.4.3 Comparison of electrical and mechanical power

With the introduction of the approximation given by 6-1 it is now possible to calculate the minimum mechanical power generated by the sonotrode. Figure 6.30 displays the force and average speed curve for a weld cycle using a top part with resonance dimensions. The force is again the measured force multiplied by the correction factor given in section 5.2. The average speed has been calculated with equation 4-25 from the measured amplitude curve.
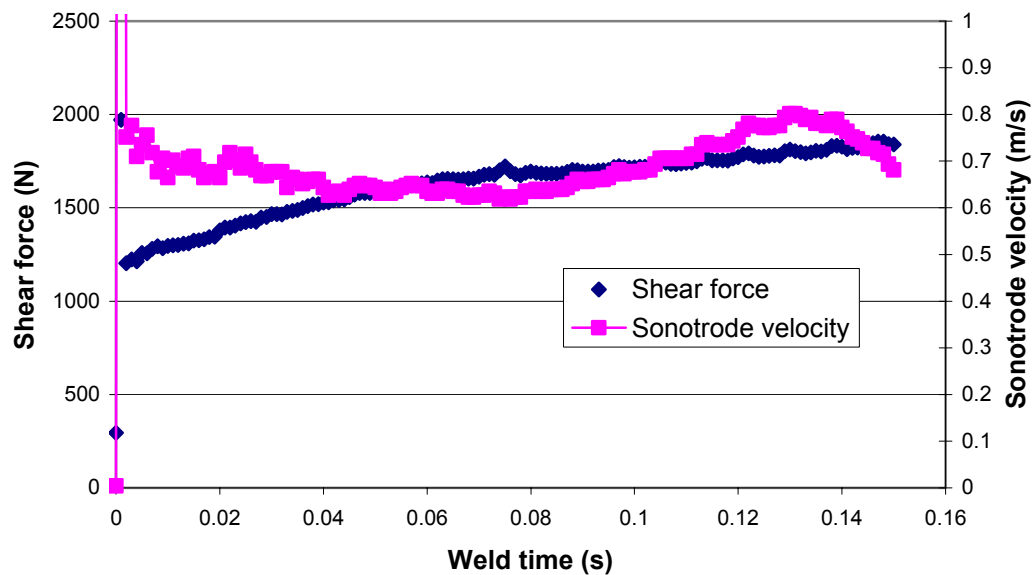
Figure 6.30: Shear force and average sonotrode speed during welding with a resonant top part.

From the results of figure 6.30 the minimum mechanical power generated by the sonotrode can be calculated. The sonotrode force must have at least the same value as the anvil force; therefore one can obtain a minimum estimate for the sonotrode acoustical power, which is simply the sonotrode speed times the sonotrode force, as given in 6-1. The resulting electrical (RMS-power calculated with the DAQ) and acoustical power curves (calculated by multiplying the values shown in 6-30 for each point in time) for a weld with 120mm extension are shown in figure 6.31. With this extension length the excitation force should be negligible because the part is in longitudinal resonance. Thus, only very little force is required to excite it with a certain amplitude, and therefore the sonotrode force is equal to the measured anvil force.
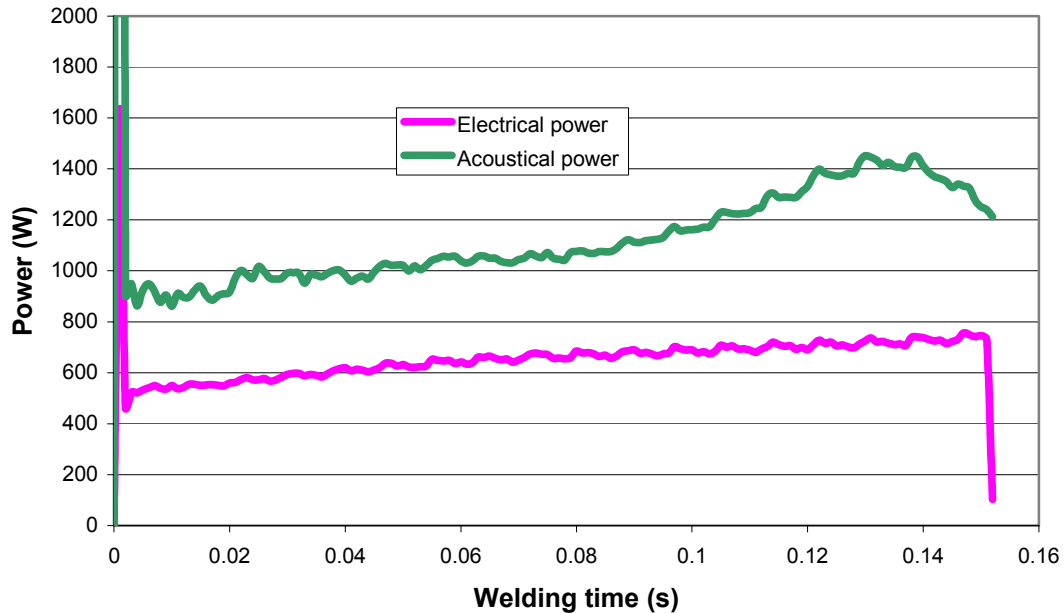
Figure 6.31: Comparison between acoustical and electrical power for welding when the top part is in resonance.

143

The error for the electrical power measured with the DAQ must be small since it is the result of the numerical integration of the original 20kHz voltage and current sampled at more then 300kHz. The average sonotrode speed is calculated from the amplitude measured with the MTI sensor. Its error is given in the calibration sheet to be - 2%, so that the speed must have the same error. These errors can not explain the big difference between electrical and acoustical power shown in figure 6.31. It is very clear from the graph that the acoustic power is almost twice as large as the electrical power. This is of course not possible, because the electrical power, which is measured at the transducer input, undergoes numerous losses between that input and the actual weld, and is thus an absolute upper limit for weld power. This can only mean that the measured anvil forces are too large, even after compensating for the frequency response of the anvil.

6.4.4 Summary of the results

The results clearly show a dependence of the weld strength and interface (anvil) forces on the top part dimensions. In Appendix B the anti-resonance frequencies were calculated to occur at extensions of 63 and 188mm for the free end, and at 126mm and at 251mm for the clamped end. In experiments with the free end it was not possible to weld at these lengths, while for the fixed end welding became very unstable or impossible.

From the model introduced earlier it was predicted that the sum of the forces acting as a reaction force to the sonotrode force (see condition 4-19) have a limit. This

144

means that if one of the forces increases, the other two will decrease. In the case of extension anti-resonance the excitation force became very large; therefore the other two forces had to decrease. Since the excitation force cannot be measured at the anvil, one instead observes a significant decrease in the anvil (interface) force.

It needs to be pointed out here that electrical power and the vibration amplitude were of the same magnitude during these experiments. This means the "welding system" itself was not capable of detecting the anti-resonant condition (i.e. the increased power at the beginning of the welding cycle can be detected, but at that time extrusion has already started). Thus, the case of anti-resonance is the "worst case scenario" from a quality control standpoint, but the affect of this event on the electrical impedance was very little. This means that the electrical impedance, electrical energy or the sonotrode vibrations may not be useful for general quality control purposes (e.g. welding larger structures at arbitrary positions and expecting the electrical impedance to be an indicator of weld quality).

The comparison of acoustical power and electrical power showed that the measured acoustical power was too large. Since there is little room for error in the speed measurement, this can only mean that the measured shear force was itself too large, even after compensating for the frequency response of the anvil set up (see figure 5.5). Of course the calculation presented there was only an estimate of the potential scaling factor, but it suggests why (at least in part why) the forces measured were consistently too large. Nevertheless, the shape of the force curve and the relative force values for different welds at different welding conditions still give valuable information about the welding process.

6.5 Separation of welding forces and frictional forces

Form earlier experiments it is known that the surface condition of the samples have a significant impact on weld quality and welding parameters. It is believed that, when a flat sonotrode is used, friction occurs around the weld zone. In figure 6.32 photographs of weld interfaces are shown. The samples were welded with and without a lubricant at the interface. One can clearly see the abrasion marks surrounding the weld spot at the interface of the non-lubricated sample. These marks are not visible on the lubricated sample. This is indicative of a reduced friction between the welded parts.
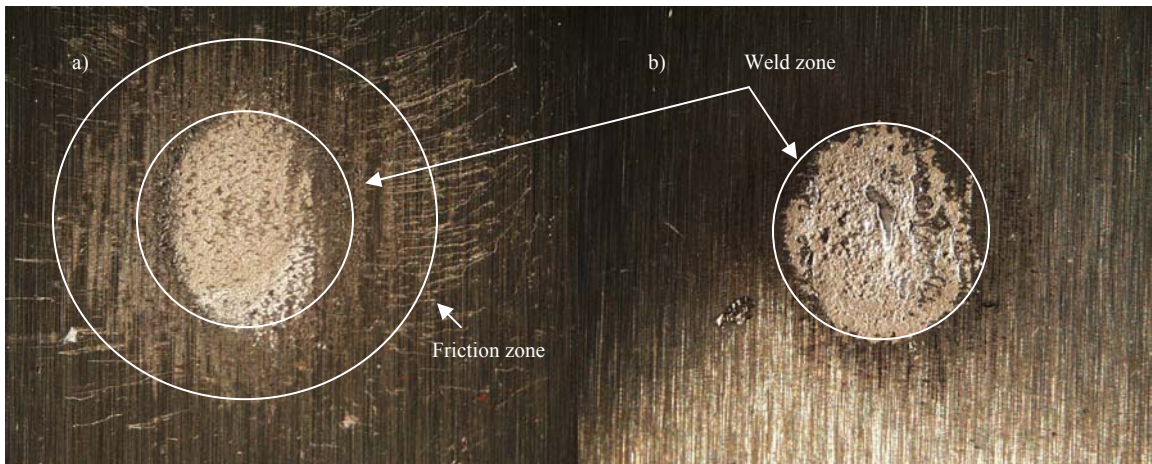
Figure 6.32: Weld interface not lubricated a) and lubricated b).

The frictional force should depend on the static load. In order to separate friction force F_{FR} and welding force F_W the normal force was changed and then the anvil force measured. The excitation force F_{AM} which can not be measured at the anvil can be neglected for small parts. The influence of a change of the static load on the welding

146

force is complex and according to the developed model, the welding force will increase with decreasing normal load at a constant temperature. The results of the numerical simulation of the temperatures and the consequent calculation of the welding force (see section 6.8) indicate that the welding forces are in fact increased for reduced normal forces. At this point it is impossible to estimate the impact of the normal force for the welding conditions used here, therefore the welding force was assumed to be constant for the examined weld and surface conditions and the friction coefficient will be calculated by the equation given by the friction law (equation 4-17, i.e. friction force is only depending on normal force) and the axis intercept on the y-axis will be the constant welding force.

Experiments were conducted for three different surface conditions of the samples. The sample size was 50mm x12.5mm, so that F_{AM} could be neglected. The thickness was 1mm. In those three experiments the surface conditions were:

- Surface condition 1: Cleaned with acetone

- Surface condition 2: Grit blasted

- Surface condition 3: Lubricated with industrial lubricant 3-36[*]

For surface condition 2 the surfaces were grit blasted so that the entire contact area of the samples was rough. The lubricant was applied, by spraying it first onto a paper towel, and then wiping only one surface of the sample on the weld interface side with that paper towel. For the three different surface conditions the load was changed from 80psi (1624N) to 60psi (1112N) to 40psi(712N) prior to welding. The welding parameters were:

---

[*] CRC Industries, Inc. No. 03005

Powerlevel: 10; Matching: E; Weld time: 0.2s

6.5.1 Results for samples with cleaned surface

In figure 6.33 the resulting shear force curves throughout the welding cycles for

cleaned samples are shown. At the beginning of the weld cycles the values are somewhat

erratic, but towards the end the values converge towards a nearly constant value. The

force values were taken at the end of the weld cycle (One can assume that the weld area

is fully developed and frictional and welding forces are acting together) and plotted

against the static weld force, as shown in figure 6.34. The slope of the linear

approximation in figure 6.34 is the calculated friction coefficient, when the welding

forces are assumed to be equal at that welding time.
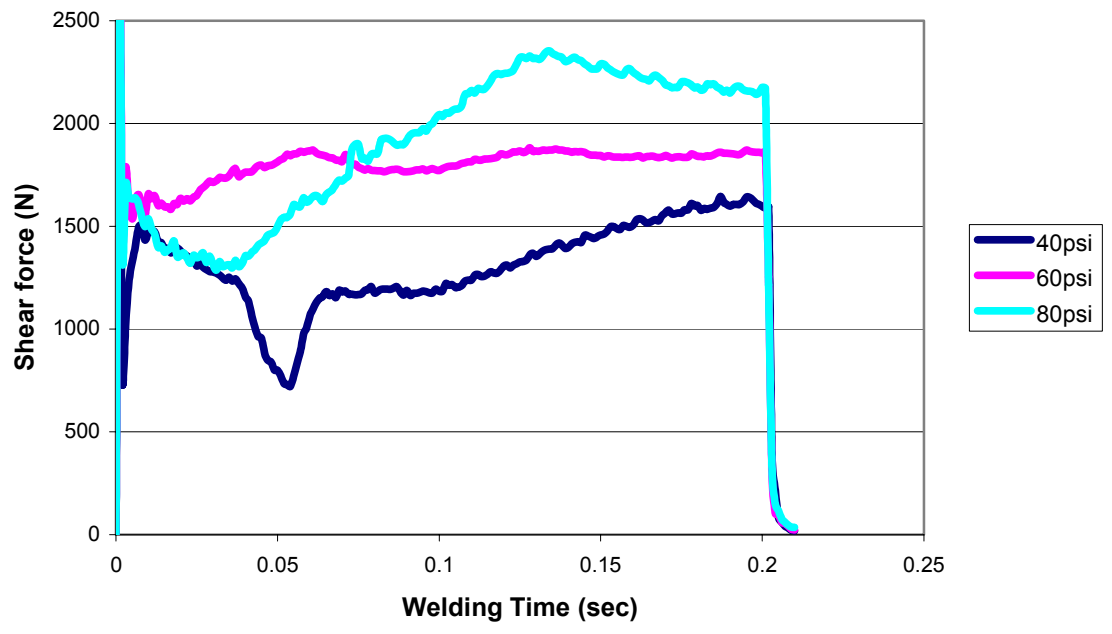
Figure 6.33: Measured shear forces for samples with cleaned surfaces for different normal loads vs. weld time.

$$y = 0.6014x + 1178.8$$
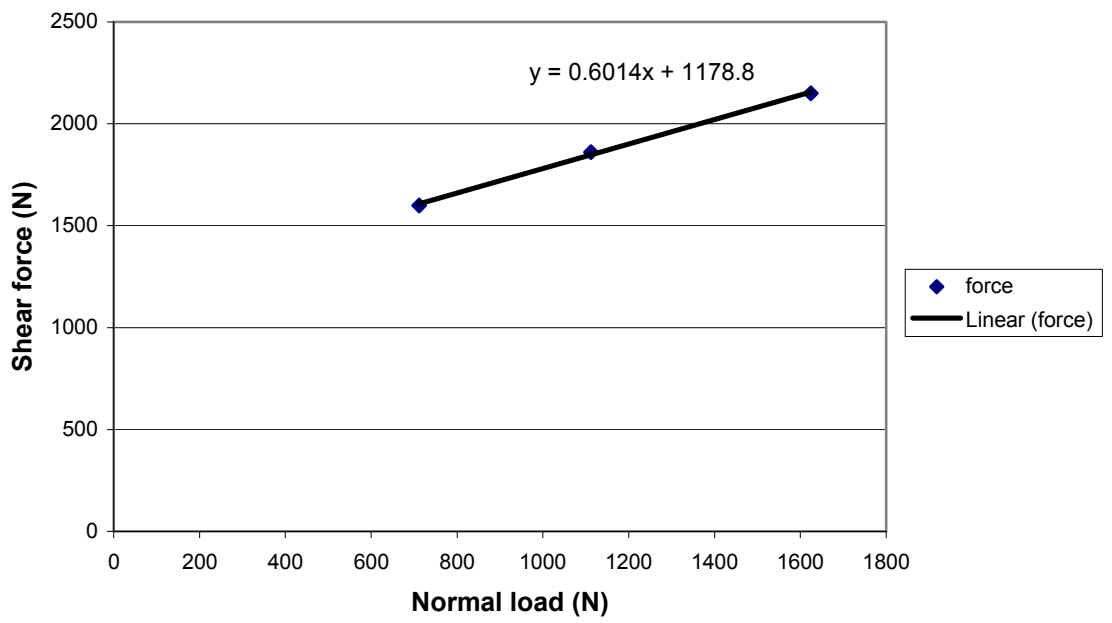
Figure 6.34: Friction coefficient approximation for cleaned surface condition.

149

From figure 6.34 the calculated static friction coefficient is 0.6 and the constant welding force is 1180N at the end of the weld cycle. Since in this case all force values are too high by the same multiple the friction coefficient calculated should not be affected. However the calculated welding force must be too high for the same reason.

Now one can also look at the power curves during the weld cycles for the different pressures. From the curves in figure 6.35 one can see, that the erratic behavior of the force curves during the beginning of the weld cycle cannot be found in the power curve.
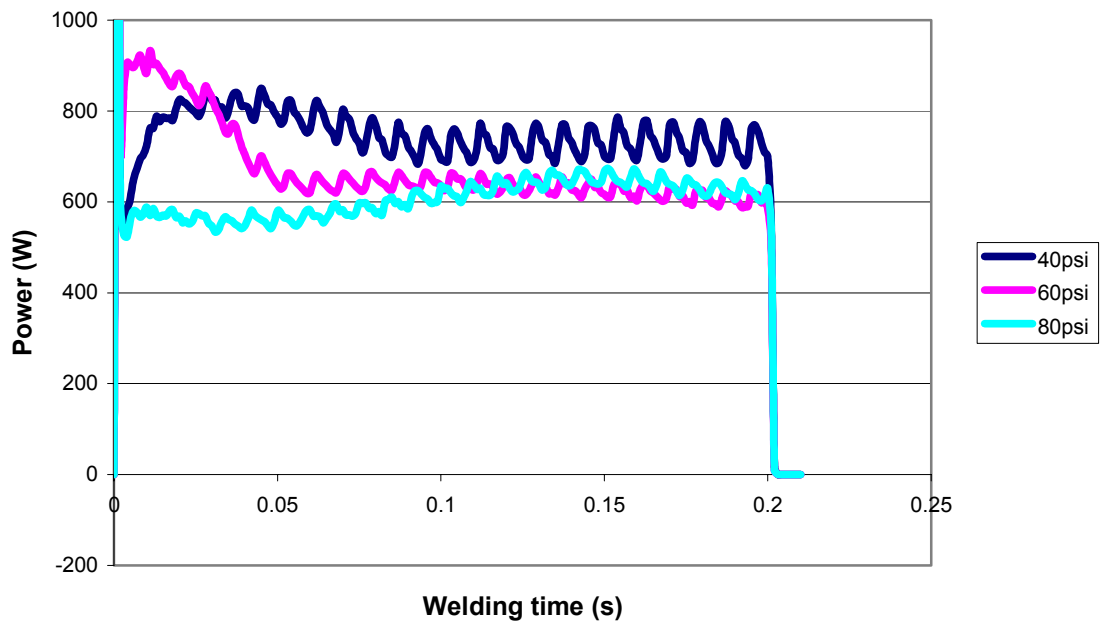
Figure 6.35: Power curves welding samples with cleaned surface.

6.5.2 Results for samples with grit blasted surfaces

Below the force curves, the friction coefficient approximation and the power curves are shown for the grit blasted samples. It was not possible to weld any of the samples that were grid blasted previous to welding. The friction coefficient has been calculated in the same way as in previous section, and again comparing the force curves (figure 6.36) and the power curves (figure 6.37), there is no indication for the huge difference in the shear force in the power curves. There is also no indication for the fact, that no welding took place.
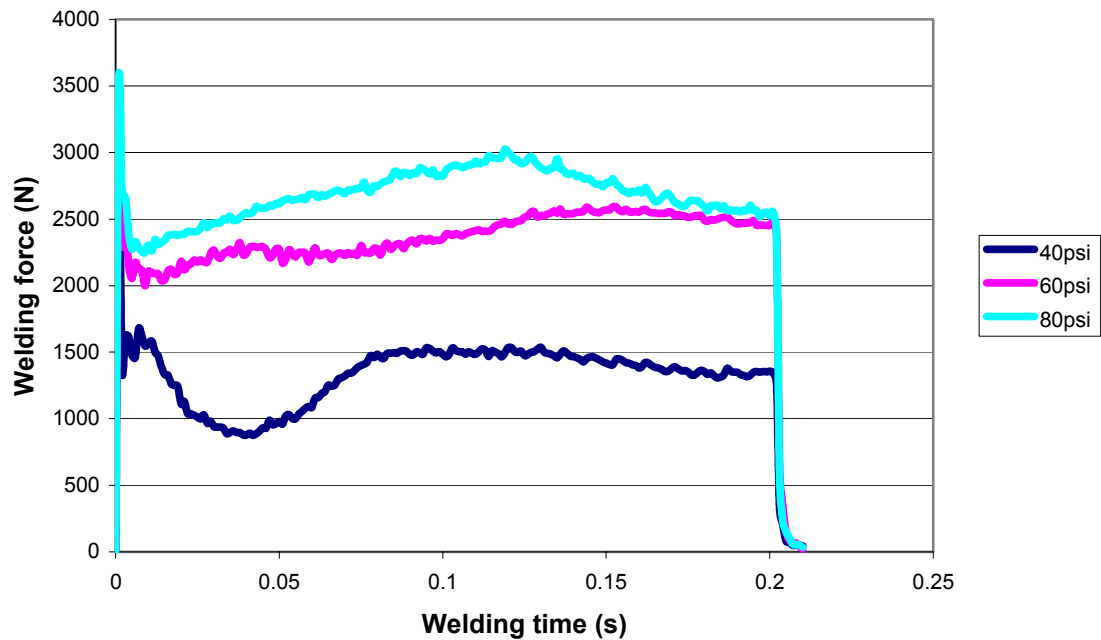
Figure 6.36: Measured shear forces for samples with grit blasted surface.
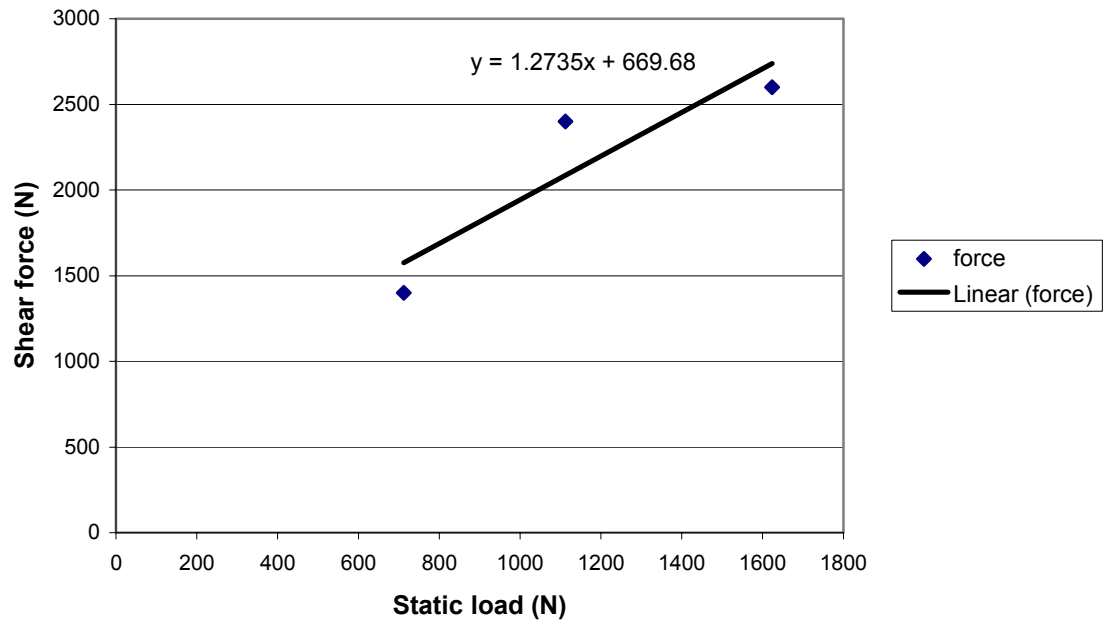
Figure 6.37: Friction coefficient approximation for samples with grit blasted surface.
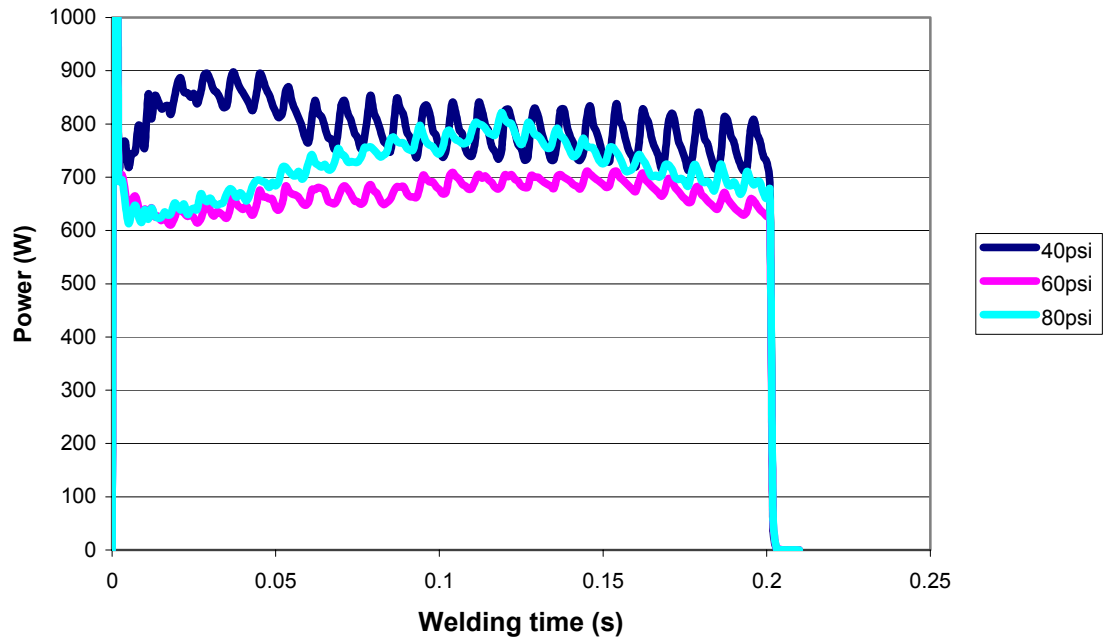
Figure 6.38: Power curves welding samples with grit blasted surfaces.

152

6.5.3 Results for samples with lubricated surfaces

The samples that where lubricated prior to welding rotated several degree with respect to each other during welding.
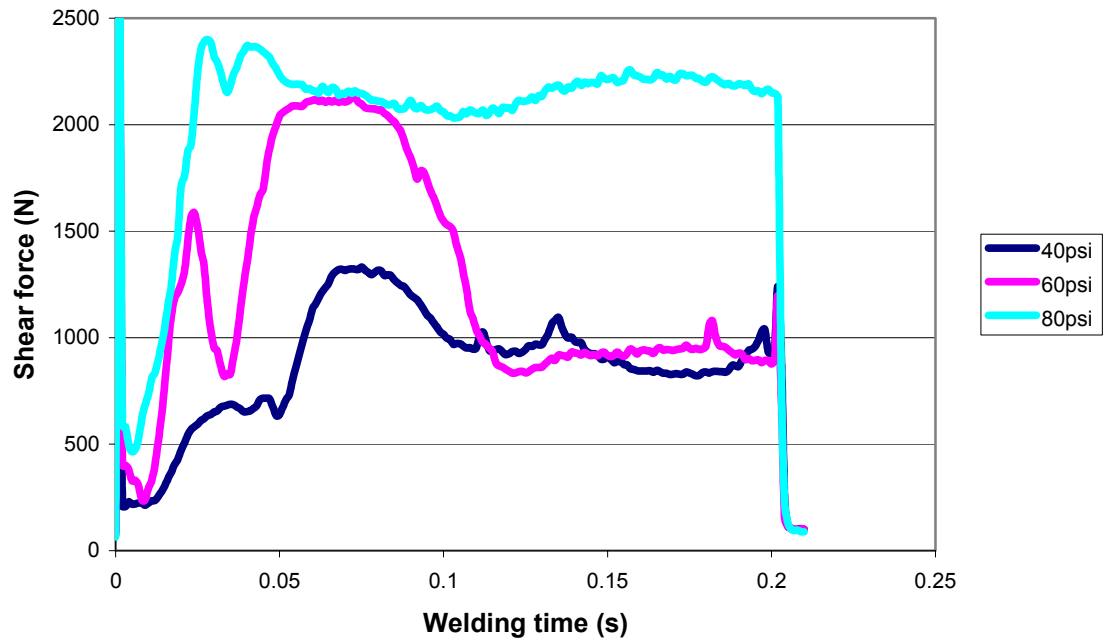
Figure 6.39: Measured shear forces for samples with lubricated surfaces.

$$y = 0.3544x$$
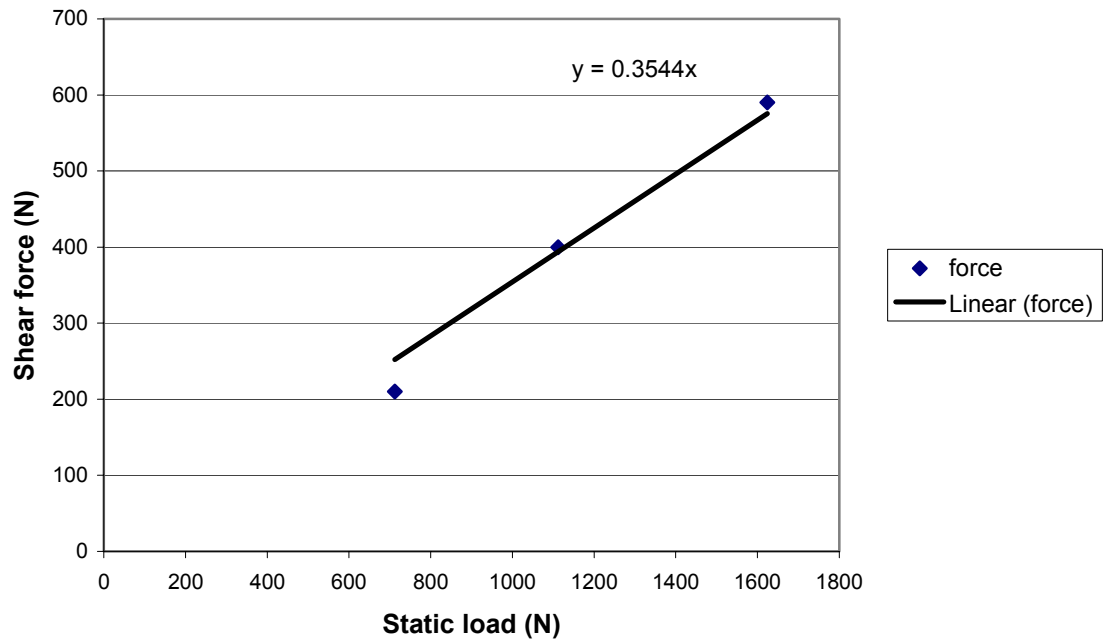
Figure 6.40: Friction coefficient approximation for lubricated surfaces.
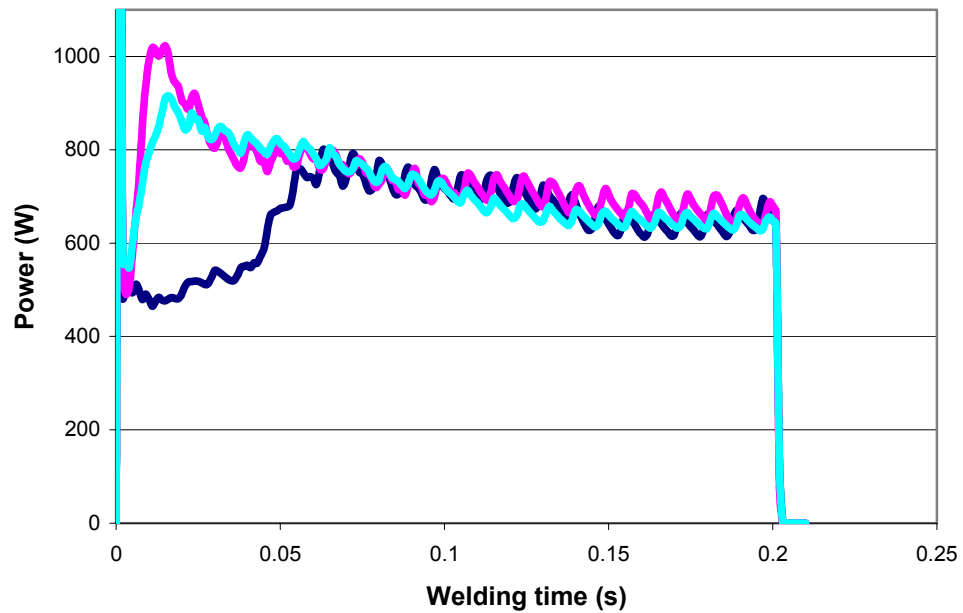
Figure 6.41: Power curves welding samples with lubricated surfaces.

154

The friction coefficient for the lubricated samples was determined differently from the previous two experiments. It had to be assumed that due to the temperature increase during welding the lubricant burns off and therefore the friction coefficient varies during welding. In figure 6.39 the erratic change in shear forces is shown very nicely. In this case the friction coefficient has been determined at the very beginning of the weld cycle. At that point in time only the frictional forces are active because the metal surfaces are not in contact with each other. At the beginning of the weld cycle the friction coefficient is then 0.35 (figure 6.40). (It must be noted that tests with this surface condition should not be repeated too often, since the high electrical mismatch at the beginning of the weld cycle leads to very high voltages which can damage the power supply of the welder). These experiments show as the two previous that the electrical power does not reflect the changes in shear forces. The drop of in shear force during the weld cycle welding with 60psi, is very significant, but the power curve for the same weld does not reflect such a drop.

6.5.4 Summary of the results

In these three experiments three different friction coefficients could be determined depending on the surface condition of the samples. The friction coefficients range from 0.35 for lubricated samples, over 0.6 for cleaned samples to 1.27 for grit blasted samples. It could also be shown, that even if the weld quality varies (grit blasted samples were not

welded at all) the electrical power curves do not show any distinct features that would make it possible to detect either a strong or weak weld. As in Section 6.4, it would again appear that weld energy or power is unsuitable as a weld quality indicator. The reason for this apparent mismatch between power and force is unclear and would need further investigation. Part of the reason could be that the vibration amplitude did change during welding or that plastic deformation occurred at the sonotrode area during welding.

The friction coefficients found during welding are slightly higher then the friction coefficients determined from static tests on the material. Furthermore the welding force does depend on the welding normal force. This leads to an error in the friction coefficient calculation. The alternative method (equation 4-16) of determining the friction coefficient would have to deal with the same problem.

It must be said that the variation of the normal force would probably not occur during the use of USMW in a production environment, because of predetermined constant normal force for all welds. The power and shear force might still give an indication for weld quality, if the normal load was held constant and other parameters were changed. This will be examined in the next section.

6.6 The influence of Power and Shear Force on weld strength

In this section the influence of shear force and power on weld strength, for a single value of static force and type of surface condition (cleaned with acetone, corresponding to Surface Condition 1 in the preceding), will be examined. The machine settings on the power supply lead to different power levels delivered to the transducer. The settings include static load (pressure), weld time, power level (voltage) and matching (current). These settings influence the sonotrode vibration amplitude and the shear force. The shear forces are determined with the shear force sensor. The shear force at the anvil is the sum of the friction and welding force at the interface as shown in figure 4.16. It will be tested here, if the measured shear force (or anvil force F_A) will indicate the weld quality, if the only change in welding conditions is the sonotrode force and velocity.

In the experiments 50mm x 12.5mm, 1mm thick, coupons were welded. The samples were clean, dry and acetone cleaned. The static load and the weld time were held constant while matching and power level were changed to obtain variations in RMS power. The phase angle between current and voltage never exceeded 20 degrees to keep the error in RMS power calculation by the DAQ low (the phase angle would enter the equation as the cosine function, this means a 20 degree phase difference between voltage and current means a 5% error in the RMS power if phase angle is neglected). The RMS power curves and the shear force curves were recorded with the data acquisition system. After welding the samples were tensile tested. Examples of the power and shear force curves obtained for different welds are shown in figures 6.42 and 6.43.

In figure 6.42 four example RMS power curves are shown for four welds (a total of 13 welds were made), with the different colors corresponding to different tensile strengths (see legend). One can see that there are two general shapes for the different welds. In the one case the power rises to a certain value and remains constant and in the second case the power rises to a certain value and then decreases.
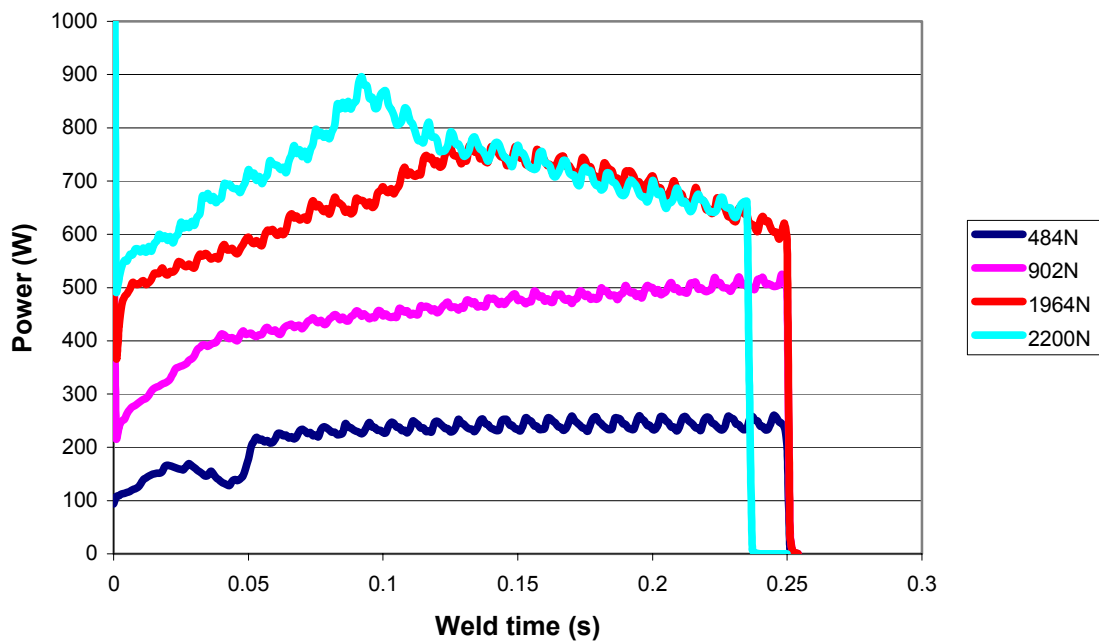
Figure 6.42: Power vs. Weld time curves for welds with different strength's.

In figure 6.43 the shear forces vs. welding time for the same welds as in figure 6.42 are shown. The rms-power and shear force curves for each individual weld are compared in figure 6.44. One can recognize the same general shapes of the shear force curves. Both curves for the 484 N and 902 N strong welds gently rise during the weld cycle, with a slight discrepancy at the beginning of the weld cycle. The shear force curve

for the 1964 N strong weld is fairly constant with a gentle upward slope at the beginning, while the power curve has a peak at approximately 0.14sec. For the strongest weld both power and shear force rise until approximately 0.1sec weld time, but after that the shear force stays constant, while the power drops off.
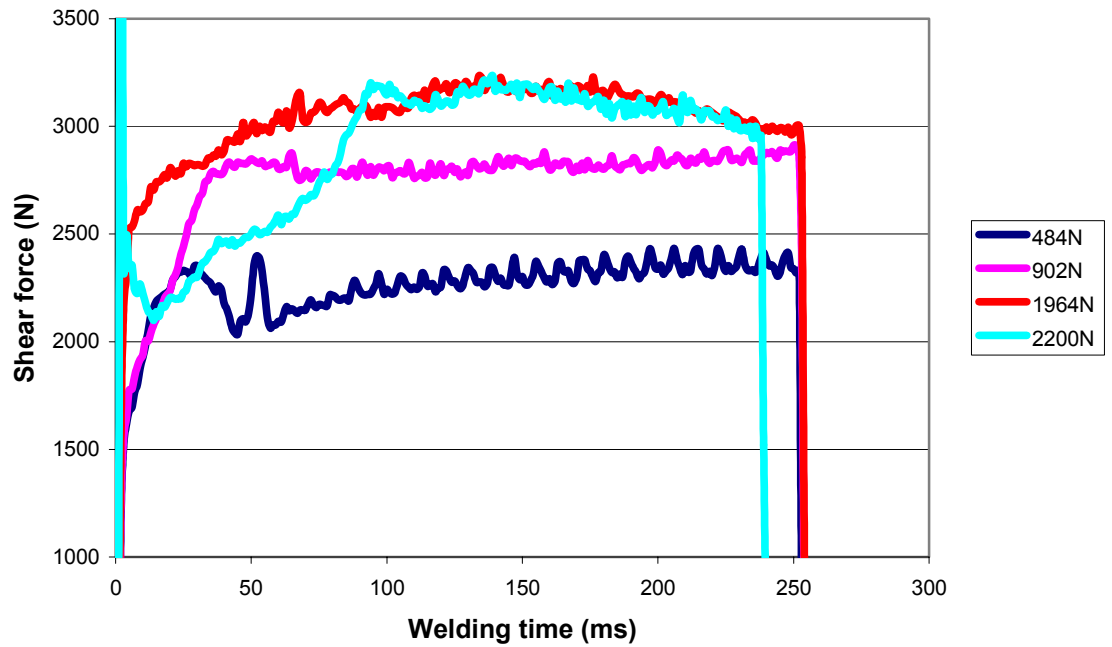
Figure 6.43: Shear force vs. welding time for welds with different weld strength's.
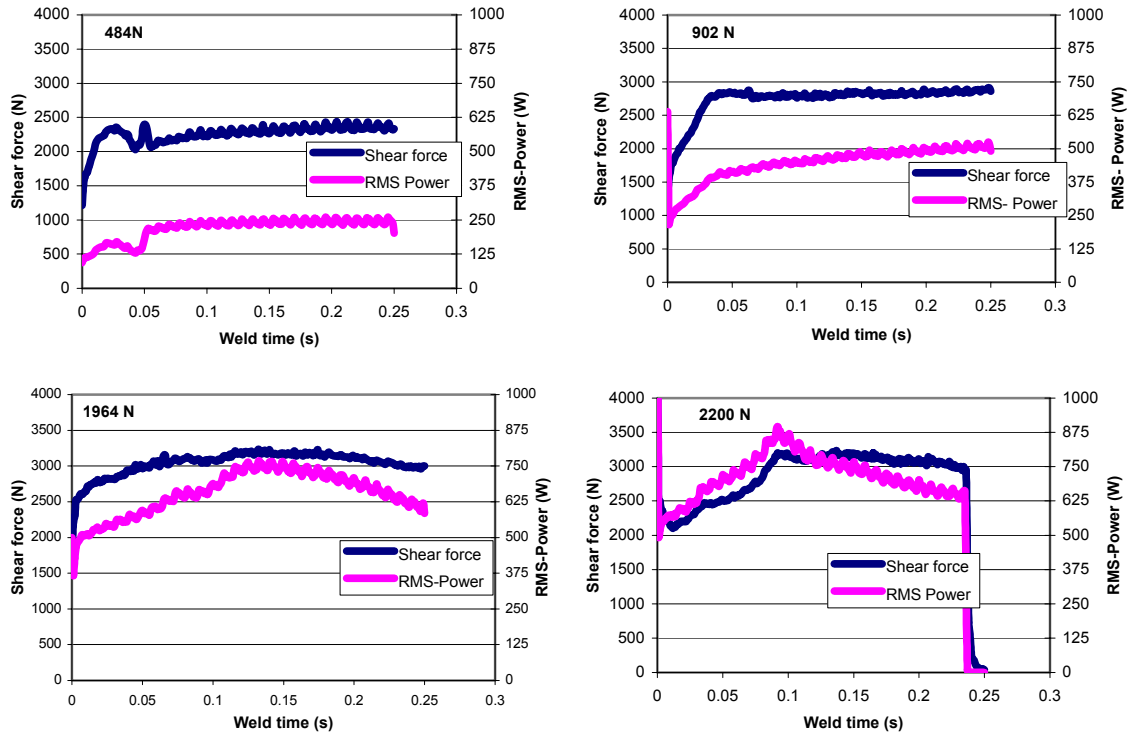
Figure 6.44: Comparison between power and shear force curves for different weld strength's.

A relative comparison of shear force and power to weld strength was then made, as shown in figure 6.45. In making this comparison, the shear force and power values were measured at the end of the welding cycles shown in figure 6.42 and 6.43. In figure 6.45, a linear fit to the shear and power data was made (solid lines) and the corresponding R^2 (coefficient of determination) obtained, where R^2 was determined from:

$$R^2 = 1 - \frac{\sum\left(Y_i - \overline{Y_i}\right)^2}{\sum Y_i^2 - \frac{\left(\sum Y_i\right)^2}{n}}$$

(Eq. 6-2)

As one can see, the general trend for both parameters is that they increase with increasing weld strength. However, the shear force has a much better correlation to the weld strength than power, which has a much greater scatter (as also evidenced by the lower R^2 value).
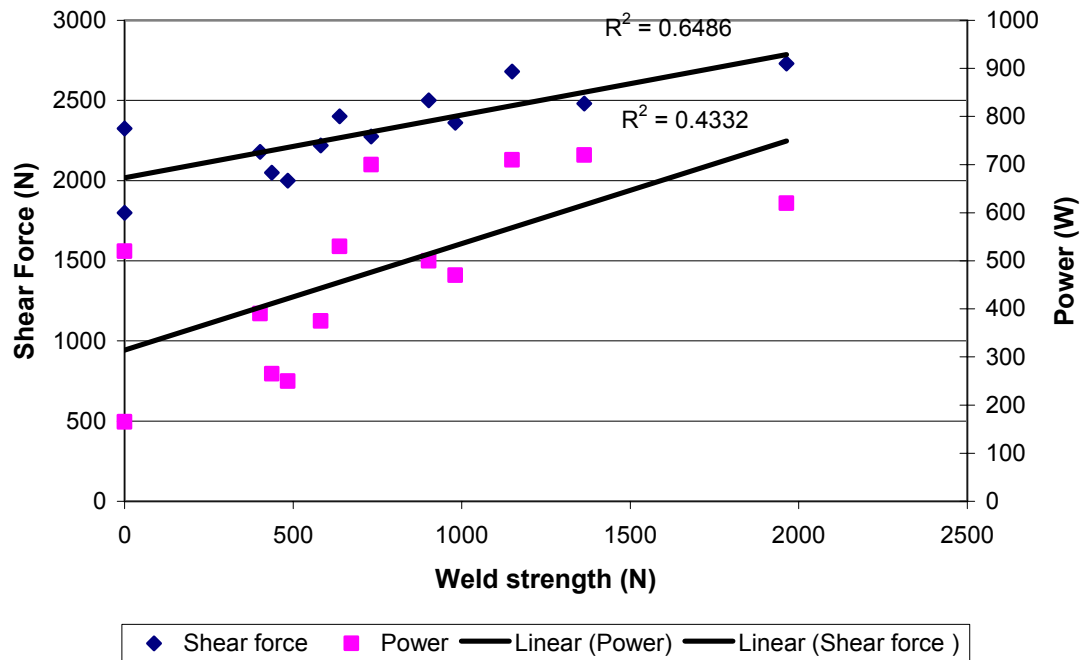
Figure 6.45: Shear force and Power vs. Weld strength.

One could conclude, from this first trial of shear force, power correlation to weld strength, that the shear force offers a more promising means of evaluating weld quality. However, one has to keep in mind that force and power data was confined to the end of cycle values, and did not attempt a more complex interpretation of the respective data curves. A single weld location was used in all of the welds, well away from anti-resonance conditions so that the influence of the part dimensions on shear force and

power should be small. Time did not permit a full range of geometry and clamping

conditions to be examined, but the expectation would have been for greater scatter in

power data, but fairly tight scatter in force data, for less optimal weld conditions.

6.7 Weld zone Temperature measurements

In this section the temperatures generated during welding, at the weld interface and at the top part surface, are measured using infrared methods. The correlation between weld strength and top part dimensions on temperatures are examined. The interface temperature is measured with the camera set up to measure the interface temperature, in the plane of the weld interface. The top part surface temperature is measured, at an angle of 30 degrees between camera view and weld area plane. The low emissivity (between 0.011 and 0.019[67]) and high reflectivity (90% to 95%) of aluminum makes precise temperature measurements more difficult than in many materials. For the present work, the accuracy of the absolute temperature measurements is in the rage of $\pm 10^0$C.

6.7.1 Compressive stress analysis for symmetric and asymmetric sample arrangement

The objective was to measure temperatures inside the weld, using IR methods. Obviously direct IR "inside the weld" is not possible. Instead, it was necessary to section the weld under the sonotrode, exposing the interior surface to the IR camera. In other words, the weld was cut in half. The geometry of the asymmetric interface is illustrated in more detail in figure 6.46 (a). Also, obviously, the stress and heat conduction conditions of the asymmetric situation are different than in usual symmetric weld situation of figure 6.46 (b).
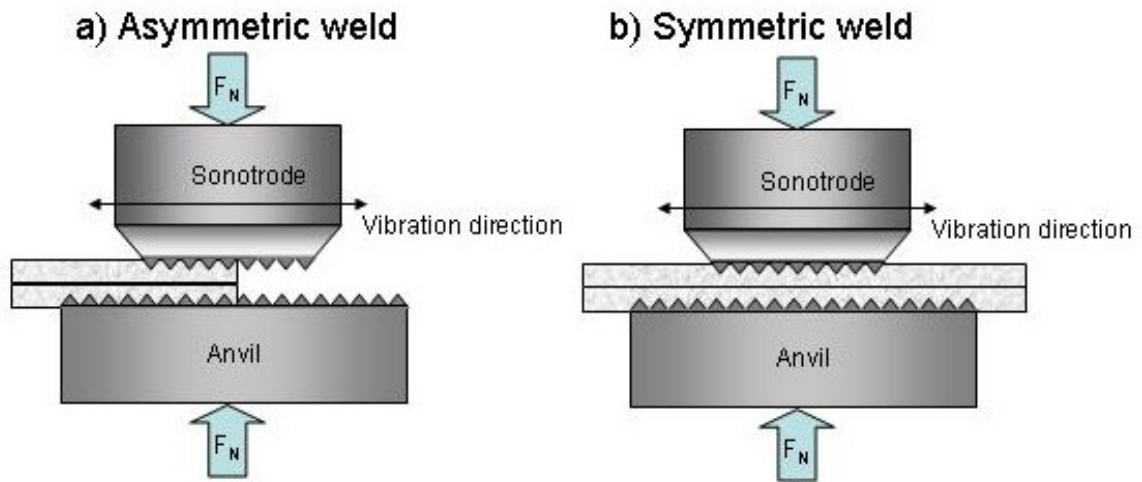
Figure 6.46: Asymmetric and Symmetrical weld arrangements.

Realizing the difference in geometries, an FEA stress analysis of the two cases was done in order to evaluate the extent to which asymmetric data could be applied to the symmetric situation [62]. FEA simulation for a symmetrical and an asymmetrical weld show the compressive stresses at the middle plane of the weld sample. The resulting compressive stresses are plotted in figure 6.47. In figure 6.48 the contour plots for both cases are shown. The plastic deformation of the top part in the asymmetrical case is clear to see.
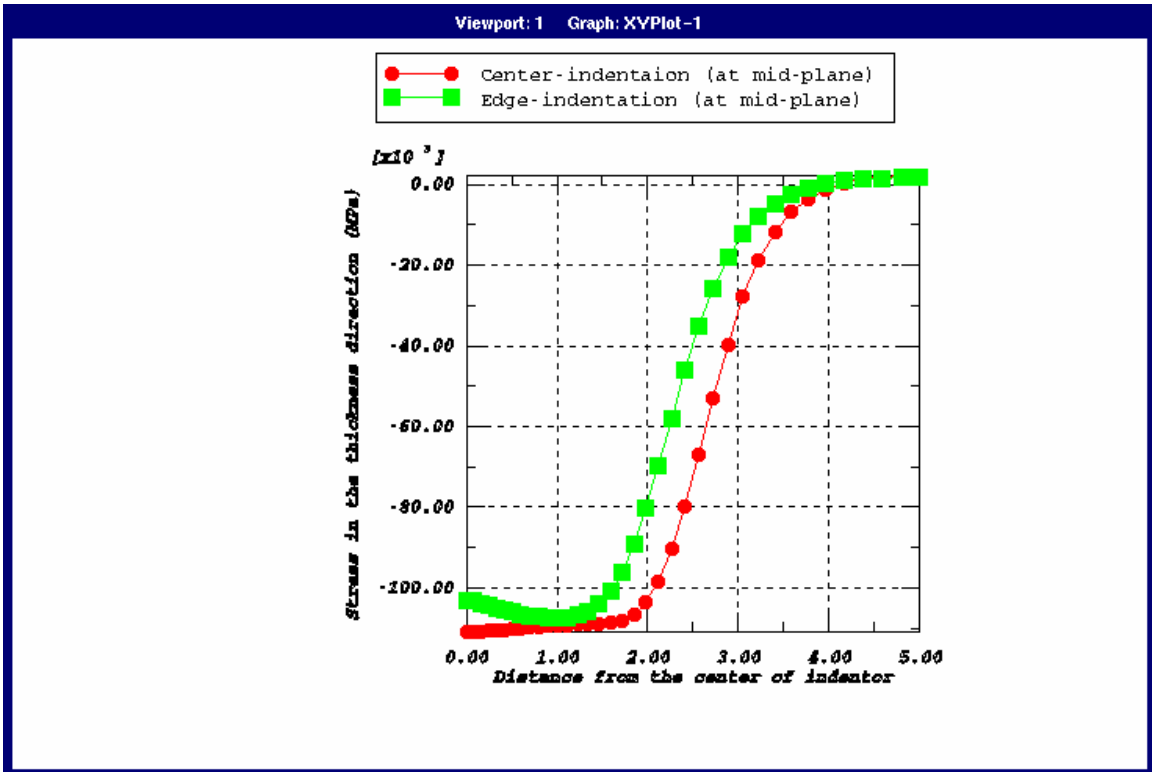
Figure 6.47: Compressive stress at the interface between the two parts.
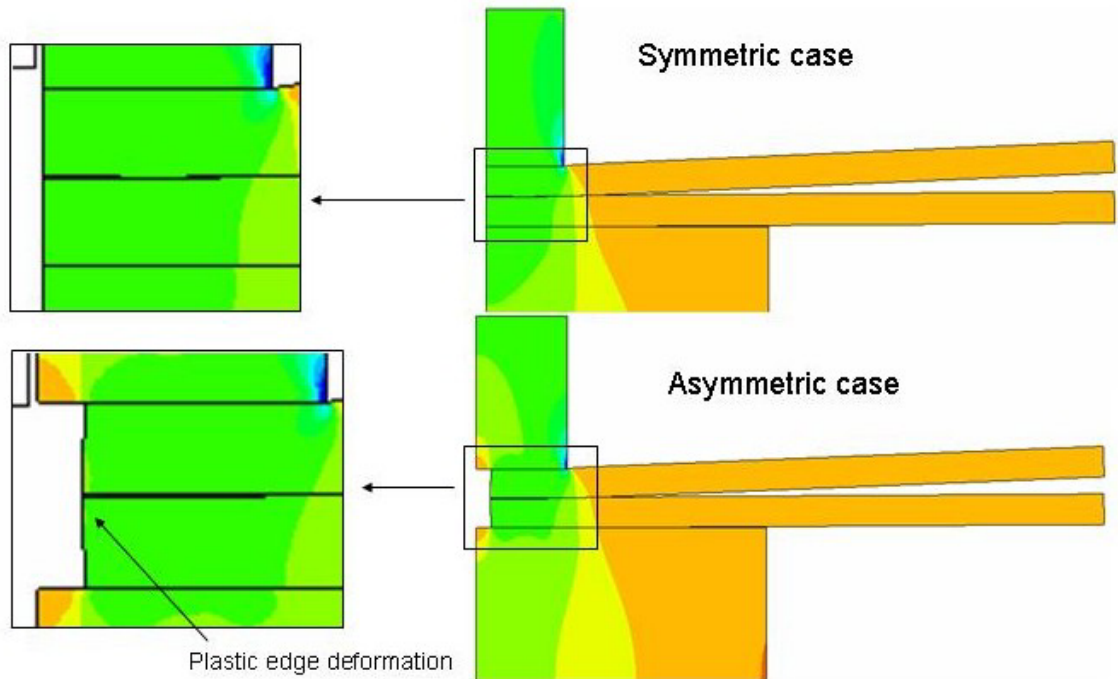
Figure 6.48: Contour plot of the contact stress analysis for symmetric and asymmetric weld set up.

One can see form figure 6.47 that the compressive stress distribution at the free surface edge (green line) is only slightly different compared to the symmetrical weld (red line). Even with the slight change in stress, the results are still valuable, since it is not the stress that generates the heat but the deformation velocity and the strength of the deformed material. Due to the increased deformation at the edge (i.e. conditions of plane stress, versus conditions of plane strain that exist in the complete weld) the stress is slightly reduced. Nevertheless, if the deformation is kept to a minimum the weld interface temperature can be measured at the edge and it is valid to assume that this represents the temperature in a "real" weld. Most important in these experiments is the interface temperature and the temperature at the sonotrode. This is, because the deformation at the interface causes the weld to be made and the deformation at the sonotrode forms a negative knurl pattern on the samples and is in the latter stages of the weld cycle responsible for sonotrode sticking and extrusion, as discussed in section 4.

6.7.2 Temperature measurements at the weld interface

The camera set up for the infrared camera is schematically illustrated in figure 6.49. The camera is set up that way, so that the temperature that occurs at the weld interface can be measured.
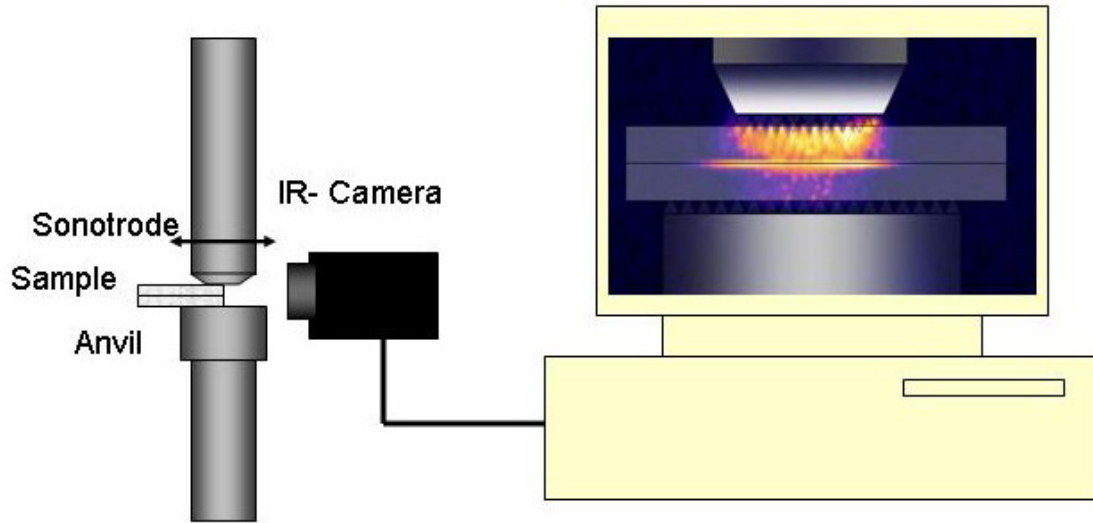
Figure 6.49: Experimental set up for infrared temperature measurements of the interface temperature.

Several samples were welded asymmetrically, all with the same parameter

settings. With samples welded in this setup, edge deformation (edge effect) had to be

avoided to the extent possible, but yet the welding process should be similar to the case

where the weld was done in the middle of the sample (symmetric case). From previous

experiments it was known that a weld at 80psi and 60J had a tensile strength of

approximately 2000N and no extrusion. For the asymmetric weld the parameters of 40psi

and 30J were chosen since only one half of the area was involved. In this way the weld

area pressure and the energy consumption per area remained the same. Any higher

energy and pressure was found to lead to extreme edge deformation, and to weld

interface temperatures out of the range of the IR system. To compare the results from the

experiments with the asymmetrical set up to the temperature that would occur in a

symmetrical weld, one weld was made as close to the edge as possible with the

167

mentioned parameters (80psi 60 J). IR images resulting from these tests are shown in

Fig. 6-50, 6-51 and 6-52. Sample 2, sample 8 and sample 9 have been chosen as

examples because they show the typical features of an asymmetrical weld, a symmetrical

weld and heavy edge deformation.

The time resolution of the IR camera was 1/60s. Therefore the exact point in time

of the beginning and end of the weld cycle cannot be observed. The weld time for

Sample 1 to Sample 6 is between 0.04s and 0.05s. The scale is automatically adjusted for

best contrast in every frame (because of the rapidly changing temperatures only a short

flash would be seen if the scale were the same for all frames). In all pictures the lowest

temperature is >78C. The highest temperatures in the entire frame (Tmax) and in the

weld zone (TWZ) are indicated below each frame.

6.7.2.1 Sample 2

Sample 2 was welded as described above with 40psi and 30J, the weld time was 0.04s. The right column shows the temperature profile along the weld interface (black) and along the sonotrode top part interface (red).

WT:0s, Tmax: 83C, TWZ: 80C	
WT:0.0166, Tmax: 156C, TWZ: 138C	
WT:0.0333s, Tmax: 220C, TWZ: 183C	
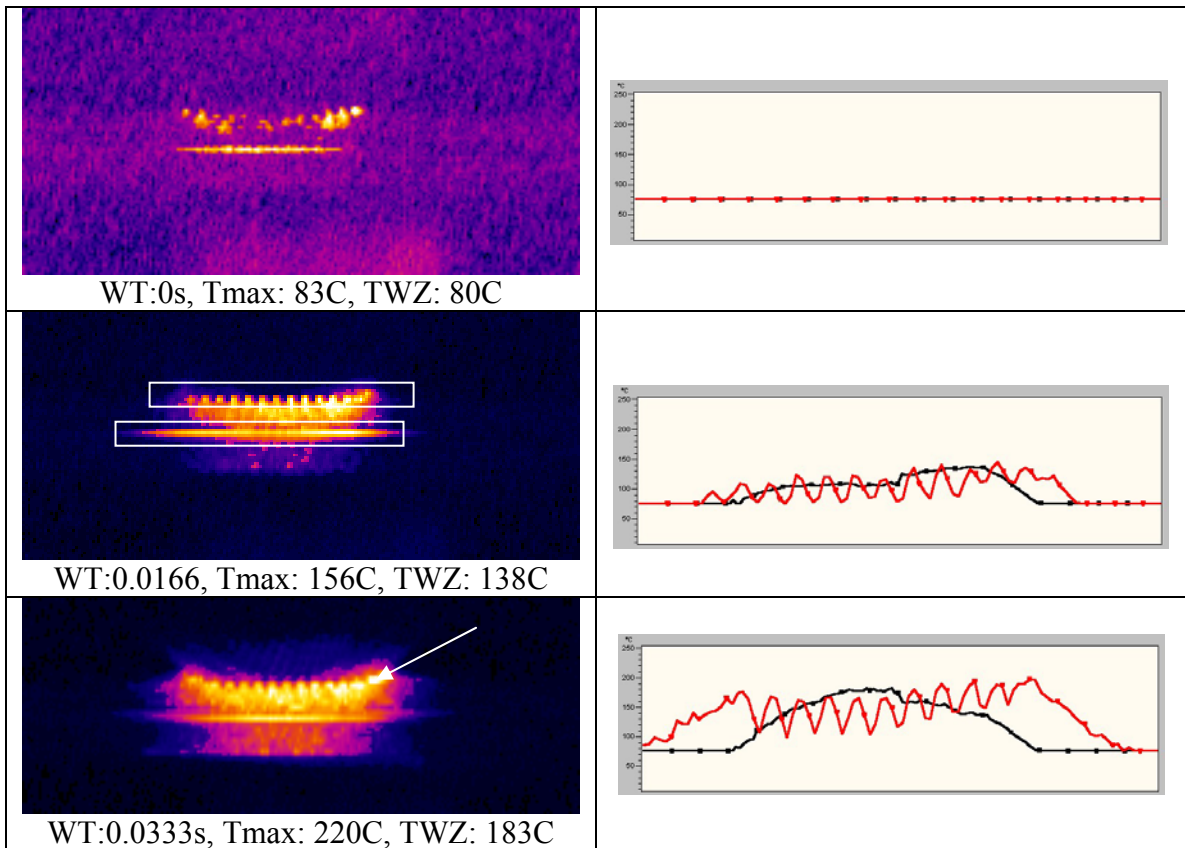
Figure 6.50: Specimen 2 infrared measurement results for the weld zone temperature for an asymmetrical weld (white areas identify selected maximum temperatures).

Figure 6.50 continued

WT:0.0500s, Tmax: 168C, TWZ: 168C	
WT:0.0666s, Tmax: 130C, TWZ: 129	
WT:0.08333, Tmax: 120C, TWZ: 120C	
WT:0.1000s, Tmax: 85C, TWZ: 94C	Knurl imprint on the top part
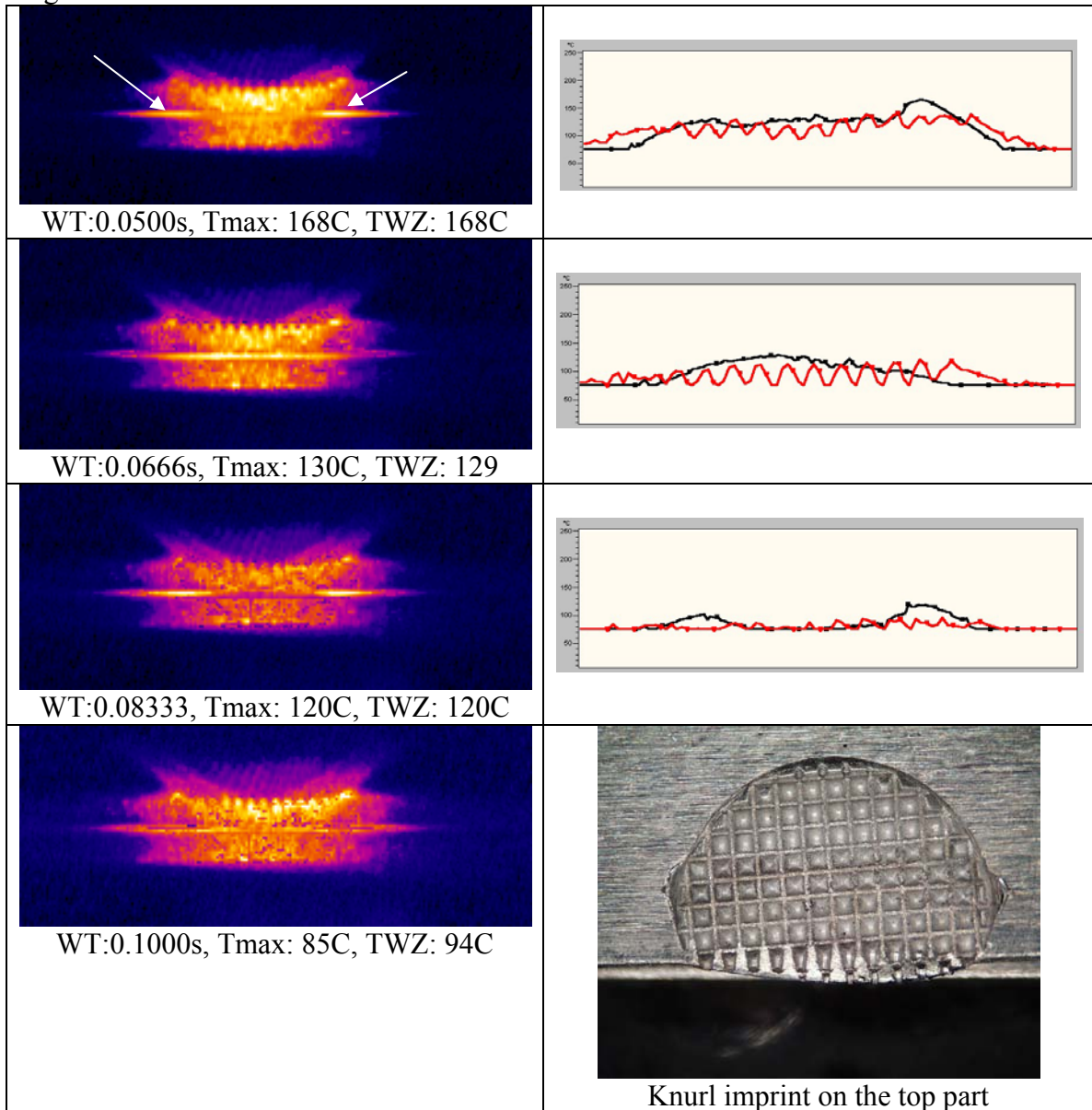
It is important to note in this sequence that the highest temperatures do not occur in the weld zone but at the sonotrode. This might indicate that the plastic deformation at the sonotrode is larger than within the weld zone. Noteworthy also is that one can see the areas within the weld zone which show the largest amount of plastic deformation. The

170

white arrows at 0.05sec weld time show that the highest temperature occurs at the edges of the deformation zone. Recalling the cross sections, this is the area where most plastic deformation occurs. One can also see that there was some external plastic deformation of the top part at the edge. This is clearly evident from the picture of the top part surface shown as the last picture in the sequence of figure 6.50, but one can see as well, that the plastic deformation was confined to the edge of the sample, where the temperature was measured. Also clear to see is that sonotrode and anvil did not heat up in this short period of time.

6.7.2.2 Sample 8

Sample 8 was welded close to the edge, as described above with 80psi and 60J, and weld time of 0.07s. Here a symmetrical weld was made and the temperature measured at the edge of the parts. This sample shows basically the same features as Sample 2. One can see that the highest temperatures do not occur in the weld area, but at the sonotrode. This weld developed somewhat higher temperatures than the other welds but considering that twice the energy was used the temperature increase was just a few degrees. The last picture in the sequence showing the top surface of the top part shows that in this case there was also some plastic deformation towards the edge (white arrows).

WT:0.0s, Tmax: 167C, TWZ: 84C

WT:0.0166s, Tmax: 207C, TWZ: 151C

WT:0.0333s, Tmax: 240C, TWZ: 173C

WT:0.0500s, Tmax: 264C, TWZ: 218C

WT:0.0666s, Tmax: 232C, TWZ: 210C

WT:0.0833s, Tmax: 205C, TWZ: 199C

WT:0.1000s, Tmax: 187C, TWZ: 175C

WT:0.1166s, Tmax: 170C, TWZ: 151C

WT:0.1333s, Tmax: 158C, TWZ: 151C

Knurl imprint on the top part
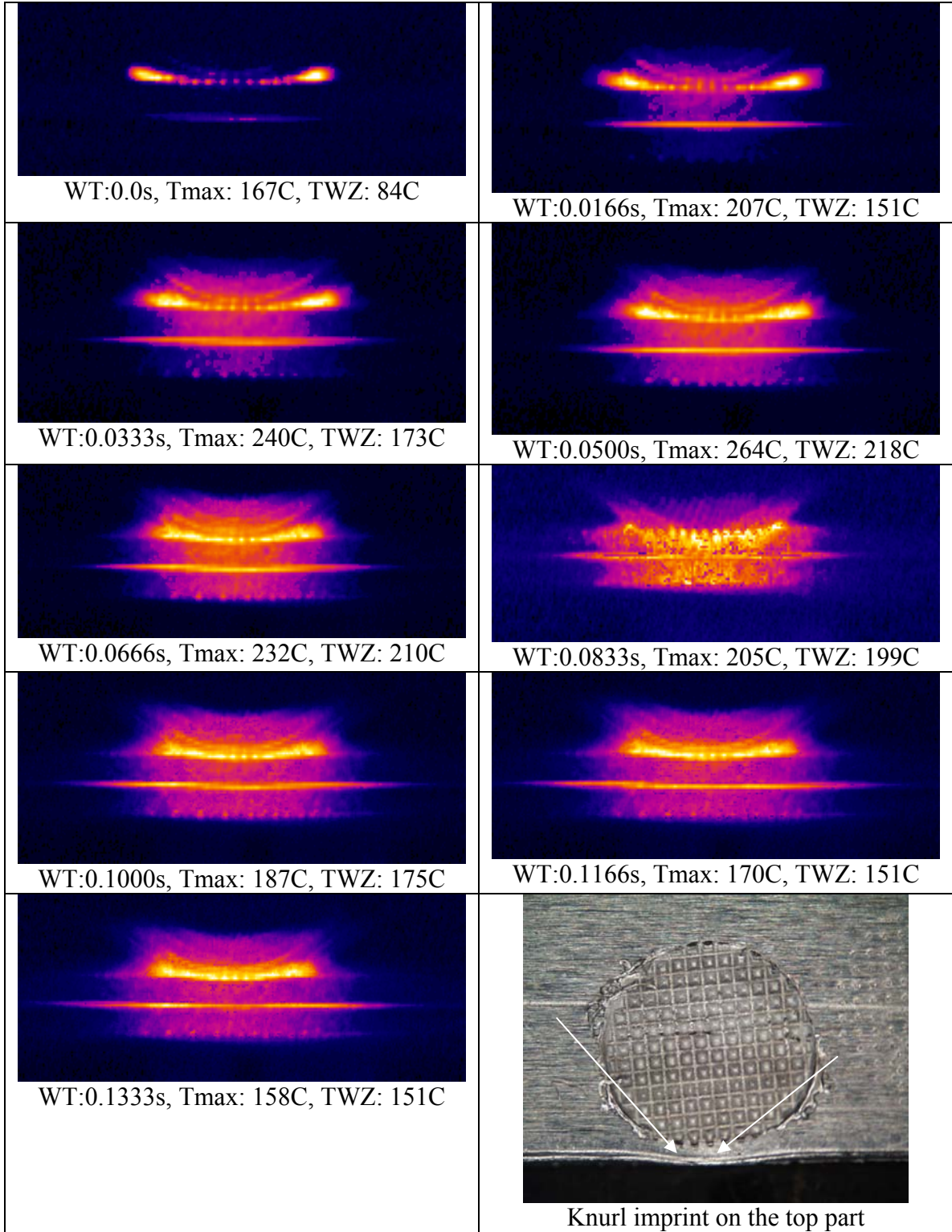
Figure 6.51: Infrared measurement results for a symmetric weld close to the edge.

6.7.2.3 Sample 9

Sample 9 is a good example of heavy edge deformation. One can see in the sequence of images how the sonotrode squeezes all the material of the top part out at the edge. The temperatures generated by this heavy external deformation are approximately 100^0C higher then in the case of no external deformation.

WT:0.0s, Tmax: 126C, TWZ: 105C

WT:0.0166s, Tmax: 204C, TWZ: 156C

WT:0.0333s, Tmax: 273C

WT:0.050s, Tmax: 278C

WT:0.0666s, Tmax: 279C

WT:0.0833s, Tmax: 322C
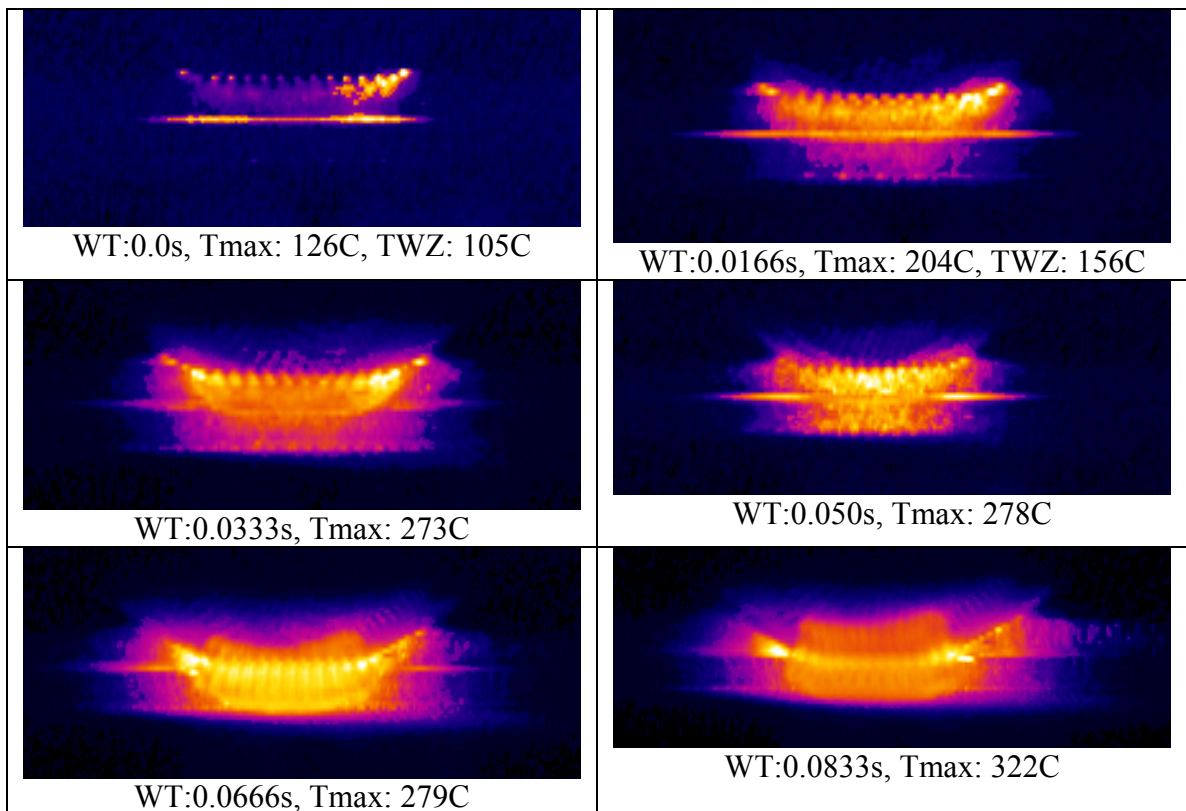
Continued

Figure 6.52: Infrared measurement results for an asymmetric weld with heavy edge deformation.

Figure 6.52 continued

WT:0.1000s, Tmax: 241C	WT:0.1166s, Tmax: 208C
WT:0.1333s, Tmax: 187C	
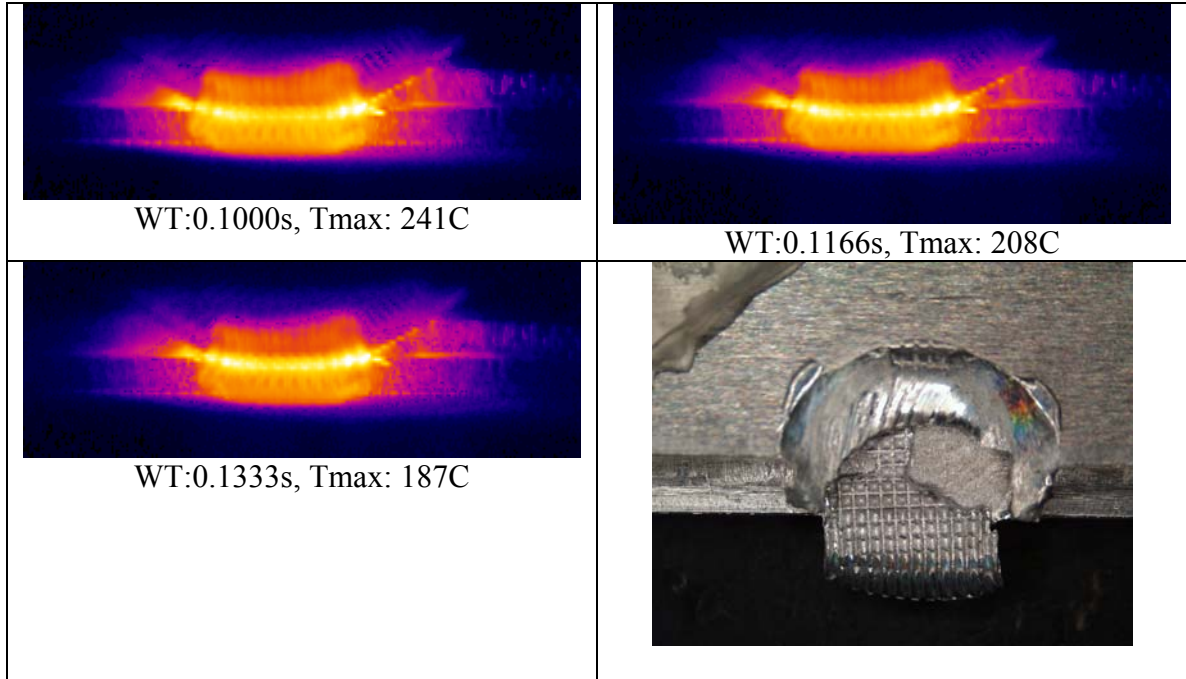
6.7.2.4 Maximum weld zone temperatures during all experiments

The maximum weld zone temperature vs. weld time is shown in figure 6.53 for various welds. From these results one can conclude that the highest temperature is reached at the end of the weld cycle. Sample 8 is welded symmetrically, close to the edge, with a welding time of 0.07s. The temperature measured is higher than for the asymmetrical welds, even though the temperature was measured approximately 1mm away from the weld area.
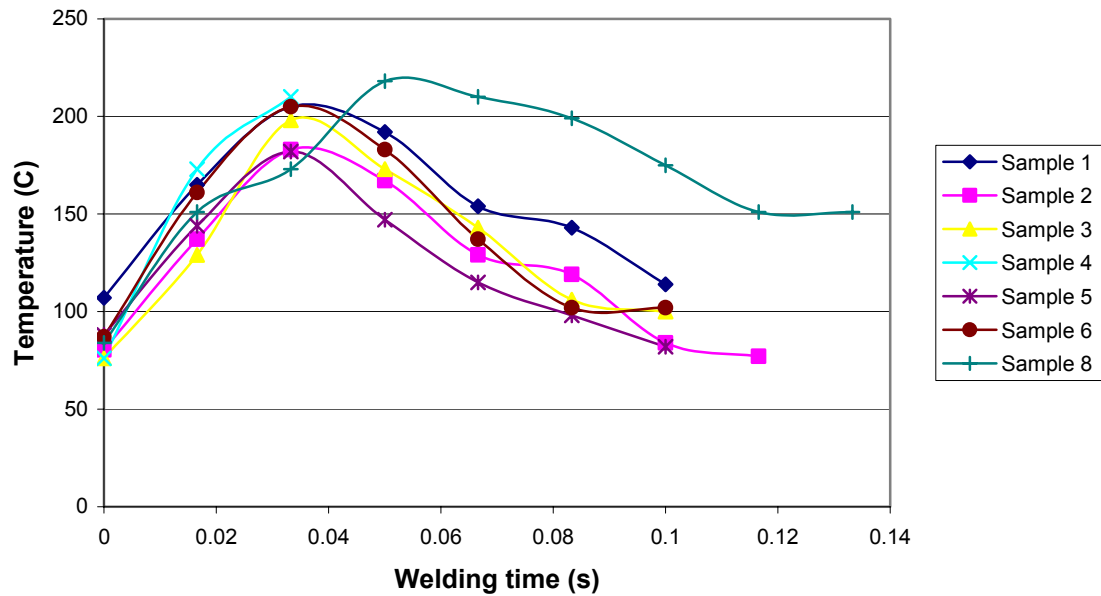
Figure 6.53: Maximum temperatures in the weld zone.

The temperature increase is very rapid at the beginning of the weld. Sample 8 shows that for longer weld times the temperature will eventually increase to yet higher temperatures. From the detailed pictures in figure 6.50 to 6.52 one can see that the highest temperatures did not occur in the weld zone, but at the edges of the sonotrode. This can be attributed to the fact that the top part experiences some amount of plastic deformation that will not be present in a real weld. This leads to the conclusion that external deformation produces more heat then the internal deformation in the weld zone.

6.7.3 Summary of the interface temperature measurements

It was found that the temperature at the interface rises very quickly - up to 200^0C in only 40 ms. During these experiments edge deformation cannot be avoided completely. Therefore the temperatures measured are lower then the temperatures that could be expected in a symmetric weld. A second finding is that heavy plastic deformation leads to temperatures that are much higher then the temperatures that occur without heavy deformation. To test this finding, in the next section symmetrical welds are made and the temperatures measured around the sonotrode are correlated to the weld strength and the amount of plastic deformation at the sonotrode.

6.7.4 Top part temperature measurements

In 6.7.2 it was shown that heavy plastic deformation causes very high temperatures at the sonotrode. In this section the correlation between the temperatures that occur around the sonotrode and weld strength will be examined, as well as the influence of the excitation force on the temperature. The experimental set up for these experiments is shown in figure 6.54.
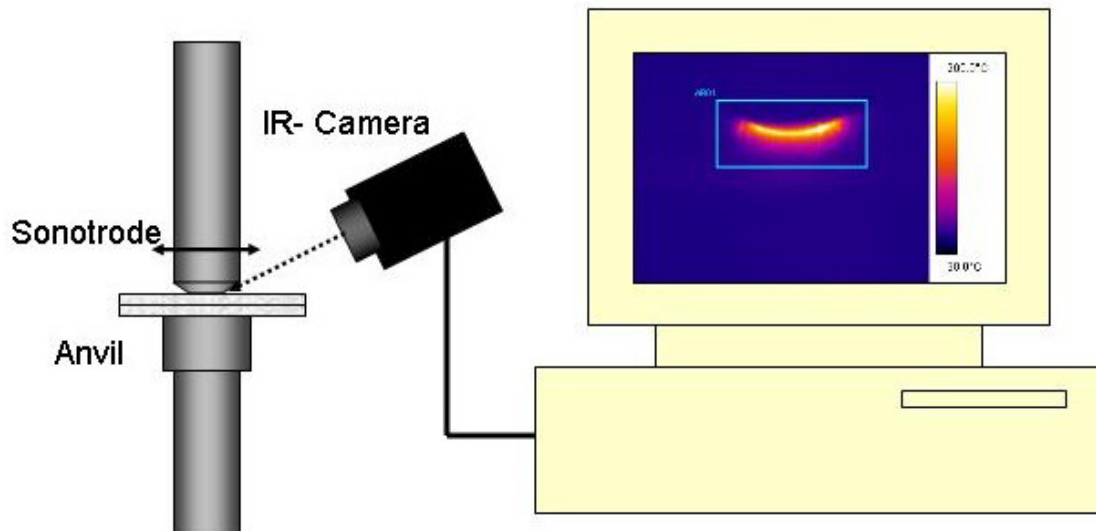
Figure 6.54: Experimental set up for infrared temperature measurement of the top part surface.

To find the correlation between temperature, weld strength and extrusion, samples of the size 50mm x 12.5mm, 1mm thick were welded under varying welding conditions. The power level and the matching were changed, while the normal force and the weld

177

time were held constant. The change of power level and matching setting resulted in different forces and amplitudes acting at the sonotrode. In figure 6.55 three examples of measured heat signatures are shown. These signatures show the highest temperatures at the end of one weld cycle. The corresponding weld strength is noted in the bottom left corner of the heat signature picture. The boxes indicate the area where the highest temperature was measured, used in figure 5.56.
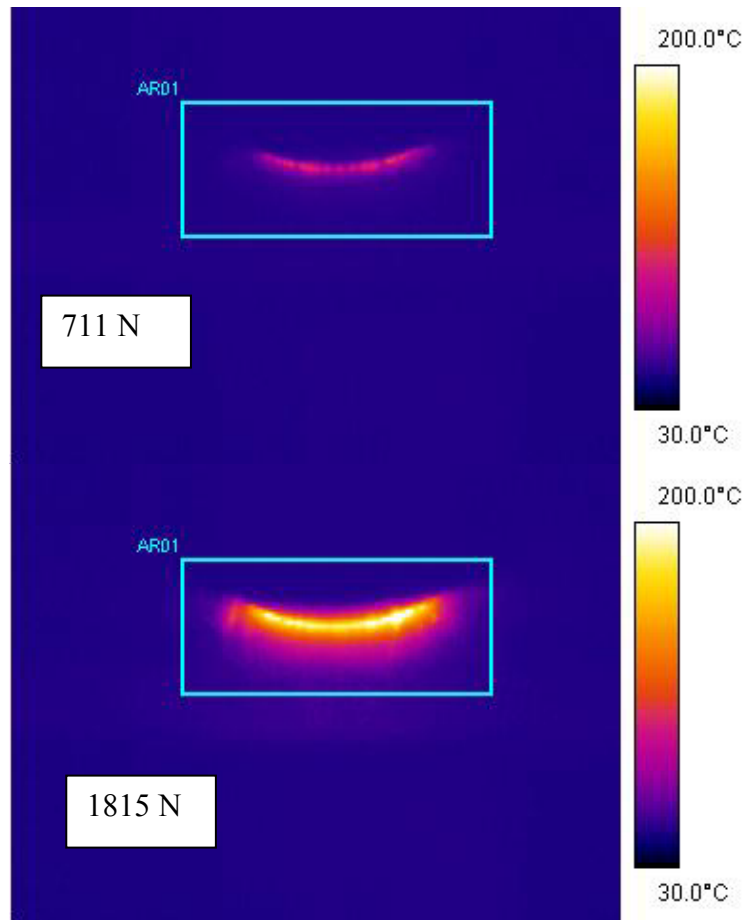
Figure 6.55: Heat signatures measured at the sonotrode on the top part surface.

Figure 6.55 continued
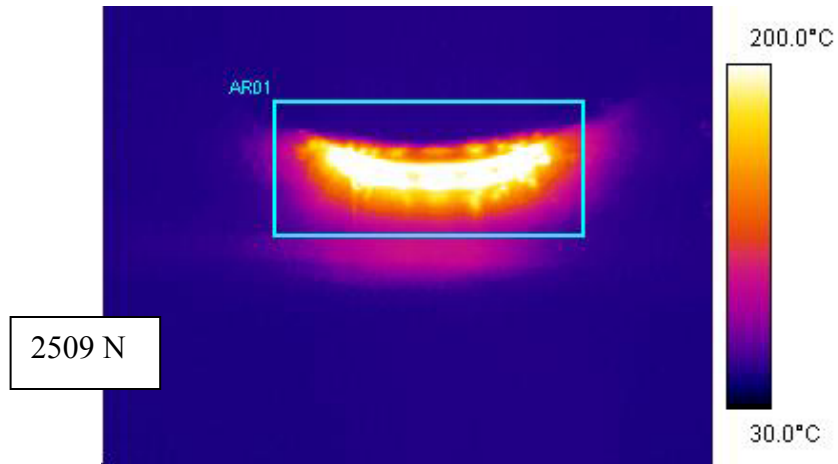
Thus, in figure 6.56 the maximum temperatures measured around the sonotrode are shown. The pictures of the sonotrode imprints on the top part surface show the amount of plastic deformation of the top part at different temperatures. The results clearly show a correlation between increasing temperatures and increasing weld strength. If this correlation between weld strength and surface temperature is generally valid is examined in the next section.
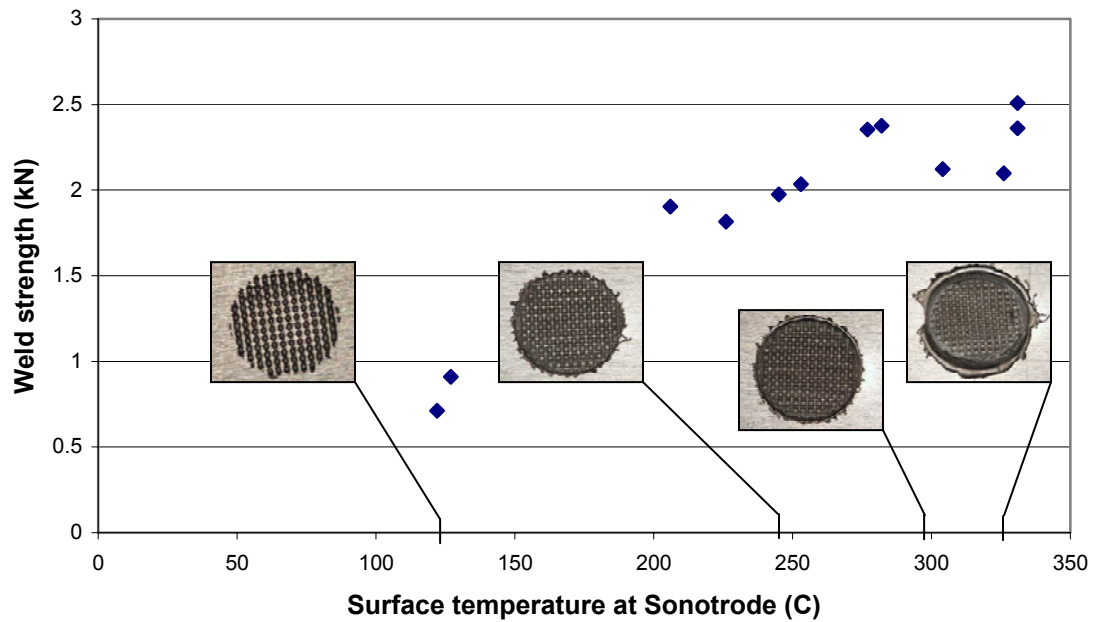
Figure 6.56: Weld strength vs. maximum temperatures at the sonotrode edge.

6.7.5 Examples of the correlation between temperature, weld strength and part dimensions

In these experiments the influence of the excitation force on surface temperatures, interface force and electrical power is examined for two extremes of part dimensions. The sonotrode force is limited by the material properties of the parts to be welded. If the sonotrode force exceeds a certain limit, extrusion and tip sticking (welding) are the consequences. This means if the excitation force is very high (i.e. exceeds the elastic limit of the material) the interface forces will decrease accordingly. This is already known from section 6.4. Here it will be examined how the temperature changes when the

top part is in anti-resonance compared to the temperatures that occur when the top part is small. This will also be a test if the temperatures measured at the sonotrode will be a generally valid quality indication. The results in the preceding section, lead to the conclusion that there is a correlation between surface temperatures and weld strength/quality. Another result from those experiments was that at a temperature above 300^0C extrusion and sonotrode welding occurs for the case of a small top part.

Two experiments were conducted; in the first the top part is small (i.e. its dimensions are below anti-resonant dimensions), while in the second the top part is in longitudinal anti-resonance. The same welding parameters were been used in both experiments, namely Power Level: 10, Matching: E, Weld time: 0.2s, Static pressure: 80psi (1600N). The two top part geometries were selected because in the first case the excitation force was negligible because of the small part mass, while in the second case the excitation force exceeded the limiting sonotrode force because of anti-resonance, thus causing extrusion and tip sticking. Anvil force and power were measured. The resulting welds were then been peeled to evaluate the quality (Here 'quality' meant that a nugget was peeled from the top piece by the bottom piece. This is contrast to pulling a nugget from the top part by the welding sonotrode.). The surface temperature of the top part at the sonotrode was measured with the IR camera.

The weld quality between the two welds differed considerably, as anticipated from Section 6.4. In the first experiment the weld peeled a nugget, in the second case the top part was welded to the sonotrode and extrusion consumed almost the entire thickness of the top part. The pictures in figure 6.57 show the resulting weld for the case of a small top part. As one can see, there was no extrusion and the weld peeled a nugget. The

181

pictures in figure 6.58 show the sample after welding at longitudinal anti-resonance of the top part. The sample was literally welded to the sonotrode, no weld strength was achieved and extrusion damaged the sample severely.
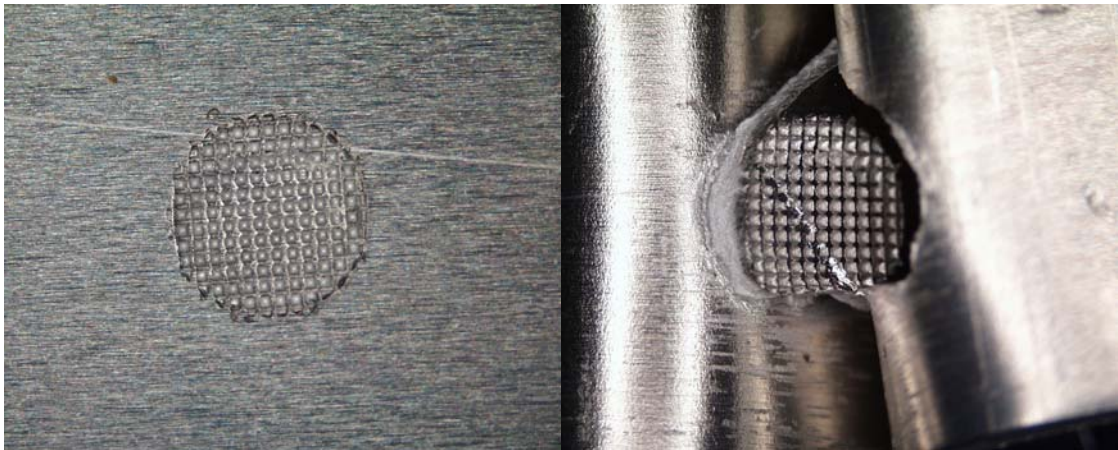
Figure 6.57: Sonotrode imprint and weld nugget for small top part weld.

Figure 6.58: Sonotrode welded to the top part and extrusion for anti-resonant top part weld.

This weld quality difference was anticipated since the sample dimensions were selected to produce one weld of good quality and one weld with maximum extrusion. In figure 6.59 the measured shear force at the anvil for both top part geometries is shown

and in figure 6.70 the power for both top part geometries. The anvil force is significantly

reduced for the anti-resonant top part, while the power is the same for the most part

during the weld. The power for the anti-resonant top part again shows a peak at the

beginning of the weld. The calculated energy was in both cases approx. 145J. These

results reconfirm those from section 6.4, again emphasizing that the electrical power or

energy can not be used to pick up this undesirable weld condition.
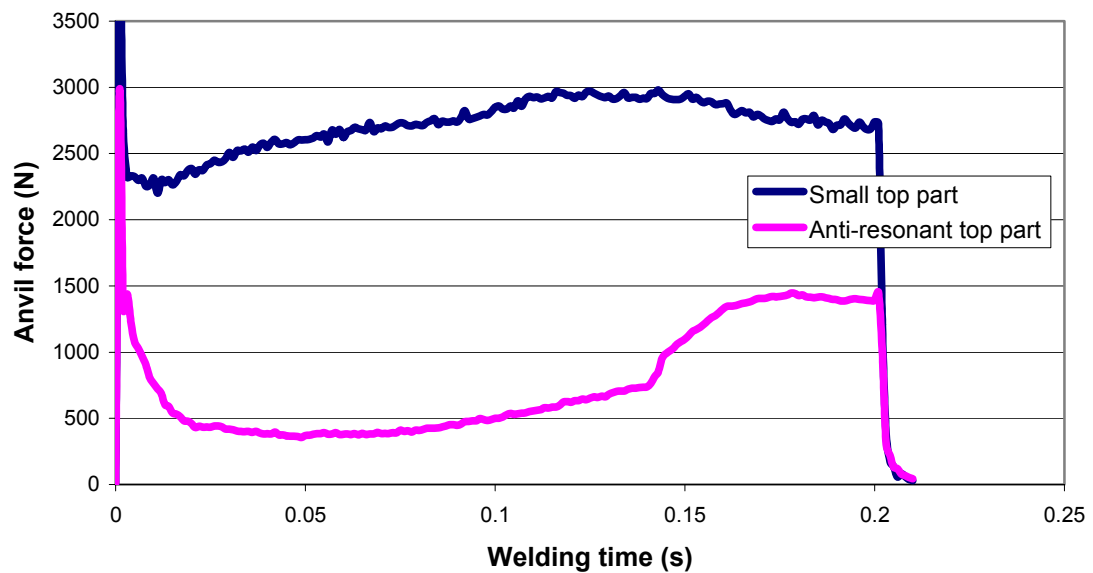
Figure 6.59: Anvil force for small and anti-resonance top part.
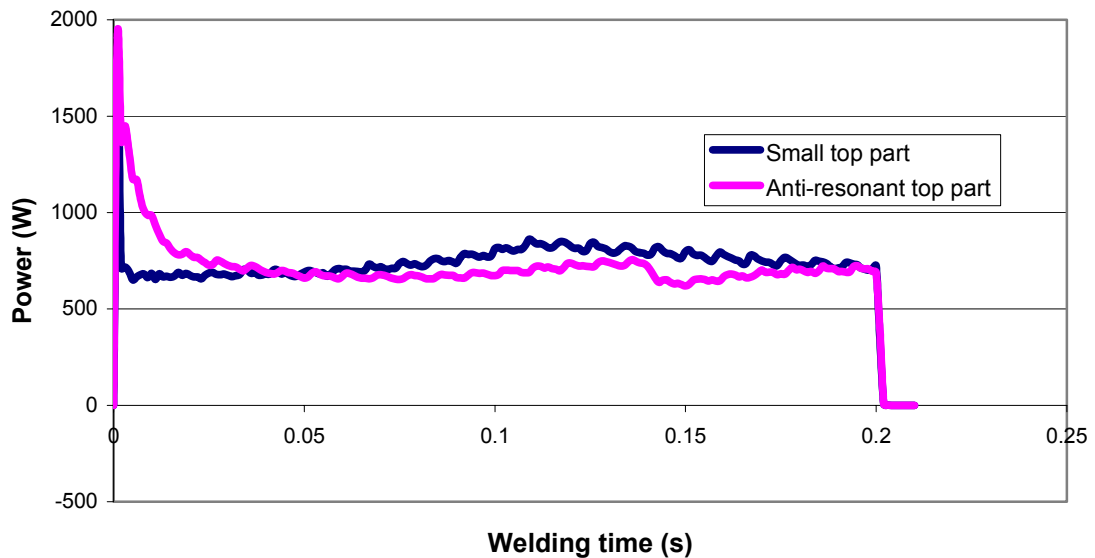
Figure 6.60: Power for small and anti-resonant top part.

The heat signatures from both welds are shown in figure 6.61. The temperature scale in both pictures is the same (76^0C-200^0C). On the left the heat signature for the small top part weld is shown, the highest temperature measured being 200^0C. On the right the heat signature of the anti-resonant weld is shown, the highest temperature measured here being 314^0C. These two welds show a very good, although negative, example that surface temperature cannot be used to predict weld quality. This means that the correlation suggested in figure 6.56 is not generally valid. The heat signature might still be useful in the detection of extrusion as suggested in the same figure.
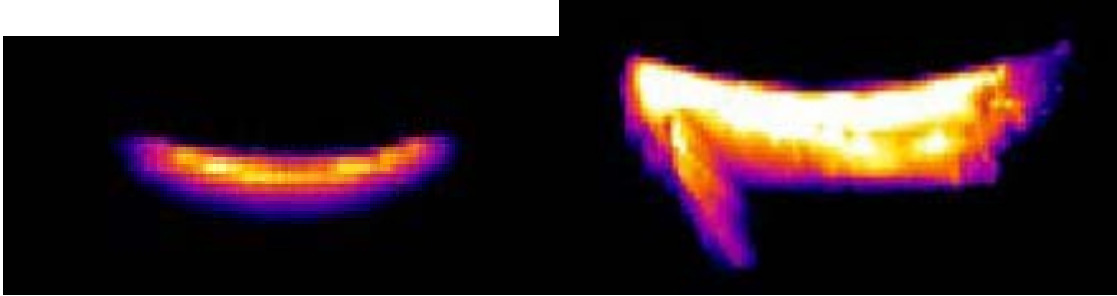
Figure 6.61: Heat signatures for small and anti-resonant top part.

In summary, for small top parts the correlation between temperature and weld strength showed that the higher the temperature the better the weld quality. In the case of arbitrary top part geometries (i.e. that it is unknown what the excitation forces will be), it was shown that this correlation is not valid. This means that the top part temperature is not suitable for predicting weld strength in a general sense, although it might be possible to detect the start of extrusion.

6.8 Temperatures and shear forces based on the Mechanics Model of USMW

At this point now, all the essential components of the mechanical model developed in sections 4.1-4.3 have been confirmed. The initial time period for tip penetration was found to be very small (section 6.1). The normal stress under the sonotrode was found to be uniform a very short distance beneath the knurl (section 6.2). The validity of equation 4-11, which predicts the interface force in case of top part anti-resonance (section 6.4) was shown. A strong influence of the friction force on the interface forces was confirmed (section 6.5) and the temperatures have been measured during welding (6.7). In this section the temperatures that occur during welding will be numerically modeled using finite element analysis and the heat flux equations developed in section 4.4. The only experimental data as input into these heat fluxes is the time dependent weld area growth function and the shear speed. From these calculated temperatures the shear forces during welding will be calculated, using equations form section 4.1-4.3 and undesirable weld conditions can be predicted.

6.8.1 Heat flux boundary for the weld area

In this section the boundary condition for the weld area is developed (equation 4-30). The boundary condition is quite complex and relating as it does the temperature dependent yield strength, the time dependent weld area, the normal force and the

186

deformation velocity at the interface. Nevertheless it will be found possible to satisfactorily approximate these conditions in a manner that still will permit analysis. For simplicity a linear approximation can be used for the temperature dependent yield strength [69], as shown in figure 6.62. The approximated linear function for the yield strength is:

$$Y(T) \approx \left(-0.649 * T/°C + 326.5\right) * 10^6 * Pa \hspace{4cm} \text{(Eq.6.3)}$$
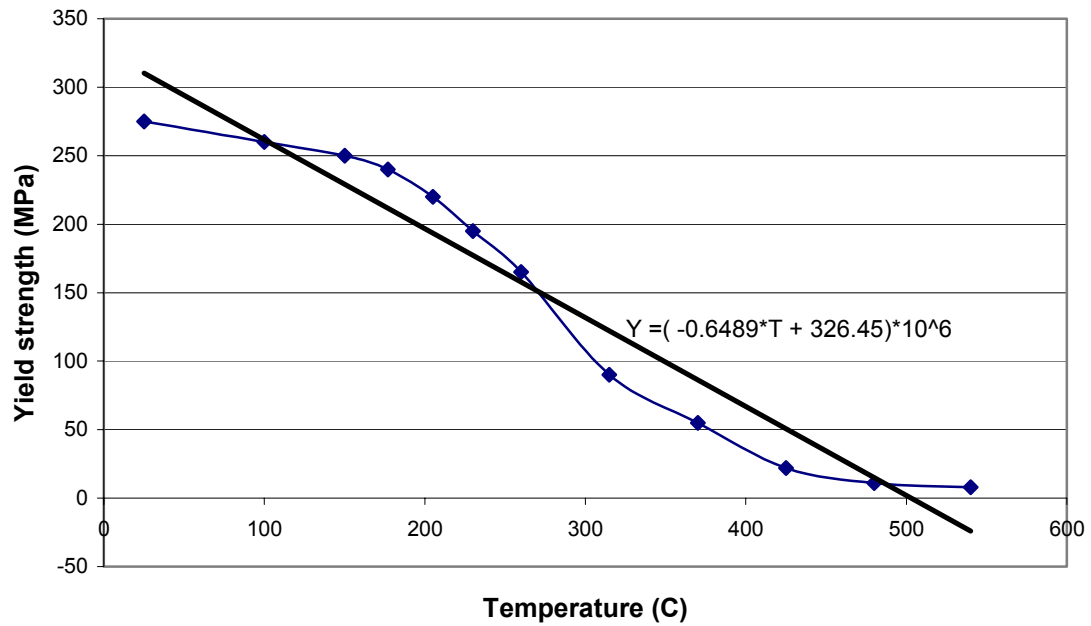
Figure 6.62: Linear approximation of the temperature dependent yield strength.

The temperature development will be modeled for three different welding conditions, having the parameters given in table 6 (Note that Condition 2 involves a lubricated interface). The welding conditions are:

- Condition 1: Low normal force, high friction

- Condition 2: High normal force, low friction

- Condition 3: High normal force, high friction

Welds of differing weld times were made and tested for strength, with the results shown in figure 6.63.

	F_N	Power level	Matching	Surface	Max. strength
Condition 1	700N	10	F	Clean	2374N
Condition 2	2000N	10	L	Lubricated	2707N
Condition 3	2000N	10	L	Clean	2495N

Table 6: Welding conditions.
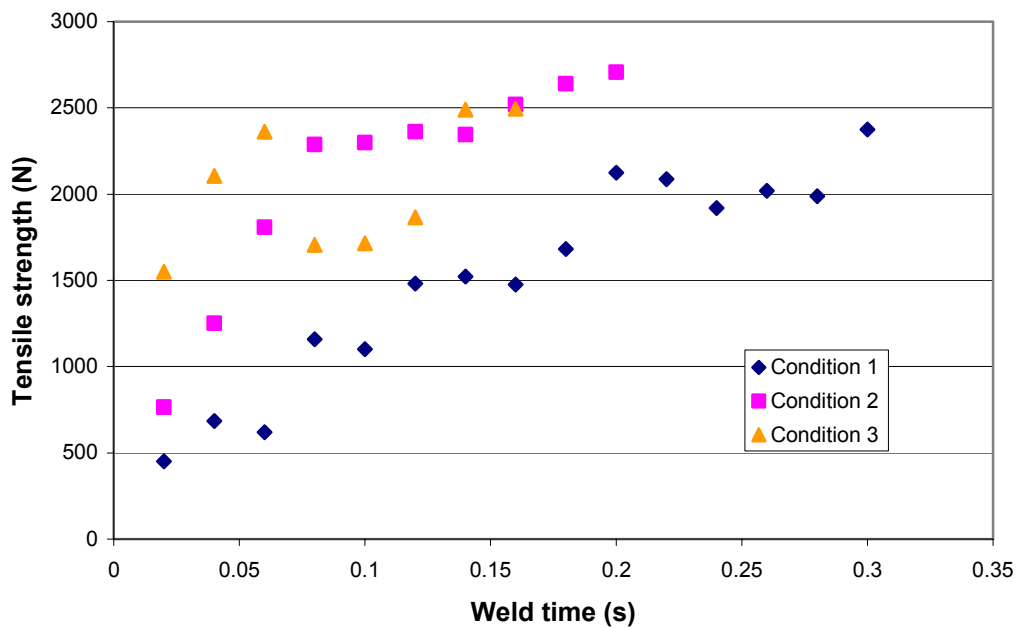
Figure 6.63: Weld strength versus weld time for the three welding conditions.

It can be seen from figure 6.63 that for the clean samples welded at high pressure (Condition 3) the weld strength increases rapidly at the beginning. This condition is not very stable as the variation in strength values shows. The weld strength for the lubricated samples welded at high pressure (Condition 2) increases more slowly, but the achieved weld strength values appear more consistent. At lower pressures the weld strength increases very slowly.

The strongest welds in this experiment peeled a nugget in the tensile test and the area of the nugget was equal to the sonotrode area (A_S=20mm^2). The experiments were stopped at different times, because extrusion and sticking sometimes became severe at different times for the different welding conditions.

Knowing how weld strength increases with time, from figure 6.63, can permit us to find how the weld area also changes with time. To find the function for the weld area growth, all weld strength values (TS) of figure 6.63 were used to obtain weld area values. This was done by normalizing all the strength values by dividing through the maximum weld strength and then multiplying by the maximum weld area, the following equation being used:.

$$A_W = \frac{TS}{2700N} * 20mm^2$$

(Eq. 6-4)

The proportionality of weld area to weld strength has been noted in prior studies [21]. We now can indicate how the weld area varies with time, as shown in figure 6.64.

Exponential approximations of the following form turn out to be good representations of the weld area growth functions.

$$A_W(t) = 20mm^2 * \left(1 - e^{\frac{k*t}{\sec}}\right)$$

(Eq. 6-5)

Where: k: constant to be determined from figure 6.64

The different values for k are then given in table 7.
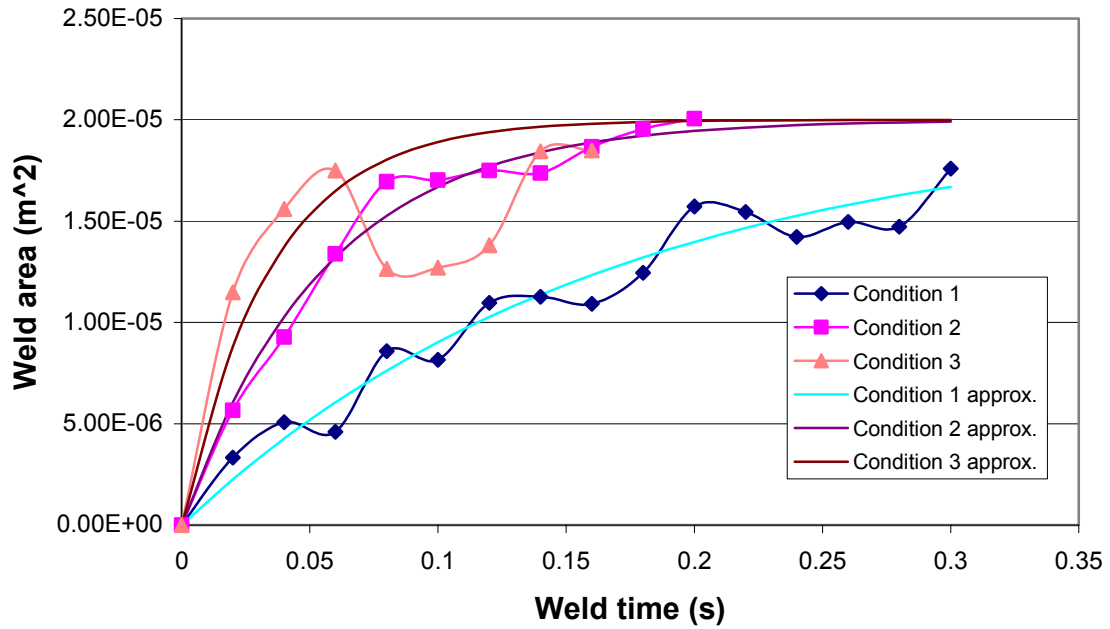
Figure 6.64: The weld area vs. weld time and the respective analytical weld area approximaions.

	Approximating function for weld area growth
Condition 1 (clean, low force)	$A_W(t) = 2\left(1 - e^{-6t/\sec}\right)*10^{-5}*m^2$
Condition 2 (lub, high force)	$A_W(t) = 2\left(1 - e^{-18t/\sec}\right)*10^{-5}*m^2$
Condition 3 (clean high force)	$A_W(t) = 2\left(1 - e^{-29t/\sec}\right)*10^{-5}*m^2$
	k
Condition 1 (clean, low force)	-6
Condition 2 (lub, high force)	-18
Condition 3 (clean high force)	-29

Table 7: Approximating functions for weld area growth.

The vibration amplitude was also measured for the three weld conditions, with the result shown in figure 6.65. It is seen that the vibration amplitude rises very quickly and reaches a relatively constant level. This constant level was then used to calculate the average velocities of figure 6.65 with equation 4-25. They are given in Table 8.
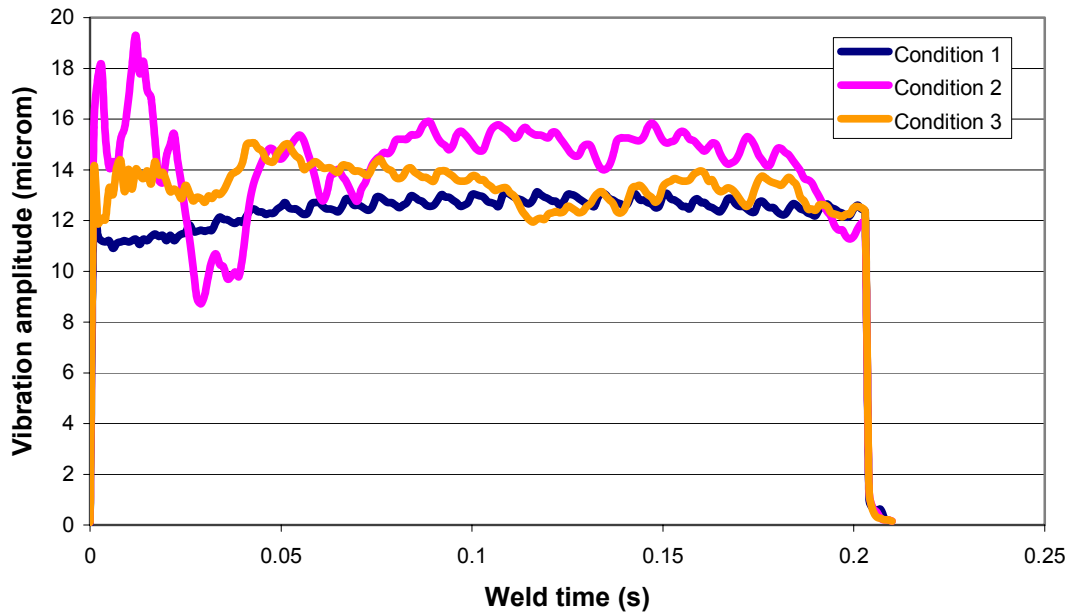
Figure 6.65: Measured vibration amplitudes for the three welding conditions.

	Average speed
Condition 1 (clean, low force)	$v_{avg} = 4*13*10^{-6}m*20000Hz = 1.04\,m/\mathrm{sec}$
Condition 2 (lub, high force)	$v_{avg} = 4*15*10^{-6}m*20000Hz = 1.2\,m/\mathrm{sec}$
Condition 3 (clean high force)	$v_{avg} = 4*13*10^{-6}m*20000Hz = 1.04\,m/\mathrm{sec}$

Table 8: Average sonotrode speed for the three parameter sets.

The sonotrode reaches the average speed within a few cycles, but at the interface it will take some time for the amplitude to reach its full value, since there is a start up period of approximately 10ms, in which the sonotrode knurls engage into the top part surface. Here it is most useful to use an exponential approximation of the form

$$v_{avg}(t) = v_{avg} * \left(1 - e^{\frac{j*t}{sec}}\right)$$

(Eq. 6-6)

Where: j: constant to be determined from the duration of the start up period

In this case the start up period is 10ms, for this time l=-500 gives a good approximation for the interface velocity, as shown in figure 6.66. Equation 6-5 and 6-6 are very similar in nature and their main advantage is that at t=0s the value of the function is zero and positive for all positive times. For the numerical simulation this is very important, because all terms in the heat flux equation must be positive at all times. The functions for the velocity shown in figure 6.66 are given in table 9.
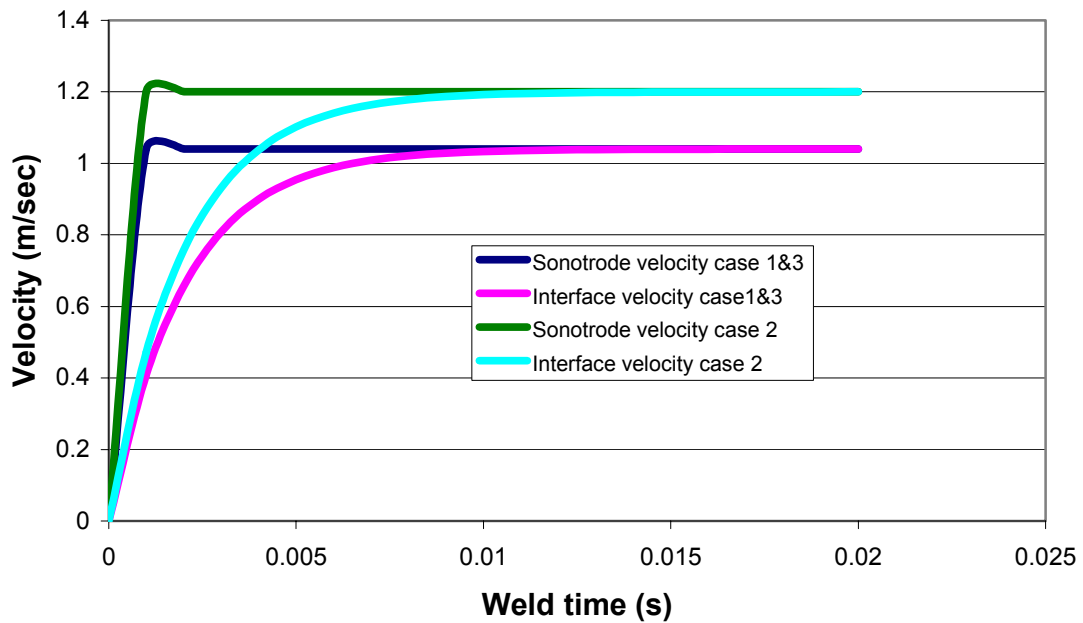
Figure 6.66: Approximation functions for the average vibration speed at the weld interface.

Conditions 1&3	$v_{avg}(t) = 1.04\left(1 - e^{-500t/\text{sec}}\right) * \dfrac{m}{\text{sec}}$
Condition 2	$v_{avg}(t) = 1.2\left(1 - e^{-500t/\text{sec}}\right) * \dfrac{m}{\text{sec}}$

Table 9: Approximation functions for the interface velocities.

One can now write down equation 4-15, with the necessary approximation functions, for the three different conditions. This gives the welding force as a function of temperature, normal force and weld area. When the weld area growth term is replaced by equation 6-6 the function for the weld force is:

$$F_W(T, F_N, t) = \sqrt{\left(\frac{Y(T)}{2}\right)^2 - \left(\frac{F_N / A_{DZ}}{2}\right)^2} * 20mm^2 * \left(1 - e^{\frac{k*t}{\text{sec}}}\right) \qquad \text{(Eq. 6-7)}$$

The approximation functions and constants for 6-7 are given in table 10. And the resulting equations for the different welding conditions are then written out. (equations 6-8 to 6-10).

	Y(T)	F_N	A_{DZ}	k
Condition 1 (clean, low force)	$\left(-0.649 * T/^{\circ}C + 326.5\right) * 10^6 * Pa$	700N	20mm^2	-6
Condition 2 (lub, high force)	$\left(-0.649 * T/^{\circ}C + 326.5\right) * 10^6 * Pa$	2000N	20mm^2	-18
Condition 3 (clean high force)	$\left(-0.649 * T/^{\circ}C + 326.5\right) * 10^6 * Pa$	2000N	20mm^2	-29

Table 10: Approximations for the weld force functions.

Condition 1:

$$F_W(T,F_N,t)=\sqrt{\left(\frac{(-0.649*T/{}^{\circ}C+326.5)*10^6*Pa}{2}\right)^2-\left(\frac{700N/20*10^{-6}m^2}{2}\right)^2}*2\left(1-e^{-6t/sec}\right)*10^{-5}*m^2$$

(Eq.6-8)

Condition 2:

$$F_W(T,F_N,t)=\sqrt{\left(\frac{(-0.649*T/{}^{\circ}C+326.5)*10^6*Pa}{2}\right)^2-\left(\frac{2000N/20*10^{-6}m^2}{2}\right)^2}*2\left(1-e^{-18t/sec}\right)*10^{-5}*m^2$$

(Eq. 6-9)

Condition 3:

$$F_W(T,F_N,t)=\sqrt{\left(\frac{(-0.649*T/{}^{\circ}C+326.5)*10^6*Pa}{2}\right)^2-\left(\frac{2000N/20*10^{-6}m^2}{2}\right)^2}*2\left(1-e^{-29t/sec}\right)*10^{-5}*m^2$$

(Eq. 6-10)

Furthermore one can write down the heat flux over the entire weld area, which is in this case equal to the sonotrode area, recalling equation 4-29 and replacing the average velocity term by the approximation function for the interface velocity, one gets:

$$\dot{q}_W = \frac{F_W(T,F_N,t)}{A_{DZ}}*v_{avg}*\left(1-e^{\frac{j*t}{sec}}\right)$$

(Eq.6-11)

The welding force is given by equations 6-8 to 6-10, the other constants are given in table 11. The resulting heat flux approximation functions are then given by equations 6-12 to 6-14.

	A_{DZ}	v_{avg}	j
Condition 1 (clean, low force)	20mm^2	1.04m/s	-500
Condition 2 (lub, high force)	20mm^2	1.2m/s	-500
Condition 3 (clean high force)	20mm^2	1.04m/s	-500

Table 11: Weld heat flux approximations.

Condition 1:

$$\dot{q}_W = \sqrt{\left(\frac{(-0.649 * T/^{\circ}C + 326.5)*10^6 * Pa}{2}\right)^2 - \left(\frac{35*10^6 \, Pa}{2}\right)^2} * \left(1 - e^{-6t/\sec}\right) * 1.04\left(1 - e^{-500t/\sec}\right) * {}^m\!/_{\sec}$$

(Eq. 6-12)

Condition 2:

$$\dot{q}_W = \sqrt{\left(\frac{(-0.649 * T/^{\circ}C + 326.5)*10^6 * Pa}{2}\right)^2 - \left(\frac{100*10^6 \, Pa}{2}\right)^2} * \left(1 - e^{-18t/\sec}\right) * 1.2\left(1 - e^{-500t/\sec}\right) * {}^m\!/_{\sec}$$

(Eq. 6-13)

Condition 3:

$$\dot{q}_W = \sqrt{\left(\frac{(-0.649 * T/^{\circ}C + 326.5)*10^6 * Pa}{2}\right)^2 - \left(\frac{100*10^6 \, Pa}{2}\right)^2} * \left(1 - e^{-29t/\sec}\right) * 1.04\left(1 - e^{-500t/\sec}\right) * {}^m\!/_{\sec}$$

(Eq. 6-14)

The units for the above do, in fact, reduce to those for a heat flux. Thus,

$$\dot{q}_W = \frac{\sqrt{\left(\frac{N}{m^2}\right)^2 - \left(\frac{N}{m^2}\right)^2}}{m^2} * m^2 * \frac{m}{\sec} = \frac{\frac{N}{m^2} * m^2 * \frac{m}{\sec}}{m^2} = \frac{Nm}{m^2 * \sec} = \frac{Watt}{m^2}$$

The equations given here can only be used to simulate the average temperature across the interface or at the sonotrode. This is because the heat flux is calculated for the entire weld area (A_{DZ}) (see section 4.4 for the derivation) for all times. In reality the heat flux is only applied at areas at which deformation takes place (i.e. the deformation islands). This level of detail and complexity is beyond the scope of what has been attempted here.

6.8.2 Heat flux for the friction area

The friction area has been determined in section 6.3.2 for 1mm thick sheets. It has twice the radius then the deformation zone area. Since the heat input through friction takes only place outside the weld area, the friction area is given by:

$$A_{Fr} = (0.005m)^2 * \pi - (0.0025m)^2 * \pi \approx 60 * 10^{-6} m^2 \qquad \text{(Eq. 6-15)}$$

Now, we have previously given the basic equation for the heat flux from the friction area as equation 4-32 (replacing the velocity term by the approximation given by equation 6-6):

$$\dot{q}_{FR} = \frac{\mu_S * F_N}{A_{FR}} * v_{avg} * \left(1 - e^{\frac{j*t}{\sec}}\right) \qquad \text{(Eq. 6-16)}$$

With the static friction coefficient as given in figure 5.12, the friction area given by equation 6-15 and the average velocity for each individual welding condition, one can write the heat flux equations for the three welding conditions (equations 6-17 to 6-19)

Condition 1:

$$\dot{q}_{FR} = \frac{0.53 * 700N * 1.04\left(1 - e^{-500t/\sec}\right) * m\big/\sec}{60 * 10^{-6} m^2} \approx 6.4\left(1 - e^{-500t/\sec}\right) * 10^6 \frac{Watt}{m^2} \quad \text{(Eq. 6-17)}$$

Condition 2:

$$\dot{q}_{FR} = \frac{0.28 * 2000N * 1.2\left(1 - e^{-500t/\sec}\right) * m\big/\sec}{60 * 10^{-6} m^2} \approx 11.2\left(1 - e^{-500t/\sec}\right) * 10^6 \frac{Watt}{m^2} \quad \text{(Eq. 6-18)}$$

Condition 3:

$$\dot{q}_{FR} = \frac{0.53 * 2000N * 1.04\left(1 - e^{-500t/\sec}\right) * m\big/\sec}{60 * 10^{-6} m^2} \approx 18.3\left(1 - e^{-500t/\sec}\right) * 10^6 \frac{Watt}{m^2} \quad \text{(Eq. 6-19)}$$

All the heat fluxes as required from figure 4.20 are now known and one can apply them to the FEM model, with geometries given in the same figure (figure 4.20 shown here as figure 6.67).
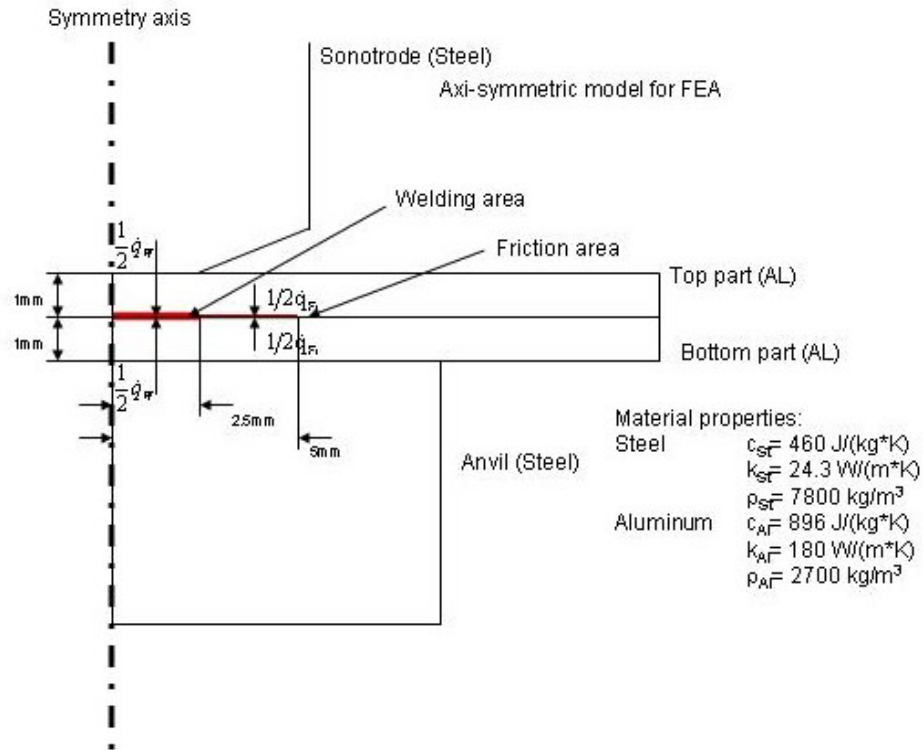
Figure 6.67: Dimensions for heat conduction model.

6.8.3 Predictions of Weld Temperatures

To model the heat flow in an ultrasonic weld, the FEA program ANSYS was used with the geometries and boundary conditions given in figure 6.67 and equations 6-12 to 6-14 and equations 6-17 to 6-19. In figure 6.68 the areas where the weld and the friction heat fluxes are applied on a contour plot are depicted as thicker lines.

199
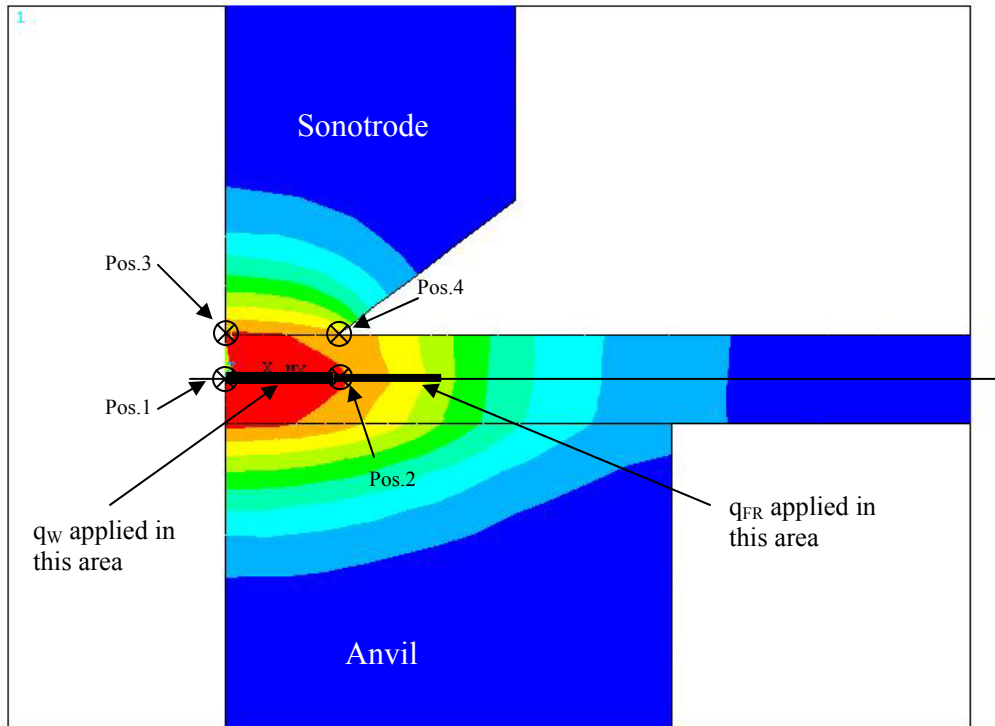
Figure 6.68: Typical contour plot obtained by the FEA after 0.5s.

It is seen that the highest temperature in this particular plot (Condition 3 after 0.5s) is approximately 350^{0}C at position 1. Of interest here are the temperatures predicted at the weld interface and the sonotrode top part interface as a function of time. These have been plotted at positions 1-4 in figures 6.69 to 6.74. In addition to the temperatures at the selected positions, the average temperatures, as a function of time over the weld area, and under the sonotrode, have been calculated based on the Position 1 and 2 data (for the weld) and Position 3 and 4 data (for the sonotrode) using:

$$T(weld\_area) = (T(pos.1) + T(pos.2))/2$$
$$T(sonotrode\_area) = (T(Pos.3) + T(Pos.4))/2$$

(Eq. 6-20)

To be able to compare the weld and sonotrode area temperatures for the three weld conditions, the average temperatures are shown in figure 6.75 and 6.76.
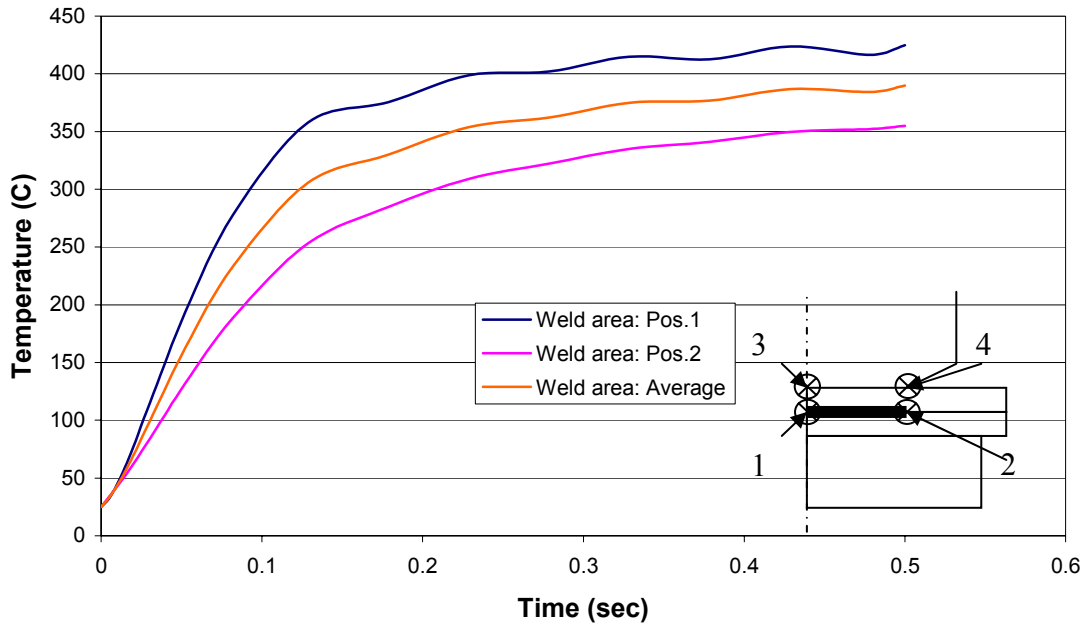
Figure 6.69: Predicted weld area temperatures for weld condition 1.
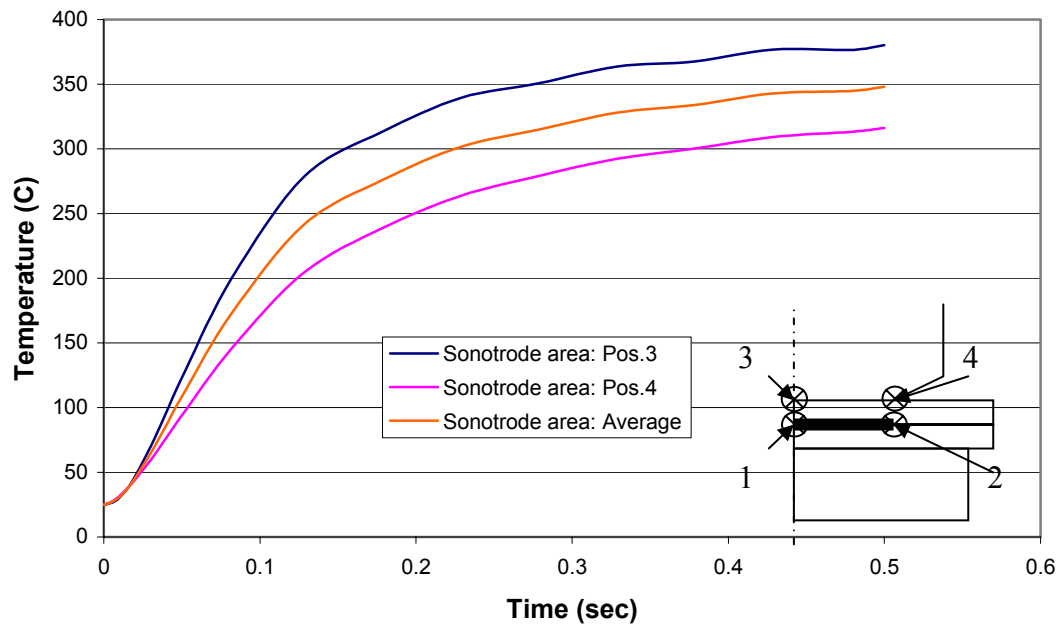
Figure 6.70: Predicted sonotrode area temperatures for weld condition 1.
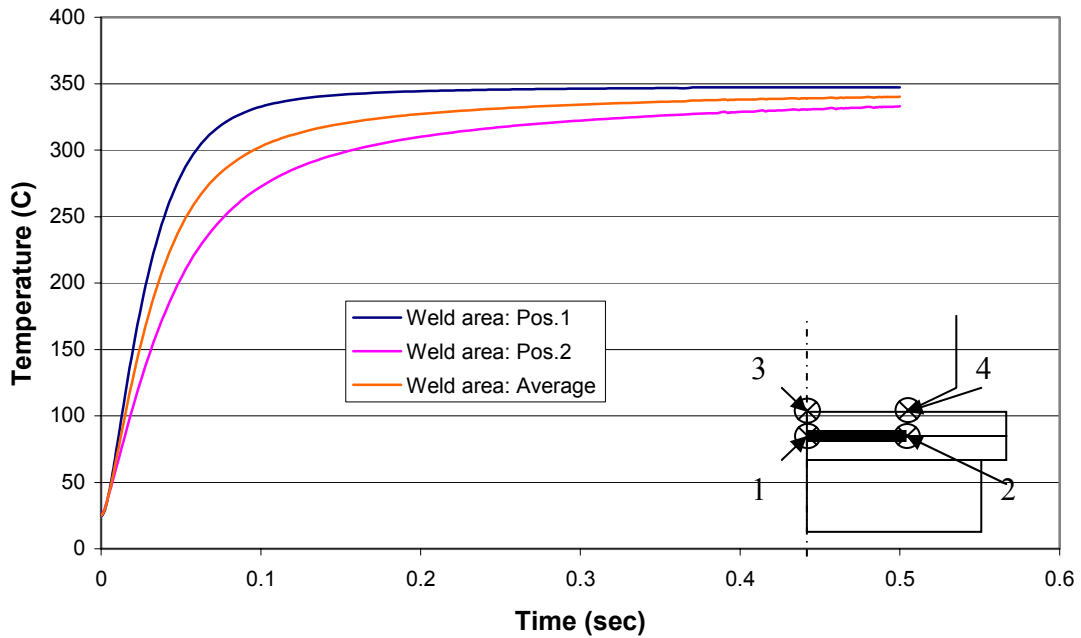
Figure 6.71: Predicted weld area temperatures for weld condition 2.

202
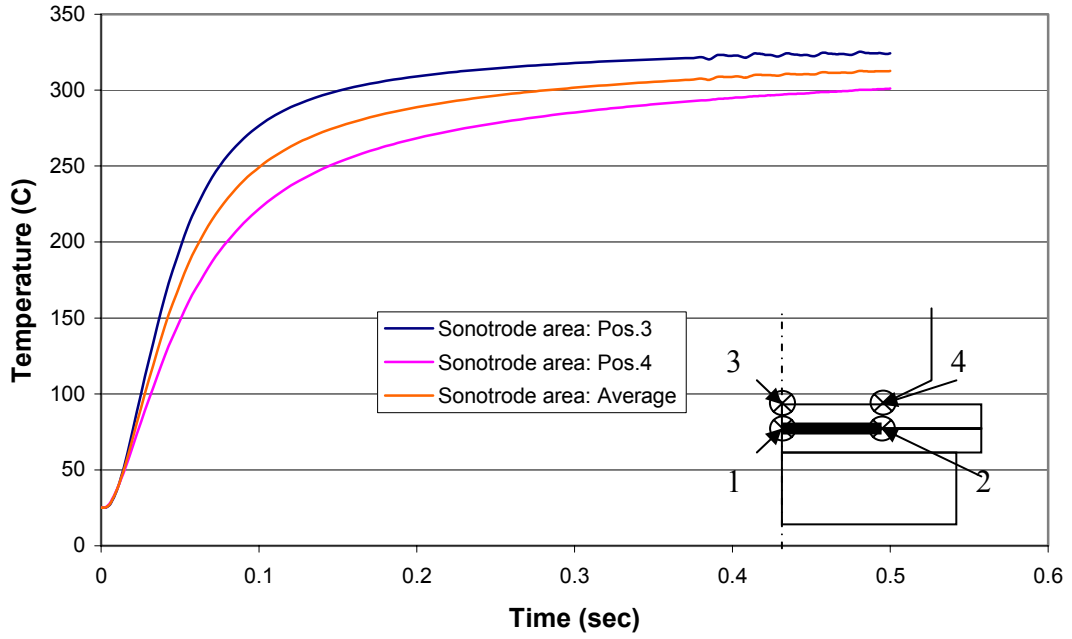
Figure 6.72: Predicted sonotrode area temperatures for weld condition 2.
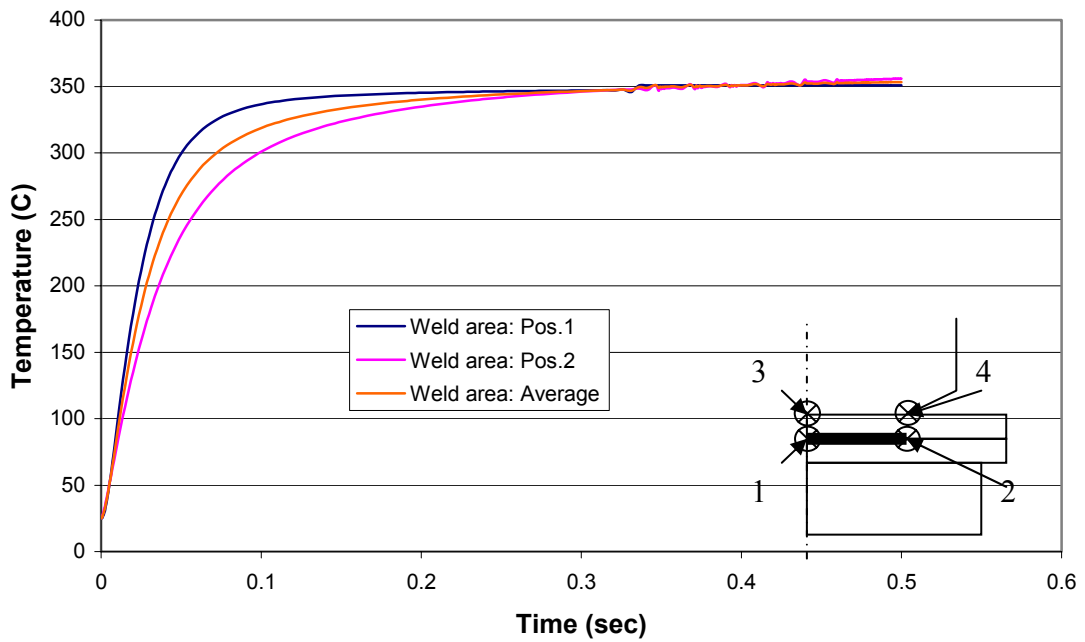
Figure 6.73: Predicted weld area temperatures for weld condition 3.

203
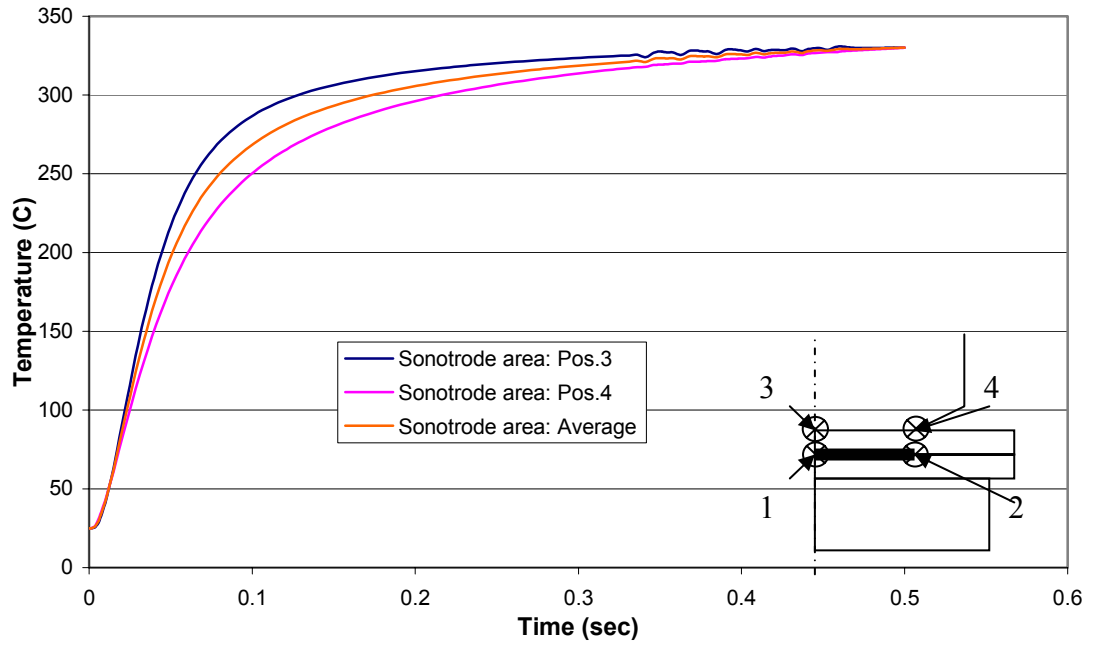
Figure 6.74: Predicted sonotrode area temperatures for weld condition 3.
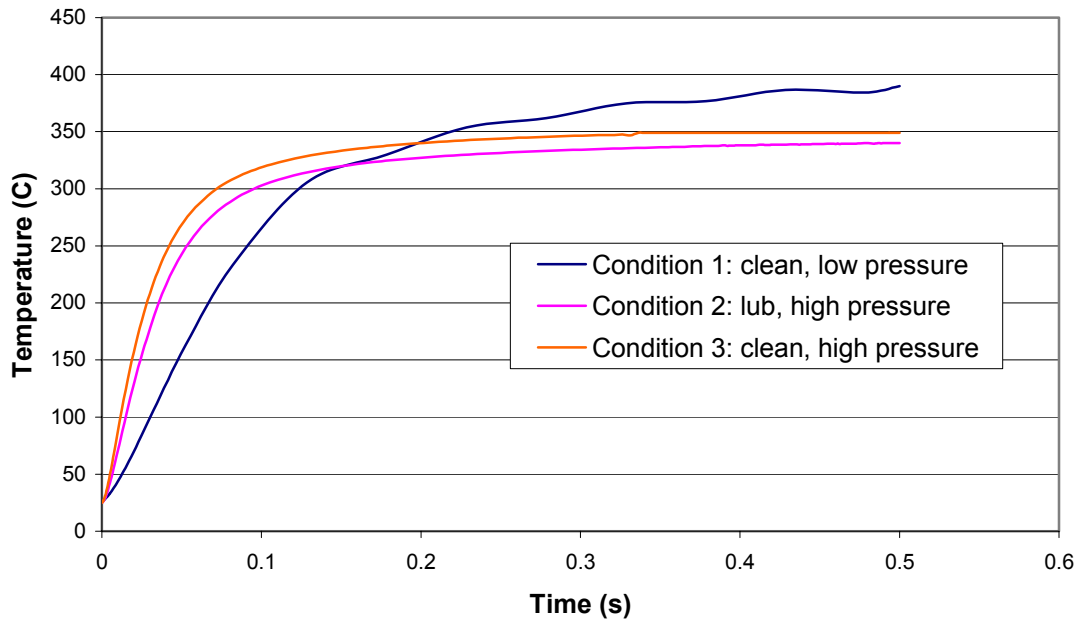
Figure 6.75: Average weld area temperatures predictions for the different weld conditions.
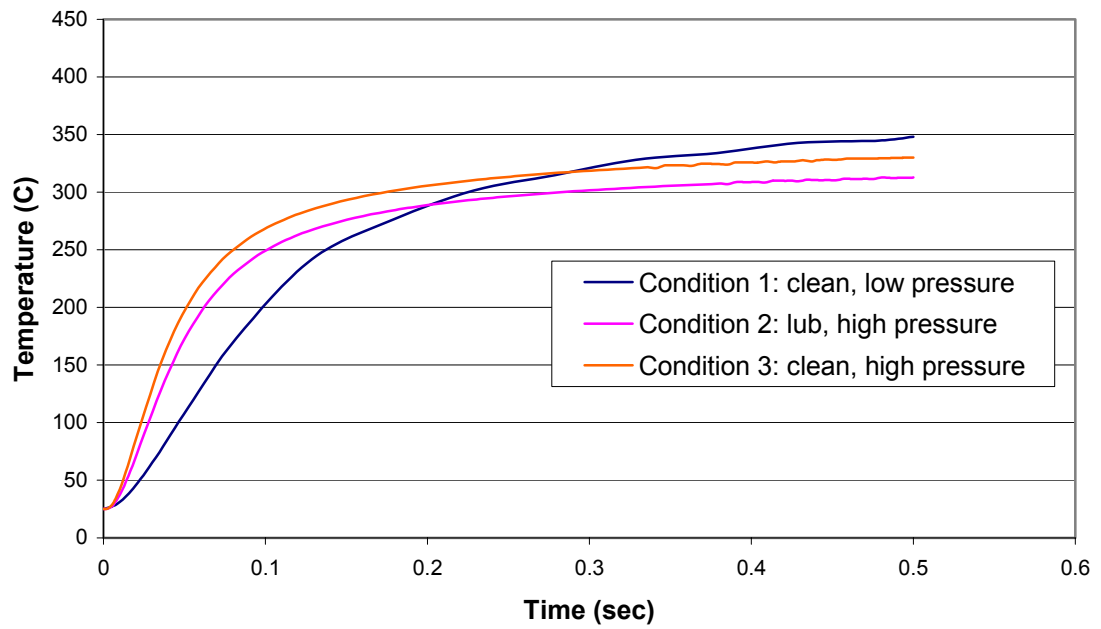
Figure 6.76: Average sonotrode area temperature predictions for the different weld conditions.

205

It can be seen from figures 6.75 and 6.76 that the temperatures at the deformation zone and the sonotrode area increase very rapidly. The temperatures from welding condition 1 (low force, high friction) increase the slowest, but it exceed the temperatures for the other welding conditions (Condition 2: high pressure, low friction, Condition 3: high pressure, low friction) and ultimately reaches the highest value. It is believed that the reason for this is that at equal temperatures the welding forces would be higher for a lower normal force, and therefore have a higher heat input at the deformation zone. This would then lead to elevation in temperature. The temperatures calculated for condition 2 and 3 increase very rapidly at the beginning of the weld cycle. The temperature increase for condition 2 is approximately 200^0C in 0.03 sec and for condition 3, 200^0C in 0.04sec. This rapid temperature increase is good agreement with the temperature increase measured experimentally (200^0C in 0.04sec, figure 6.53). It must be noted that the interface velocity for condition 2 was higher then for condition 3. This would mean that, everything else being equal, one would expect a higher final temperature for weld condition 2, but as figure 6.75 shows the opposite is the case. This can only mean that the higher temperature predicted for condition 3 must be the result of the higher heat input due to the difference in friction between the two sheets (condition 2: low friction, condition 3: high friction). This reconfirms the relatively low importance of the elastic shear strain found in section 4.5 (it was found there that the heat input was dominated by the weld area growth at the beginning of the weld cycle and by the temperature at elevated temperatures).

One can see from the figures above, that the model predicted successfully a higher weld temperature at reduced normal force [47]. Secondly the predicted steady state temperatures are in a range of 350- 430^{0}C (see section 3.3, table 1), again, the results are in very good agreement with temperatures measured by previous researchers.

At this point it is necessary to point out that the temperatures calculated are in fact very high and that the yield strength of the material is relatively low throughout the bulk of the material. In this particular study a flat face sonotrode is used, so that the compressive stress at the interface is uniform and the plastic deformation takes place only within a thin layer at the interface. Nevertheless, a spherical sonotrode would produce a significantly different compressive stress state with stress singularities if superimposed by a tangential force component [24]. This could then, without doubt, lead to plastic deformation deep into the bulk of the material.

6.8.4 Comparison of model results with force measurements

In this section the interface forces will be calculated that occur during welding. Up to now, the temperatures that occur during welding were "unknown" essentially only available by measurements. In the previous section though, the temperatures have been computed, so that they are no longer "unknown.

With the temperatures given in figure 6.75 and equations 6-8 to 6-10 the welding forces ($F_W(T,F_N,t)$) can be calculated. The results are shown in figure 6.77. It can be seen in this figure, that for condition 1 the force rises slowly and reaches a peak and then decreases very slowly. The welding forces for condition 2 and 3 reach peaks after a very

207

short period of time and then decrease with different decay rates (welding force for condition 3 decreases the fastest). It is very important to note here that even though for condition 1 the highest temperatures were predicted towards the end of the simulated time, that the weld forces are in fact the highest for this condition. This behavior is the result of the decreased compressive stress and the thereby changed yield condition. For the two other conditions (both have high normal forces). The welding force behaves like one would expect that for the weld condition with the higher temperature (condition 3) - the weld forces are reduced towards the end of the simulated time period.
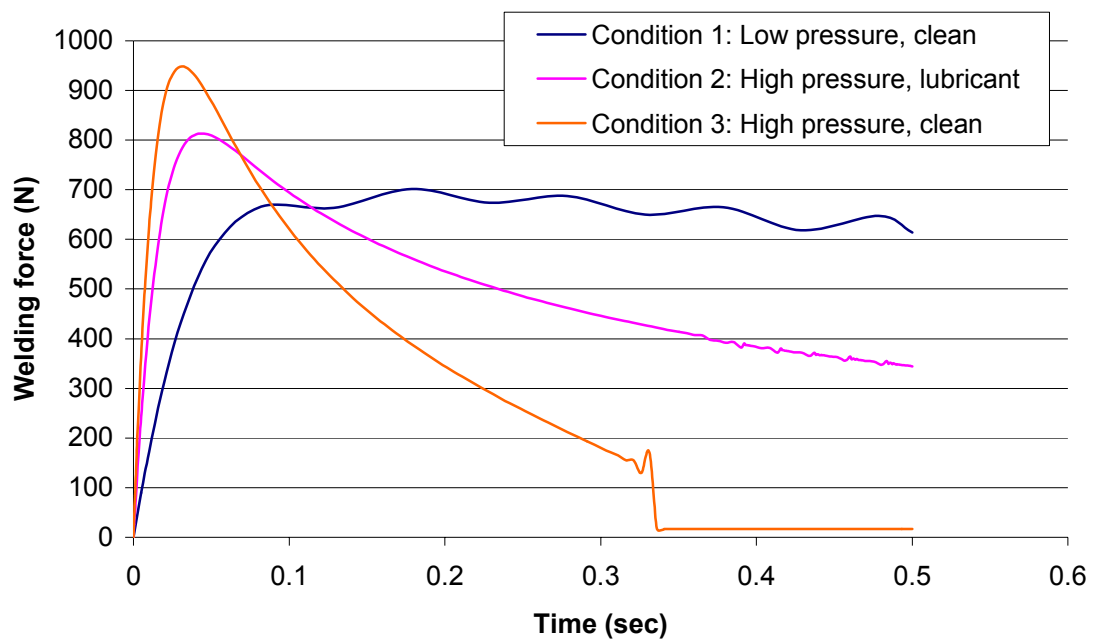
Figure 6.77: The welding forces for the different welding conditions.

At this point now one needs to recall condition 4-19. In this case the F_{AM} can be assumed small, because in the experiments small parts well below any anti-resonance condition have been used. The term $m*d^2\xi_{max}/dt^2$ is small as well, so we have

$$F_W + F_{FR} \leq \sqrt{\left(\frac{Y(T)}{2}\right)^2 - \left(\frac{F_N/A_S}{2}\right)^2} * A_S \qquad \text{(Eq. 6-21)}$$

In this equation the l.h.s. is the interface force during welding, comprised of the welding force (figure6.77) and the friction force (equation 4-17 with the friction coefficient for the corresponding surface condition, i.e. lubricated $\mu_S=0.28$, clean $\mu_S=0.53$) and the r.h.s. is the maximum sonotrode force. This is as well the maximum shear force that can occur during welding, because this is the value at which yielding occurs during welding. In figures 6.78 to 6.80 the interface forces and the maximum sonotrode forces are calculated with the temperatures that resulted from the numerical simulation. The intersection of the two curves in the graphs indicates the point in time, when condition 6-21 becomes equality. This means at that point in time yielding will occur at the sonotrode and the maximum shear force will be governed by the maximum sonotrode force. This condition is predicted for different welding times for the different welding conditions:

Condition 1 (clean, low pressure): 0.4s

Condition 2 (lubricated, high pressure): 0.12s

Condition 3 (clean high pressure): 0.04s

209
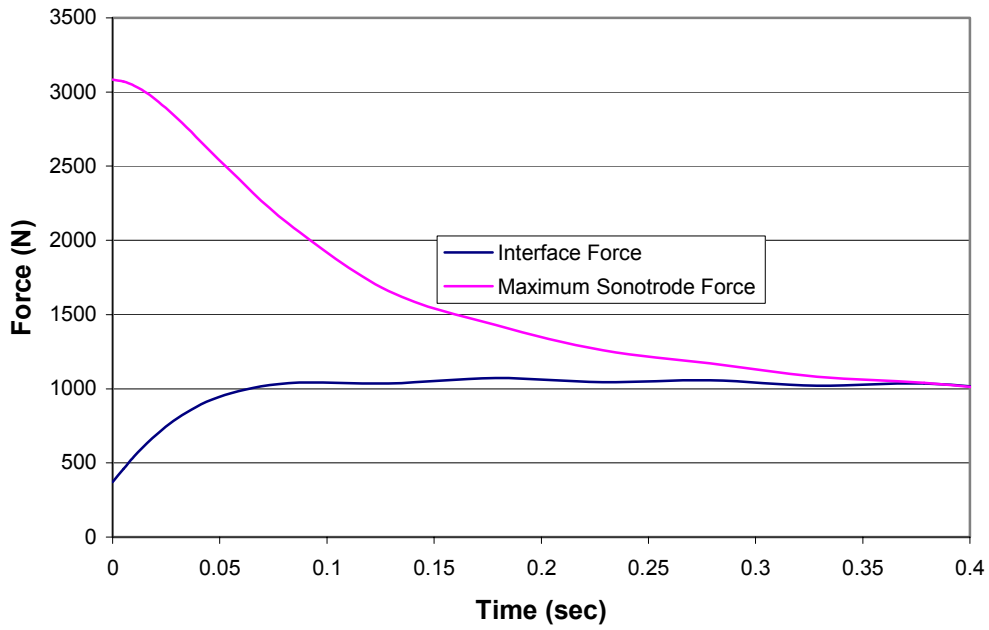
Figure 6.78: Calculated sonotrode and interface forces for welding condition 1.
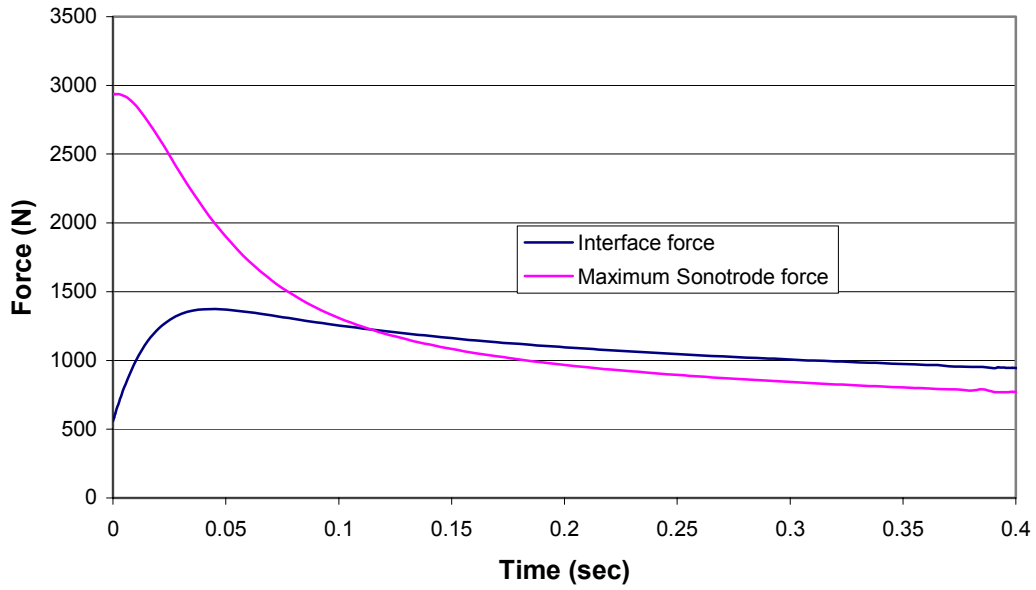
Figure 6.79: Calculated sonotrode and interface forces for welding condition 2.

210
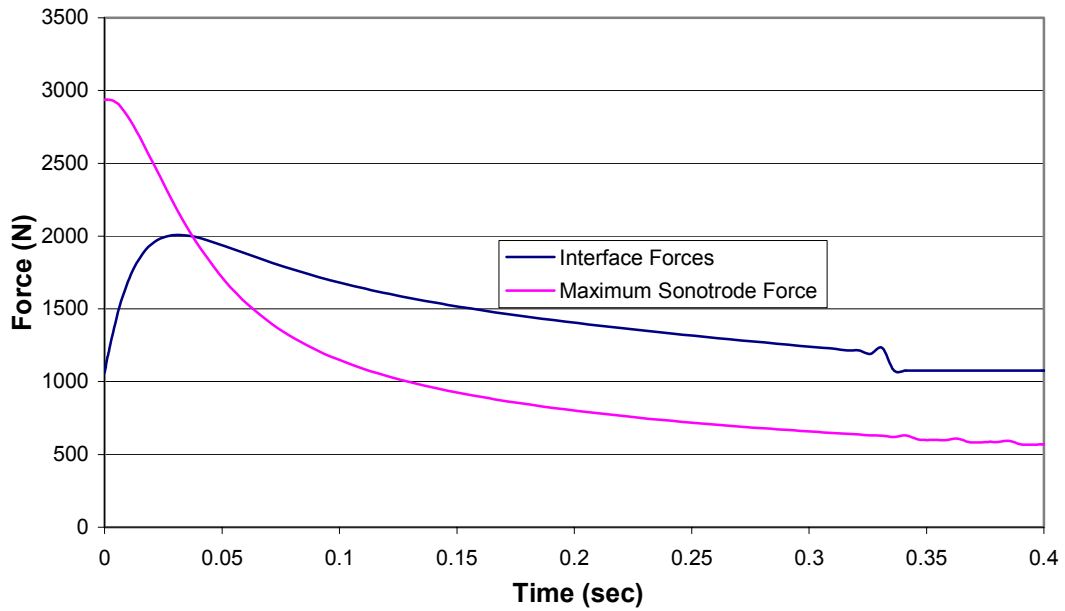
Figure 6.80: Calculated sonotrode and interface forces for welding condition 3.

In order to compare the measured anvil force with the calculated forces, equation 6-21 has been applied to figures 6.78 to 6.80, the results for each weld condition are shown in figure 6.81. The measured shear forces are shown in figure 6.82.

211
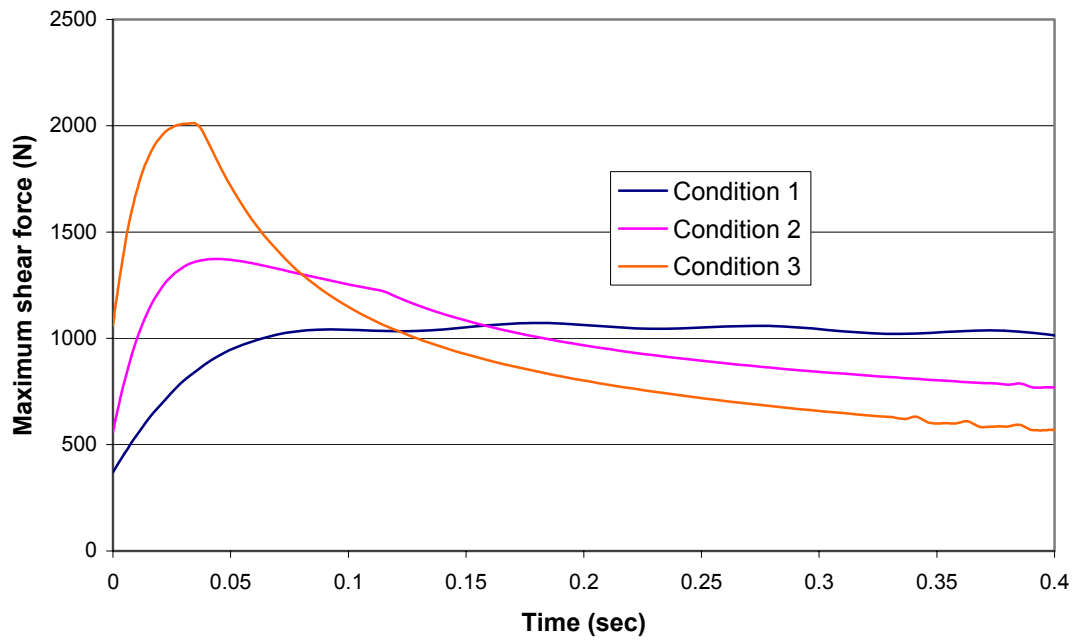
Figure 6.81: Anvil forces predicted by the model for the different welding conditions.
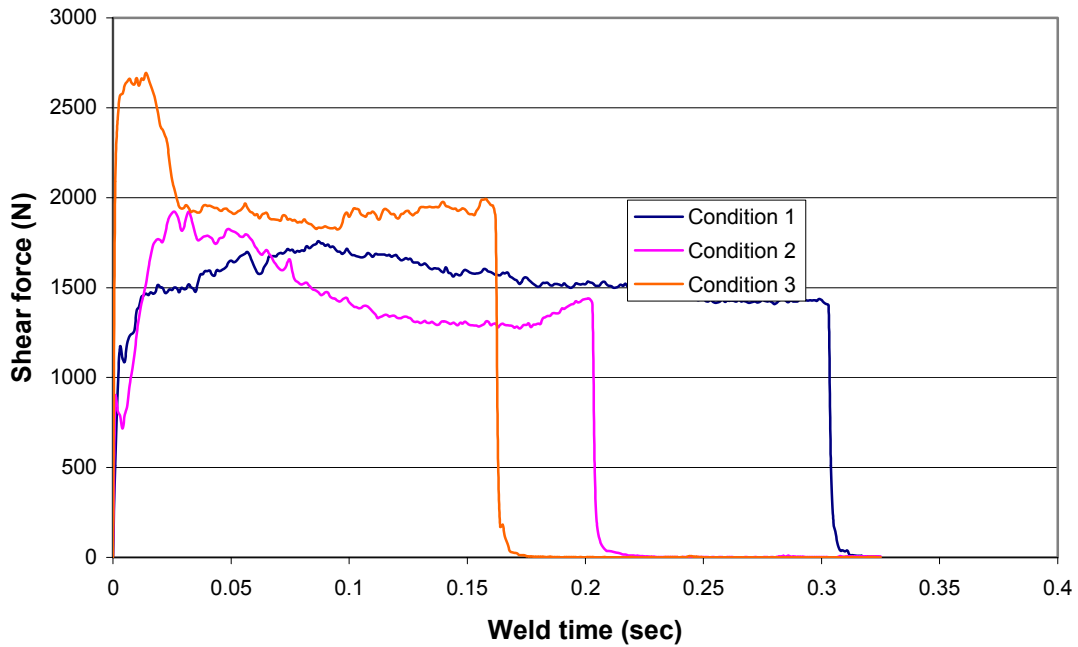
Figure 6.82: Measured anvil forces for the three welding conditions.

212

It is interesting to note the relative values and general shapes of the curves in figure 6.82 (realizing the absolute values are too high as shown in 6.4). The force curve for welding condition 1 (i.e. low pressure, high friction) rises relatively slowly and levels off slowly and has the lowest peak value. The curve for welding condition 2 (high pressure, lubricant) rises more quickly and levels off more quickly then the curve for welding condition 1. The peak value for welding condition 2 is higher than for welding condition 1; it is reached after approx. 0.03-0.04sec. The curve for welding condition 3 has the highest peak value and rises very rapidly, after a short period of time (approx.0.02s) the force drops rapidly and remains constant. Looking at these curves it has to be kept in mind that the weld time reflects the advent of sonotrode extrusion and severe sonotrode adhesion for the respective welding conditions.

The calculated interface forces (figure 6.81) are very similar in shape to the measured forces, as are their relative values. For welding condition 1 sonotrode force and interface force do not cross over up to a time of 0.4s. For welding condition 2 the forces cross over at 0.12 sec and for welding condition 3 at 0.04 sec. The maximum force is reached between 0.04-0.05sec for welding condition 2 and at 0.03sec for welding condition 3. These times are in very good agreement with the measured forces, as one can see easily by comparing figure 6.81 to 6.82 for each individual welding condition. The slope of the curves at their cross over seems to be indicative of the sharpness of the advent of sonotrode extrusion. It was realized during the experiments that for welding condition 3 extrusions occurred very abruptly and with varying intensity. The weld strength values achieved are also very unstable (see figure 6.64).

It is now possible, in light of the modeling results, to interpret the sharp drop in force after a short weld time using welding condition 3. According to the calculated results, sonotrode and interface forces might have crossed so that sonotrode and interface forces became equal (according to equation 6-21), and partial extrusion occurred. The force measured after that drop off is in fact the maximum sonotrode force. Thus, with this model it was possible to verify the experimental results and offer explanations for certain features in the measured force.

In summary, it has been possible to predict not only an unstable weld condition under which sonotrode sticking occurs, but also which welding conditions would be stable, for what period of weld time. Also the shape of the measured force curves could be replicated with great accuracy. With this model it will be possible to calculate the influence of changes in the welding process. As an example one could calculate the impact on the interface forces, when the thermal conductivity of the anvil is changed and due to this, changing the amount of heat conducted away from the interface. The temperatures at the interface and at the sonotrode could then be analyzed as well as the forces that occur during welding. It is also possible to increase the thickness of the parts, and then calculating the forces (by assuming one could actually achieve a weld area growth similar to what has been used in the calculations in this section, which is of course not possible with the equipment used here) that would have to occur during welding.

6.9 The mechanics and mechanism of USMW

A summary will now be presented, describing how the theoretical mechanical and thermal considerations, developed in the forgoing, better define the USMW process. The weld will be shown, under proper conditions, to occur in two steps (or phases). Only under so-called "overwelding" will a third undesirable step, be seen to emerge. It may be recalled, from section 3.2, that Wodara described USMW as a three phase process based on the metallurgical events taking place during welding. The description set forth here will be distinct from that.

A fundamentally different approach has been taken here from prior work. As evident by the nature of the developments in this dissertation, the overall mechanism of welding, and hence the three welding phases suggested here, are based on a mechanical or continuum mechanics, versus metallurgical, model of the process. The main underlying idea of this model of weld evolution is that the force acting on the sonotrode is comprised of three components (as described in chapter 4).

The three force components are the welding force (F_W), frictional force (F_{FR}) between the parts and the excitation force (F_{AM}) which is dependent on the top part geometries and boundary conditions. F_W and F_{FR} can be combined to the weld interface force (F_I). The welding force F_W is the force component that causes the plastic deformation at the interface and is responsible for the weld development. Or more accurately, F_W is the force that is necessary to plastically deform the deformation zone at a given temperature and weld area. The frictional forces do not contribute to the plastic

215

deformation or weld development, but only act to hinder the relative movement of the parts. The magnitude of this force depends on the friction coefficient of the parts and the normal force. The excitation force F_{AM} needs to be considered for top parts which have dimensions close to anti-resonance or if the top part is fixed close to the weld. Anti-resonance effects can occur theoretically in all vibration modes of the top part. The case of longitudinal anti-resonances that was examined in section 6.4 was one example of this effect, but in-plane shear vibrations of a beam and various in-plane plate vibration modes can lead to this effect as well.

As a generalization it can be said, that if the weld is attempted at an anti-resonance point, where the driving point impedance has a singularity, it will not be possible for the sonotrode to vibrate the top part with a given velocity or amplitude, so that a weld will not be possible. The reason for this is that the sum of all forces is limited by the temperature dependent material properties and sonotrode area. This maximum sonotrode force is given by equation 4-1. If these forces exceed the shear yield strength (at the sonotrode) then sonotrode motion relative to the top part and yielding of the top part at the sonotrode top part interface occurs. This would then lead to sonotrode sticking and extrusion of material and to inferior weld strength, because the relative movement between those two parts would decrease. In figure 6.83 it is schematically illustrated how the force components develop during welding.

216
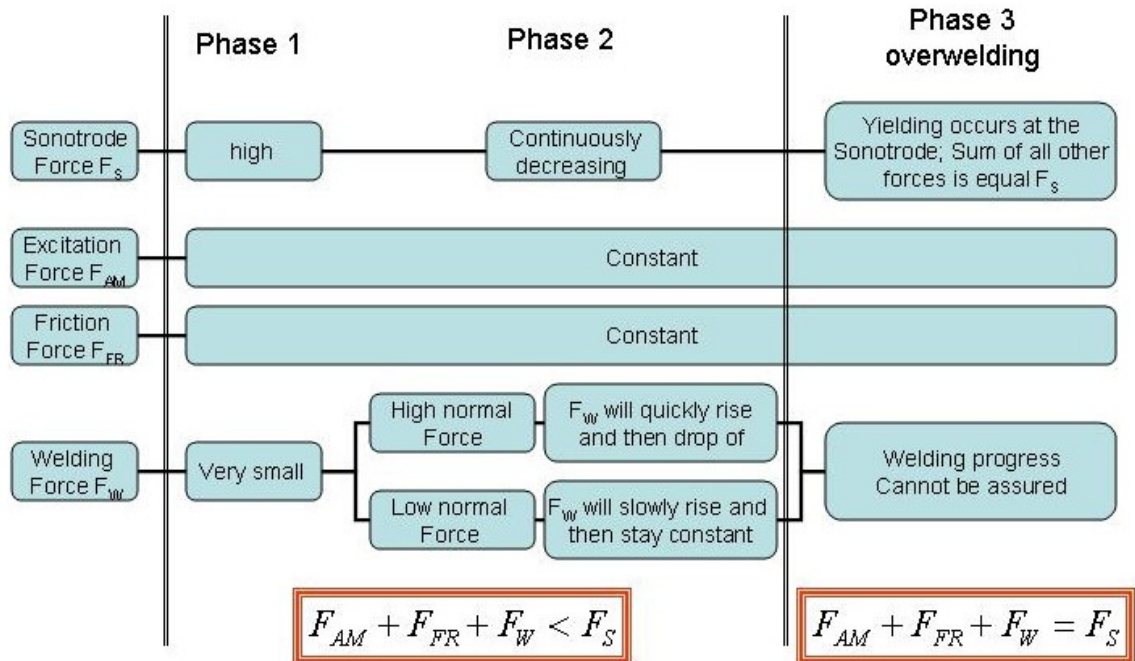
Figure 6.83: Schematic of the Forces during welding.

Another important aspect of the welding process is the heat generation in the deformation zone and the surrounding friction area. The heat generated has an effect during the weld progression and on the material properties of the parts. In general, the heat generation in the deformation zone decreases with decreasing yield strength. At this point one needs to recall figure 4.18. It shows schematically the deformation islands within the deformation zone. The deformation zone is comprised of many of these islands, which ultimately grow together, so that the entire deformation zone is covered.

Since the volume of these islands is very small compared to the base materials and the heat generation rate at low temperatures is very high (initially the parts are cold), the heat generated within the deformation can be regarded as uniformly distributed. The

217

heat generation due to friction is approximately constant during one welding cycles. The heat generated and the heat conducting into the parts will very quickly reach a quasi equilibrium. The modeling results predict this equilibrium temperature after approximately 0.2sec (see figure 6.75 the point in time when the temperature increases only very slowly). The heat generated by friction during the welding process plays a role in the latter stages during welding. In the latter stages the heat generated by plastic deformation will become small because only little force is necessary to plastically deform the material. Since the heat input due to friction is approximately constant during the weld cycle, the continued generation of heat will effect the final temperature of the weld. As a generalization it can be said that everything else being equal, that the final temperature will be increased with increased friction force.

This general phenomenology will now be organized into a mechanics based 'three phases of welding.'

Phase 1: Weld initiation, coupling between the parts

In the 1st phase, the sonotrode penetrates the top surface of the top part and is anchored to it. At the end of the 1st phase sonotrode and top part will move together. In this phase the friction force is acting against the sonotrode movement (independent of velocity). The duration of this phase for the welding conditions used in this study was approximately 10 ms but never longer then 20 ms (out of a typical 0.2s to0.3s for a full weld cycle).

218

Phase 2: The formation of the weld

This phase begins when the top part has become fixed to the sonotrode. The intense plastic deformation inside the weld area will cause a significant temperature increase at the interface. This heat input from the deformation zone will in turn heat up the parts, sonotrode and anvil. This temperature increase leads then to a change in material properties, away from the immediate weld area. Since the heat is generated at the interface between both sheets there will be a temperature gradient throughout the cross section of the sheets. The temperature in the vicinity of the sonotrode will rise very quickly. The shear yield strength of the metal at the interface will decrease; therefore the shear force necessary to cause the plastic deformation at the interface will also decrease, assuming the weld area remains constant.

Simultaneously the shear yield strength of the material at the sonotrode-top part interface will also decrease, so that the limit sonotrode force steadily decreases. This will cause a problem, because the excitation and the friction forces are unaffected by the temperature increase. The result is that the temperature at the sonotrode will always rise to a point were the material elastic limits are exceeded and extrusion and sonotrode welding occurs.

The conditions described here gives some guidance in predicting welding conditions for which the interface force exceeds the limiting sonotrode force very rapidly, leading to unstable welding conditions (see condition 3 in section 6.8). In a properly made weld a balance has to be found between weld area growth and heat development, so

that the weld area has grown to its full extent and the process can be terminated prior to entering the third phase.

Phase 3: Overwelding, sonotrode sticking

The 3rd phase starts when the excitation force and the interface forces exceed the limiting sonotrode force given in equation 4-1. The plastic deformation leads to an instability in the welding process. Because of the relative motion between top part and sonotrode the velocity at the interface will be reduced thereby causing a drop in temperature and an increase in welding force. On the other hand the plastic deformation at the sonotrode will cause heating at that location, thus reducing the maximum sonotrode force even further. The temperature increase at the sonotrode surface will then promote sonotrode adhesion and material build up in the knurl pattern. The welding process has literally shifted from the weld interface to the sonotrode top part interface. It is because of this instability that it is absolutely imperative that relative motion between sonotrode and top part must not happen.

While USMW has now been described in terms of three phases, as already noted, a "good" ultrasonic weld is, in fact, a two-phase process. If the welding parameters are such that the third phase is reached, then one has failed in making a "good" weld.

CHAPTER 7

CONCLUSIONS

A mechanics based model for USMW has been developed which can successfully predict the interface forces during welding and their effect on the weld quality. This model, based on the forces and temperatures that occur during welding is applicable for a wide variety of welding problems. The limitations are given by the particular geometry of the sonotrode surface. In this case a knurled flat sonotrode was used, which made it possible to use the two dimensional stress state to calculate the yield condition.

The model explains the influence of material properties and surface conditions as well as process variables such as vibration amplitude and normal force on the weld behavior. It is now known what forces are necessary to produce a weld and how they are influenced.

The surface condition, in particular the friction coefficient of the material has been found to be very important on weld quality and avoidance of sonotrode welding. The influence of the geometry of the welded parts on the weld quality has been known for a long time, but has not received proper attention. The top part dimensions and boundary conditions have a crucial influence on the weld quality. In this study the forced vibration problem for the top part has been solved. The solution for the problem of

longitudinal vibrations serves as an example how much more complex problems can be tackled. This result also showed that the length of the extension of the top part has to be considered as compared to the total part dimensions. The forced vibration problem predicted exactly for what top part extension dimensions welding is not possible. It is expected that for complex structures FEA methods are needed to solve for the "ideal" weld locations, i.e. locations were the driving point impedance is as low as possible. FEA methods were also used to model the heat generation and conduction during the USMW process, because an analytical description would become very complicated.

With the presented model and calculations, two very unfavorable welding conditions could be explained and predicted. First, the case of top part anti-resonance was calculated and it was shown that for that condition welding is impossible. By measuring the anvil forces the judgment can be made if extrusion and sonotrode welding occurred due to high interface forces or, if it occurred because of top part anti-resonance. Second, it has been shown that excessively high interface forces due to high friction or very rapid weld area growth can also lead to an unstable welding condition.

The results of this study lead to first trials of ultrasonic projection welding (USPW). The use of USPW (Appendix E) can theoretically lead to a great improvement in weld quality consistency and sonotrode sticking issues. The greatest advantage would be that the forces at the interface can never exceed the maximum sonotrode force, because of the temperature gradient within the parts and the lack of friction outside the weld area. Initial trials indicated a great improvement in weld strength when thicker sheet material was welded. Further research is necessary about this process variation, but theoretical advantages are evident.

BIBLIOGRAPHY

[1] Devine, J. Sonobond Ultrasonoics, personal conversation.

[2] Foster, R. AmTech Ultrasonics, personal conversation.

[3] Adam, T., "Ultraschallschweissen ausgewaehlter Aluminiumlegierungen mit erhoehter Festigkeit", Dissertation, Otto von Guericke University, 1998.

[4] Ward, S. Ford Motor Company, personal conversation.

[5] Johns, J., DePrisco, C.,"The Application of Ultrasonic Energy to Cold Welding of Metals", Research report n. 53-77, Aeroprojects Inc. November,1953.

[6] US Patent, 3,695,500.

[7] de Vries, E., "Development of ultrasonic welding process for stamped 6000 series Aluminum", Diploma Thesis, University of Applied Science, Emden, 2000.

[8] Jones, J.; Powers, J., "Ultrasonic Welding", The Welding Journal, Aug. 1956, pp761-766.

[9] Aljochin, V., Wodara, J., Eckhardt, S.,"Ein Beitrag zur Verbindungsbildung beim Ultraschallschweissen von Metallen", Wissenschaftliche Zeitschrift der Technischen Hochschule Otto von Guericke, Magdeburg 24 (1980) Heft 1, pp. 63-66.

[10] Niebuhr, F., Stoeckel, D., "Ultrasonic metal welding-an alternative or replacement process", DVS Berichte 1981, pp. 128-135.

[11] Dippe, W.; Heymann, E., "A survey of the theories and applications of the ultrasonic welding of metal", Wissenschafltliche Zeitschrift der Technischen Hochschule "Otto von Guericke" 1967, pp. 701-711.

[12] Baladin, G., Kuznetsov, V., Silin, L., "Fretting action between members in the ultrasonic welding of metals", Welding Production 1967, n. 10, pp. 77-80.

[13] Pfluger, A., Sideris, X., "New developments in Ultrasonic Welding", Sampe Quarterly, Oct. 1975, v. 7, n. 1, pp. 9-19.

[14] Neville, S., "Ultrasonic welding", British welding Journal 1961, pp. 177-187.

[15] Ginzburg, S., Mitskevich, A., Nosov, Y., "Formation of the Joint in Ultrasonic Welding", Welding Production, May 1967, v.13, n. 5, pp. 45-47.

[16] Jones, J., Powers, J., "Ultrasonic Welding", The Welding Journal, Aug. 1956, pp. 761-766.

[17] Weare, N., Antonevich, J., Monroe, R., "Fundamental Studies of Ultrasonic welding", Welding Research Supplement 1960, pp. 331-341.

[18] Chang, U. I., Frisch, J., "On Optimization of Some Parameters in Ultrasonic Metal Welding", Welding Journal, Jan. 1974, v.53, n. 1, pp. 24-35.

[19] Rozenberg, L., Mitskevich, A., "Ultrasonic welding of Metals", Physical Principles of Ultrasonic Technology, V.1, Part 2, Acoustic Institute Academy of Sciences of the USSR, Moscow, USSR,1970, Plenum Press, New York 1973.

224

[20] Harthoorn, J., "Joint formation in Ultrasonic Welding compared with fretting Phenomena for Aluminum", Ultrasoncis International 1973, Conference Proceedings, pp. 43-51.

[21] Harthoorn, J., "Ultrasonic metal welding", Dissertation, Technical University Eindhoven, 1978.

[22] Joshi, K., "The Formation of Ultrasonic Bonds between Metals", Welding Journal, December 1971, No.12, pp. 840-848.

[23] Heymann, E., Koehler, B., "Influence of the work piece preparation on Ultrasonic Welding", ZIS-Mitteilungen, Jan. 1969, v.11, n. 1, pp. 180-190.

[24] Mindlin, R. D., Mason, W. P., Osmer, J. F., Deresiewicz, H., "Effects of an oscillating tangential force on the contact surfaces of elastic spheres", Proceedings of the first National Congress of Applied Mechanics, 1953, pp. 203-208.

[25] Kreye, H., Wittkamp, I., "On the bonding mechanism in Ultrasonic Spot welding", Schweissen & Schneiden, Mar. 1975, V.27, n. 3, pp. 97-100.

[26] Kreye, H., "Melting phenomena in solid state welding processes", Welding Journal, V.56, n. 5, May 1977, pp. 154-158.

[27] Heymann, E., Pusch G., " Contribution to the study of the role of recrystallisation in the formation of the joint in ultrasonic welding", Schweisstechnik, Dec. 1969, v.19, n. 12, pp. 542-545.

[28] Beyer, W., "The bonding process in the ultrasonic welding of metals", Schweisstechnik, Jan. 1969, v.19, n. 1, pp. 16-20.

[29] Hazlett, T., Ambekar, S., "Additional Studies on Interface temperatures and bonding mechanism of Ultrasonic welds", Welding Journal, May 1970, pp. 196-200.

[30] Pfluger, A., Sideris, X., "New developments in Ultrasonic Welding", Sampe Quarterly, Oct. 1975, v. 7, n. 1, pp. 9-19.

[31] Stemmer, R., "Factors affecting bonding of Copper and Aluminum to glass by Ultrasonic joining", Metall, Nov. 1968, n. 22, pp.1103-1108.

[32] Reuter, M., Roeder, E., "Ultrasonic welding of Glass and Glass-Ceramics to Metal", Schweissen Schneiden, 45 (4), E62-E65, Apr. 1993.

[33] Wodara, J., "Joint formation in the Ultrasonic welding of Metallic Substances", ZIS-Mitteilungen, 1986, v.28, n. 1, pp. 102-108.

[34] Mitskevich, A., Ginzburg, S., Kholopov, Y., "On the Mechanism of the Ultrasonic welding of metals", Ul'trzvuk. Tekh., n. 2, p. 7, 1966.

[35] Wittke, K., "The system of processes to produce unbreakable joints", Schweisstechnik, Berlin 22, 1972, n. 3, pp. 97-100.

[36] Nikolalew, G.A., Olschanski, N.A., "Special welding Methods", Moscow: Publisher Maschinostrojenije 1975.

[37] Karakosow, E.S., "Joining of Metals in the Solid State", Publisher metallurgy 1976.

[38] Abramow, W.W., Efimow, W.A., "Plastic deformation of Weld Materials and calculation of the welding regime for Pressure Welding with preheating", Moscow: Industry for medicine technology, 1976, n. 10, pp. 1-56.

226

[39] Aljochin, V. P., "Basics of the joint formation in the Solid Phase", Talk on the RGW-specialists conference to the topic "Ultrasonic Welding", Nove Mesto nad Vahom, CSSR, 1977.

[40] Thiele, M., "On the weldability of the material combinations Al/Al, Al/Au, on the substrate $GaAs_{0.6}P_{0.4}$ with consideration of automatic welding processes" Dissertation A, Humboldt-University, Berlin 1983.

[41] Eckhard, S., "Model of the thermal and mechanical processes during Ultrasonic Welding of metals", Dissertation A, TH Magdeburg 1983.

[42] Neumann, A., Krause, W., "Contribution to the basics of estimating the friction weld ability of material combinations", ZIS-Mitteilunge, Halle 26, 1984, n. 1, pp. 79-86.

[43] Wodara, J., Eckhardt, S., "Use of Thermovision in Ultrasonic welding" Schweisstechnik, June 1982, v. 32, n. 6, pp. 247-249.

[44] Wodara, J., Eckhardt, S., "Determination of temperature fields in the ultrasonic welding of metals", Schweisstechnik, Oct. 1982, v. 32, n. 10, pp. 436-437.

[45] Richter, H., "Investigations into the processes involved when joining together metallic materials by means of ultrasonic welding", Schweissen und Schneiden, Feb. 1970, v. 22, n. 2, pp. 70-73.

[46] Neppiras, E., "Ultrasonic welding of metals" Ultrasonics, July-Sep. 1965, v. 3, pp. 128-135.

[47] Jones, J., Maropis, N., Thomas, J., Bancroft, D., "Fundamentals of Ultrasonic Welding" Phase I , Aeroprojects Incorporated Research Report No. 59-105, May 1959.

[48] Jones, J., Maropis, N., Thomas, J., Bancroft, D., "Fundamentals of Ultrasonic Welding" Phase II , Aeroprojects Incorporated Research Report No. 60-91, December 1960.

[49] Okada, M., Shin, S., Miyagi, M., "Joint mechanism of Ultrasonic welding", Japan. Inst. of Metals, 1963, v. 4, pp. 250-256.

[50] Baladin, G., Silin, L., "Methods for obtaining steady conditions in the Ultrasonic Welding of Metals", Welding Production 1961, No.12, pp. 1-6.

[51] Wagner, J., Schlicker, U., Eifler, D., "Bond formation during the ultrasonic welding of ceramic with metal", Schweissen Schneiden, 50, No.10, pp. 636, 638, 640-642.

[52] Mason, W., "Electromechanical Transducers and Wave Filters", Second Edition, October 1948, D. van Nostrad Company, Inc., Princeton, New Jersey.

[53] Povstyan, V., Kholopov, Yu. V., "An approximate method of calculating power in the ultrasonic welding of metals" Automatic Welding, V 30, n. 12, Dec.1977, pp. 44-45.

[54] Bilgutay, N., Li, X.; McBrearty, M., "Development of non-destructive bond monitoring techniques for ultrasonic bonders." Ultrasonics, V.24, n. 6, Nov.1986, pp. 307-317.

[55] Kuznetsov, V., Silin, L., "On-line Control of ultrasonic welds in Copper sheet" Welding Production, 1966, v.13, n. 10, pp. 10-17.

[56] Grigorashvili, Y., Sheel, W., Thiede, M., "Characterizing Ultrasonic Weld Joints by Measuring the Electrical Transition Resistance", Schweisstechnik, vol. 34, no 10, pp.468-470, 1984.

[57] Wodara, J., Sporkenbach, D., "Choice of suitable measurement parameters for the control of ultrasonic welding processes", Wissenschaftliche Zeitschrift der Technischen Hochschule Otto von Guericke Magdeburg, 1985, v.29, n. 8, pp. 77-88.

[58] Adam,T., Martinek, I., Wodara, J., "Quality assurance in ultrasonic welding of metallic materials", DVS Berichte, #170, Welding and cutting '95, Proceedings, Conference Dresden, pp. 305-309.

[59] Wodara, J., "Relation between component geometry and the quality of ultrasonically welded metallic joints", Wissenschaftliche Zeitschrift der Technischen Universitaet Otto von Guericke Magdeburg, Aug. 1989, v. 33, n. 8, pp. 64-68.

[60] Vitek, J., Miklanek, L., "Technological requirements for quality assurance at the ultrasonic welding of Metals", Schweisstechnik, 1978, v.28, n. 7, pp. 316-317.

[61] Welding Handbook (4th edition) Sec.3. American Welding Society, New York, 1964.

[62] Jung, G., EWI Project No. 46412

[63] MTI-2000 Fotonic Sensor, Instruction Manual

[64] Huang, T. C., EWI, Project No. 46412

[65] Ultrasonic Weld Monitor User Manual, EWI

[66] Thermovision 550, Operating Manual, Agema Infrared Systems

[67] IRwin Research 2.01, Operating Manual, Agema Infrared Systems

229

[68] http://www.visiblesolutions.com/

[69] Kaufman, J.,"Properties of aluminum alloys : tensile, creep, and fatigue data at high and low temperatures" Materials Park, Ohio: ASM International, Washington, D.C.: Aluminum Association, c1999.

[70] Instruction manual "Pocket Surf" by Federal.

[71] Stokes, V., "Vibration Welding of Thermoplastics. PartII: Analysis of the welding Process", Polymer Engineering and Science, June 1988, v.28, n.11.

[72] http://www.crispconsortium.com/docs/contmech.pdf

[73] http://www.efunda.com/formulae/solid_mechanics/mat_mechanics/plane_stress_principal.cfm

[74] Sonobond Ultrasonics, Instruction Manual 2025FC

APPENDIX A

THE TWO DIMENSIONAL STRESS STATE AND THE

CORRESPONDING SHEAR YIELD CONDITION

A.1 The two dimensional stress state

Here a closer look shall be taken at stresses in general to clarify Trescas yield stress criteria. One can consider one little cube inside the deformation zone in the weld interface (figure A.1) [72], [73].
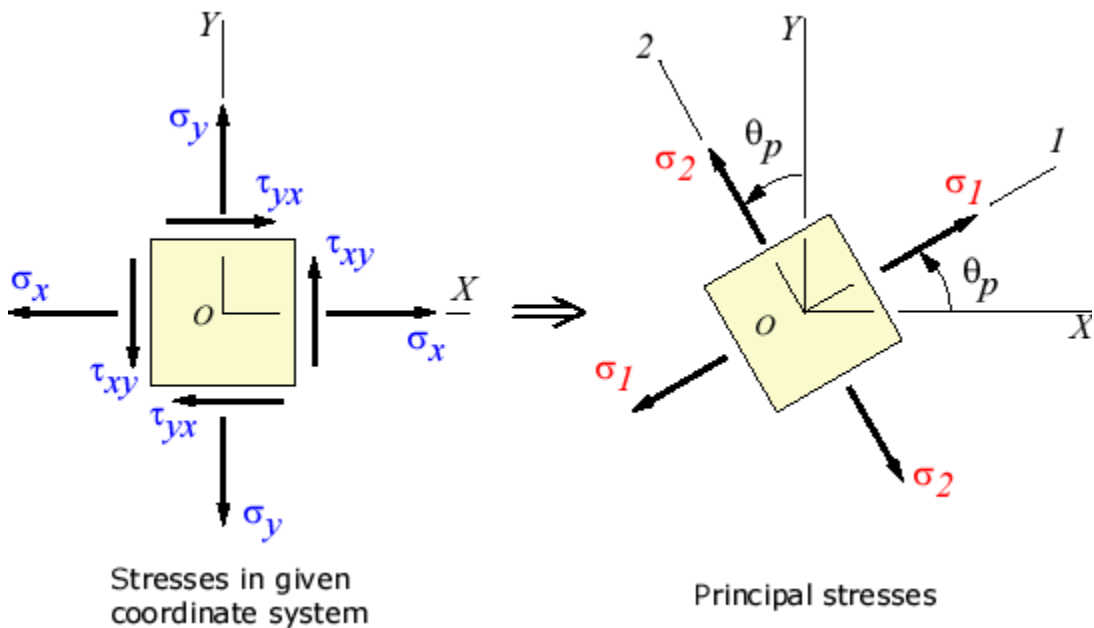
Figure A.1: The real stress state and its transformation into the principal stress state [72].

In the case at hand σ_y is a compressive stress depending on the normal pressure applied from the sonotrode ($\sigma_y(F_N)$) and $\sigma_x=0$. The shear stress τ_{xy} is unknown but it has to be sufficiently large, that plastic deformation (yielding) takes place. These stresses can

then be transformed into the principal stresses where all shear stresses are zero using equation A-1 and A-2.

$$\tan 2\theta_P = \frac{2\tau_{xy}}{\sigma_x - \sigma_y}$$ (Eq.A-1)

$$\sigma_{1,2} = \frac{\sigma_x + \sigma_y}{2} \pm \sqrt{\left(\frac{\sigma_x - \sigma_y}{2}\right)^2 + \tau_{xy}^2}$$ (Eq.A-2)

For the case at hand (σ_x=0) the resulting angle and principal stresses are given in equations A-3 to A-5.

$$\theta_P = \frac{1}{2} * \tan\left(\frac{2\tau_{xy}}{\sigma_y(F_N)}\right)$$ (Eq.A-3)

$$\sigma_1 = \frac{\sigma_y(F_N)}{2} + \sqrt{\left(\frac{\sigma_y(F_N)}{2}\right)^2 + \left(\tau_{xy}\right)^2}$$ (Eq.A-4)

$$\sigma_2 = \frac{\sigma_y(F_N)}{2} - \sqrt{\left(\frac{\sigma_y(F_N)}{2}\right)^2 + \left(\tau_{xy}\right)^2}$$ (Eq.A-5)

A.2 Yield functions

The basic idea of a yield function for a two dimensional stress state is, to hold one stress constant and increase the second stress perpendicular to it until yielding occurs. In the case of ultrasonic welding the shear stress at the interface has to be increased to the point that yielding occurs within the weld zone. The yield function then describes the combinations of stresses that cause yielding.

A.3 Tresca's yield function

In Tresca's yield function yielding takes place when the maximum value of $|\sigma_1-\sigma_2|$, $|\sigma_2-\sigma_3|$ or $|\sigma_3-\sigma_1|$ equals a critical value (2k) which is the yield stress in uniaxial tension. This can be interpreted (by considering Mohr's circles) as being equivalent to limiting the maximum shear stress on any plane in the material to being less then or equal to k (figure A.2).
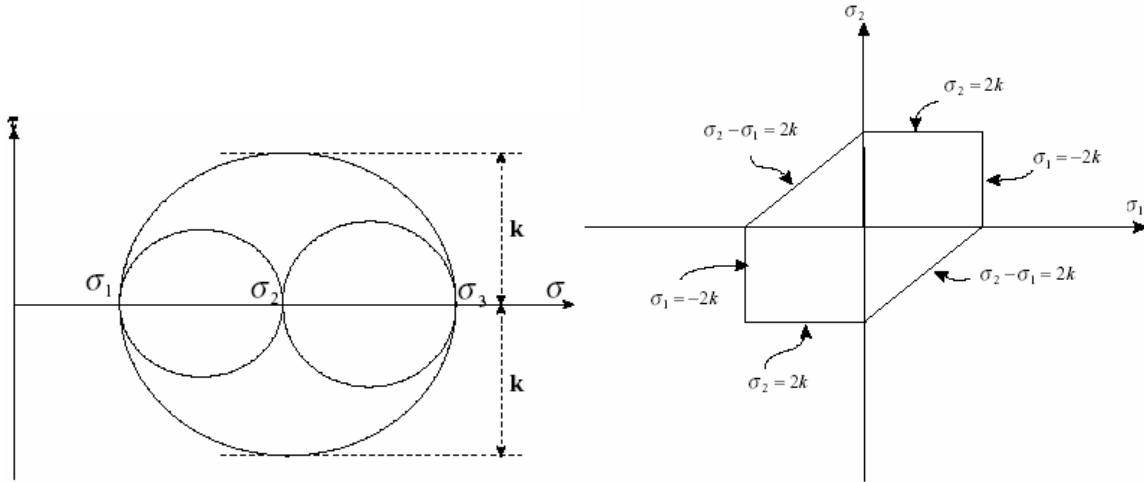
Figure A.2: Mohr's circle to interpret k and Tresca's yield function [71].

In figure A.2 the resulting yield function for the two dimensional stress space is illustrated as well. For the case at hand, the absolute values of the stress differences have to be evaluated, in this case $\sigma_3 = 0$.

The result is:

$$|\sigma_1 - \sigma_2| = 2 * \sqrt{\left(\frac{\sigma_y(F_N)}{2}\right)^2 + (\tau_{xy})^2}$$

$$|\sigma_2 - \sigma_3| = \frac{\sigma_y(F_N)}{2} - \sqrt{\left(\frac{\sigma_y(F_N)}{2}\right)^2 + (\tau_{xy})^2}$$ (Eq.A-6)

$$|\sigma_3 - \sigma_1| = -\frac{\sigma_y(F_N)}{2} - \sqrt{\left(\frac{\sigma_y(F_N)}{2}\right)^2 + (\tau_{xy})^2}$$

It can easily be shown, that the first of equations A-6 is the maximum stress difference. Then one can write:

$$2 * \sqrt{\left(\frac{\sigma_y(F_N)}{2}\right)^2 + (\tau_{xy})^2} = 2k = Y \Leftrightarrow \tau_{xy} = \sqrt{\frac{Y^2}{4} - \frac{\sigma_y(F_N)^2}{4}} \qquad \text{(Eq.A-7)}$$

To solve for the unknown shear stress τ_{xy} that is necessary to cause plastic shear deformation in the volume inside the weld interface. The necessary shear force (F_S) is then related to the shear stress through:

$$\tau_{xy} = \frac{F_S}{A_{weld}} \qquad \text{(Eq.A-8)}$$

APPENDIX B

DRIVING POINT IMPEDANCE ANALYSIS FOR FORCED
LONGITUDINAL ROD VIBRATIONS

B.1   Forced vibrations of a rod

In USMW the extension of the top part can be treated as a rod being exited at one end with a certain velocity, since the vibration velocity of the sonotrode is approximately constant throughout the welding cycle. Given by the vibration amplitude (ξ) of the sonotrode and its vibration frequency (ω), the velocity equation is:

$$v = \frac{d\xi}{dt} = \Omega * \xi * \sin(\Omega t + \phi) \qquad \text{(Eq.B-1)}$$

Typical values in USMW are 10-50µm for the amplitude and $2\pi*20000Hz$ for the circular frequency. The forces are unknown to this point but are limited by the shear yield strength of the aluminum at the sonotrode top part interface and the area of that interface. Solving the one dimensional wave equation

$$\frac{\partial^2 u}{\partial x^2} = \frac{1}{c^2}\frac{\partial^2 u}{\partial t^2} \qquad \text{(Eq.B-2)}$$

for the velocity excited/free rod and calculating the excitation forces, one gets:

$$F(x,l) := E \cdot A \cdot \left(\xi_0 \cdot \tan\left(\frac{\Omega}{c} \cdot l\right) \cdot \cos\left(\frac{\Omega}{c} \cdot x\right) \cdot \frac{\Omega}{c} - \xi_0 \cdot \sin\left(\frac{\Omega}{c} \cdot x\right) \cdot \frac{\Omega}{c} \right) \qquad \text{(Eq.B-3)}$$

Equation B-3 is the solution for the forces acting at any given point x in the rod for certain length's l. Using for $E=68*10^9$Pa, $A=12.7$mm^2, $\xi_0=10\mu$m, $c=5018$m/s and $\Omega=2*\pi*20000$Hz one can calculate the forces acting at x=0 (excitation point) depending on the rod length (l). The resulting graph is shown in fig.B-1. The result can be compared to the resulting force if only rigid body motion is considered. The forces necessary to excite rigid body motion only can be calculated with:

$$F_m(l) := \rho \cdot A \cdot l \cdot \Omega^2 \cdot \xi_0$$

(Eq.B-4)

Comparing the two results, one can see that for this problem the forces for rigid body motion and excitation forces start to differ for a part length of approx. 2cm.
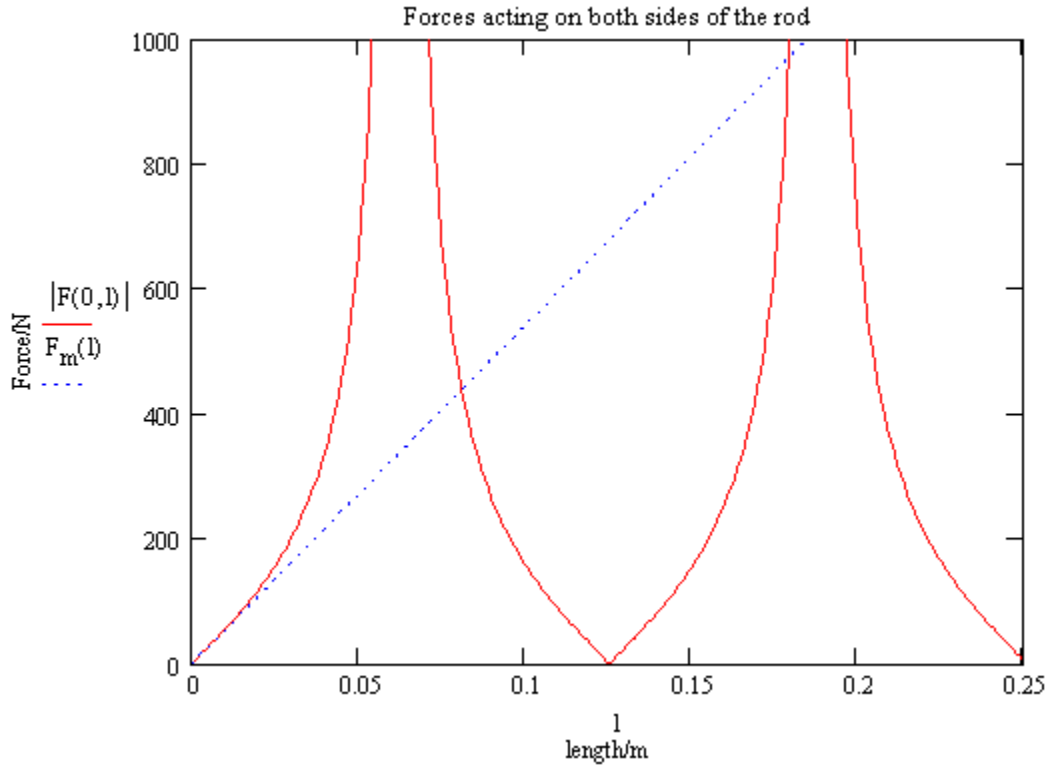
Figure B.1: Forces at excitation point.

The graph clearly shows singularities in the forces at the excitation point if a certain amplitude is maintained. The longitudinal wavelength for aluminum at 20kHz is 0.251m. So the singularities occur for a rod length of $l=(2n+1)/4*\lambda$, while for $l=n/2*\lambda$ the excitation forces vanish.

In the same way one can calculate the forces at excitation point and at the clamped position of the excited rod. The results are shown in fig. 2.

The response for a rod clamped at x=l is:

$$F(x,l) := E \cdot A \cdot \left(-\xi_0 \cdot \cot\left(\frac{\Omega}{c} \cdot l\right) \cdot \cos\left(\frac{\Omega}{c} \cdot x\right) \cdot \frac{\Omega}{c} - \xi_0 \cdot \sin\left(\frac{\Omega}{c} \cdot x\right) \cdot \frac{\Omega}{c} \right)$$

(Eq.B-5)
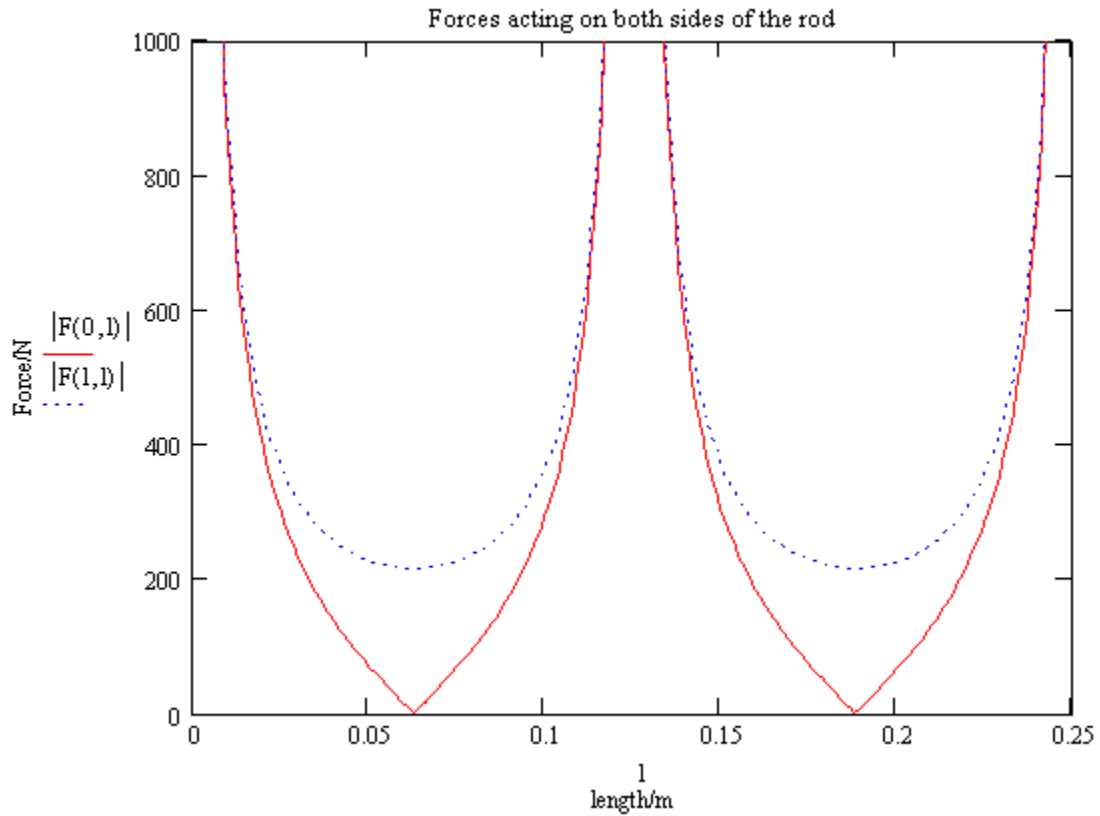
Figure B.2: Forces at excitation and fixed point.

Now the situation is exactly opposite than in case of a free end. The excitation forces vanish at $l=(2n+1)/4*\lambda$ and have singularities at $l=n/2*\lambda$ (for $n=0,1,2..$). Interesting to note here that at the fixed end the forces never vanish but behave generally the same way than the excitation forces.

241

APPENDIX C

OPTICAL 'FOTONIC' SENSOR

Fiber optic level displacement sensors utilize adjacent pairs of light transmitting and light receiving fibers. The operating basis is the interaction between the field of illumination of the transmitting, or source fibers and the field of view of the receiving, or detector fibers. A simplified illustration of this principle is depicted in figure C.1.
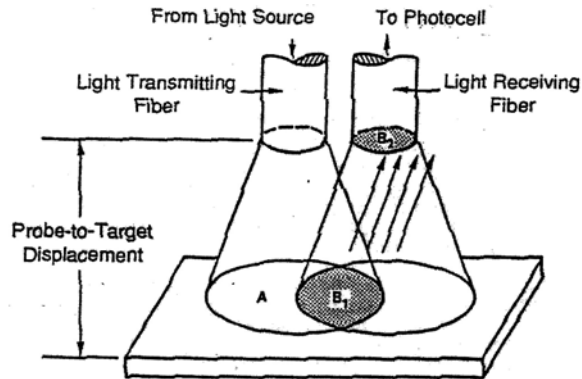
Figure C.1: Displacement sensing method of adjacent fiber optic elements [63].

At contact, or zero gap, all of the light transmitted thru the source fiber is reflected back into the same fiber and no light can be detected by the detector fibers producing zero output. An increase in the probe to target distance will result in some reflected light being captured by the receiving fiber. This relationship between increased distance and more light being captured will continue until the entire face of the receiving fiber is illuminated with reflected light. Further increases in distance will cause the diverging field of reflected light to exceed the field of view of the receiving fiber, thus causing a reversal in the output versus distance response curve shown in figure C.2.

243
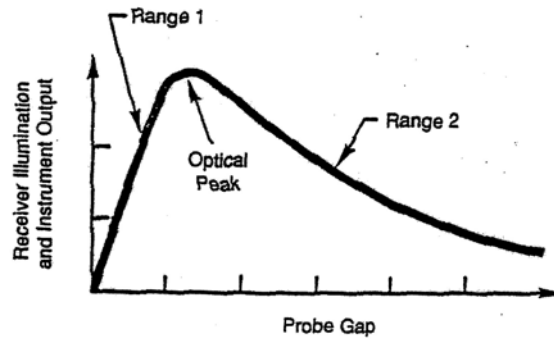
Figure C.2: Typical Fiber-Optic calibration curve [63].

Also shown in figure C.2 are "Range 1", "Range 2" and the "Optical peak".

Range 1 is the initial, highly sensitive positive slope response extending from direct

contact to the optical peak or maximum receiver output. Range 2 is less sensitive,

negative slope of the response extending from the peak to larger gaps. The optical peak

is the zero slope portion of the response curve, where the receiver fibers capture the

maximum amount of reflected light relative to a given amount of source intensity, surface

reflectivity and path attenuation.

The Range 1 characteristic is a function of the fiber diameter, the relative position

of the transmitting and receiving fibers, and the numerical aperture of the fibers. The

Range 2 response characteristic is primarily field intensity depending on the inverse

square law. The measurements were made by storing the signal of the displacement

change with the data acquisition. The voltage of the MTI can then be transformed into

real displacement measurements with following equation:

244

$$Dispacement = SlopeFactor * OtputSignal[mV] \hspace{3cm} \text{(Eq. C-1)}$$

The slope factor is a given constant for each individual sensor. With the data acquisition system used in this study the displacement was calculated automatically by the computer, eliminating the need to do this calculation manually in cases where an oscilloscope was used. Additional details of system operation can be found in [63]

APPENDIX D

DATA ACQUISITION SYSTEM AND ULTRASONIC WELD MONITOR
SOFTWARE

Hardware components

The overview of the complete system consisting of the following components:

- Computer

- Plug-In Data Acquisition Card

- Break-Out Box for transducer connectivity

- Sensors and probes for measuring various inputs at their corresponding USMW system position (current and voltage probe are connected inside the power supply at their appropriate positions).

is sown in figure D.1.
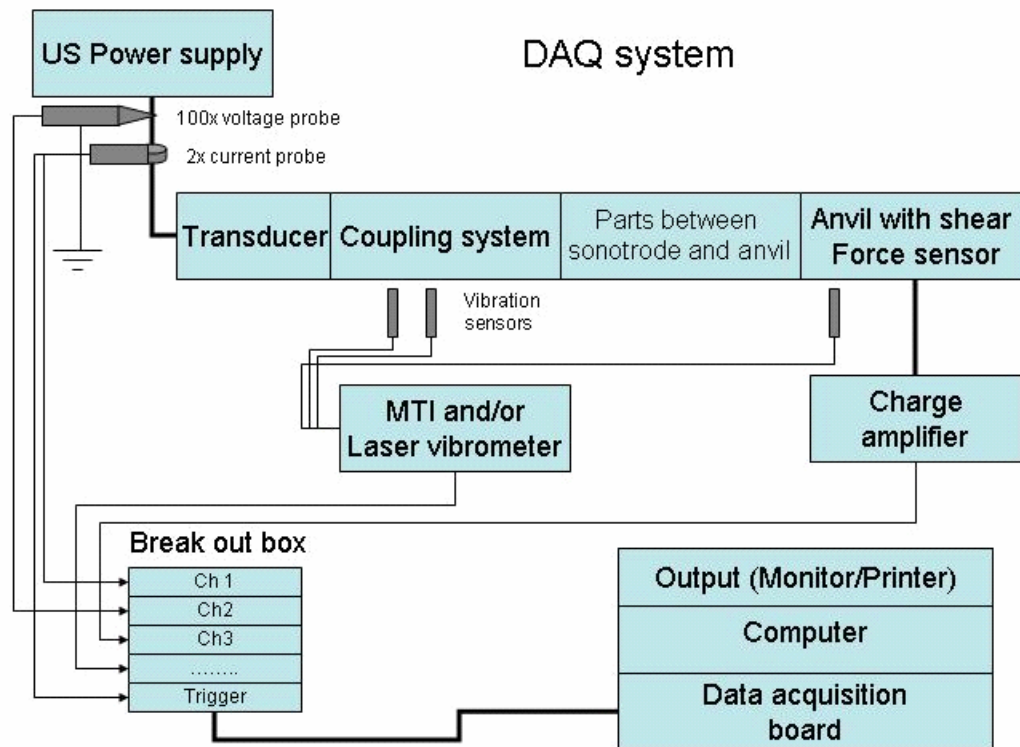
Figure D.1: Ultrasonic welding data acquisition system (DAQ) hardware components.

The computer is a 2.8 GHz DELL® Dimension 4600 desktop computer with the hardware listed in Table 12.

Hardware	Specifition
Processor Speed	Pentium-4 2.8 GHz
Memory Size	512 MB
Hard Drive Size	120 GB
Video	GeForce® MX 440 AGP 8X
Operating System	Windows ® XP Professional

Table 12: DAQ computer specifications.

The Plug-In Data Acquisition Card used is PCI-6070E (PCI-MIO-16E-1) from National Instruments®. This card is selected due to the capability of handling data sampling rates of up to 1.25 MHz for data streaming applications, with a widely accepted driver package that supports a great number of programming environments. The Break-Out Box, (model: BNC-2110 from National Instruments®) responsible for receiving the signals from the transducers into the data acquisition device, was selected for this purpose. This breakout box features up to 8 differential channels of BNC connector inputs for connecting transducers to the data acquisition device. In addition, all of the analog and digital I/O connectors are available on the box, including the trigger connectors used in the software for easy connectivity.

The analysis software

The software allows for rapid input analysis. Channels 0 and 1 are programmed exclusively for current and voltage measured in the power supply. The original 20kHz signal is immediately multiplied by the proper scaling factors and is then broken up into 1ms intervals and the RMS values of these 1ms intervals are then calculated with following equation:

$$V_{RMS} = RMS(\sum_{i=1}^{n} V_i), I_{RMS} = RMS(\sum_{i=1}^{n} I_i), \qquad \text{(Eq. D-1)}$$

Where: V_{rms} and I_{rms} are arrays of data points after reduction.

$$RMS(Power) = V_{RMS-i} \times I_{RMS-i}, \qquad \text{(Eq. D-2)}$$

Where: $RMS (V_i)$ and $RMS(I_i)$ are individual points of readings (*RMS Power* is an array)

$$RMS(R) = V_{RMS-i} \div I_{RMS-i}, \qquad \text{(Eq. D-3)}$$

Where: $RMS (V_i)$ and $RMS (I_i)$ are individual points of readings (*RMS Resistance* is an array)

From the RMS current and the RMS voltage the RMS power and resistance are calculated. The phase angle between voltage and current is measured as well, to have the possibility to correct the power curve in case the phase angle exceeds reasonable values (reduction of RMS power 6% for a phase angle of 20^0).

For channels 2-7 the input is multiplied by the proper scaling factor as well, and then the maximum and minimum values in 1ms intervals are found to calculate the

average maximum from those two values (this is done to compensate for any offset in the original signal).

The DAQ enables any operator to analyze power, force, vibrations, etc. immediately after a weld is done.

APPENDIX E

ULTRASONIC PROJECTION WELDING

It has been learned from this study that friction forces at the interface and the reduction in contact stress for increasing part thickness are very undesirable. Therefore a new method of ultrasonic metal welding has been developed, identified here as "Ultrasonic projection welding", in an effort to eliminate or reduce the effects of friction in the weld process. For example, using the projection technique, it was found possible to increase the weld strength from 500N to 2500N for 2 mm sheets, while using the same welding parameters.

In the projection concept, it was found that if the top part was indented at the weld location, thicker material could be successfully welded. In figure E.1 a cross section of an ultrasonic projection weld is schematically shown. In this case the projection (or dent) in the
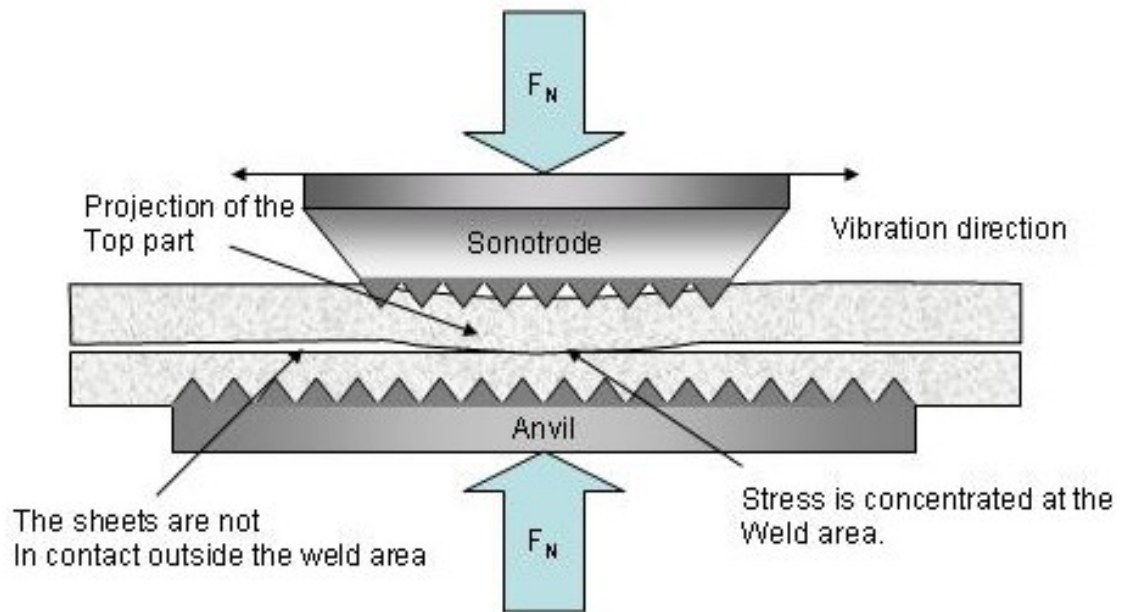
Figure E.1: Schematics of an ultrasonic projection weld.

top part was made with a center punch and a hammer. This was of course a very crude way but already showed the great potential for this application. Not only does this new welding process improve the weld strength of thicker sheets, but it also makes the process less sensitive to different surface conditions, especially different amounts of surface lubrication. The excitation forces for the top part still need to be considered.

More work is necessary to explore all the benefits of this new kind of USMW, for example the best dimensions for the projections have to be found and the welding parameters have to be optimized. In future applications, when for example stamped parts are welded, the projections could be stamped right into the part at predetermined weld locations, with no added cost.